

# Mission Planning Tool for space debris studies with the MeerKAT radar

**Ashiv Rao Dhondea**

BSc(Eng) UCT

*A dissertation submitted to the Department of Electrical Engineering,  
**University of Cape Town,**  
in fulfilment of the requirements for the degree of  
**Master of Science in Engineering***

October 15, 2018



The copyright of this thesis vests in the author. No quotation from it or information derived from it is to be published without full acknowledgement of the source. The thesis is to be used for private study or non-commercial research purposes only.

Published by the University of Cape Town (UCT) in terms of the non-exclusive license granted to UCT by the author.

# Declaration

1. I know that plagiarism is wrong. Plagiarism is to use another's work and pretend that it is one's own.
2. I have used the IEEE convention for citation and referencing. Each contribution to, and quotation in, this dissertation from the work(s) of other people has been attributed, and has been cited and referenced.
3. This dissertation report is my own work.
4. I have not allowed, and will not allow, anyone to copy my work with the intention of passing it off as their own work or part thereof.

Signature of Author  
A.R. Dhondea  
Vacoas, Mauritius

Signed by candidate
---------------------

October 15, 2018

# Abstract

The Radar Remote Sensing Group at the University of Cape Town is currently investigating the feasibility of building an active radar system employing the MeerKAT radio telescope as receiver for space debris detection, tracking and imaging. This dissertation details the development of a Mission Planning Tool (MPT) to perform sensor scheduling and to support the performance prediction and analysis of the proposed MeerKAT radar.

The MeerKAT radar project proposal is made in the context of developing space surveillance and tracking capacities in South Africa. The MeerKAT radar is intended to operate bistatically, with a transmitter located in Bredasdorp (South Africa) and the MeerKAT radio telescope as receiver. The system design and radar signal processing design are currently under development in another RRSg project. Before the feasibility study can progress further, a Mission Planning Tool has been developed to assist in scheduling the bistatic radar to perform an observation experiment, to calculate the predicted radar measurements and errors as well as to estimate the orbit of the observed object.

This report documents how these objectives were met by the MPT software developed in Python. Given a LEO space object of interest's Two Line Element set, the MPT performs orbit propagation with an SGP4 method to generate trajectories for radar performance evaluation. The MPT determines the most opportune epoch (the longest possible target dwell-time within the antenna beam) for executing an observation experiment with the MeerKAT radar. Space objects investigated in this project were found to have spent between 4.5 s to 12.8 s in the transmitter's illuminating beam. The MeerKAT radio telescopes are tasked to act as receivers at the appropriate antenna pointing and time period. Based on the bistatic geometry of the specific observation experiment, the MPT predicts the signal-to-noise ratio at the radar receiver as well as the bistatic range, bistatic Doppler shift and look angles. The integrated SNR values for the experiments considered in this report ranged from 11 dB to 68 dB. From the coherently integrated SNR, the MPT estimates the radar measurement errors. Finally, the orbit determination module was engineered with two radar measurement schemes: a bistatic



---

range and Doppler shift scheme and a bistatic range and look angles scheme. Monte Carlo experiments were run to evaluate the tracking performance resulting from the two tracking schemes. The Gauss-Newton tracking filter based on the first scheme fails to converge whereas it produces accurate results with the second scheme (estimated position error of 2 m and velocity error of 0.08 m/s). It is therefore recommended to opt for the bistatic range and look angles measurement scheme in future work. Since the current MeerKAT radar design cannot create look angles measurements, an observables estimation scheme was adopted. It was found that this scheme produced accurate elevation and azimuth angles with an estimation error of  $\pm 0.04^\circ$ . Since the quoted values result from a preliminary design of the MeerKAT radar, they are bound to change in the final design. Therefore the MPT should be loaded with the final radar design's parameters and run again to produce useful results.

This reports shows that, with the help of the Mission Planning Tool developed in this project, the proposed MeerKAT radar can be feasibly scheduled to observe and track space objects in the LEO regime based on a single target pass.

# Acknowledgements

I am thankful for the guidance which my supervisor Emeritus Professor Mike Inggs provided me. His mastery of multiple fields and his engineering insight are an inspiration to me. I hope that I have assimilated much of this critical thinking, yet I still have a lot left to learn in the future. I am grateful for having been given the opportunity to study a number of fields (astrodynamics and target tracking) which I had never encountered during my bachelor's in electrical engineering at UCT. I am proud to have contributed to one of Prof Inggs' engineering projects in the [RRSG](#) and gained some expertise in astrodynamics, target tracking, radar systems, and software engineering along the way.

I would like to express my gratitude to Dr. Norman Morrison for sharing his knowledge of tracking filter engineering with me. I greatly appreciated our conversations on linear algebra, dynamical systems theory and target tracking.

I would like to thank the South African [SKA](#) for their financial assistance under a block grant held by Professor Inggs.

I am thankful for the technical discussions I have had over the years with Mrs. Doreen Agaba and Mr. Andrew Nicol. They were the pioneers in engineering radar systems for space debris and Near-Earth Object studies in the [RRSG](#).

My thanks also go to Dr. Simon Winberg and Dr. Lerato Mohapi for helping me with administrative tasks and with running simulations on the compute server. Dr. Winberg has taken a keen interest in our MeerKAT radar for space debris studies project and his advice on project management, on software engineering recommended practices and on doing conference presentations was very beneficial to me. Dr. Lerato Mohapi always had kind words of encouragement, especially when I went through several unfortunate events over the past couple of years.

I would also like to thank Mr. Abhishek Bhatta, Mr. Bilal Mirza, Mr. Dane Du Plessis, Mr. Dominique Gouveia, Miss Ming Gao, Mr. Randy Cheng, Mr. Simon Lewis and Mr. Stephen Paine for their friendship and help during my master's degree.

---

Special thanks to Mr. Dominique Gouveia for taking the time to proofread my dissertation and to suggest many improvements, all of which were adopted. Dominique has been a constant source of help throughout this master's project and a great study buddy during all-nighters and weekends in the Radar Lab over the years. Thank you also to Miss Subha Singh for proofreading my dissertation. She made many suggestions, all of which were adopted.

Many thanks to Mr. Molaoa Molaoa for being a great friend throughout these years in Cape Town. He has been a helpful sounding board for my project ideas, not to mention a cool friend to hang out and watch football with.

I am deeply grateful to my parents and sister Dr. Ashwini Dhondea-Ramsamy for their encouragement and support - both moral and financial - during my time in Cape Town.

Finally, my heartfelt thanks to my girlfriend Daksha Dabee for her love and patience over the course of this project.

# Contents

Plagiarism Declaration	i
Abstract	ii
Acknowledgements	iv
Table of contents	viii
List of Figures	xi
List of Algorithms	xii
List of Tables	xiii
List of Abbreviations	xiv
List of Symbols	xix
<b>1 Introduction</b>	<b>1</b>
1.1 Background to Project .....	1
1.2 Objectives of Study .....	7
1.3 Scope and Limitations .....	8
1.4 Dissertation Outline .....	9
1.4.1 Literature review .....	10
1.4.2 Dynamics and Measurement Models .....	11
1.4.3 Scheduling the MeerKAT radar .....	12
1.4.4 Orbit Determination and Analysis .....	15
1.4.5 Conclusions and Recommendations .....	16
<b>2 Literature review</b>	<b>18</b>
2.1 Introduction .....	18
2.2 Background on space debris .....	18
2.2.1 History .....	18

2.2.2	Nature .....	21
2.2.3	Space object population .....	23
2.3	Background on SSA .....	25
2.3.1	Components of SSA .....	26
2.4	Sensors for space debris studies .....	28
2.4.1	Bistatic radars which operate in stare mode.....	31
2.5	Summary .....	41
2.5.1	Discussion .....	41
2.5.2	Conclusion .....	42
<b>3</b>	<b>Dynamics and Measurement Models</b>	<b>44</b>
3.1	Introduction .....	44
3.2	Space object dynamics .....	44
3.2.1	Describing an orbit .....	44
3.2.2	Reading a TLE set .....	48
3.2.3	Propagating an orbit .....	49
3.3	Sensor dynamics .....	57
3.4	Measurement modelling .....	65
3.5	Summary .....	69
<b>4</b>	<b>Scheduling the MeerKAT Radar</b>	<b>71</b>
4.1	Introduction .....	71
4.2	Sensor parameters .....	71
4.3	Target passage identification .....	73
4.4	Sensor scheduling .....	78
4.4.1	Tasking the transmitter .....	78
4.4.2	Tasking the receivers .....	90
4.4.3	Experiment geometry .....	92
4.5	SNR calculations & radar measurement errors .....	95
4.5.1	SNR calculations .....	95
4.5.2	Radar measurement errors .....	99
4.6	Summary .....	102
<b>5</b>	<b>Orbit Determination and Analysis</b>	<b>104</b>
5.1	Introduction .....	104
5.2	Orbit determination background .....	104
5.3	Radar measurement schemes and results.....	106
5.3.1	Bistatic range and Doppler shift measurements .....	107
5.3.2	Bistatic range and look angles measurements .....	120

5.3.3	Comparison of BIRDOPP and BIRAZEL filters .....	127
5.3.4	Observables estimation .....	128
5.4	Summary .....	132
<b>6</b>	<b>Conclusions and Recommendations</b>	<b>134</b>
6.1	Conclusions .....	134
6.2	Recommendations .....	138
6.2.1	End-to-end simulations in conjunction with FERS .....	140
	<b>Bibliography</b>	<b>142</b>
<b>A</b>	<b>Astrodynamics aspects</b>	<b>150</b>
A.1	Resident space objects simulated in this project .....	150
A.2	Generating a trajectory with the two body plus J2 model .....	150
<b>B</b>	<b>Gauss-Newton filtering</b>	<b>152</b>
B.1	The dynamical model .....	152
B.2	The observation model .....	154
B.3	The Case 4 filtering strategy .....	155
B.4	The Kalman observability matrix .....	157
B.5	The Gauss-Newton Filter structure .....	157
B.6	Filter implementation .....	159
<b>C</b>	<b>Derivations for the OD problem</b>	<b>160</b>
C.1	Expressions relating to the target dynamic model .....	160
C.1.1	Equations of Motion .....	160
C.1.2	State sensitivity matrix .....	161
C.2	Expressions relating to the measurement model .....	162
C.2.1	Deriving the expression for range .....	162
C.2.2	Deriving the expression for Doppler shift .....	164
C.2.3	Measurement Jacobian matrix for the BIRDOPP scheme .....	166
C.2.4	BIRAZEL measurements .....	167
<b>D</b>	<b>Code</b>	<b>169</b>
<b>E</b>	<b>Ethics Form</b>	<b>171</b>

# List of Figures

1-1	Space junk in LEO .....	2
1-2	Map showing MeerKAT's layout.....	3
1-3	Map showing the location of the Tx in Bredasdorp and Rx at Carnarvon .....	4
1-4	BPE geometry for a multistatic radar.....	5
1-5	Simulation flow diagram.....	9
1-6	Map showing the location of the Tx and Rx and local coordinate frame orientation	12
1-7	Bistatic plane showing the target trajectory and sensor scheduling.....	14
2-1	Debris spreading in orbit after the 2007 Chinese ASAT test .....	19
2-2	Gabbard diagrams showing tracked debris particles from the 2009 collision .....	20
2-3	Impact on HST solar panel .....	22
2-4	A Payload Assist Module used to launch a satellite crashed in a desert .....	22
2-5	Population of orbiting objects in January 2015.....	24
2-6	Long-term forecast of the evolution of the space object population.....	25
2-7	Space surveillance and tracking block diagram .....	27
2-8	Cobra Dane radar.....	29
2-9	Haystack radar system .....	30
2-10	US SSN sensor locations .....	30
2-11	Bistatic radar with multiple receiving beams.....	31
2-12	GRAVES radar .....	32
2-13	The TIRA system as radar Tx and the Effelsberg radio telescope as radar Rx ....	33
2-14	Radar geometry for BPE at TIRA/Effelsberg .....	34
2-15	BIRALES and BIRALET systems .....	35
2-16	BIRALES radar:TOPORADEC profile for target passage.....	36
2-17	BIRALES radar simulator architecture .....	37
2-18	MWA layout .....	39
2-19	2015 ISS observation experiment scenario at MWA .....	40
3-1	Kepler orbit .....	45
3-2	Keplerians of celestial body .....	46
3-3	Space object orbit around the Earth. ....	47

## LIST OF FIGURES

---

3-4	Three approaches in propagating an Earth orbit .....	50
3-5	Ground track of Cosmos-2251 debris 33759 .....	51
3-6	Relative influence of various perturbing forces in different orbit regimes .....	53
3-7	Ground track for ISS orbit generated with Cowell's formulation .....	56
3-8	Evolution of position and velocity states over three orbits .....	56
3-9	Normalized ACF to find orbit period numerically .....	57
3-10	Relationship between the ECI and ECEF frames .....	58
3-11	Cross-section of an oblate Earth .....	59
3-12	Transforming from the ECEF to the SEZ frame .....	60
3-13	Transforming the target trajectory from ECEF frame to the local frame .....	60
3-14	Map showing the location of the Tx & Rx .....	61
3-15	The topocentric SEZ frame .....	62
3-16	Radar vectors from the Rx to the target .....	63
3-17	Bistatic radar configuration .....	64
3-18	Bistatic angle, range and Doppler shift measured at the Rx .....	65
3-19	<i>Tiangong-1</i> ground track used to illustrate light time correction .....	66
3-20	Uplink and downlink time for the <i>Tiangong-1</i> transit .....	67
3-21	Measured bistatic range based on the time delay of the received signal .....	68
3-22	Measured bistatic Doppler shift based on the time delay of the received signal....	69
4-1	ISS ground track for Target Passage Identification .....	74
4-2	Radar vectors from the Tx to the target .....	75
4-3	Elevation angle at Tx .....	76
4-4	Transmitter's Field of Regard shown on a map .....	77
4-5	Elevation and azimuth angles at Rx0 .....	78
4-6	Space object trajectory through antenna beam .....	79
4-7	Azimuth angle at the Tx time-series .....	80
4-8	Elevation angle against corrected azimuth angle plot .....	81
4-9	Elevation versus azimuth plot for the target trajectory .....	82
4-10	Plot of transmitter illumination time .....	83
4-11	Elevation versus azimuth angle plot indicating the best beam pointing .....	84
4-12	Elevation angle to the transmitter .....	85
4-13	Transmitter's Field of View shown on a map .....	86
4-14	Elevation versus azimuth plot: square beam model .....	87
4-15	Transmitter beam centre pointing: from square beam to circular beam model ....	87
4-16	Transmitter beam centre pointing: circular beam model .....	88
4-17	Elevation versus azimuth plane for trajectories with a position error .....	89
4-18	Topocentric right ascension declination profile for the target's passage .....	91



## LIST OF FIGURES

---

4-19	Target-radar geometry during the experiment .....	92
4-20	Target-radar geometry projected onto the bistatic plane .....	93
4-21	Target observation geometry visualized on the bistatic plane .....	94
4-22	SNR at the receivers .....	98
4-23	Bistatic angle, bistatic range resolution and Doppler resolution .....	100
4-24	Range measurement error during the target's passage .....	101
4-25	Doppler measurement error at each dish during the target's passage .....	101
5-1	General overview of tracking filtering .....	106
5-2	Bistatic range and Doppler shift measurements at receiver .....	108
5-3	Rank of the observability matrix with the BIRDOPP scheme .....	109
5-4	Measurement residuals for different iteration steps .....	112
5-5	WRMS measurement residuals at different iteration steps .....	113
5-6	Comparison of state estimates with the BIRDOPP scheme with true values .....	114
5-7	ANRMSE in position and velocity with the BIRDOPP scheme .....	115
5-8	3 sigma test results with the BIRDOPP scheme .....	116
5-9	ANEES for estimates with the BIRDOPP scheme over 1000 Monte Carlo runs ...	118
5-10	Bistatic range, elevation and azimuth angle measurements at receiver .....	120
5-11	Rank of the observability matrix with the BIRAZEL scheme .....	122
5-12	Comparison of state estimates with the BIRDOPP scheme with true values .....	123
5-13	ANRMSE with the BIRAZEL scheme .....	124
5-14	3 sigma test results with the BIRAZEL scheme .....	125
5-15	ANEES for the BIRAZEL scheme .....	126
5-16	Errors in polynomial fit for the right ascension/declination profile .....	130
5-17	Estimation errors in polynomial fit for the right ascension/declination profile .....	131
6-1	Processing chain to run an RSO observation experiment .....	141
D-1	SORADSIM repository structure .....	170

# List of Algorithms

A.1	Generate a nominal trajectory . . . . .	151
-----	---	-----

# List of Tables

1-1	Key parameters for the proposed MeerKAT radar .....	6
1-2	Observation window length .....	13
1-3	Maximum SNR at Rx for different targets .....	15
4-1	Sensor parameters relating to observation geometry .....	72
4-2	Observation window length .....	90
4-3	Parameters for the proposed MeerKAT radar .....	95
4-4	Maximum SNR at Rx for different targets .....	99
5-1	BIRDOPP-based ISS tracking with a small initial perturbation vector .....	119
5-2	BIRAZEL-based ISS tracking with a small initial perturbation vector .....	127
5-3	Tracking errors with BIRDOPP & BIRAZEL filters for 3 initial perturbations ...	128
A-1	NORAD ID for objects under investigation.....	150

# List of Abbreviations

**ANRMSE** Average Normalized Root Mean Square Error. 15, 114, 115, 118, 124, 132

**ANEEs** Average Normalized Estimation Error Squared. 15, 117, 118, 120, 125–127, 132, 136, 137

**BIRDOPP** A radar measurement scheme consisting of bistatic range and bistatic Doppler shift measurements in the context of target tracking.

$\mathbf{y} = [\rho_b \ f_{b,d}]^T$ . 15–17, 104, 107–109, 113–121, 123, 127, 128, 132, 133, 136, 137, 140, 154, 162, 166, 167

**BIRALES** Bistatic RAdar for LEO Survey.

An Italian bistatic radar system whose Tx is the Flight Termination Service facility and whose Rx is the Northern Cross radio telescope. 10, 31, 34–38, 41–43, 91, 128, 129, 132, 135, 137

**BIRALET** Bistatic RAdar for LEO Tracking.

An Italian bistatic radar system whose Tx is the Flight Termination Service facility and whose Rx is the Sardinia Radio Telescope (SRT). 10, 34, 35, 38, 41–43

**BIRAZEL** A radar measurement scheme consisting of bistatic range, azimuth angle and elevation angle measurements in the context of target tracking.

$\mathbf{y} = [\rho_b \ \theta \ \psi]^T$ . 15–17, 104, 120–128, 132, 133, 137–139, 154, 162, 167

**BPE** Beam-park experiment.

A RSO observation experiment in which the radar operates in beam-park mode: its beam is kept fixed in a certain direction for the entire duration of the experiment. xvi, xvii, 4, 27, 28, 33, 34, 78, 79, 95, 102

**CA** Conjunction Analysis. 28, 37, 138

- CPI** Coherent Processing Interval. [xxii](#), [xxiii](#), [68](#), [69](#), [95–98](#), [108](#)
- DCM** Direction Cosine Matrix. [xxii](#), [58](#), [59](#), [162](#), [168](#)
- DE** differential equation. [50](#), [52](#), [54](#), [55](#), [70](#), [105–107](#), [140](#), [152](#), [153](#), [161](#)
- EGM 2008** Earth Gravity Model 2008. [38](#), [42](#)
- EKF** Extended Kalman Filter. [34](#), [41](#), [105](#), [106](#)
- EOM** Equations of Motion.  
A set of coupled, nonlinear differential equations which characterize the dynamics of a space object. [11](#), [50](#), [54](#), [69](#), [138](#), [140](#), [160](#)
- ECEF** Earth Centered, Earth Fixed frame. [11](#), [46](#), [57–61](#), [70](#), [79](#), [135](#), [162–166](#), [168](#)
- ECI** Earth Centered, Inertial frame. [xxii](#), [11](#), [57–60](#), [70](#), [135](#), [162–164](#), [168](#)
- ECM** Error Covariance Matrix. [xxii](#), [15](#), [27](#), [28](#), [37](#), [38](#), [115–120](#), [124–126](#), [132](#), [136](#), [137](#), [158](#), [159](#)
- ESA** European Space Agency. [2](#), [22](#), [25](#), [26](#)
- FERS** Flexible Extensible Radar Simulator. [7](#), [8](#), [141](#)
- FoR** Field of Regard. [xix](#), [7](#), [9](#), [72–79](#), [83](#), [84](#), [86](#)
- FoV** Field of View. [7](#), [15](#), [28](#), [32–36](#), [38](#), [78](#), [79](#), [84–88](#), [90](#), [91](#), [95](#), [99](#), [101](#), [108](#), [129](#), [136](#), [139](#)
- FIM** Fisher Information Matrix. [xxi](#), [111](#), [158](#), [159](#)
- GEO** Geostationary Earth Orbit. [25](#), [29](#)
- GMST** Greenwich Mean Sidereal Time. [xxiii](#), [58](#), [91](#), [130](#), [162–166](#)
- GNA** Gauss-Newton Algorithm. [111](#), [157](#)
- GNF** Gauss-Newton Filter. [xix](#), [xxi–xxiv](#), [15](#), [16](#), [104](#), [106](#), [110–112](#), [114](#), [121](#), [123](#), [132](#), [133](#), [137](#), [140](#), [152](#), [156](#), [157](#), [159](#)
- ISO 8601** an international formatting standard for representing date and time for international interchange developed by the International Organization for Standardization (ISO) in 1988. The updated standard ISO 8601:2004 is adopted throughout this project. [48](#), [49](#), [70](#)

- IADC** Inter-Agency Space Debris Coordination Committee. 18
- ISS** International Space Station. 11, 12, 25, 39, 40, 54–57, 61, 63, 71, 74, 75, 90, 97, 100, 102, 108, 119, 120, 127, 150, 169
- IVP** Initial Value Problem. 54, 55, 153, 154
- LoS** Line of Sight. 5, 12, 70, 74, 96, 97, 99
- LEO** Low Earth Orbit which ranges from 150 km up to 2000 km above the Earth’s surface. xiv, 1, 2, 5, 8, 10, 18, 25, 28, 30, 52, 53, 79, 89
- MPT** Mission Planning Tool. 7–13, 16, 17, 32, 34, 39, 41, 42, 44, 45, 48, 49, 51, 55, 58, 69, 70, 73, 76, 79, 92, 95, 102, 103, 106, 109, 121, 133–138, 140, 141, 154, 156, 159, 169
- MSL** Mean Sea Level. xxi, 58, 72
- MWA** Murchison Widefield Array  
A radio telescope in Western Australia which is a precursor to the Square Kilometre Array (SKA). It has also been used to conduct BPEs as Rx in a FM-based passive bistatic radar. 10, 31, 38–43, 135
- MeerKAT** an SKA radio telescope consisting of 64 dishes in South Africa. 2, 3, 5–13, 16, 17, 26, 27, 29, 31, 38, 41–43, 49, 50, 52, 58, 65, 66, 68, 71, 72, 76, 77, 83, 84, 86, 87, 89–91, 94–96, 98, 99, 102, 104, 106, 107, 109, 110, 119, 122, 128, 130, 132–140, 162, 169
- MEO** Medium Earth Orbit. 25
- MVA** Minimum Variance Algorithm. 152
- NORAD** North American Aerospace Defense Command. 13, 15, 24, 36, 44, 48, 57, 89, 90, 99, 150
- NASA** National Aeronautics and Space Administration. xvi, 18, 22–25, 29, 55
- ODPO** NASA’s Orbital Debris Program Office. 22, 23, 29
- OD** Orbit Determination. 7–11, 15, 17, 27, 33, 37, 38, 41, 43, 50, 55, 70, 79, 104, 106, 109, 132, 134, 135, 138–140, 152
- OP** Orbit Propagation. xx, 7–11, 38, 40, 42, 44, 48–51, 55, 57, 59, 73, 75, 134, 138, 162
- PRF** pulse repetition frequency in hertz. xvii, 6, 7, 73, 86, 95, 98, 102, 139

- PRI** pulse repetition interval in seconds. The Pulse Repetition Interval is the reciprocal of the PRF. 86, 87, 96
- RRSG** Radar Remote Sensing Group at the University of Cape Town. iv, 2, 3, 6, 7, 16, 26, 29, 133, 140
- RCS** Radar Cross Section. 23, 24, 33, 96, 98, 139
- RK4** Runge-Kutta fourth order method. 55, 106, 138, 150, 151, 154
- RMSE** root means squared error. xiv, xx, 15, 114, 123, 132
- SKA** Square Kilometre Array. iv, xvi, 1–3, 38, 140
- SST** Space Surveillance and Tracking, a major component of SSA. 2, 10, 26, 27, 41
- SEZ** South East Zenith frame. 11, 12, 59–62, 70, 135, 162, 164, 167, 168
- SGP4** Simplified General Perturbations 4. xix, xx, 11, 37, 39–42, 48, 50, 51, 69, 70, 73, 75, 86, 88, 105, 135
- SOD** Statistical Orbit Determination. 17, 27, 37, 104, 138
- RSO** Resident Space Object. xiv, xviii, xx–xxii, xxiv, 2, 4, 5, 8, 9, 11, 12, 15, 17, 19, 23, 25–28, 31, 32, 34, 37, 38, 44, 47–52, 58, 60, 62, 65–67, 70, 71, 76, 77, 79, 83, 84, 87–91, 95, 96, 98, 99, 103, 109, 129, 130, 134–138, 140, 141, 160
- SSA** Space Situational Awareness. xvii, 2, 10, 18, 26–28, 30, 41, 43, 104, 135
- STM** State Transition Matrix. xxii, 150, 151, 153–155
- SNR** Signal to Noise Ratio. 6–10, 14–17, 33, 35, 36, 38, 41–43, 71, 95–103, 129–131, 133, 134, 136, 137
- TEME** True Equator Mean Equinox. 51, 57
- TIRA** Tracking and Imaging RAdar  
A high-power monostatic radar purpose-built for space debris tracking and imaging located in Wachtberg, Germany. It has also been used to conduct BPEs in a bistatic configuration featuring the Effelsberg radio telescope as Rx. 10, 31–34, 41–43, 135
- TOPORADEC** Topocentric right ascension  $\Delta\alpha_t$  versus topocentric declination  $\Delta\delta_t$  plot. 36, 37, 39, 90, 91, 129–133, 139

**TLE** Two Line Element set, a data format containing the orbital elements of a [RSO](#) as well as an associated epoch. [7](#), [9](#), [11](#), [13](#), [15](#), [16](#), [20](#), [37](#), [39](#), [44](#), [48–52](#), [54–57](#), [69](#), [71](#), [73](#), [89](#), [90](#), [99](#), [103](#), [110](#), [127](#), [133](#), [140](#), [141](#)

**USSN** United States Space Surveillance Network. [24](#), [29](#), [48](#)

**UTC** Coordinated Universal Time, a time standard commonly used across the world. [42](#), [48](#), [49](#)

**WGS84** World Geodetic System 1984. [xxi](#), [xxii](#), [51](#), [58](#), [70](#)



# List of Symbols

$\mathbf{A}$  the Jacobian matrix of the function  $\mathbf{f}$ .  $\mathbf{A} \in \mathbb{R}^{d_x \times d_x}$ .

$\mathbf{A}$  is called the state sensitivity matrix in the GNF framework. 151, 153, 154, 161

$\omega$  argument of perigee in degrees.

The argument of perigee is a Keplerian element used in defining the orientation of an orbit. 45, 47, 48

$\psi$  azimuth angle in radians. xiv, xix, xxiii, 61–63, 72, 73, 75, 77, 80, 81, 83, 84, 86–89, 91, 104, 120–122, 128, 130, 132, 154, 167, 168

$\Theta_{3 \text{ dB}}$  beamwidth in degrees.

The angular width of a slice through the main lobe of the radiation pattern of an antenna in the azimuth or elevation plane. 34, 35, 38, 72, 73, 79, 80, 82, 84, 86, 88, 91, 136

$\mathbf{B}_{\psi}^{\text{FoR}}$  azimuth angle range in FoR. 72, 73, 75, 77, 86

$\mathbf{B}_{\theta}^{\text{FoR}}$  elevation angle range in FoR. 72, 73, 75, 77, 78

$B^*$  starred ballistic coefficient of a space object in units of inverse Earth radius  $R_e$ . It is used in SGP4 theory for orbit propagation. 48, 140

$B$  the radar signal's bandwidth in hertz. 6, 95, 97, 99

$L_b$  baseline in a bistatic radar in kilometres

The straight line distance from the transmitter to the receiver in a bistatic radar. 4, 5, 32, 34, 38, 39, 63, 93

$\beta$  bistatic angle

The angle in radians subtended by the Tx-to-target line segment to the target-to-Rx line segment in a bistatic radar. 64, 65, 99

$\Delta\rho_{\mathbf{b}}$  bistatic range resolution in kilometres. 99, 100

$\rho_{\mathbf{b}}$  bistatic range in kilometres. xiv, 64, 65, 67, 68, 104, 107, 112, 120, 154, 162, 164–167

$c$  speed of light in metres per second. xx, xxi, 66–68, 99

$\Delta_t$  fixed time step in seconds used in Orbit Propagation. 51, 52, 55, 57, 67, 73, 75, 78, 82, 84, 86–88, 96, 131, 151

$d_x$  dimensionality of the state vector  $\mathbf{x}$ . xix, xx, xxii, xxiv, 47, 108, 109, 115–117, 121, 125, 150, 153–159, 161, 167

$d_y$  dimensionality of the observation vector  $\mathbf{y}$ . xx–xxii, xxiv, 108, 109, 113, 121, 154–158, 167

$E$  eccentric anomaly in degrees.

The eccentric anomaly is a Keplerian element used in specifying the RSO’s position within its orbit. 45, 46

$\mathbf{e}$  objective function. 111, 158

$\theta$  elevation angle in radians. xiv, xix, xxiii, 61–63, 72–78, 80, 81, 83, 84, 87–89, 91, 104, 120, 122, 128, 130, 132, 154, 167, 168

$\hat{\mathbf{e}}_{\mathbf{WRMS}}$  weighted RMS of estimated error vector (weighted RMSE). 113

$e$  eccentricity.

The eccentricity is a Keplerian element which defines the shape of an orbit. 45–48, 158

$\mathbf{f}_{\mathbf{SGP4}}$  dynamics function used in SGP4 OP.  $\mathbf{f}_{\mathbf{SGP4}} : \mathbb{R}^{d_x} \mapsto \mathbb{R}^{d_x}$ . 51, 86

$\mathbf{f}$  dynamics function of the target’s dynamic model.  $\mathbf{f} : \mathbb{R}^{d_x} \mapsto \mathbb{R}^{d_x}$ . xix, xx, 49, 54, 105, 151, 153, 161

$\Delta f_{\mathbf{b,d}}$  bistatic Doppler resolution in hertz. 100

$f_{\mathbf{b,d}}$  bistatic Doppler shift in hertz. xiv, 64, 65, 68, 104, 107, 112, 154, 165–167

$f_{\mathbf{c}}$  the radar signal’s carrier frequency in hertz

$f_{\mathbf{c}} = c/\lambda_{\mathbf{c}}$ . xxi, 95

$\mathcal{N}$  Gaussian distribution. xxiv, 154

$\mathbf{g}$  radar measurement function.  $\mathbf{g} : \mathbb{R}^{d_x} \mapsto \mathbb{R}^{d_y}$ . xx, xxi, 15, 105, 107, 109, 111, 120, 121, 133, 154, 155, 167

- H** the Jacobian matrix of the measurement function **g**.  $\mathbf{H} \in \mathbb{R}^{d_y \times d_y}$ . 15, 107, 109, 111, 120, 121, 133, 155–157, 167
- $h$  height above [Mean Sea Level](#) in metres. 72
- I** the identity matrix of suitable dimensions. 150, 151, 154
- $i$  inclination in degrees.  
The inclination is a Keplerian element which is used in defining the orientation of an orbit. 45, 47, 48, 52, 55
- $i$  general index used as iteration count.  
It is used as index in fixed-point iterations such as the solution of the light-time equation and the Gauss-Newton algorithm. 66, 67, 110, 112, 113, 117
- $J_2$  the second zonal harmonic in the [WGS84](#) standard. 11, 34, 41, 42, 50, 52–54, 69, 105, 135, 138, 160–162
- J** Fisher information matrix ([FIM](#)). 158, 159
- $k_B$  the Boltzmann constant. 97
- $k$  discrete time variable as an independent parameter to a general function. 68, 69, 80, 82–84, 87–89, 97, 105, 108, 109, 111–113, 115, 116, 121, 124, 125, 153–157
- $K_d$  wave number of transmitter.  $K_d = -1/\lambda_c$ . 64, 68, 100, 165–167
- $L$  filter window length in the [GNF](#) framework. 108, 110, 111, 113, 114, 121, 155–159
- $\phi_{\mathbf{gc}}$  geocentric latitude. 58, 60, 72
- $\phi_{\mathbf{gd}}$  geodetic latitude. 58
- $\lambda$  longitude. 60, 72, 162
- $\lambda_c$  wavelength of the radar signal’s carrier frequency in metres  
 $\lambda_c = c/f_c$ . xx, xxi, 72, 95, 96, 99
- $M$  mean anomaly in degrees.  
The mean anomaly is a Keplerian element used in specifying the [RSO](#)’s position within its orbit. 45, 46, 48
- $\mu_{\oplus}$  the Earth’s gravitational parameter. 52, 54, 160–162

- N** total error vector in the [GNF](#) paradigm. 156–158
- $N_{\text{CPI}}$  number of pulses transmitted during one [CPI](#). 68, 69, 95–97
- $n$  mean motion in revolutions per day. 48
- $N_{\text{MC}}$  number of Monte Carlo runs. 114, 117, 118, 123–127
- $n$  index of Monte Carlo run. 114, 117
- $\mathcal{O}$  Kalman observability matrix. 109, 121, 157
- $\omega_{\oplus}$  the Earth’s average rate of rotation in the [WGS84](#) standard, in radians per second. 58, 165
- $\hat{\mathbf{P}}$  estimated error covariance matrix (estimated [ECM](#)). 106, 111, 115–117, 119, 124, 127, 158, 159
- R<sub>y</sub>** Total Observation Covariance Matrix in the [GNF](#) paradigm. 111, 157–159
- R<sub>x</sub>** radar receiver. xiv, xvi, xvii, xix, xxii, xxiii, 3–5, 7, 10, 12–16, 31, 33–36, 39–43, 58, 60, 61, 63–67, 71, 72, 77, 78, 90–92, 94–97, 99, 102, 103, 120–122, 128, 130, 132–134, 136, 162–168
- I<sup>R<sub>x</sub></sup>** location of [radar receiver](#). 59, 66, 162
- ROT** an Euler rotation matrix (i.e. a [DCM](#)) of a specified angle about a specified axis. 58, 162
- R** measurement noise covariance matrix  $\mathbf{R} \in \mathbb{R}^{d_y \times d_y}$ . xxiv, 16, 105, 106, 110, 111, 113, 116, 117, 122, 133, 154, 156, 157
- $\Omega$  right ascension of ascending node in degrees. Also known as [RAAN](#).  
The [RAAN](#) is a Keplerian element used in defining the orientation of an orbit. 45, 47, 48
- $\rho$  slant-range in kilometres. 61–65, 68, 74, 80, 96, 162–168
- $R_e$  the Earth’s equatorial radius as defined in the [WGS84](#) standard. xix, 48, 54, 59, 160–162
- $R_p$  the Earth’s polar radius as defined in the [WGS84](#) standard. 59
- r** position vector of a [RSO](#) in the [ECI](#) frame. 47, 52, 54, 160–162
- $\Phi$  state transition matrix ([STM](#)).  $\Phi \in \mathbb{R}^{d_x \times d_x}$ . 109, 111, 121, 151, 153–157

$a$  semi-major axis in kilometres.

The semi-major axis is a Keplerian element which determines the size of an orbit. [xxiii](#), [45–47](#)

$\sigma_{\psi_{\mathbf{R}\mathbf{x}}}$  the radar measurement error in [azimuth angle](#) to the radar  $\mathbf{R}\mathbf{x}$ , measured in radians. [122](#), [132](#)

$\sigma_f$  the radar measurement error in Doppler, measured in hertz. [100](#), [102](#), [110](#)

$\sigma_{\theta_{\mathbf{R}\mathbf{x}}}$  the radar measurement error in [elevation angle](#) to the radar  $\mathbf{R}\mathbf{x}$ , measured in radians. [122](#), [132](#)

$\sigma_\rho$  the radar measurement error in range, measured in kilometres. [100](#), [102](#), [110](#), [122](#)

$\mathbf{T}$  Total Observation Matrix in the [GNF](#) paradigm. [111](#), [131](#), [156–159](#)

$\mathbf{T}\mathbf{x}$  radar transmitter. [xiv](#), [xix](#), [xxiii](#), [3–5](#), [7](#), [12–14](#), [17](#), [31](#), [33–35](#), [39](#), [40](#), [58](#), [61](#), [64](#), [66](#), [67](#), [71–81](#), [83–89](#), [91](#), [92](#), [94–96](#), [99](#), [102](#), [103](#), [134](#), [136](#), [137](#), [139](#), [141](#), [162–167](#)

$\mathbf{I}^{\mathbf{T}\mathbf{x}}$  location of [radar transmitter](#). [59](#), [67](#), [162](#)

$\tau$  Pulse width in seconds. [6](#), [95](#)

$T_{\mathbf{CPI}}$  duration of one [CPI](#) in seconds. [40](#), [68](#), [95–97](#), [99](#), [108](#)

$T$  Keplerian period in seconds.

The period of a Keplerian orbit is a function of the semi-major axis  $a$ . [56](#), [57](#)

$\mathbf{t}$  target location in the radar’s topocentric coordinate frame. [60–62](#), [66](#), [67](#), [162](#), [168](#)

$\tau_d$  downlink time in seconds. [66–69](#)

$\tau_u$  uplink time in seconds. [67](#), [68](#)

$\theta_{\mathbf{GMST}}$  [GMST](#) angle in radians. [58](#), [91](#), [162–166](#)

$T_{i,Tx}$  the time duration in seconds that the target spends in the [transmitter’s](#) beam. [13](#), [79](#), [83](#), [88](#), [90](#), [95](#), [96](#), [136](#), [139](#), [141](#)

$\Delta\delta_t$  topocentric declination in degrees. [xvii](#), [36](#), [39](#), [90](#), [91](#), [96](#), [97](#), [129](#), [130](#), [132](#)

$\Delta\alpha_t$  topocentric right ascension in degrees. [xvii](#), [36](#), [39](#), [90](#), [91](#), [96](#), [97](#), [129](#), [130](#), [132](#)

$t$  continuous time variable as an independent parameter to a general function. [49](#), [54](#), [55](#), [66–68](#), [105](#), [108](#), [109](#), [111](#), [121](#), [129](#), [151–157](#), [167](#)

$\dot{\mathbf{t}}$  target velocity vector. 60, 168

$\nu$  true anomaly in degrees.

The true anomaly is a Keplerian element used in specifying the RSO's position within its orbit. 45–47

$\boldsymbol{\nu}$  measurement noise term  $\boldsymbol{\nu} \in \mathbb{R}^{d_y}$ .

$\boldsymbol{\nu} \sim \mathcal{N}(0, \mathbf{R})$ . 105, 112, 116, 117, 154–156

$\delta \hat{\mathbf{x}}$  estimated perturbation vector.  $\delta \hat{\mathbf{x}} \in \mathbb{R}^{d_x}$ . 111, 158, 159

$\delta \mathbf{x}$  perturbation vector. 110, 111, 119, 127, 128, 152, 153, 155–158

$\hat{\mathbf{x}}$  estimated state vector.  $\hat{\mathbf{x}} \in \mathbb{R}^{d_x}$ . xxiv, 106, 110–112, 114, 117, 119, 123, 126, 127, 153, 159

$\mathbf{x}^*$  nominal state vector in the GNF framework.  $\mathbf{x}^* \in \mathbb{R}^{d_x}$ . 109–112, 117, 119, 121, 127, 150–157, 159, 161

$\mathbf{x}$  state vector for the target,  $\mathbf{x} \in \mathbb{R}^{d_x}$ . xx, xxiv, 27, 37, 38, 47, 49, 54, 55, 58, 105, 110–112, 114, 117, 119, 123, 127, 152–155, 158, 161, 162, 164–168

$\tilde{\mathbf{x}}$  error in the estimated state vector  $\hat{\mathbf{x}}$ . 111, 114–119, 124–128

$\hat{\mathbf{y}}$  estimated measurement vector.  $\hat{\mathbf{y}} \in \mathbb{R}^{d_y}$ . 111

$\delta \mathbf{y}$  total observation perturbation vector in the GNF paradigm. 111, 156–159

$\delta \mathbf{y}$  observation perturbation vector. 111, 155, 156

$\mathbf{y}^*$  simulated observation nominal vector in filters of the GNF family. 111, 112, 121, 155

$\mathbf{y}$  observation vector  $\mathbf{y} \in \mathbb{R}^{d_y}$ . xiv, xx, xxiv, 16, 38, 104–107, 110–113, 120, 133, 154, 155, 166, 167

$\mathbf{y}$  total observation vector in the GNF paradigm. 111, 155, 159

$\tilde{\mathbf{y}}$  measurement residual  $\tilde{\mathbf{y}} \in \mathbb{R}^{d_y}$ . 16, 111–113, 116, 117, 121, 133

$T_k$  span of transition between sampling instants or time elapsed between consecutive measurements. 153–155

# Introduction

This chapter introduces the major themes of this dissertation. It first establishes the background and motivation for the overall project on space debris detection and tracking with a bistatic radar featuring the SKA's radio telescopes as radar receiver. Section 1.1 also contextualizes the purpose of the work presented in this report within the overarching aims of the main project. In light of the foregoing discussion, the objectives of this study are delineated in Section 1.2. Section 1.3 states the scope and limitations of the project. Finally, Section 1.4 provides a detailed overview of the dissertation.

## 1.1 Background to Project

The Space Age dawned on October 4, 1957 when the Soviet Union successfully placed the first man-made satellite, *Sputnik-1* in orbit. In the ensuing six decades, thousands of satellites have been launched. Sustained human activity in Space has had the unfortunate consequence of creating space debris which accumulate in orbit. Orbital debris, also called space junk or space debris, consist of artificial objects such as spent rocket stages, inoperative satellites, lost pieces of equipment and fragments from past collisions and explosions in Earth orbit.

Space debris pose an extremely concerning collision threat to Man's valuable spacecraft in orbit: not only can a piece of space rubble collide with a spacecraft at a very high relative velocity and put it out of commission, it can also collide with another piece of junk, thereby creating a multitude of smaller particles which eventually spread out in orbit and increase the chances of collision with an important space asset.

The figure below, from the European Space Agency shows that a rubble belt arose in the Low Earth Orbit (LEO) regime.

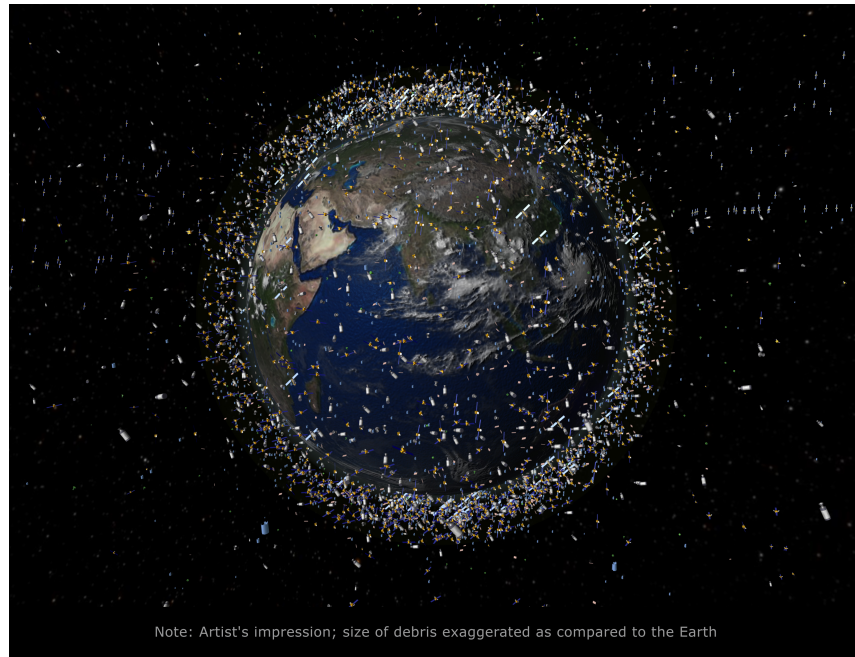


Figure 1-1: Artist's impression of space junk in Low-Earth Orbit. It should be noted that the debris are not to scale. Source: European Space Agency (ESA) [1].

The clutter in the [LEO](#) regime depicted in the above figure will grow exponentially over time if no countermeasures are taken. As a result, future spaceflight in the [LEO](#) regime will be in jeopardy, a consequence of the so-called Kessler effect [2].

The rising uncertainty in the safety of the space environment in the early 2000s led to the emergence of the concept of [Space Situational Awareness \(SSA\)](#) [3]. [SSA](#) is defined as the thorough knowledge of the space environment, which incorporates the ability to track and predict the location of space objects ([RSOs](#)) at any time [4]. The [ESA](#) outlines three aspects of [Space Situational Awareness](#) in [5, 6]:

- [SST](#): Space Surveillance and Tracking of resident space objects.
- [SWE](#): Space Weather monitoring
- [NEO](#): Near-Earth Object detection and tracking.

The University of Cape Town's Radar Remote Sensing Group ([RRSG](#)) is interested in the first area. The space surveillance and tracking segment is concerned with using sophisticated sensing systems (hardware and software) to detect, image, track, monitor and inventory resident space objects ([RSOs](#)). Resident space objects comprise active spacecraft and space junk.

The South African Square Kilometre Array ([SKA](#)) organization is currently building the Meer Karoo Array Telescope<sup>1</sup> ([MeerKAT](#)) in the Northern Cape of South Africa which will consist

---

<sup>1</sup> *Meer* means *more* in Afrikaans.



of 64 dishes to be used for radio astronomy and to demonstrate technological progress towards building the [Square Kilometre Array](#), the world's largest radio telescope in 2024. Orbital debris detection, tracking and imaging was identified early on as a potential non-astronomy application of the [SKA](#) radio telescopes. [7]

Figure 1-2 below shows the location of the 64 dishes forming the [MeerKAT](#) array in Carnarvon, South Africa.

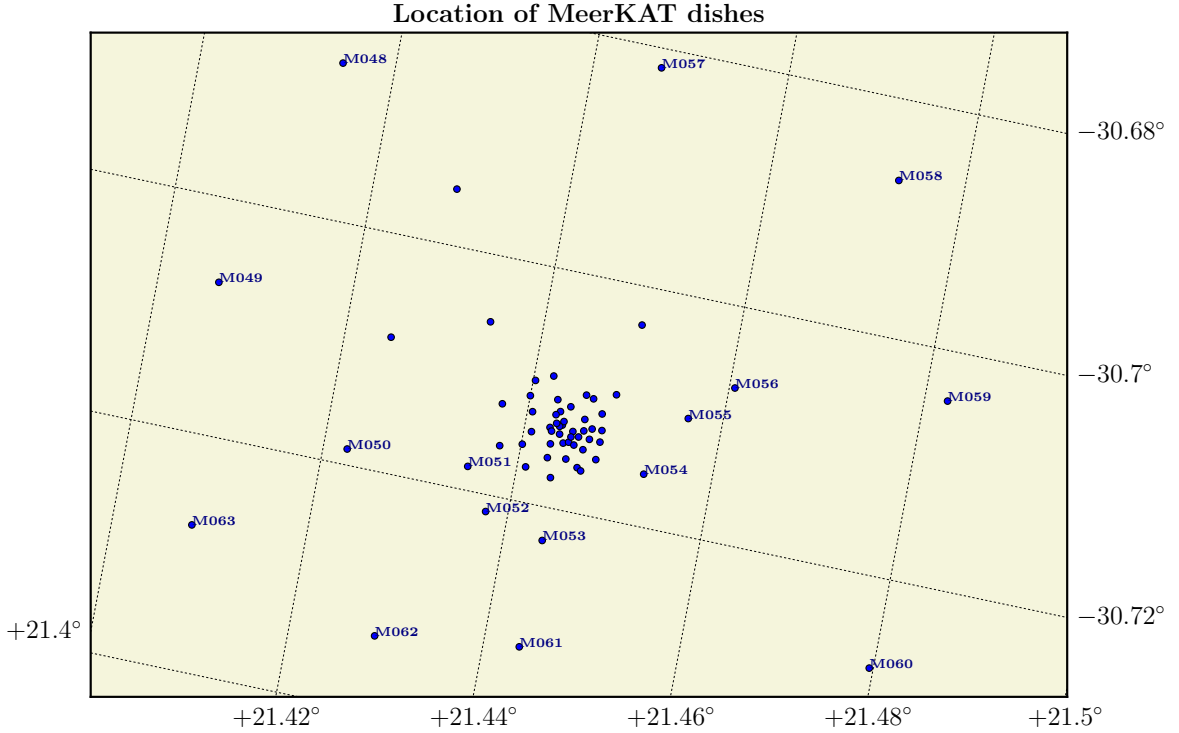


Figure 1-2: Map showing [MeerKAT](#)'s layout. The MeerKAT receptors are referred to as **M000** to **M063**. The MeerKAT dishes' locations were determined with a two-dimensional Gaussian distribution. The longest baseline is 7.697 km (between **M048** & **M060** and between **M058** & **M063**). The inner core consists of 48 dishes. They are not annotated in this figure because their markers are too close to each other.

The [RRSG](#) envisages developing a bistatic radar system whose transmitter (**Tx**) will be located at Denel Dynamics's Overberg test range in Arniston, Bredasdorp (Western Cape, South Africa) and whose receiver (**Rx**) will be the [MeerKAT](#) radio telescope in the Northern Cape of South Africa. The main purpose of the proposed [MeerKAT](#) radar is the detection and tracking of resident space objects. The radar design and analysis is the subject of a current [RRSG](#) PhD project, run by Mrs. Doreen Agaba, entitled "*Radar System Design for Detection, Tracking and Classification of Space Debris*". This PhD thesis focusses on the design of a powerful radar system using local radio telescopes as radar receivers to detect, track and image space junk. It covers the radar design and radar signal processing design aspects [8].

The figure below is a map indicating the location of the radar Tx and Rx.

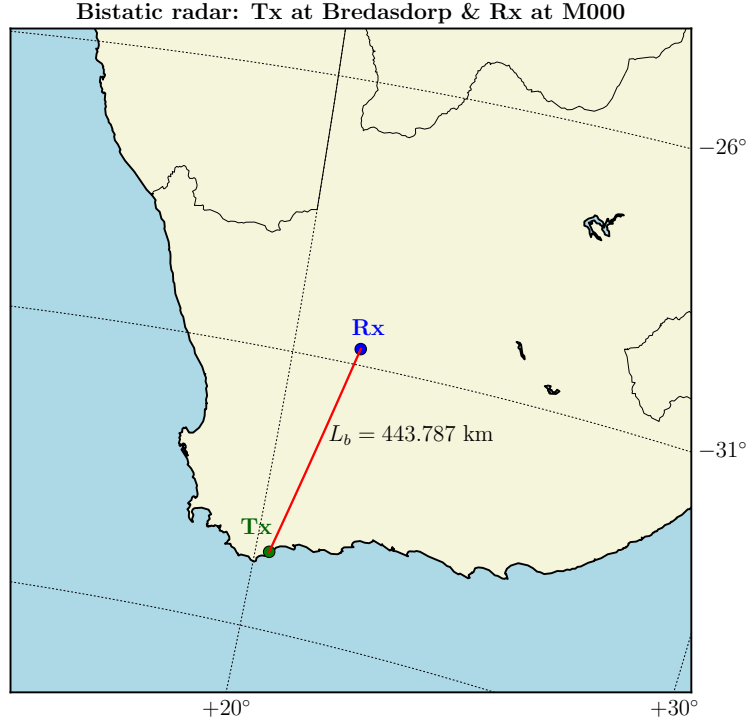


Figure 1-3: Map showing the location of the [transmitter](#) in Bredasdorp at  $34.6^\circ\text{S}$  and  $20.3^\circ\text{E}$  and [receiver](#) at Carnarvon at  $30.7^\circ\text{S}$  and  $21.4^\circ\text{E}$ . The bistatic baseline  $L_b$ , indicated by the red line, is 443.787 km long.

Radar-based space surveillance studies have been carried out since at least the first decade of the Space Age. However, relatively few experiments have been performed with the radar configuration of interest: a bistatic radar employing a sensitive radio telescope as radar receiver operating in beam-park mode. In this mode, the radar beam is aimed at a fixed point in the sky and kept in that direction during the course of the entire experiment. Space objects transiting through the beam would lead to target returns being recorded at the radar receiver. [3] Experiments done with a radar in such a configuration are called beam-park experiments (BPEs).

Figure 1-4 shows a sketch of the hypothetical radar geometry for a beam-park experiment with a multistatic radar system. The space object's trajectory is shown as a dashed black line. The direction of travel of the [RSO](#) is not specified in Figure 1-4 since it does not influence the radar geometry. The orientation of the beams of the directional antennas of the transmit and receive nodes are shown in colour.

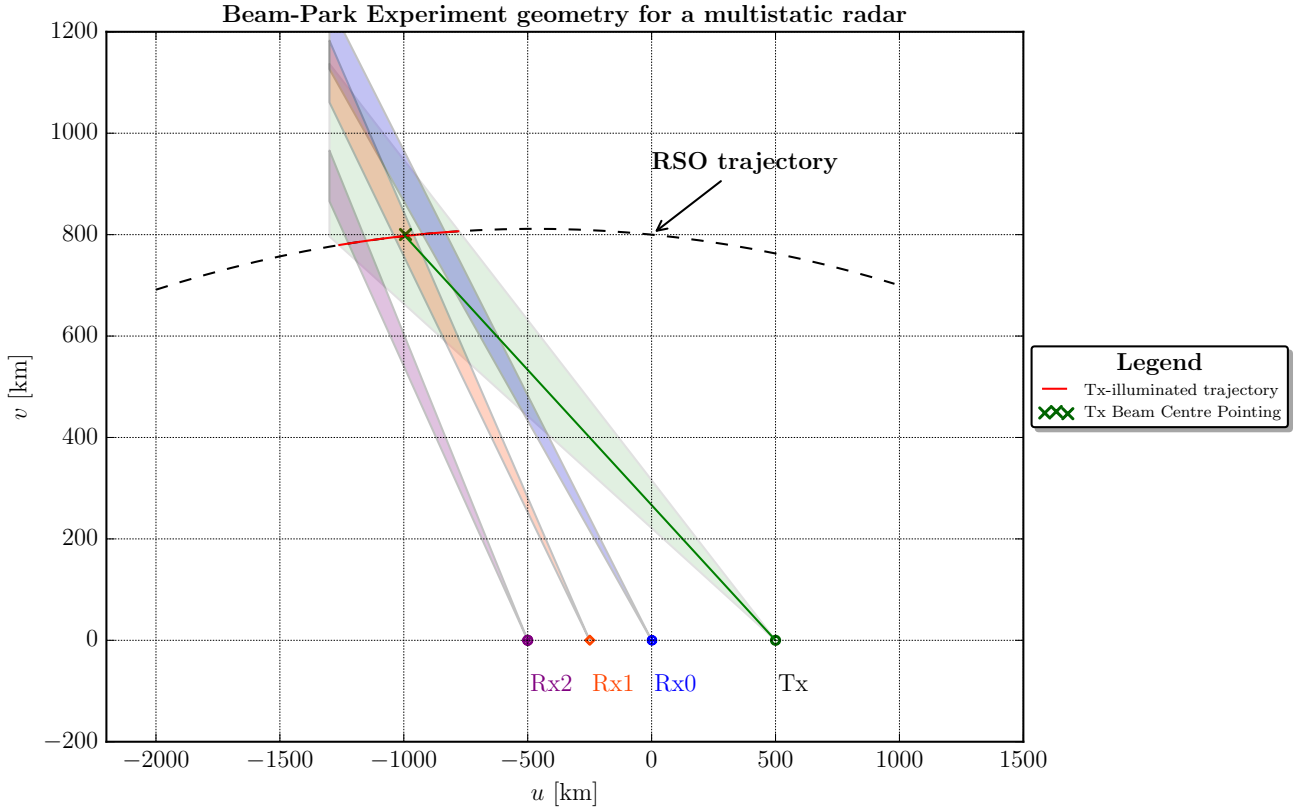


Figure 1-4: Radar geometry for a multistatic radar operating in beam-mode park to observe an RSO transit. The Tx beam (shown in green) is larger than the receive beams (in blue, orange and purple). The portion of the target trajectory illuminated by the Tx is shown in red. The Tx antenna's beam centre pointing is indicated by the green cross.

In Figure 1-4, the receivers are placed far apart (baselines of at least 250 km) and the antenna beamwidths are exaggerated to better illustrate how the parked beams intersect to give the observation volume. However, in the case of the proposed MeerKAT radar, the receivers are much closer to each other.

The following aspects of the proposed MeerKAT radar should be considered: (i) The targets of interest in the LEO regime have orbits which are in the range of 200 km to 2000 km above the surface of the Earth. (ii) The bistatic baseline  $L_b$  to the transmitter is 443.787 km whereas (iii) The longest baseline between MeerKAT dishes is only 7.697 km. The spatial separation of the MeerKAT receivers is very limited (less than 10 km) compared to the Line of Sight (LoS) range between a LEO target and the Tx and Rx and the bistatic baseline (several hundred kilometres). This suggests that the MeerKAT receivers are effectively colocated and that the MeerKAT radar will essentially be operating as a bistatic system.

The MeerKAT radar's transmitter and receiver dishes cannot track a space target, that is, change their beam pointing during a transit to follow it, due to the RSO's high speed of about 7 km/s. This means that only a parked beams approach is feasible for space object observation

experiments with the MeerKAT radar.

The MeerKAT radar will have a very good potential as radar receiver for space surveillance for the following reasons: Firstly, the extremely low system noise temperature of 23 K of the MeerKAT front end will be critical in detecting very small, distant targets such as space debris in orbit around the Earth. Secondly, all 64 MeerKAT dishes can be tasked to cover a target trajectory, resulting in an improved signal-to-noise ratio (SNR) at the radar receiver. Lastly, MeerKAT can also operate as an interferometric array which can image the space object trajectory at very high angular resolution.

The following table from the RRSg technical report [9] summarizes the main parameters in the MeerKAT radar’s pulse-Doppler design.

Table 1-1: Key parameters for the proposed MeerKAT radar

Parameter	Value
Transmit power	2 MW
Centre frequency	1350 MHz
Wavelength	0.2222 m
Bandwidth	10 MHz
Pulse width	5 $\mu$ s
Pulse repetition frequency	75 kHz

The MeerKAT radar is designed to operate with a bandwidth of 10 MHz centred at 1350 MHz (L-band). The high pulse repetition frequency (PRF) of 75 kHz means that the radar system operates as an interrupted continuous-wave (ICW) system. The quoted PRF and the pulse width of  $\tau = 5 \mu$ s lead to a maximum unambiguous range of only 1.249 km and a duty cycle of 37.5%. These two figures from the preliminary radar specifications in the technical report [9] are not realistic and will be updated in the final design in [8]. The PRF value, in particular, should be much smaller to prevent range aliasing from occurring.

The simulations for this master’s project were done before subsequent work in the PhD project showed that the PRF value of 75 kHz is not feasible. The pulse width  $\tau$  only appears in the signal processing block of the radar system. Since the signal processing block is not implemented in this project, the pulse width is not discussed in this report. On the other hand, the PRF of 75 kHz, referred to as the *nominal PRF*, is very relevant to this project because it (i) establishes the simulation time step in most simulations shown in this report; (ii) determines the integrated SNR calculations; (iii) impacts the radar measurement errors predictions and tracking performance evaluation of the radar system.

Given that the PRF is bound to change in the final design in [8], the simulations shown in this report will have to be re-run to update the results. Due to the short time interval between

being informed of the design change and the deadline for submission of this dissertation, we could not re-run the simulations to update the results. The discussion and results shown in this report are valid given the SNR values used and are instructive in the feasibility study of the MeerKAT radar project regardless of the actual PRF used.

The PhD project [8] focusses mainly on designing the overall system operation and the radar signal processing of the proposed MeerKAT radar. Two points need to be clarified before the MeerKAT radar's feasibility study progresses further. First, the question of when is a favourable time to do an observation experiment for an object of interest and how to schedule the radar to successfully detect and track this object. The second point relates to predicting the radar's measurements for a particular scenario and using these collected data to perform orbit determination (OD). These two points motivate the need for building a mission planning tool (MPT) steeped in astrodynamics. This dissertation focusses on the development of the MPT to perform sensor scheduling and to support the performance prediction and analysis of the MeerKAT radar.

## 1.2 Objectives of Study

As stated in Section 1.1, the Mission Planning Tool's aims are to assist in scheduling the bistatic radar to perform an observation experiment, to calculate the predicted radar measurements and errors as well as to estimate the orbit of the observed object. To achieve these aims, the following objectives must be met.

- Given an object of interest's Two Line Element (TLE) set, perform orbit propagation with a suitable scheme to generate trajectories which can be used for radar performance evaluation.
- Identify the most opportune epoch for executing an observation experiment with the MeerKAT radar. Perform sensor tasking for the transmitter and receiver.

This will entail (i) estimating the target's dwell time in the Tx beam at every point in the target's trajectory within the Field of Regard (FoR); (ii) finding the antenna pointing for the Tx which corresponds to the longest dwell-time; and (iii) finding the antenna pointing for the minimum number of MeerKAT dishes to cover the entirety of the Tx-illuminated portion of the trajectory. The length of time that the target spends within the Tx's Field of View (FoV), the antenna pointing for the Tx and Rx and the target's trajectory in a sensor-centered frame are key parameters which are needed to run realistic radar simulations with the RRSg's Flexible Extensible Radar Simulator (FERS) in the future.

- Calculate the single-pulse and coherently integrated [signal-to-noise](#) ratio of the received signal at each [MeerKAT](#) dish by taking into account the beamshape loss and bistatic radar geometry. Calculate the measurement error (standard deviation) in the measured bistatic range and Doppler shift.
- Develop a module to perform [orbit determination](#) with the measurements made available by the [MeerKAT](#) radar.

This involves (i) analysing the requirements of an [OD](#) scheme; (ii) developing a suitable tracking filter; (iii) establishing how the [OD](#) performance is influenced by the nature, quality and quantity of the radar’s measurements. The results of the [OD](#) analysis will guide future optimizations of the [MeerKAT](#) radar design.

## 1.3 Scope and Limitations

The scope of this project is to develop a [Mission Planning Tool](#) to schedule space object detection and tracking experiments with the proposed [MeerKAT](#) radar and to process radar data to estimate [RSO](#) orbits in the [LEO](#) regime.

Brooker in [10] describes two classes of radar simulators, namely *result simulators* and *signal level simulators*. The latter category, of which [FERS](#) is a member, simulates the raw return signal recorded at the radar receiver. For instance, [FERS](#) outputs the signal emerging from the Analogue-to-Digital Converter. On the other hand, result simulators operate at a data processing level of abstraction and calculate the expected results produced by the signal processing block. The [MPT](#) discussed in this report is a result simulator. Hence, signal processing concerns will not be addressed.

Another limitation of the [MPT](#) is that its [OP](#) methods can only generate trajectories for Earth-orbiting objects and not for Sun-orbiting objects such as asteroids. Also, due to the exploratory nature of the [MeerKAT](#) radar project, we have opted not to incorporate atmospheric refraction modelling in the simulator at this stage. Atmospheric refraction models can be incorporated into the [Mission Planning Tool](#) once the performance with the signal processing block in the simulation processing chain is established.

Space objects spin about their centre of mass as they move in orbit. This spinning motion creates a micro-Doppler effect [11] in the electromagnetic energy scattered by [RSOs](#). The rotational aspect influences the images created by a radar sensor [12]. Since the [MeerKAT](#) radar project is still in its infancy, it was deemed that modelling the micro-Doppler effect may be extremely complicated and may cause an unnecessary delay to the project. Hence, only translational motion of a [RSO](#) is considered in this dissertation.

Although the [MPT](#) was created specifically to support development and analysis of the [MeerKAT](#) radar project, it is flexible and extensible and can be used for other applications. Scripts can be written to include any number of transmitters and receivers with arbitrary locations. The software can easily be modified to create simulation scenarios with multiple space targets transiting through the sensor's [Field of Regard](#).

## 1.4 Dissertation Outline

The structure of this dissertation was established according to how the Mission Planning Tool simulates the transit of an object of interest. The simulation flow diagram in [Figure 1-5](#) shows the processing pipeline used for an observation scenario. First, the [RSO's](#) Two Line Element ([TLE](#)) set is acquired. Then, the object's orbit is propagated over a certain time period. [Chapter 3](#) concerns [TLE](#) set acquisition and orbit propagation ([OP](#)). Target passage identification is done to determine when the object of interest will transit in the vicinity of the radar system. Sensor scheduling is done after the target passage is identified to find the radar configuration (antenna pointing and other parameters) which is the most suitable to execute the observation experiment. This is followed by the measurements prediction stage. In this stage, various quantities relating to the radar geometry and radar measurements (bistatic range, [SNR](#) and bistatic Doppler shift, for instance) are predicted. [Chapter 4](#) implements the Passage identification, Sensor scheduling and Measurements prediction blocks. The final block concerning [Orbit Determination](#) concerns estimating the orbit of the target of interest based on the predicted radar measurements. [OD](#) is discussed in [Chapter 5](#).

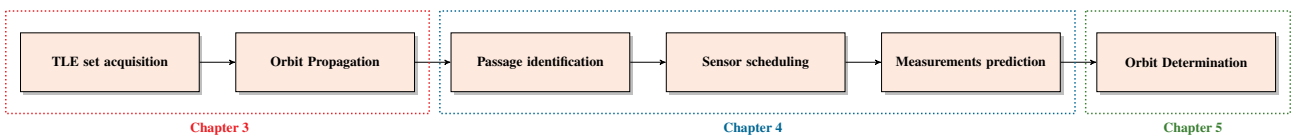


Figure 1-5: Simulation flow diagram to analyse a space object's transit. The chapter relevant to each processing block is labelled.

The other chapters in this report are : (i) [Chapter 1](#) which provides an introduction and overview of the report. (ii) [Chapter 2](#) which surveys the literature on topics which are relevant to this project. (iii) [Chapter 6](#) which concludes this report and puts forth recommendations for future work on the [MeerKAT](#) radar project.

### 1.4.1 Literature review

This chapter presents a survey of the literature concerning the major themes of the overall **MeerKAT** radar project and specific themes relevant to this dissertation.

It firstly elaborates, in Section 2.2, on the origins, nature and evolution of the space debris population over the years. The need for space debris studies and **Space Situational Awareness (SSA)** is established.

An overview of **SSA** is then given in Section 2.3. This describes the main components of **SSA** of which the **Space Surveillance and Tracking** aspect is the most relevant for the **MeerKAT** project. A system level block diagram (Figure 2-7) of **SSA** reveals that there are three elements related to the **SST** segment: the sensor block, the **orbit determination** block and the sensor tasking element which acts as feedback from the latter to the former. These three blocks are implemented later on in Chapters 3, 4 and 5.

Section 2.4 reviews worldwide sensors which have been used in space debris studies. The focus is kept on bistatic radar systems which operate in stare mode in Subsection 2.4.1. Of these, the systems which incorporate a radio telescope facility as radar receiver have a similar configuration to the proposed **MeerKAT** radar: (i) The Tracking and Imaging Radar (**TIRA**) with the Effelsberg radio telescope in Germany. (ii) The Bistatic RAdar for **LEo** Survey (**BIRALES**) and Bistatic RAdar for **LEo** Tracking (**BIRALET**) radars in Italy. (iii) The passive FM radar with the Murchison Widefield Array (**MWA**) as receiver in Australia.

With regard to the objectives of this project stated in Section 1.2, the literature on these radar systems is reviewed in terms of the following points (i) Target dynamic model and orbit propagation (ii) Sensor scheduling (iii) Radar measurements prediction (iv) **Orbit determination** (v) Time conventions and geodetic standards.

Conclusions are drawn from the literature review to guide the development in the subsequent work chapters. With regards to the five points mentioned above, the following conclusions arise: (i) This dissertation will investigate the suitability of the two target dynamic models found in the literature review and their corresponding **OP** approaches for the purposes of the **MPT**. (ii) The literature review has not found a fully-detailed sensor scheduling approach. A sensor scheduling scheme suitable for the **MeerKAT** radar will be developed in this report. (iii) The **MPT** will predict the single-pulse **SNR** at the radar **Rx** using the method described in the literature on the **BIRALES** system. It will also predict radar measurements of bistatic range and Doppler shift. (iv) A tailored tracking scheme will be developed for the **MPT** based on the one described in the papers on the **BIRALES** system. (v) Suitable conventions for time, timestamp representation and geodetic model will be adopted to ensure our results are meaningful to the research community.



### 1.4.2 Dynamics and Measurement Models

This chapter provides an in-depth development of target and sensor dynamics and measurement modelling built into the [MPT](#). It thus lays the groundwork for the other two work chapters [4](#) and [5](#).

The chapter begins by explaining how the dynamics of a [RSO](#) are modelled in the [MPT](#): by using classical Keplerian elements and Cartesian elements. It is shown in Subsection [3.2.2](#) that the [MPT](#) can process a space object's source [TLE](#) to extract its Keplerian elements. These elements can be converted into Cartesians. The [SGP4](#) and two body plus  $J_2$  dynamics models identified in the literature review were implemented. [Orbit propagation](#) was done in Subsection [3.2.3](#) by (i) numerically integrating the two body plus  $J_2$  Equations of Motion ([EOM](#)). (ii) using a library which implements [SGP4](#) theory. For both approaches, results are shown to prove their correct performance. The accuracy, fidelity and suitability for integration in [OD](#) routines are also discussed.

Section [3.3](#) concerns sensor dynamics. The three main coordinate frames ([ECI](#), [ECEF](#), [SEZ](#)) used by the [MPT](#) in the modelling of sensor dynamics are defined and shown in several figures to clearly explain their mechanics. Figure [1-6](#) is a map showing an International Space Station ([ISS](#)) transit in the vicinity of the proposed [MeerKAT](#) radar. This map is the result of the target dynamics modelling (from Section [3.2](#)) and the sensor dynamics modelling in Section [3.3](#).

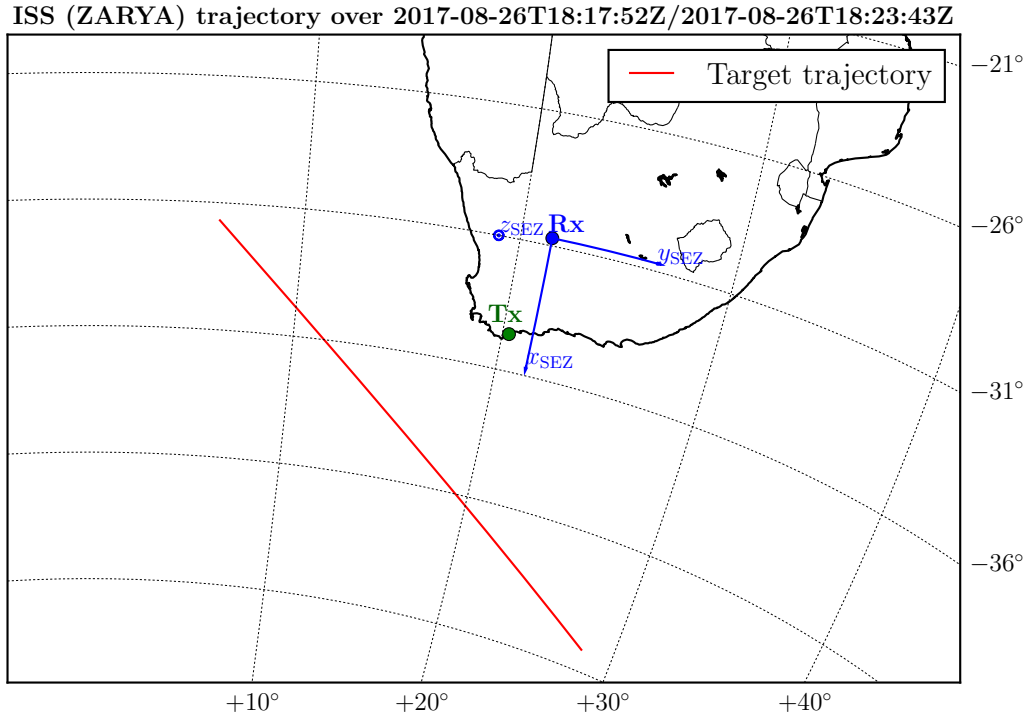


Figure 1-6: Map showing the location of the  $T_x$  at  $34.6^\circ\text{S}$  and  $20.3^\circ\text{E}$  and  $R_x$  at  $30.7^\circ\text{S}$  and  $21.4^\circ\text{E}$ . The  $x$ -axis of the local  $SEZ$  coordinate frame at the  $R_x$  points due South, the  $y$ -axis points due East and the  $z$ -axis points out of the plane of the map (at the zenith). The red curve denotes the  $ISS$ 's trajectory in the vicinity of the radar sensor.

Radar measurement quantities such as bistatic range, bistatic Doppler shift, elevation angle and azimuth angles are derived based on the sensor dynamics framework developed in this section.

Section 3.4 then explains how a radar range measurement differs from the geometric range (which is the *Line of Sight* distance between a radar and a target) when the target is distant. It explains the concept of light-time correction which needs to be performed when observing  $RSOs$  from a ground station. Expressions are given for bistatic range and Doppler shift which account for light-time correction. Simulation results are shown to prove that the  $MPT$  can compute both the ideal and the actual bistatic range and Doppler shift.

All of the work shown in the following chapters on sensor scheduling and orbit determination is built on the space debris dynamics and sensor modelling framework developed in this chapter. Relevant notation used in the following chapters are defined and detailed in this chapter to ensure self-consistency both in the report and in the software developed in this project.

### 1.4.3 Scheduling the MeerKAT radar

This chapter explains in detail the process of scheduling a space object observation experiment at the *MeerKAT* radar with the help of the *Mission Planning Tool* designed during this project.

First, the radar sensor's parameters which influence the tasking process are calculated in Section 4.2. Based on these parameter values, the target passage identification phase of the MPT is developed in Section 4.3. This phase determines when the space object of interest will be observable at the MeerKAT radar.

The MeerKAT radar is expected to operate in beam-park mode, so its transmitter antenna beam is kept in a fixed direction during the entire course of an observation experiment, as shown in Figure 1-4. The process of Tx tasking is explained in Subsection 4.4.1 and the best possible illumination for 8 scenarios investigated in this chapter are given in the following table.

Table 1-2: Observation window length for various space targets for the bistatic staring configuration

#	NORAD ID	TLE Epoch	Observation epoch	$\max\{T_{i,Tx}\}$ [s]
1	25544	2017-08-26T04:25:02Z	2017-08-26T17:47:20.732133Z	7.713080
2	37820	2017-08-30T18:22:58Z	2017-08-30T22:00:16.331227Z	5.997947
3	29754	2017-09-17T18:44:19Z	2017-09-17T21:29:07.287787Z	12.836933
4	33773	2017-09-10T03:30:54Z	2017-09-10T04:08:38.473107Z	8.572013
5	25544	2017-05-07T13:15:38Z	2017-05-07T13:25:09.818173Z	9.257107
6	25544	2017-09-10T22:31:16Z	2017-09-11T10:18:39.811080Z	6.463280
7	33759	2017-01-29T12:46:42Z	2017-01-29T15:24:52.174960Z	7.817173
8	37820	2017-04-25T14:26:58Z	2017-04-25T15:08:32.133520Z	4.492253

The subsequent component of sensor scheduling is Rx tasking which is discussed in Subsection 4.4.2. Given that the MeerKAT radar project is still in a preliminary phase, only the first three MeerKAT receivers are considered in this project. It is shown that these three receivers are sufficient to cover the Tx-illuminated portion of the trajectory. Various visualizations are developed in the MPT to instruct radar engineers on how to run the observation experiment for a chosen scenario. One of these is given below to summarize the outcome of this sensor scheduling chapter. Figure 1-7 shows the target trajectory projected onto the bistatic plane during the target transit which is predicted by the sensor scheduling phase.

Bistatic plane for object 25544 transit during 2017-09-11T10:17:22Z/2017-09-11T10:19:22Z

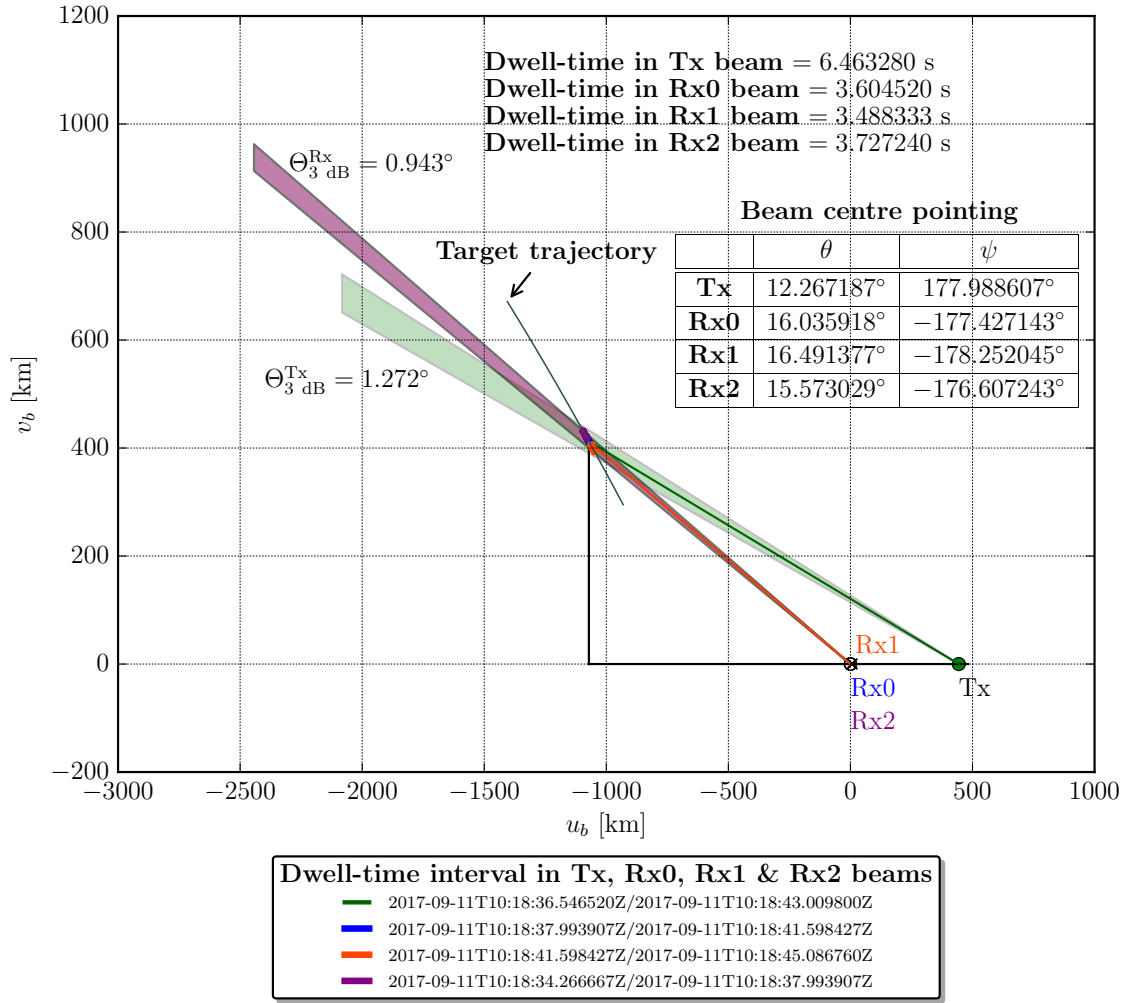


Figure 1-7: Bistatic plane showing the target trajectory and Tx and Rx beam pointing determined by sensor scheduling methods. The Tx's beam is shown in green.

Using the results from the sensor scheduling section, the single-pulse and coherently-integrated SNR at the receivers are calculated in Section 4.5. Table 1-3 shows the maximum SNR measured at the radar receiver for the 8 scenarios investigated in this chapter.

Table 1-3: Maximum integrated SNR at Rx for different RSOs' passes through the radar's FoV.

#	NORAD ID	TLE Epoch	RCS [m <sup>2</sup> ]	max{[SNR] <sub>CI</sub> } [dB]
1	25544	2017-08-26T04:25:02Z	401.801	68.501406
2	37820	2017-08-30T18:22:58Z	19.5231	60.388199
3	29754	2017-09-17T18:44:19Z	0.0121	11.107066
4	33773	2017-09-10T03:30:54Z	0.543	27.184846
5	25544	2017-05-07T13:15:38Z	401.801	66.745778
6	25544	2017-09-10T22:31:16Z	401.801	65.861252
7	33759	2017-01-29T12:46:42Z	0.079	21.872829
8	37820	2017-04-25T14:26:58Z	19.5231	57.545919

From the integrated SNR values, the radar measurement errors relating to bistatic range and bistatic Doppler shift are found. These radar measurement errors are vital to the tracking and orbit determination module discussed in the next chapter.

#### 1.4.4 Orbit Determination and Analysis

This chapter on OD first discusses how the Gauss-Newton filter (GNF) is used to estimate a space object's trajectory in Section 5.2. In Section 5.3, it defines the tracking schemes used in this project, namely the BIRDOPP scheme which involves processing measurement vectors consisting of bistatic range and bistatic Doppler shift and the BIRAZEL scheme whose measurement vectors consist of bistatic range and elevation and azimuth angles at the Rx.

To assess the performance of the trackers, Monte Carlo simulations are performed in Subsections 5.3.1.2 and 5.3.2.2. The average normalized RMSE<sup>2</sup> (ANRMSE) in the state estimates is calculated as primary figure of merit. Two filter consistency tests, namely the 3 $\sigma$ -ECM<sup>3</sup> test and the Average Normalized Estimation Error Squared (ANEES) test, are used to assess the filtering results. It is found that the Bistatic Range and Doppler (BIRDOPP) scheme always fails the second test but occasionally passes the first one. The Bistatic Range, Azimuth and Elevation (BIRAZEL) scheme always passes both consistency tests, indicating that there is covariance consistency and that there are no bias errors in the GNF BIRAZEL tracker. It is found that bias errors exist in the BIRDOPP tracker. This means that the Gauss-Newton filter which processes BIRDOPP measurements is either incorrectly implemented or it is correctly implemented but it converges to an incorrect (local) solution for the initial nominal trajectories considered in this investigation. The only difference between the failing BIRDOPP GNF and the correct BIRAZEL GNF lies in the quantities relating to the measurement model, that is, the measurement function  $\mathbf{g}$  and its Jacobian matrix  $\mathbf{H}$ . All of these derivations and the resulting

<sup>2</sup> RMSE is the root means squared error

<sup>3</sup> ECM: Error Covariance Matrix

code were verified by hand several times. Furthermore, the decrease in measurement residuals with each successive iteration of the **BIRDOPP** filter in Section 5-4 indicates that the filter is working properly. The final measurement residuals in Section 5-4 look very similar to zero-mean white Gaussian noise, devoid of structure, which means that the tracker is successfully filtering the noisy measurement vectors  $\mathbf{y}$ . The measurement residuals  $\hat{\mathbf{y}}$  of the **BIRDOPP** filter indeed pass the  $3\sigma$  test based on the measurement covariance matrix  $\mathbf{R}$ , giving further evidence that the **BIRDOPP GNF** is operating correctly. These observations lead to the conclusion that the second scenario occurred: the **GNF** converges to the wrong local minima instead of the global one when the filter iterates through the **BIRDOPP** measurements.

The target state estimates from both **BIRDOPP** and **BIRAZEL** filters are converted to Keplerian elements so that part of the target's **TLE** set can be reconstructed by the **MPT**. Furthermore, another set of Monte Carlo experiments showed that the **BIRAZEL**-based tracker produces estimates which improve the accuracy of the initial nominal trajectory, even when the latter differs greatly from the target's true trajectory. However, the **BIRDOPP**-based filter produces extremely inaccurate target state estimates when the initial nominal trajectory available to the filter is not close to the true trajectory.

Since the **MeerKAT** radar as per the current **RRSG** design can only measure bistatic range and bistatic Doppler shift and not the elevation and azimuth angles at the receiver, as required by the **BIRAZEL** scheme, a so-called 'observables estimation' phase is elaborated to estimate these two angles from the radar **SNR** measurements, the sensor tasking and the known nominal trajectory. The observables estimation phase assumes that time-parametrised second-degree polynomials can approximate the topocentric right ascension/declination profile resulting from the target passage. This profile is then transformed into timestamped arrays of elevation and azimuth angles from the **Rx** to the target.

The performance of the observables estimation is then assessed and it is seen that the elevation and azimuth angles can be estimated with a high accuracy. These estimated elevation and azimuth angle pseudo-measurements are then combined with the measured bistatic range to form the measurement vector in the **BIRAZEL** scheme, which works satisfactorily.

### 1.4.5 Conclusions and Recommendations

This chapter presents the conclusions and recommendations for future work.

With reference to the objectives of this project originally stated in Section 1.2, it outlines how each chapter has successfully met its intended objective(s). It also discusses how this report has described the engineering process behind the development of an **MPT** for the **MeerKAT** radar project.

It is explained that, from the astrodynamics point of view, the proposed [MeerKAT](#) radar can be feasibly used to observe space targets. This report has shown that, with the help of the [MPT](#), it is possible to schedule [RSO](#) observation experiments at the [MeerKAT](#) radar. It has been shown that a space target's illumination time within the proposed radar's [Tx](#) beam can be predicted by the [MPT](#). The [MeerKAT](#) receivers can be scheduled along with the [Tx](#) to observe a given object of interest. The [MPT](#) can predict (i) the radar geometry during a scheduled experiment. (ii) radar measurements such as bistatic range, bistatic Doppler shift and elevation and azimuth angles from [MeerKAT](#) to the target of interest. (iii) the single-pulse and coherently integrated [SNR](#) in the signals measured at the [MeerKAT](#) receivers as well as the resulting radar measurements.

With appropriate radar measurements made by the proposed [MeerKAT](#) radar, statistical orbit determination ([SOD](#)) is possible with a single target pass to a rough degree of accuracy. Based on [BIRAZEL](#) measurements, the [OD](#) phase of the [MPT](#) can improve a preliminary orbit, even when the latter deviates significantly from the true state vector. The orbit estimation performance improves greatly with increasing number of data points made available to the [OD](#) phase. Tracking based on [BIRDOPP](#) measurements consisting of bistatic range and Doppler shift as per the current [MeerKAT](#) radar design does not give satisfactory results.

# Literature review

## 2.1 Introduction

This chapter serves as a literature review on space junk. It firstly elaborates, in Section 2.2, on the origins, nature and evolution of the space debris population over the years. The need for space debris studies and SSA will be elucidated. An overview of Space Situational Awareness will then be given in Section 2.3. The different types of sensor systems employed in such endeavours will be discussed in Section 2.4. In particular, Subsection 2.4.1 will present ground-based sensors which exploit radio telescopes as receive node, in a similar configuration as the one under consideration in this project, in detail.

## 2.2 Background on space debris

This section provides general background information regarding the history of space debris. The Low Earth Orbit (LEO) environment will be characterised in terms of the debris population and nature.

### 2.2.1 History

The National Aeronautics and Space Administration (NASA) and the Inter-Agency Space Debris Coordination Committee (IADC) specify that space debris are man-made and hence meteorites are not considered as space junk. The history of space debris thus began in the early years of the Space Age.

The first artificial satellite, *Sputnik-1* was launched in October 1957 and de-orbited in January 1958. *Vanguard-1*, a US satellite launched shortly after, in 1958, is still in orbit to this day and



thus is the oldest piece of space debris. In 1961, the upper stage of the US launched rocket *Thor-Ablestar* exploded at an altitude of about 900 km, producing some 300 trackable RSOs. The end-result was an increase by a factor of 3.5 in the then population of man-made objects in orbit. [13] This event was the very first break-up in orbit. Nearly 200 of the Thor-Ablestar fragments are still in orbit today. [14]

In the ensuing five decades, about 8000 objects have been launched into space. Of the 4303 satellites in orbit (as of February 2017 [15]), the majority have decayed. Only some 1700 satellites are active according to [16] and [17], suggesting that nowadays the majority of space objects are actually pieces of space waste. The space object population will be discussed in more details in Subsection 2.2.3.

The first unintentional collision between two resident space objects occurred in July 1996 when the French *Cerise* military satellite collided with an *Ariane-1* rocket fragment. [18] Other notable events which created space debris include the 2007 Chinese anti-satellite (ASAT) test which destroyed a *Fengyun* satellite and the 2009 collision between the *Iridium-33* and *Cosmos-2251* satellites.

The Chinese ASAT test in 2007 produced 2087 debris objects which are routinely tracked by the US Space Surveillance Network. [19]. The following figure shows a Satellite ToolKit (STK) simulation of the 2007 event.

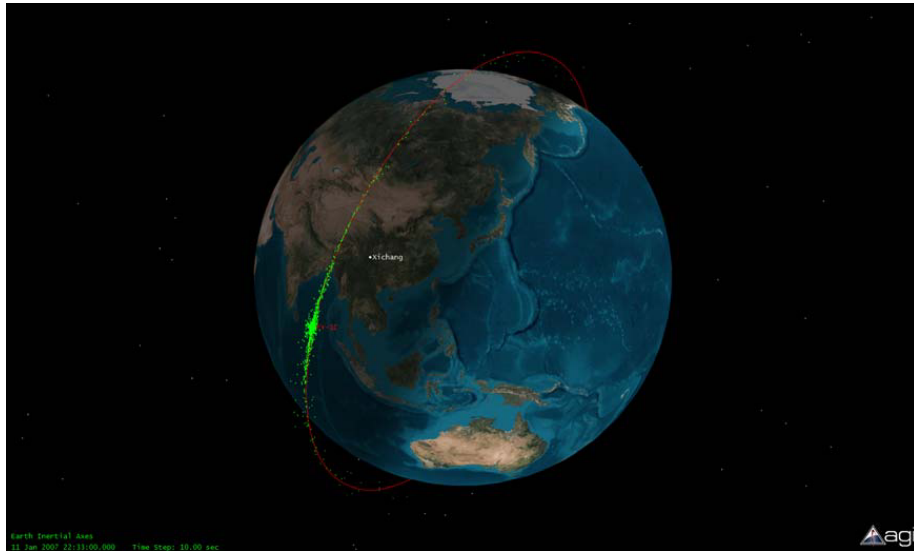
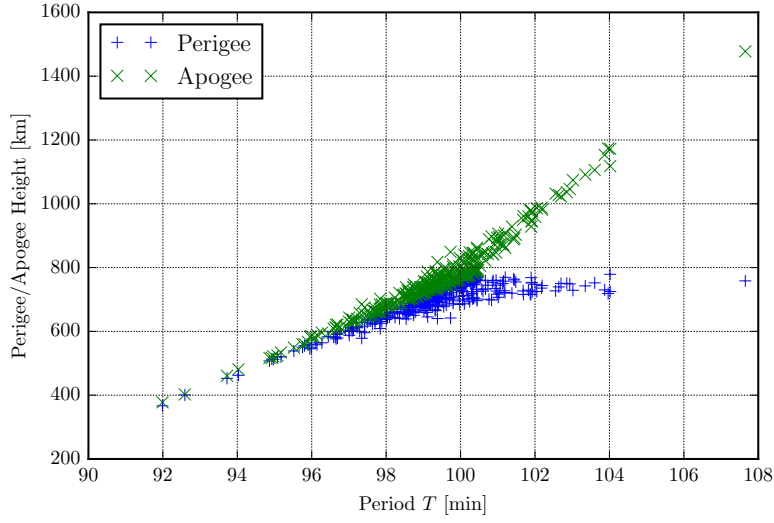


Figure 2-1: STK simulation of the Fengyun-1C ASAT test from [19] showing debris (in green) spreading over the orbit (in red) five minutes after the impact.

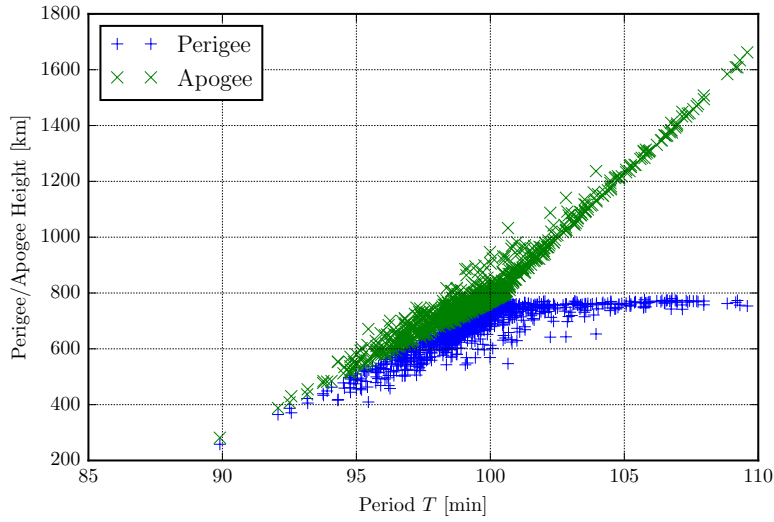
In the 2009 collision, the Russian *Cosmos* military satellite was defunct since 1995 and was no longer actively controlled whereas the *Iridium* satellite, a civilian communications satellite, was active. Figures 2-2a and 2-2b are Gabbard diagrams showing the perigee and apogee of tracked particles emanating from *Iridium-33* and *Cosmos-2251* against their Keplerian period.

Gabbard diagram for Iridium-33 debris at epoch 2017-04-09T22:01:42+00:00



(a) Tracked Iridium-33 debris

Gabbard diagram for Kosmos-2251 debris at epoch 2017-04-09T20:20:47+00:00



(b) Tracked Kosmos-2251 debris

Figure 2-2: Gabbard diagrams showing the tracked debris particles resulting from the 2009 collision between the Iridium-33 and Kosmos-2251 satellites as of April 9, 2017. The 320 objects originating from the Iridium-33 satellite are shown in (a) at the epoch 2017-04-09T22:01:42 while the 1039 tracked objects from the Kosmos-2251 satellite are shown in (b) at the epoch 2017-04-09T20:20:47. (TLEs sourced from [celestrak.com](http://celestrak.com).)

Debris particles from the 2009 collision have periods between 90 to 110 minutes and perigee and apogee heights between 200 km to 1800 km. Such diagrams are useful in visualizing debris scenarios in conjunction analysis.

### 2.2.2 Nature

Space debris can be classified according to whether they originate from a fragmentation event or not. Non-fragmentation debris include

- solid rocket motor effluents
- derelict satellites
- rocket upper stages and components released during spacecraft separation from the launch vehicle
- lost equipment such as screwdrivers and gloves lost by astronauts.

Fragmentation debris comprise of

- objects produced by intentional or non-intentional collisions
- flecks of paint from spacecraft surfaces
- debris produced by small particle impacts on satellites

Rocket upper stages and defunct satellites are typically between ten centimetres and ten metres in size and are thus considered as large pieces of debris. Rocket motor effluents including drops of coolant (such as sodium-potassium alloy) vary from 0.1 mm to 4 cm in size. Paint flecks are comparatively much smaller as their sizes vary between 2  $\mu\text{m}$  to 0.2 mm. [20, 21] Despite their small size, paint flecks still pose a threat to space assets due to the immense momenta involved in collisions. The following figure shows the impact of a debris object on a Hubble telescope solar panel.

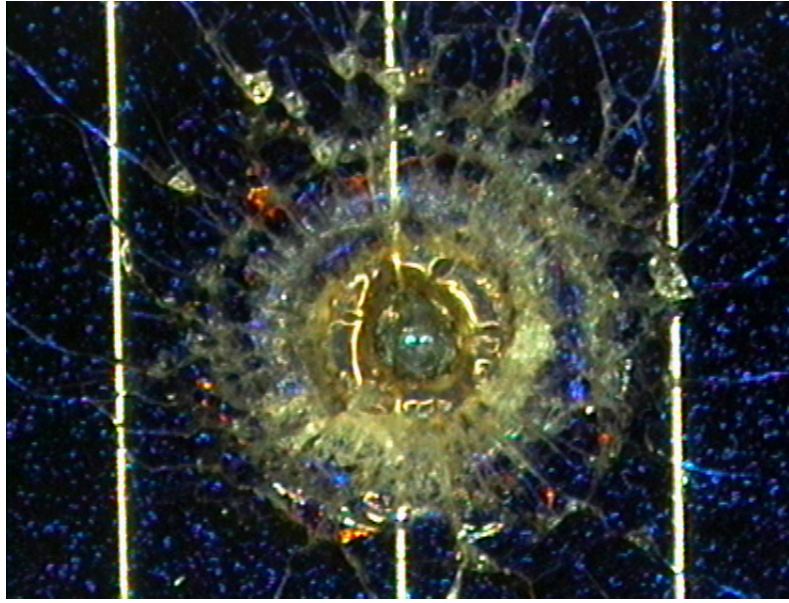


Figure 2-3: Impact on Hubble Space Telescope solar panel. Source: [ESA](#) [22]

Larger pieces of space junk may survive de-orbiting, that is, they do not burn up in the atmosphere and may even reach the surface of the Earth. A Payload Assist Module used to launch a satellite crashed in the Saudi Arabian desert in 2001 and reached the ground without disintegrating, as can be seen in the following figure.



Figure 2-4: A Payload Assist Module(PAM) used to launch a satellite crashed in the Saudi Arabian desert in 2001. [23]

According to the [NASA](#) Orbital Debris Program Office (ODPO) in [24], reentering orbital junk has never caused any injury to human beings or property damage. Debris bodies which are in orbit of 600 km or less are eventually de-orbited due to atmospheric drag and most likely burn up as they reenter the atmosphere.

Space debris can vary significantly in terms of properties such as area-to-mass ratio, chemical composition and radar cross section (RCS) among others. It is generally agreed that objects with high area-to-mass ratios (HAMRs) should be the focus of research in space environment studies because their small size makes them very hard to detect and track with optical and radar sensors. HAMR objects have a large surface area in comparison to their small mass due to their complex shapes. They have reduced fluctuating radar cross sections because (i) they tumble about their centre of mass due to solar radiation pressure and (ii) their complex shapes scatter radar waves away from the illuminating source.

### 2.2.3 Space object population

The ODPO pioneered the study of the space object population and its evolution over the years. The most prominent papers on the space environment are thus based on work done at NASA. The number of man-made objects in orbit has increased steadily as our activities in space grew over the years. Figure 2-5 shows the evolution of the population of resident space objects (RSOs) from 1957 to 2017. The total number of space objects (brown curve) which consists of active spacecraft (blue curve) and space junk comprising of rocket bodies (green curve), mission-related debris (orange curve) and fragmentation debris (purple curve). Due to the Chinese ASAT test in which a Fengyun satellite was destroyed (mentioned in Subsection 2.2.1), the fragmentation debris population increased sharply in 2007. The smaller jump in the fragmentation debris curve in 2009 was due to the Iridium-33 and Cosmos-2251 collision event.

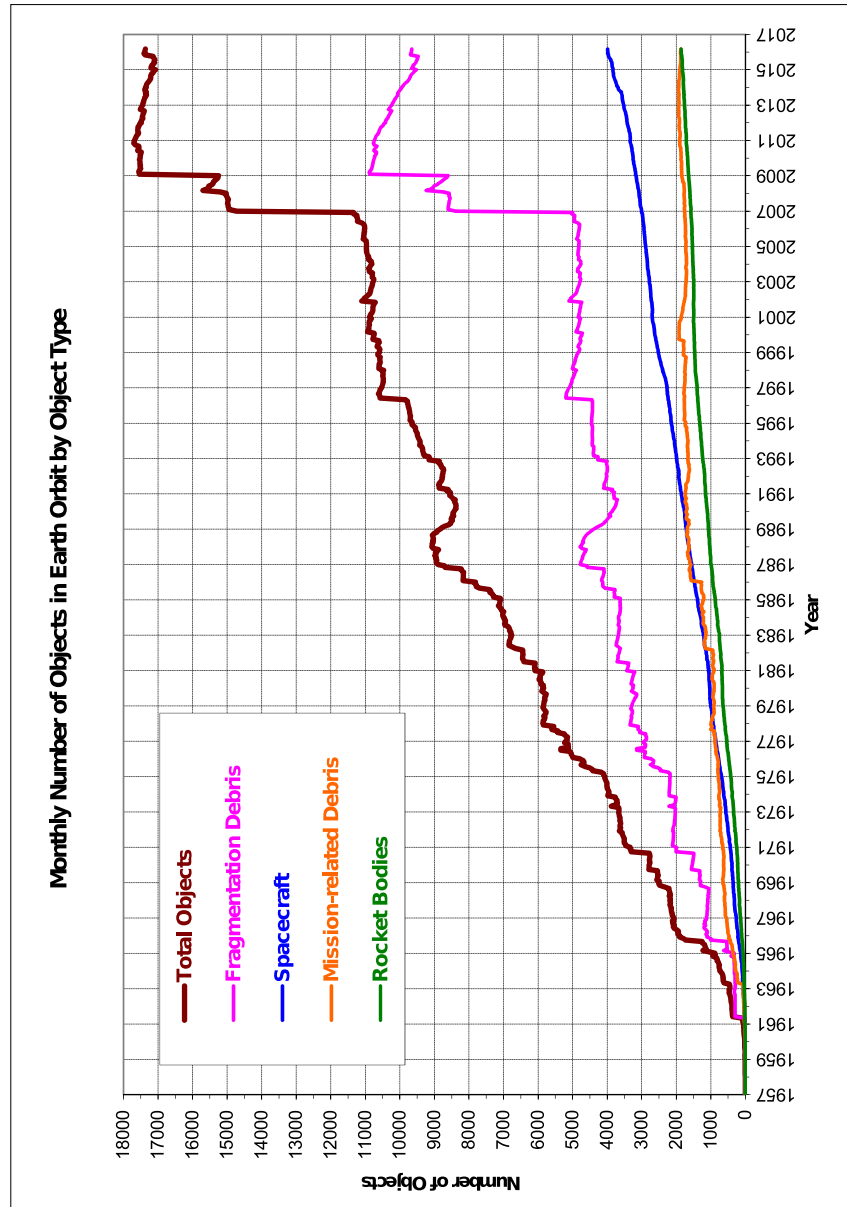


Figure 2-5: Orbiting space debris objects catalogued by the [USSSN](#) as of January 2016. “Mission-related debris” means objects brought about as a result of a planned mission. “Fragmentation debris” refers to debris resulting of satellite breaking down. [25]

[NASA](#)’s ODPO states that there are more than 21000 space debris particles which exceed 10 cm in size in Earth orbit. These are objects whose radar cross-section ([RCS](#)) is large enough for them to be consistently tracked and catalogued by [NORAD](#). It is estimated that there are more than 100 million particles which are smaller than 10 cm in size. [24] Understandably, such small particles have very small radar cross-sections and are thus very hard to track and catalogue. These particles are nevertheless still a threat to valuable assets in space. Thus, developing an ability to track very small debris objects has been identified as an urgent need by the research community [14, 3].

## 2.3 Background on SSA

Collisions between resident space objects (RSOs) in near-Earth orbits produce a formidable quantity of smaller particles. The latter will accumulate in orbit indefinitely unless they get de-orbited by atmospheric drag. The debris particles take part in more and more collisions over time, producing an ever-growing number of smaller bodies. The resulting chain reaction, called the Kessler syndrome [14], leads to an inexorable net growth of the space object population, if no palliative measures are taken. This phenomenon was theorized in 1978 by NASA scientists Kessler and Cour-Palais in [2]. The following figures from [14] show long-term predictions of the debris population if no mitigating actions are taken.

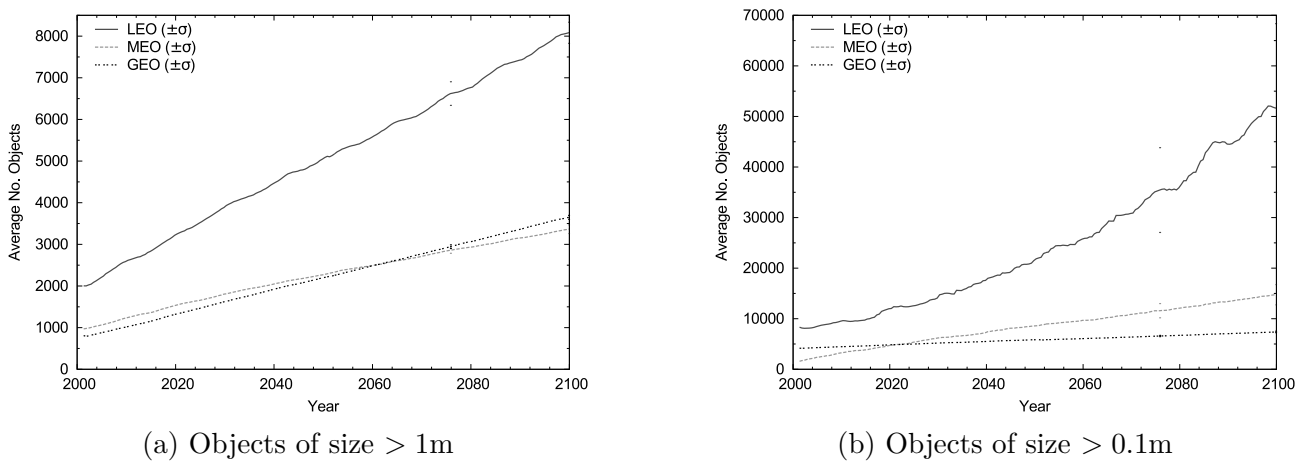


Figure 2-6: Long-term forecast of the evolution of the debris population [14] indicating a general increase at all three orbit regimes. The LEO regime is more populated than the other two because it contains more satellites. Over the 100 year time span, the Kessler effect in LEO causes the steeper growth in the small debris population in (b) than in the big debris population in (a). The  $\sigma$  symbol in the legend indicates the standard deviation confidence interval predicted based on the Monte Carlo runs.

These results were drawn from 10 Monte Carlo runs of the European Space Agency's MASTER 2001 space environment modelling software. The number of RSOs in the LEO, Medium Earth Orbit (MEO) and Geostationary Earth Orbit (GEO) regimes are predicted to increase significantly over this time span. The situation is most alarming for the LEO regime: a fourfold increase in the regime which contains the highest population of key spacecraft. For example, the ISS which orbits in the LEO regime has shields which can only withstand impacts of objects up to 1cm in size. Currently, the International Space Station has to execute one manoeuvre on average per year to avoid a collision with a tracked space object. It is obvious that avoidance procedures will occur more frequently in the future, at a high financial cost for the satellite operator and a high energy expenditure for the satellite's thrusters.

Artificial satellites in orbit are used for telecommunication, weather forecasting, navigation,



Earth observation and other purposes. These space assets are extremely valuable to mankind. Measures of protection under the realm of [SSA](#) aim to be pre-emptive and efficient. The following section will shed some light on available measures of protection.

### 2.3.1 Components of SSA

[SSA](#) is defined as the thorough knowledge of the space environment, which incorporates the ability to track and predict the location of space objects ([RSOs](#)) at any time [\[4\]](#). The [ESA](#) outlines three aspects of [Space Situational Awareness](#) in [\[5, 6\]](#):

- [SST](#): Space Surveillance and Tracking of resident space objects.
- SWE: Space Weather monitoring
- NEO: Near-earth object detection and tracking.

Space Surveillance and Tracking is the main area of interest for the [RRSG](#)'s [MeerKAT](#) radar project. Figure [2-7](#) depicts the main processes involved in [SST](#).



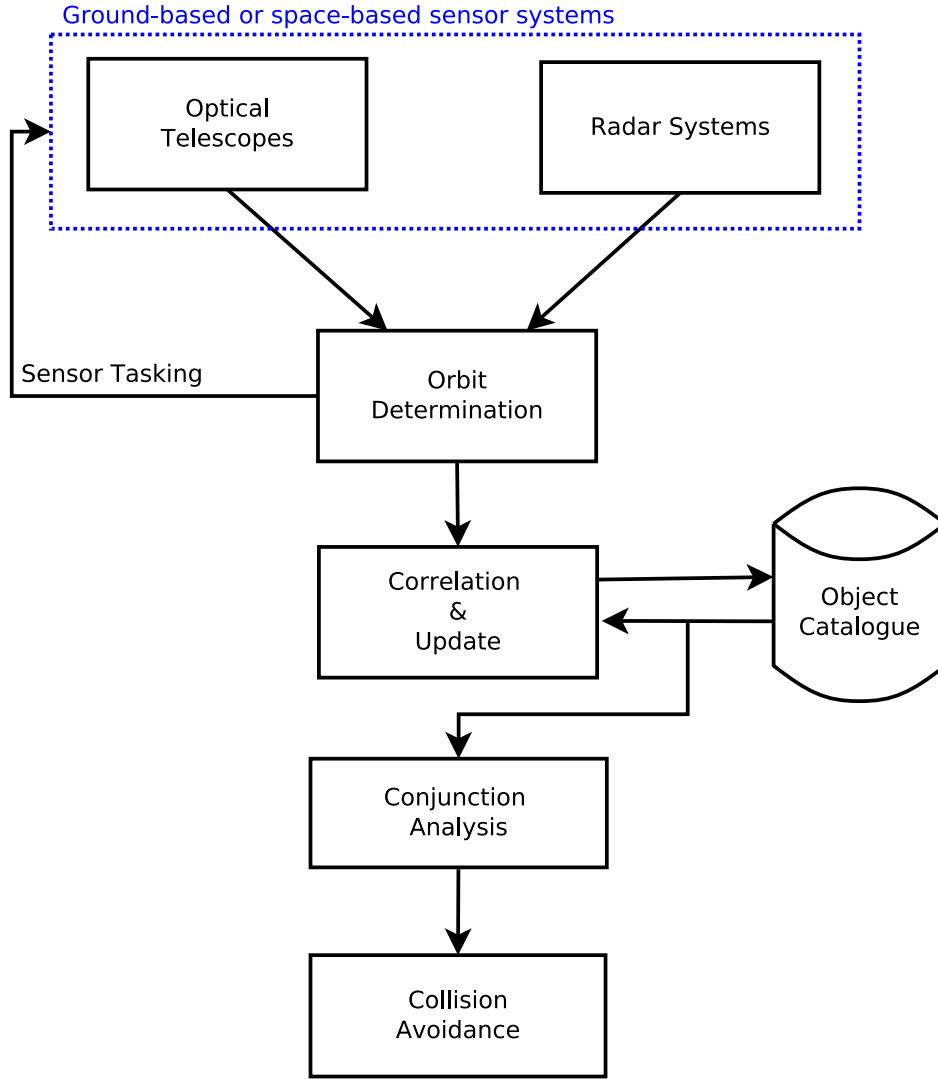


Figure 2-7: System level block diagram of Space Surveillance and Tracking aspect of SSA

The first major constituent of the SST section is the **sensor block**. Sensor facilities can be ground-based or space-based. They can be further categorised as optical telescopes and radar systems. In the context of the MeerKAT radar, the sensor is a ground-based bistatic radar system operating in beam-park mode (BPE).

Data measured by the sensor is sent to the **orbit determination block** where the **state vector** and estimated error covariance matrix (ECM) at the observation epoch are estimated through **Statistical Orbit Determination (SOD)** techniques. The state vector consists of the position and velocity of the orbiting body and is sometimes referred to as the *ephemeris* of the RSO. Space object orbits estimated by the OD block are used to determine the **sensor** tasking required to collect more observational data.

The ephemeris of the target body is then tested for correlation with the ephemerides of bodies present in the catalogue in the **correlation block**. The target is said to be a persistent resident

space object if the catalogue already documents its existence [26]. On the other hand, if the object is deemed new, it is added to the catalogue in the **high accuracy catalogue block**.

Conjunction analysis (**CA**) is performed on the high accuracy catalogue to find out the probability of collision between known **RSOs** in the **conjunction analysis block**.

If a collision risk is evaluated to be above a certain threshold, the relevant satellite operator is notified so that they may instruct their satellite to avoid the collision (**collision avoidance block**). Estimated state vectors and their associated **ECMs** from the object catalogue are used to evaluate the probability of collision between **RSOs**.

## 2.4 Sensors for space debris studies

Optical (telescope and LIDAR) and radar sensors are employed for observing space debris. These can be categorised as ground-based or space-based. Ground-based systems are located on the surface on the Earth while space-based systems are built on top of satellites. Ground-based radars employed for **SSA** are usually used to observe space debris in the Low Earth Orbit regime only. This is due to the radar propagation loss being proportional to the fourth power of the range to the target. For this reason, existing bistatic radars which exploit a radio telescope as radar receiver, such as the Murchison Widefield Array, only do observation experiments on **LEO** targets.

Radar sensors used in space surveillance operate in tracking mode, beam-park mode or stare and chase mode [27]. In the first mode, the radar dish rotates to follow the target of interest as it transits in the sky. This means that the **RSO** spends a lot of time within the radar's **Field of View**, typically five to six minutes. The tracking radar thus collects a large number of measurements which may consist of range, Doppler shift, elevation and azimuth angle to the target. Since the slant-range, elevation and azimuth angles are sufficient to unambiguously identify a point in three dimensional space, a tracking radar which makes such measurements can accurately estimate the position of a target and, using the target's dynamic model, it can also accurately estimate its velocity vector. In beam-park mode, the radar beam is aimed at a fixed point with respect to the Earth and kept in that direction during the course of the entire experiment (called a **BPE**). This mode is ideal to conduct surveys of the space debris population. When a **BPE** is run for 24 hours, a circular strip of the sky in the right ascension plane is scanned through as the Earth rotates about its axis. This results in a snapshot of all orbital debris within that orbit regime. Since space objects spend a limited amount of time within the radar's **FoV** in beam-park mode, they lead to a small number of radar measurements which are insufficient to accurately estimate their orbital elements. The stare and chase mode is a mixed mode in which the radar starts a **BPE** and then chooses a particular object of interest

and follows it in tracking mode. [27] The MeerKAT radar design envisaged by the RRSg is meant to work in beam-park mode.

As the first creators of space debris, the United States pioneered the study of space debris using optical and radar sensors. The United States Space Surveillance Network (USSSN) collects observational data routinely using their radar systems (monostatic and multistatic) and their electro-optical systems which are better suited than radar for observing objects further away in GEO. The Cobra Dane radar is a passive electronically scanned array radar which participates in the US Space Surveillance Network. This facility also cooperates with the NASA Orbital Debris Program Office (ODPO). The Cobra Dane radar has a peak power of 15.4 MW and a beamwidth of  $0.6^\circ$  [28]. Its measurement errors in range and angle are 3 m and  $0.02^\circ$  respectively [29].



Figure 2-8: The Cobra Dane radar is an L-band passive electronically scanned array radar situated at Shemya Island, Alaska (North America). It can track objects which are as small as 5 cm in size. [30]

Other major radar systems in the US Space Surveillance Network include the Millstone Hill radar, the Haystack Radar and the Haystack Auxiliary Radar which are all three in Westford, Massachusetts, the tracking radar at Pirinçlik Air Base in Turkey and the Goldstone radar in the Mojave desert, California. [30]



Figure 2-9: The Haystack and Haystack Auxiliary radar [30]

The Haystack radar system is an X-band radar and can detect objects in the [LEO](#) regime which are as small as 1 cm in size. Both the Haystack and the nearby Haystack Auxiliary radar (HAX), which works in the Ku-band, can operate in beam-park mode: they can stare at a fixed direction in the sky and collect observational data over a given period of time. The Millstone Hill radar works in L-band, with a peak power of 3 MW. Its measurement errors are 5 m in range, 0.0005 m/s in range rate and  $0.01^\circ$  in both elevation and azimuth angle. [31] The Cobra Dane, the Millstone and Haystack radars are all monostatic sensors. On the other hand, the Goldstone radar operates bistatically. An overview of radar facilities used for space debris observation as of 1999 is given in [27, Table 1]. The following figure from [32] shows the United States' network of optical and radar sensors which participate in [SSA](#)-related activities.

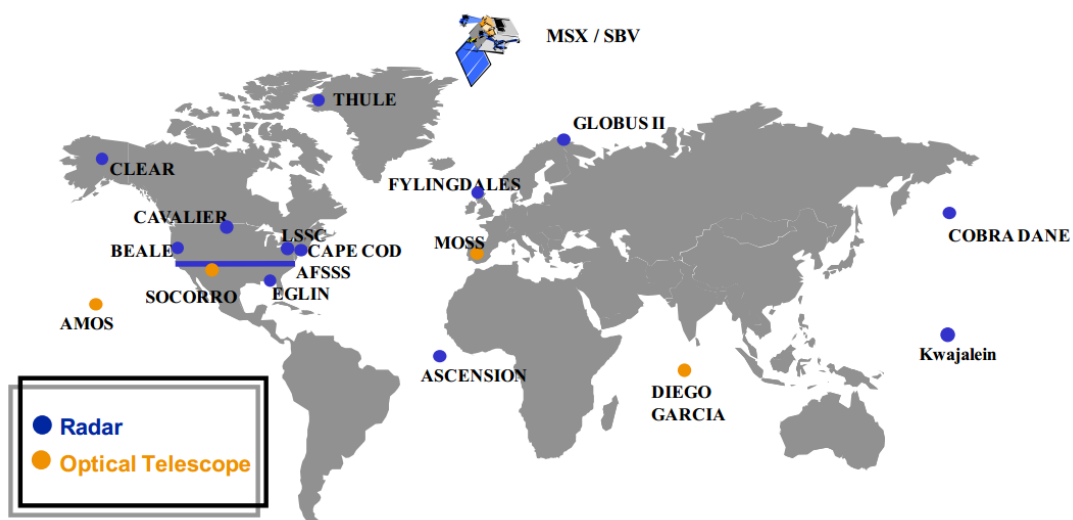


Figure 2-10: The US Space Surveillance Network's array of optical and radar sensors spread around the world. [32]

### 2.4.1 Bistatic radars which operate in stare mode

The proposed [MeerKAT](#) radar will be a bistatic radar which operates in stare mode. Radar systems in a similar configuration are described in this subsection. Such systems have a general configuration as shown in Figure 2-11. During the experiment, the [transmitter](#)'s beam centre is kept fixed at a given point in the sky typically. The [receiver](#) may consist of several antennas which are located very close to each other which can operate as a phased array.

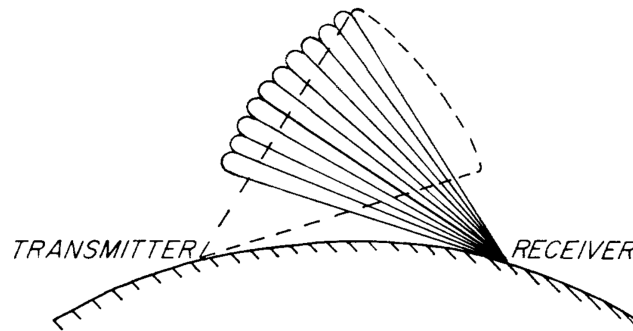


Figure 2-11: Bistatic radar with multiple receiving beams [33, Figure 3]

The radar sensors discussed in this subsection have a receiver which is either a radio telescope facility (for example, the Medicina radio telescope for the Italian [BIRALES](#) radar in Subsection 2.4.1.3) or a dedicated radar receiver such as the GRAVES radar system in Subsection 2.4.1.1. According to [34], bistatic radars featuring radio telescopes as receivers have the general characteristics:

- the [transmitter](#) is an antenna with a wide beamwidth which can transmit at high power to illuminate space targets.
- the [receiver](#) is a radio telescope dish with precise beam pointing due to its large diameter. Typically, radio telescopes have high sensitivity which helps in detecting the faint target returns from small, distant [RSOs](#).

The main radar systems operating in the configuration are the GRAVES radar in France, the [TIRA](#) radar with the radio telescope at Effelsberg in Germany, the [BIRALES](#) radar in Italy and the [MWA](#) passive radar in Australia.

#### 2.4.1.1 GRAVES

The Grand Réseau Adapté à la VEille Spatiale (GRAVES, French for Large Array for Space Surveillance) is a continuous-wave bistatic radar operating in the VHF band. It consists of

phased-array transmitters in Dijon and phased-array receivers 380 km away. [35] The smallest debris that can be detected by the GRAVES system are 10 cm in size. [36] Each transmitter in the GRAVES radar has a maximum power of 2 kW [35].

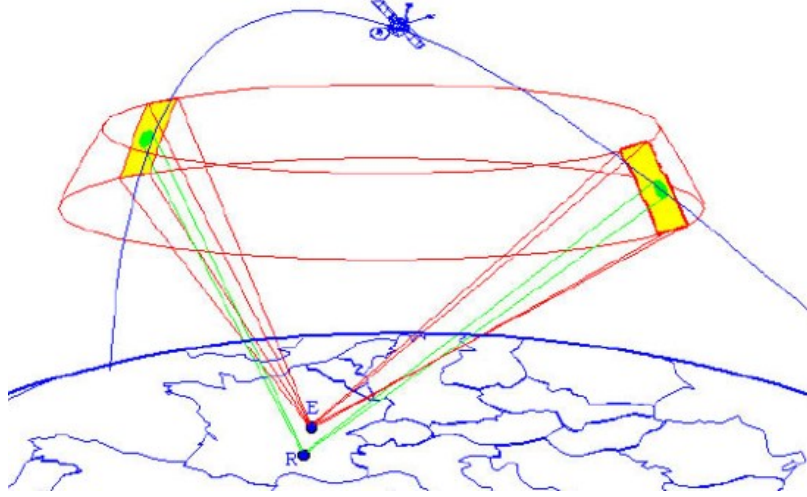


Figure 2-12: The GRAVES radar in France is a bistatic sensor. The emitter is denoted by ‘E’ and the receiver is denoted by ‘R’. The bistatic baseline is  $L_b = 380$  km. [36]

As can be seen in Figure 2-12, a space target flies through the sensor’s two FoVs which are separated in space. This leads to additional radar measurement vectors which are separated in time, which help in determining the object of interest’s orbit more accurately.

The GRAVES system records radar measurements of bistatic Doppler shift and thanks to its phased-array nature, it can also make measurements of elevation and azimuth angles to space targets from the receivers [37]. By processing radar measurement vectors consisting of Doppler shift and elevation and azimuth angles, the GRAVES orbital data processor can accurately estimate a RSO’s orbital elements from a single target pass. The system’s radar measurement errors are not given in the literature. The Mission Planning Tool used to predict RSO sightings and the radar signal and data processing software for the GRAVES sensor are not discussed in the literature [35, 37, 36, 14].

#### 2.4.1.2 TIRA with the radio telescope at Effelsberg

The Tracking and Imaging RAdar (TIRA) located in Wachtberg near Bonn, Germany routinely tracks space objects with an L-band radar and images them with a Ku-band imaging radar. This facility is run by Fraunhofer Institute for High Frequency Physics and Radar Techniques (FHR). The powerful (1 MW) tracking radar’s dish has a beamwidth of  $0.5^\circ$ . Distant small space junk particles can be detected when the radio telescope at Effelsberg, 21 km away from

**TIRA**, is used as bistatic radar receiver. [3] Radio telescopes are engineered to be more sensitive than radar systems, so they can detect small, distant targets more easily.

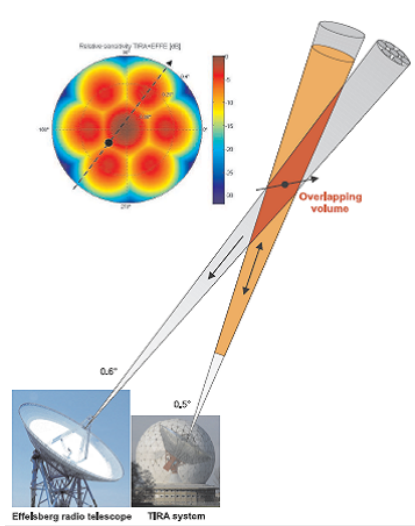


Figure 2-13: The **TIRA** system as Tx and the Effelsberg radio telescope as radar receiver. The Effelsberg radio telescope's antenna has 7 horns with individual feeds. [38] A target's transit through the Rx's beam is shown in the upper left corner.

In 1996, a space debris observation experiment was done with a bistatic radar formed with the **TIRA** system as radar transmitter and the Effelsberg radio telescope as radar receiver. The COoperative BEAM-park mode (COBEAM) experiment [39] lasted 24 hours and produced observational data on objects as small as 0.9 cm in size at a range of 1000 km. [3] Several BPEs have been done at the **TIRA**/Effelsberg radar since the 1996 campaign [39, 40, 41, 42]. The literature does not mention orbit determination being successfully done during these BPEs and does not address the issue of why OD was not done. Orbit determination was done in observation experiments in which **TIRA** was operating in monostatic mode[43]. Tracking operations at **TIRA** are done in stare and chase mode [43]. Three inconvenient characteristics of observational data collected by **TIRA** in monostatic stare mode are given in [43] as (i) limited quantity of recorded data points due to the short amount of time (1 to 3 seconds) spent by space targets in the observation volume. (ii) reduced range accuracy due to the use of unmodulated pulses. (iii) poor SNR in the received signal arising from echoes off distant targets with small RCS. The first two issues mentioned are resolved in the chase mode because the radar's FoV tracks the motion of the target of interest and because modulated pulses are used. The third issue is not a factor with the bistatic radar thanks to the high sensitivity of the radio telescope used. The following figure shows the radar geometry occurring when BPEs are done with the bistatic **TIRA**/Effelsberg radar.



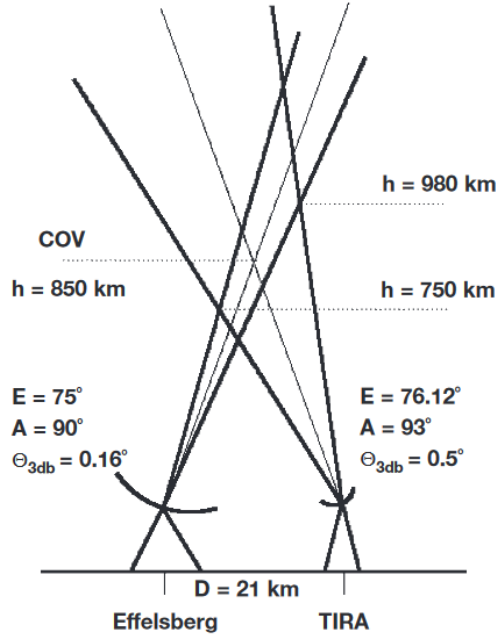


Figure 2-14: Radar geometry for the BPE at TIRA/Effelsberg. [3] The bistatic baseline  $L_b = 21$  km is represented by D. The beamwidths  $\Theta_{3\text{ dB}}$  of the Tx and Rx are  $0.5^\circ$  and  $0.16^\circ$  respectively. The elevation and azimuth angle pointing of the dishes are given by E and A. COV means the centre of the overlapping volume.

While TIRA can accurately track space targets in monostatic tracking mode, it most likely cannot estimate the orbit of RSOs when operating in a bistatic configuration with the Effelsberg radio telescope. In this configuration, space targets spend an extremely short amount of time in the overlapping volume<sup>1</sup> with the radar unable to move its antenna beams to track the target and gather additional data points. This leads to an insufficient quantity of data for orbit determination to be done. The TIRA monostatic tracking paper [43] states that, in the orbit determination module of their MPT, the space object dynamics are assumed to be the two body model perturbed by the  $J_2$  effect and the tracking filter used is the Extended Kalman filter (EKF). The radar measurement vector and the associated radar measurement errors are not discussed. The tracking results shown in [43] were obtained through numerical simulation and not from real-world experiments.

### 2.4.1.3 BIRALES and BIRALET

In Italy, two bistatic radar systems named BIRALES and BIRALET were developed for space debris surveillance. For both radars systems, the transmitter is the Flight Termination System

<sup>1</sup> Given that the Rx antenna beamwidth is only  $0.16^\circ$ , it can be inferred that the overlapping volume is mainly constrained by the receiver's beam. The target transit through the FoV will take less than the 1 to 3 seconds dwell time of the monostatic mode.



(FTS) radar facility of the Italian military located at Salto di Quirra Joint Test Range (Poligono sperimentale e di addestramento Interforze di Salto di Quirra) in Sardinia [44]. The Bistatic RAdar for LEO Survey (BIRALES) sensor [45] employs the Northern Cross radio telescope in Bologna, Italy as radar receiver. The Sardinia Radio Telescope (SRT) in San Basilio, Cagliari (Italy) is the Rx in the Bistatic RAdar for LEO Tracking (BIRALET) system [34]. The transmitter for BIRALET and BIRALES, FTS, emits in continuous-wave (CW) mode with an average power of 4 kW. It operates in the UHF band (more specifically, in the range 400 MHz to 455 MHz) [46]. The half-power beamwidth,  $\Theta_{3\text{ dB}}$ , of the FTS transmitter is  $30^\circ$  [34].

The following figure shows the transmitter and receiver for the BIRALES radar as well as the overlap of the antenna beams. To observe space debris, the Northern Cross radio telescope works as a multi-beam receiving antenna.

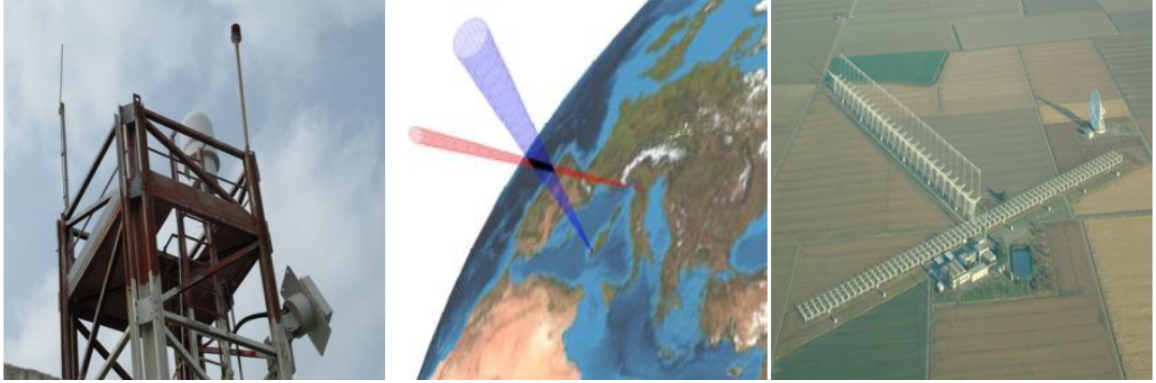


Figure 2-15: The BIRALES and BIRALET systems use the FTS facility at Salto di Quirra (left hand side image) as radar Tx. The middle image shows the Tx and Rx beams (red and blue cones, respectively) overlapping in space for the BIRALET system. The Rx in BIRALET is located in Sardinia. The right hand side image shows the Northern Cross radio telescope which is the Rx in the BIRALES sensor. [44]

### BIRALES

The latest research papers [45, 47] concerning the BIRALES system document the development of a radar simulator for space debris observation scenarios which involves an orbit determination processor operating on simulated trajectories. No real world experiments with the BIRALES radar are discussed. The BIRALES sensor produces radar measurement vectors which consist of bistatic range and Doppler shift. Their orbital processing unit makes use of the time-indexed signal to noise ratio (SNR) measured at each receiver, the nominal target trajectory and the Tx's and the receiver's beam pointing to estimate the evolution of the elevation and azimuth angles to the target during its passage through the radar's FoV. This so-called *observables estimation* phase produces pseudo-measurements of elevation angle and azimuth angle at the Northern Cross radio telescope. Since the elevation and azimuth angles at the antenna are not

directly measured using some signal processing-level technique for the **BIRALES** system, the elevation and azimuth angles should be seen as pseudo-measurements. However, the **BIRALES** papers do not mention that these are not actual radar measurements and so do not use the term ‘pseudo-measurements’. The two estimated quantities (elevation and azimuth angles) are combined with the actual measurements of bistatic range and bistatic Doppler shift and fed to the orbit determination module [47]. Figure 2-16 shows the passage of the space object with **NORAD** ID 32477 through the **BIRALES** sensor’s FoV in the topocentric right ascension  $\Delta\alpha_t$  versus right declination plane  $\Delta\delta_t$ . The ellipses in the **TOPORADEC**<sup>2</sup> plot denote the multi-beams in the receiver’s Field of View. The long black arrow denotes the target’s trajectory.

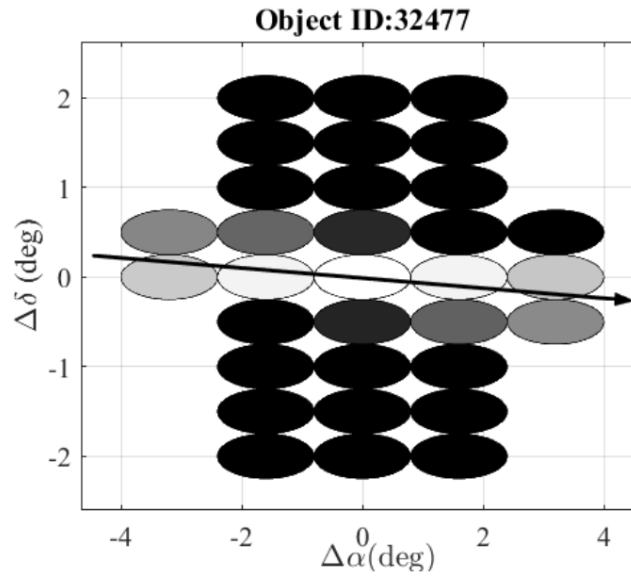


Figure 2-16: BIRALES radar: **TOPORADEC** profile for target passage. [47]

Beams in Figure 2-16 are shaded according to their maximum **SNR** value normalized with respect to the overall maximum **SNR** received. When the target transits exactly through a beam centre, there is no attenuation due to beamshape loss and the **SNR** received is maximal, leading to a beam shaded white in Figure 2-16. Beams through which the target does not transit are shaded black to indicate the lowest **SNR**. The elevation and azimuth pointing of each **Rx** beam centre is known and can be mapped to the  $(\Delta\alpha_t, \Delta\delta_t)$  plane. When the **SNR** is at its maximum value for a beam, the target is at its closest to the beam centre  $(\Delta\alpha_t, \Delta\delta_t)$ . Researchers at the Italian **BIRALES** radar assumed that it is possible to approximate the target’s profile in Figure 2-16 with two time-parametrised second-degree polynomials (one for topocentric right ascension, one for topocentric declination). A weighted curve fit using the normalized maximum **SNR** for each beam as weight is then used to estimate the target’s **TOPORADEC** profile. This

<sup>2</sup> Topocentric Right Ascension and Declination plane

**TOPORADEC** profile is then mapped into an elevation-azimuth profile which is used in the radar measurement vector in the **OD** module mentioned previously.

The system's radar measurement errors in bistatic range and Doppler shift are not given in the **BIRALES** papers. Furthermore, none of these papers discuss potential model truncation errors which arise due to the mismatch between the target's true **TOPORADEC** profile and the assumed time-parametrised second-degree polynomials. Expressions for radar measurement errors in topocentric right ascension and declination (and the resulting measurement errors in elevation and azimuth angles) are not presented. The **BIRALES** system seemingly performs an ordinary (unweighted) least squares estimation to determine **RSO** orbits. This is highly unusual because orbit determination processors conventionally make use of statistics (sometimes called statistical orbit determination [48]) to be able to provide an estimated error covariance matrix (**ECM**) to quantify the uncertainty in the estimated **state vector** (position and velocity) of the target. **Statistical orbit determination** requires knowledge of the measurement errors which are not used in the **BIRALES** system. Since the actual radar measurement errors are not properly derived in the **BIRALES** papers, the **OD** results contain untrustworthy error covariance matrices (**ECMs**). This means that the uncertainty in the estimates is not quantified properly, which is very concerning given that tracked objects' **ECMs** are needed for conjunction analysis (**CA**, see Subsection 2.3.1).

**BIRALES** papers also describe the development of a custom bistatic radar simulator to analyse the performance in detecting and tracking space objects. The following figure from [47] shows the architecture of the **BIRALES** radar simulator.

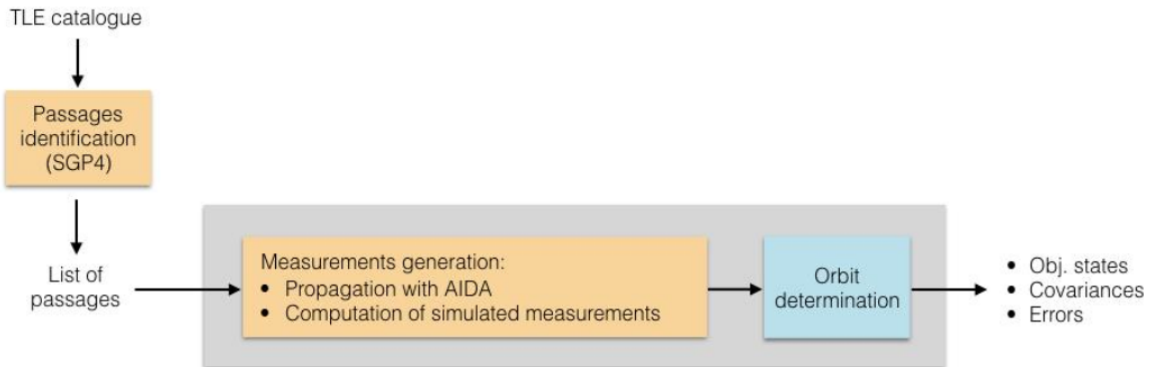


Figure 2-17: **BIRALES** radar simulator architecture [47].

From a space object two line elements (**TLE**) set catalogue, the **BIRALES** simulator imports **TLEs** and extracts their state vector (position and velocity vectors) and propagates their orbits using Simplified General Perturbations # 4 (**SGP4**) theory. It also determines when these **RSOs** will transit in the vicinity of the radar in the **Passage Identification** block. Based

on the predicted space object passages, a list of passages along with the relevant epoch and antenna pointings is derived. The **Measurements Generation** block uses the state vector of a space debris of interest at epoch and performs orbit propagation (OP) using the AIDA (Accurate Integrator for Debris Analysis) software. From the simulated target trajectory and the radar geometry, simulated radar measurements are generated. The latter are input to an **orbit determination** module which estimates the RSO of interest's state vector. The estimated error covariance matrix associated with the target state estimate and error in the estimated state are output by the OD module. As was explained previously, the input to the OD module comprises of the radar measurement vector and radar measurement errors. The target dynamic model and OP method employed in the AIDA software are not mentioned in [47]. The measurement model takes into consideration an Earth Gravity Model 2008 (EGM 2008), atmospheric drag, third body effects and solar radiation pressure.

### BIRALET

The BIRALET sensor has a longer baseline ( $L_b \approx 40$  km) than the BIRALES sensor since its receiver is located in Sardinia. [49] The Sardinia radio telescope's beamwidth is  $0.8^\circ$  while the FTS transmitter's beamwidth is  $30^\circ$  [34]. In contrast to the BIRALES sensor, the BIRALET system has indeed run real life experiments, in April and June 2014. The journal paper [34] documents a space debris observation campaign on April 17, 2014 in which six known RSOs were successfully detected. The internal technical report [49] discusses the April 17 campaign as well as the April 14 and 15 campaigns and the June 4, 5, 6 campaigns. At least six objects were successfully detected at the correct epoch and with similar Doppler shifts as predictions made by BIRALET tailor-made mission planning software. Tracking the resident space objects and determining their orbit were not done. The BIRALET radar simulator is very similar to the BIRALES simulator. In addition to the passage identification and measurements generation modules, the BIRALET radar simulator determines the SRT pointing (to three decimal places) necessary for running a suitable observation experiment for each RSO of interest. It also determines the length of time spent by an RSO within the sensor's FoV as well as the SNR during this so-called observation window. [34]

#### 2.4.1.4 Australian radar using the Murchison Widefield Array as receiver

The Murchison Widefield Array (MWA) in Western Australia, just like MeerKAT in South Africa, is a precursor to the Square Kilometre Array (SKA). This radio telescope consists of 128 antenna elements called 'tiles' spread in a sparse layout [50] similar to the MeerKAT instrument, as can be seen in Figure 2-18. The MWA has a dense inner core of antennas with the rest of the tiles spread over a much larger area similarly to MeerKAT (shown in Figure 1-2).

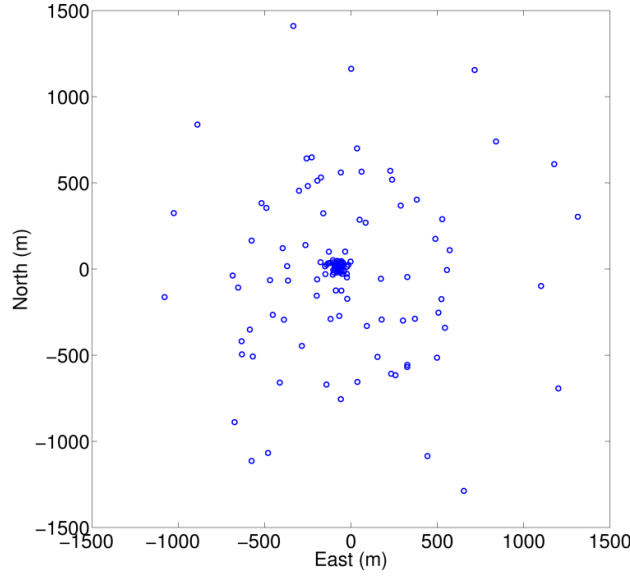


Figure 2-18: Murchison Widefield Array layout. A receiver or ‘tile’ is represented by a blue circle. [50]

The [MWA](#) is used as radar [receiver](#) in a passive bistatic radar system operating in the commercial FM broadcast band. The radar [transmitter](#) radiates omnidirectionally at 99.3 MHz with a bandwidth of 50 kHz. It is located in Perth which means that the bistatic baseline is  $L_b \approx 670$  km. Tingay et al. in a 2013 paper [51] report on an experiment done with the [MWA](#) FM radar in November 2012 to observe the [ISS](#). Only 32 of the 128 [MWA](#) tiles were used in this experiment. With an integration time of 1 s, the [MWA](#) imaged the sky using radio astronomy techniques and not radar signal and data processing techniques. Consequently, the results from processing are high resolution images in the [TOPORADEC](#) plane (for instance, Figure 3 and Figure 4 in [51]). These two quantities (topocentric right ascension  $\Delta\alpha_t$  and declination  $\Delta\delta_t$ ) are angular information which are usually used in conjunction with range and Doppler shift measurements in radar tracking. The latter quantities, bistatic range and Doppler shift are not measured in the first [MWA](#) demonstration and no actual target tracking results are shown in [51].

The operation and capabilities of the [Mission Planning Tool](#) developed for the [MWA](#) radar come up tangentially in the 2013 paper [51]. The [MWA](#) software tool predicts when specific space targets will transit over Australia based on [SGP4](#) propagation of their [TLEs](#). Time stamps are stated with a precision of 1 s using the Universal Time standard. The [MPT](#) also determines the antenna pointing needed for the [MWA](#) array to execute an experiment. These elevation and azimuth angles are stated at a resolution of  $1^\circ$ .

In 2017, Palmer et al. published a paper on the radar signal processing development done for the [MWA](#) radar to create measurements of bistatic range and Doppler shift [50]. An observation

experiment was done in April 2015 with an FM transmitter in Adelaide as the intended passive Tx. The observation scenario is illustrated on the map in Figure 2-19.

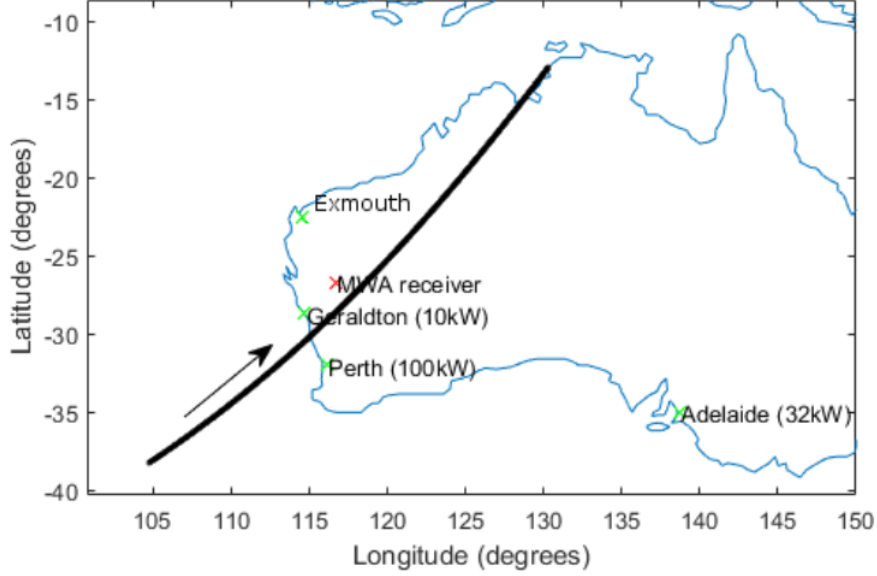


Figure 2-19: The 2015 ISS observation experiment with the MWA radar: location of the passive Txs (green crosses) and the Rx (red cross) and the ISS trajectory lasting two minutes. The powers of the Txs are shown in brackets. [50]

The experiment was initially intended to use the bistatic pair consisting of the MWA and the Adelaide Tx but it was later found that target echoes originated from the Perth and Geraldton FM transmitters. Due to failure of one of the MWA tiles, only 127 receive antennas were able to collect observational data. The coherent integration time used in the signal processing block was one second ( $T_{CPI} = 1$  s). Range-Doppler processing was performed on the received signals to create measurements of bistatic range and Doppler shift. Measurements of elevation and azimuth were made through interferometric processing. These four quantities were combined to form the radar measurement vector fed into the tracking filter. The corresponding measurement covariance matrix was derived with the following values as standard deviation:  $0.1^\circ$  in azimuth  $0.2^\circ$  in elevation, 1 range bin and 15 Doppler bins. The target dynamics were simulated by SGP4 OP and the tracking algorithm was a Markov Chain Monte Carlo (MCMC). [50]



## 2.5 Summary

### 2.5.1 Discussion

It is evident from the literature survey presented in Section 2.2 that space debris are a major cause of concern in the field of space science and engineering. The consensus in the international space community is that developing [Space Situational Awareness](#) capacities is extremely urgent. Section 2.3 described the main components of [SSA](#) of which the [SST](#) aspect is the most relevant for the [MeerKAT](#) project. In the system level block diagram in Figure 2-7, three elements correspond to the space surveillance and tracking ([SST](#)) segment: the sensor block, the orbit determination block and the sensor tasking element which acts as feedback from the latter to the former. The following Section 2.4 reviews sensors located around the world which have been used in space debris studies. The focus is kept on bistatic radar systems which operate in stare mode in Subsection 2.4.1. Of these, the systems which incorporate a radio telescope facility as radar receiver are the most similar to the proposed [MeerKAT](#) radar:

- [TIRA](#) with the Effelsberg radio telescope in Germany  
The [MPT](#) employed is only mentioned tangentially in the literature. The mechanics of the sensor tasking used is not explained. Orbit determination has not been addressed in papers concerning this bistatic radar configuration. However, [TIRA](#) can perform [OD](#) when operating monostatically. The chosen target dynamic model is the two body plus  $J_2$  model. The radar measurement vector and the associated radar measurement errors are not discussed. The [EKF](#) is used as tracking filter.
- The [BIRALES](#) and [BIRALET](#) radars in Italy  
A tailor-made [MPT](#) was developed for these two Italian radars. It features [SGP4](#) orbit propagation in the target dynamic model. The [MPT](#) determines the antenna pointing required to execute correct debris observation experiments which constitutes sensor tasking. It can also predict radar quantities of interest such as the signal to noise ratio and radar measurement vectors. For the [BIRALES](#) sensor, the measurement vectors comprise of the bistatic range, bistatic Doppler shift, elevation and azimuth at the [Rx](#). An ordinary least squares technique was used to solve the [OD](#) problem. Since the elevation and azimuth angle at the receiver cannot be directly measured, they are approximated by a so-called observables estimation technique which makes use of the known nominal trajectory and the [SNR](#) measurements in the signals received by the multi-beam receiver. The [BIRALET](#) sensor did not do any orbit determination.
- The passive FM radar with the [MWA](#) as receiver in Australia  
The [MPT](#) developed for the Australian passive radar is only mentioned tangentially in

the literature. The results from sensor tasking are shown but the actual mechanics of the sensor tasking element in the [MPT](#) is not discussed. The [MPT](#) features [SGP4](#) orbit propagation in the target dynamic model. The radar measurement vector consisted of bistatic range, bistatic Doppler shift, elevation and azimuth angle at the [Rx](#). The first two quantities result from range-Doppler processing while the angles were obtained from interferometric processing. The orbit determination was done with a MCMC-based algorithm<sup>3</sup>.

The geodetic and time conventions adopted by the [MPTs](#) are also of interest. The literature on the [TIRA](#) system does not clarify which geodetic and time conventions are used. The Italian radars' [MPT](#) used the [EGM 2008](#) gravitational model and represented timestamps using the [UTC](#) (Universal Coordinated Time) standard. Timestamps in the [BIRALES](#) and [BIRALET](#) papers are represented in a 24-hour clock system with the format `hh:mm:ss`. The [MWA](#) papers use a similar clock system and format for timestamps in the [UT](#) (Universal Time) standard. The literature on the [MWA](#) sensor does not clarify which earth gravity model is employed in their [MPT](#).

### 2.5.2 Conclusion

Based on the foregoing discussion, the following conclusions are drawn, with regard to the objectives of this project stated in [Section 1.2](#):

- Target dynamic model and Orbit Propagation

Two target dynamic models were mentioned in the literature: the [SGP4](#) model and the two body plus  $J_2$  model. For the former model, [SGP4](#) theory must necessarily be used for [OP](#). Various numerical schemes are suitable for propagating the latter model. This dissertation will investigate the suitability of these two models for the purposes of the [MPT](#).

- Sensor scheduling

While sensor scheduling was performed by software tools built for the radar systems reviewed in [Subsection 2.5.1](#), its mechanics were not expounded. A sensor scheduling scheme suitable for the [MeerKAT](#) radar will be elaborated in this report.

- Radar measurements prediction

The [BIRALES](#) papers discussed how the [SNR](#) at the radar receiver is calculated while taking into account beam-shape loss and the radar geometry of the observation scenario.

---

<sup>3</sup> MCMC: Markov Chain Monte Carlo



The [SNR](#) will be calculated in a similar way in this report. Furthermore, the bistatic range and Doppler shift and their corresponding measurement errors will also be calculated.

- Orbit determination module

The radar measurement vector for the [BIRALES](#) and Australian radar was comprised of the bistatic range, bistatic Doppler shift, elevation and azimuth angles at the [Rx](#). Since the [MeerKAT](#) radar cannot measure elevation and azimuth (the [BIRALES](#) radar also cannot), an observables estimation phase has to be elaborated as well. The [BIRALES](#) radar used a tracking filter based on least squares estimation whereas [TIRA](#) used an Extended Kalman filter and the [MWA](#) radar used an MCMC-based algorithm. A suitable tracking filter will have to be found for the [OD](#) module developed in this project.

Finally, it was seen that the papers on the [BIRALES](#) and [BIRALET](#) systems have clearly specified which gravitational model and time conventions were used in their work. This ensures that their results can be interpreted by other researchers and be integrated into global [SSA](#) endeavours. Suitable conventions for time, timestamp representation and geodetic model will have to be adopted to ensure that the results presented in this document are meaningful to the research community.

# Dynamics and Measurement Models

## 3.1 Introduction

This chapter provides an in-depth development of space object dynamics in Section 3.2 and sensor dynamics in Section 3.3. To be able to eventually present mathematical models for the target and sensor motion, suitable coordinate and time reference frames are defined and described in both of these sections. Examples proving the validity of the mathematical models and their software implementation are given. Section 3.4 is a discussion of how the apparent bistatic range and Doppler shift (measured by the radar system) differ from the ideal (calculated) bistatic range and Doppler shift. The chapter concludes with a summary of the work presented here.

## 3.2 Space object dynamics

This section explains how the dynamics of a [RSO](#) are modelled in the [MPT](#). To be able to eventually generate the trajectory of a [RSO](#), its orbit must be described appropriately. Subsection 3.2.1 explains how to describe an orbit and then Subsection 3.2.2 outlines how an orbit description is encoded in a [NORAD Two Line Element set](#). Finally, Subsection 3.2.3 concludes this section by showing how [orbit propagation](#) is done over a given time interval.

### 3.2.1 Describing an orbit

Space object orbit modelling can be done in three geocentric coordinate systems: the Keplerian, Cartesian and equinoctial systems. The first two coordinate systems mentioned are the most popular in the space target tracking literature. Keplerian elements and Cartesians are used in

conjunction in the [MPT](#) to facilitate analysis by both types of intended users: astrodynamacists and radar engineers. Conversion algorithms between the relevant coordinate systems are shown in [\[52, 53\]](#).

### 3.2.1.1 Keplerian orbital elements

The position and velocity of an Earth-orbiting body can be described by six classical orbit elements, known as *Keplerian elements* or simply *Keplerians*.

- The size and shape of the orbit are given by the *semi-major axis*  $a$  and *eccentricity*  $e$  of the ellipse.
- The orientation of the orbit is indicated by the *right-ascension of the ascending node* (RAAN)  $\Omega$ , the *inclination*  $i$  and the *argument of perigee* ( $\omega$ ).
- The position within the orbit is determined by any one of the three parameters
  1.  $\nu$ , the *true anomaly*.
  2.  $E$ , the *eccentric anomaly*.
  3.  $M$ , the *mean anomaly*.

The figure below shows that the Earth is at one focus of the ellipse in the orbital plane.

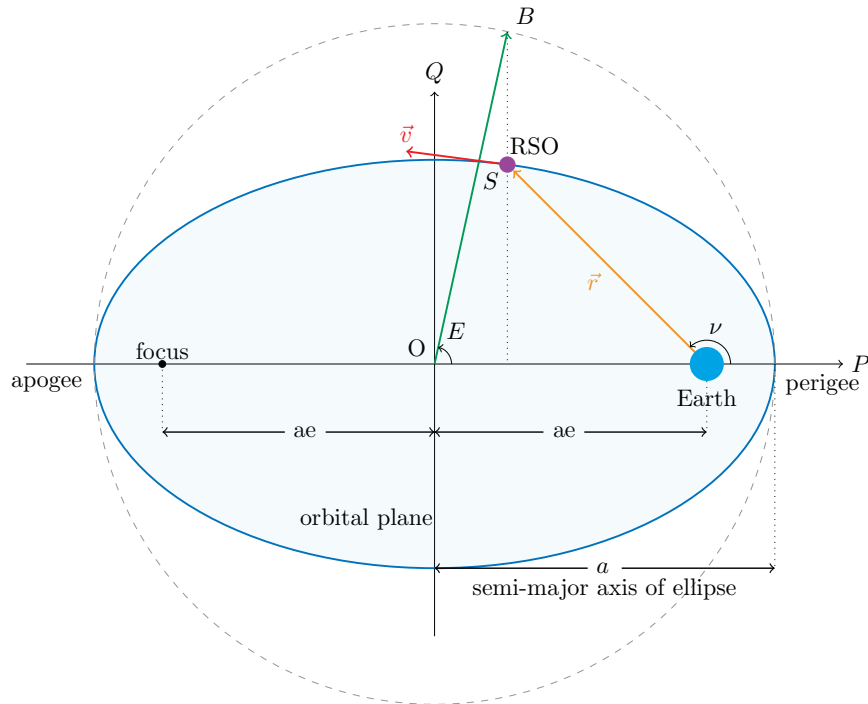


Figure 3-1: Kepler orbit

The elliptical orbit is circumscribed by the auxiliary circle. The point at which the satellite is closest to the Earth is called the *perigee*, which can be seen on the right of the figure above. The furthest point is the *apogee*, on the left.<sup>1</sup> The semi-major axis,  $a$ , is the radius of the circumscribing circle. The eccentricity  $e$  is

$$e = \frac{f}{a} \quad (3-1)$$

where  $f$  is the distance from the centre 0 to the focus.

The angle which its position vector  $\mathbf{r}$  subtends to the line  $OP$  is called the true anomaly,  $\nu$ . As the satellite moves along its orbit, the true anomaly angle changes, as well as the Eccentric Anomaly angle,  $E$  (the angle indicated at the origin). The mean anomaly,  $M$  can be calculated from Kepler's equation:

$$M = E - e \sin(E) \quad (3-2)$$

It is clear that any one of the three parameters  $\nu$ ,  $E$  and  $M$  identifies the position of the satellite in the orbital plane. The orientation of the orbital plane is depicted in the figure below.

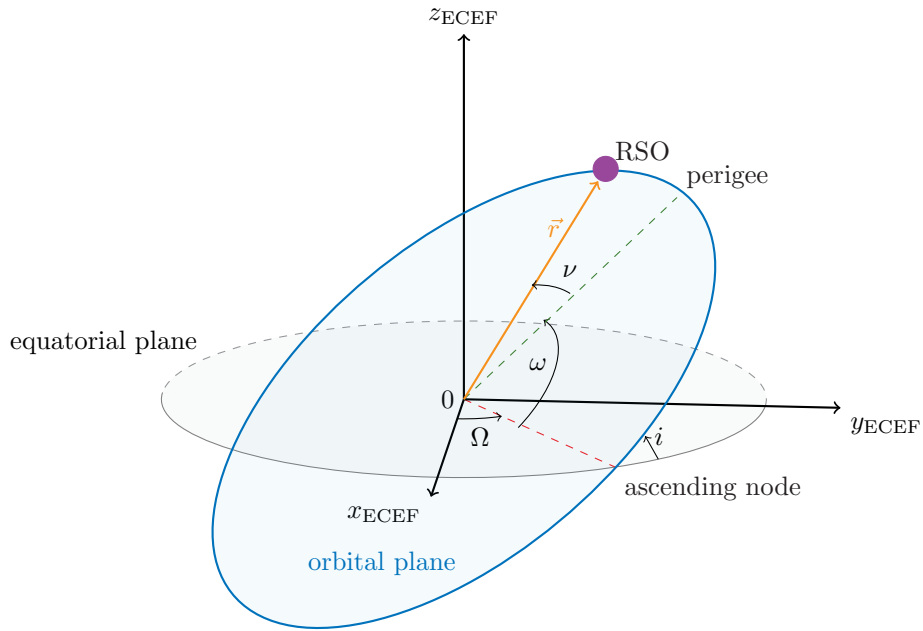


Figure 3-2: Keplerians of celestial body. The Cartesian coordinate system with axes  $(x_{\text{ECEF}}, y_{\text{ECEF}}, z_{\text{ECEF}})$  will be defined in the following section.

The plane of reference is the equatorial plane. The orbit crosses the equatorial plane from south to north at the *ascending node*. (The *descending node*, which is not labelled here, is the

<sup>1</sup> General (i.e. not Earth-specific) terms for these are pericentre and apocentre.

opposite.) The angle between the orbital plane and the plane of reference is the inclination angle  $i$ . The RAAN angle,  $\Omega$  and the argument of perigee angle  $\omega$  give the orientation in the remaining two degrees of freedom. One set of elements  $\{a, e, i, \Omega, \omega, \nu\}$  with an implicit timestamp form an *ephemeris*.

### 3.2.1.2 Cartesian representation

A different representation of the ephemeris of a **RSO** is the Cartesian state vector,  $\mathbf{x}$ .

$$\mathbf{x} = \begin{bmatrix} x & y & z & \dot{x} & \dot{y} & \dot{z} \end{bmatrix}^T \quad (3-3)$$

The dimensionality of the state vector is  $d_x = 6$ . The position vector  $\begin{bmatrix} x & y & z \end{bmatrix}$  in the Cartesian plane forms the position vector  $\mathbf{r}$ , shown in the figure below.

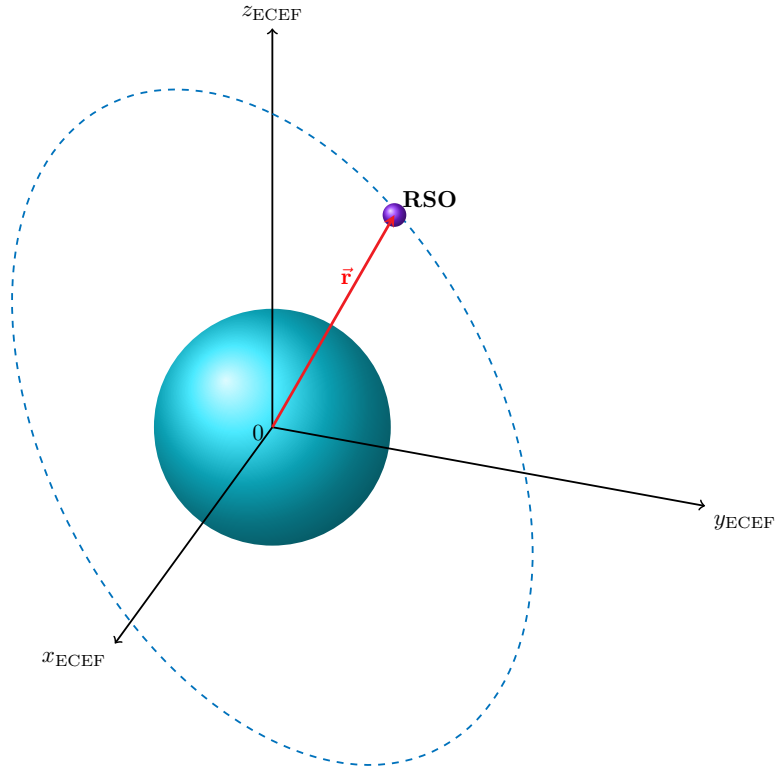


Figure 3-3: Space object orbit around the Earth.

### 3.2.2 Reading a TLE set

The [NORAD Two Line Element](#) format is a data storage format used to encode a [space object](#)'s Keplerian elements (defined in Subsection 3.2.1.1) as computed at a given epoch. The canonical reference for the [TLE](#) format definition and description is *Spacetrack Report # 3* published in 1980 [54].

The Space-Track catalogue maintained by the United States Strategic Command inventories the [TLEs](#) of [RSOs](#) currently being tracked by the United States Space Surveillance Network (USSSN) with their network of optical and radar sensors spread all over the world, as explained in Section 2.4. USSTRATCOM publishes<sup>2</sup>an abbreviated catalogue which does not contain [TLEs](#) pertaining to classified satellites.

The [TLE](#) of a space debris emanating from the Cosmos-2251 satellite which took part in the 2009 collision with an Iridium-33 satellite is shown below.

```
COSMOS 2251 DEB
1 33759U 93036G    17029.53243639 .00000982  00000-0  27135-3 0  9992
2 33759  74.0214  46.9222 0023404 219.5296 259.6480 14.47946858418372
```

The following information is read by the [MPT](#):

- 33759 is the [NORAD](#) satellite catalog number which uniquely identifies this [RSO](#).
- 17029.53243639 is the epoch of validity of this [TLE](#). [TLE](#) timestamps adopt the [UTC](#) standard. 17029.53243639 means the 29.53243639<sup>th</sup> day of 2017. The equivalent timestamp which complies with the [ISO 8601](#) standard is 2017-01-29T12:46:42Z.
- 74.0214 is the orbital inclination  $i$  in degrees.
- 46.9222 is the right ascension of the ascending node  $\Omega$  in degrees.
- 0023404 indicates that the eccentricity  $e$  of the orbit is 0.0023404.
- 219.5296 is the argument of perigee  $\omega$  in degrees.
- 259.6480 is the mean anomaly  $M$  in degrees.
- 14.47946858418372 is the mean motion  $n$  in revolutions per day.
- 27135-3 is the starred ballistic coefficient  $B^*$ , a term defined in [SGP4 OP](#) theory for modelling aerodynamic drag.  $B^* = 27135 \times 10^{-3} R_e^{-1}$ .

---

<sup>2</sup>[space-track.org](https://space-track.org). [TLEs](#) can also be downloaded from [celestrak.com](https://celestrak.com) with no registration required.

Relevant values read from the [TLE](#) are passed as parameters to the [OP](#) methods discussed in the following subsection. Timestamps are formatted according to the [ISO 8601](#) standard in the [MPT](#) to avoid misinterpretation when communicating the [MeerKAT](#) radar results with the international community later on. All epochs shown in this dissertation are in [UTC](#). This is represented by a ‘Z’ appended to the end of a time expression, e.g. 2017-01-29T12:46:42Z. The local time in South Africa is therefore two hours ahead of the [UTC](#) time shown by the [MPT](#). Conventionally, times are represented as `yyyy-mm-ddThh:mm:ssZ` in the [ISO 8601](#) standard, where `yyyy` means the four-digit year, the following `mm` means the two-digit month, `dd` means the two-digit day of that month, `T` separates the date and time elements, `hh` means the two-digit hour, `mm` represents the two-digit minutes, `ss` means the two-digit seconds and `Z` means [UTC](#) time. This implies that the resolution is 1 s. The [ISO 8601](#) standard allows the addition of extra digits to denote decimal fractions of a second. Therefore, up to six additional digits are added to timestamps in this report when the use of higher precision representations is necessary. Such timestamps would have the format `yyyy-mm-ddThh:mm:ss.ffffffZ` where `ffffff` represents the decimal fraction of a second. This means that the resolution is 1  $\mu$ s.

### 3.2.3 Propagating an orbit

[Orbit Propagation](#) is a process which generates a trajectory for a space object based on its ephemeris.

As discussed in Subsection 3.2.1, the position and velocity of a space object are expressed as a state vector  $\mathbf{x}$  which can comprise of Cartesian or Keplerian elements. An orbit propagator essentially calculates the state vector of a [RSO](#) at a different time instant (future<sup>3</sup> or past<sup>4</sup>) based on the state vector at a given time.

The orbit propagation function  $\mathbf{f}_{\text{OP}}$  can be expressed as

$$\mathbf{x}(t + \zeta) = \mathbf{f}_{\text{OP}}(\mathbf{x}(t), \zeta) \quad (3-4)$$

where  $\zeta$  can be a positive or negative time step.

The following figure shows a comparison between the three approaches to [OP](#) that exist.

---

<sup>3</sup> a prediction.

<sup>4</sup> a retrodiction.

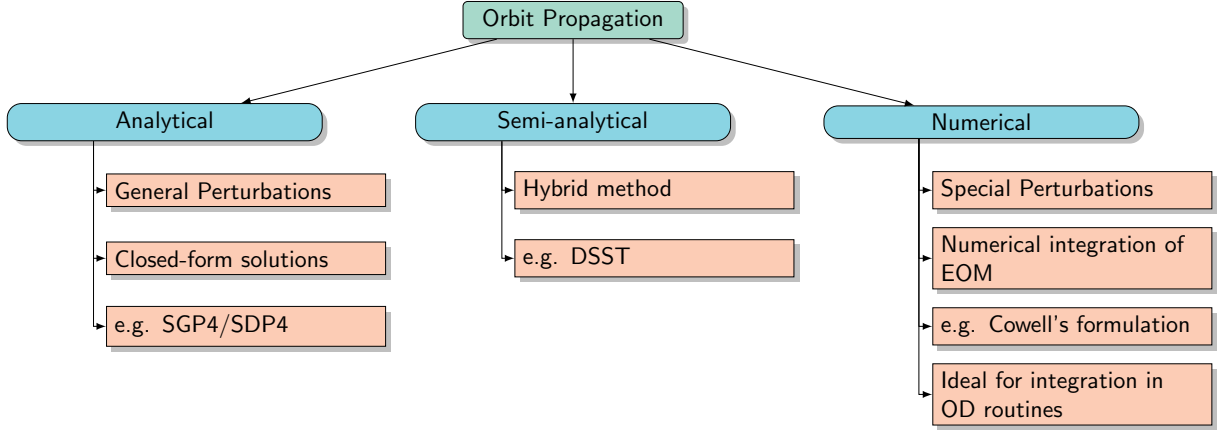


Figure 3-4: Three approaches in propagating an Earth orbit. **EOM** means Equations of Motion; **SGP4/SDP4** mean Simplified General Perturbation Version 4/ Simplified Deep-space Perturbation Version 4; DSST means Draper Semi-analytical Satellite Theory

As shown in Figure 3-4, there are three categories of orbital propagators: analytical, semi-analytical and numerical. Numerical propagators evidently perform numerical integration of the **RSO**'s differential equations of motion (**EOM**) with the effects of perturbing accelerations factored in. Thus, they do not provide a closed-form solution. On the other hand, analytical propagators provide a closed-form solution to the **OP** problem by using analytical expressions to account for the effect of perturbing forces on the **RSO**'s motion. Semi-analytical techniques adopt a hybrid approach featuring numerical methods and closed-form expressions. The perturbations mentioned above are caused by the Earth, Moon and Sun's gravitational forces as well as by atmospheric drag, solar radiation pressure and the Earth's asphericity.

The degree of fidelity of a propagator relates to how close its predicted orbit matches the true orbit. Depending on which perturbing forces are taken into account and which are ignored by the propagator, its results can be said to be low-fidelity or high-fidelity. Two **OP** methods are employed in this project: an analytical propagator which implements **SGP4** orbit propagation theory and a numerical propagator adopting Cowell's formulation [52] with **EOM** accounting for two-body forces and the  $J_2$  effect. The first one is a medium-fidelity propagator while the second one produces low-fidelity results. Even though the second method generates lower fidelity orbits, its inclusion in this report is justified because it uses **differential equations** (DE) as target dynamic model, which is necessary in **orbit determination** (Chapter 5). High-fidelity orbit propagation is not necessary at this stage of the **MeerKAT** project.

### 3.2.3.1 The SGP4 orbit propagator

Simplified General Perturbations # 4 (**SGP4**) orbit propagation theory was developed specifically to propagate space object orbits based on **Two Line Element** sets. It is thus natural to employ



**SGP4** orbit propagation this project. Simplified perturbations models take into account the gravitational effects of the Earth, Sun and Moon as well as perturbing effects arising from the Earth’s shape, atmospheric drag and solar radiation pressure. The reference implementation of **SGP4** theory is described in *SpaceTrack Report # 3* [54]. Vallado, Kelso et al. revisited the report in 2006 [55] and provided source code in C++. The Python package **sgp4** 1.4 developed by Brandon Rhodes<sup>5</sup> can be seen as a wrapper to the C++ source code provided in [55] and passes all unit tests in the 2006 paper. The package documentation also provides Python code examples demonstrating how to propagate an orbit using the **SGP4 OP** function  $\mathbf{f}_{\text{SGP4}}$  with an assumed **WGS84** Earth gravity model [56]. The **WGS84** standard is also widely used in the GPS systems. It is therefore convenient to use in the **MPT** developed in this project. **sgp4** 1.4-propagated position states are reported in [56] to be within 0.1 mm of the C++ results from [55]. **SGP4** trajectories have position errors of approximately one kilometre at epoch. This is inevitable since **SGP4** theory does not factor in all forces which perturb the **RSO**’s motion. As a result, the **SGP4** orbit propagator produces medium-fidelity trajectories.

The following figure shows the satellite ground track for object 33759 obtained by **SGP4** orbit propagation of the **TLE** set given in Subsection 3.2.2 with a simulation time step of  $\Delta_t = 1.0$  s. **OP** with the  $\mathbf{f}_{\text{SGP4}}$  function produces orbits in the true equator, mean equinox frame (**TEME**). The **RSO**’s position vectors were converted into longitude and latitude to create the ground track plot.

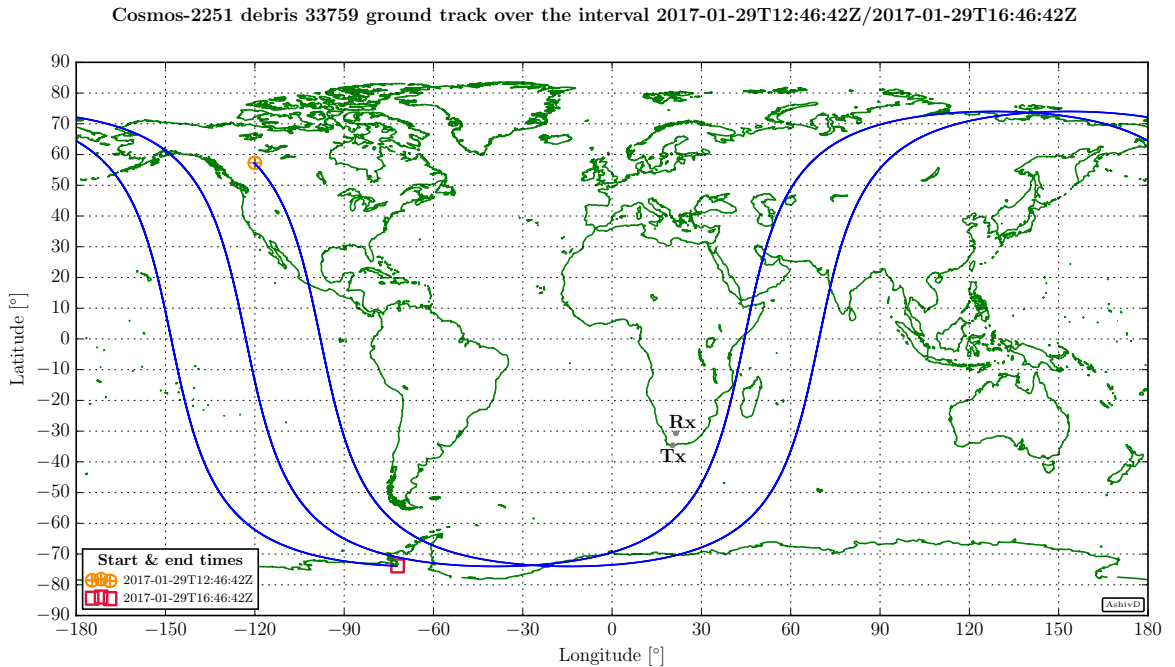


Figure 3-5: Ground track of Cosmos-2251 debris 33759 obtained by **SGP4** orbit propagation of the **TLE** set over four hours. The start time is the **TLE** epoch in Subsection 3.2.2

<sup>5</sup> <https://pypi.python.org/pypi/sgp4/>

The inclination angle quoted in the source [TLE](#) was  $i = 74.0214^\circ$ . The maximum value of the latitude in the ground track plot in [Figure 3-5](#) was  $74.0115^\circ$ , which is the same as the inclination angle in the source [TLE](#) to one decimal place. A single decimal place is considered accurate here because the simulation step of one second is rather coarse. Significantly smaller time steps  $\Delta_t$  are used in [Chapter 4](#) when investigating real-life mission planning situations. These will ensure that the trajectories generated are accurate enough for executing experiments at the [MeerKAT](#) radar.

### 3.2.3.2 The two body plus J2 propagator

The acceleration of a space object ([RSO](#)), under the sole influence of the Earth's conservative gravitational field, can be represented by the following differential equation ([DE](#)):

$$D^2 \mathbf{r} = -\frac{\mu_\oplus}{r^3} \mathbf{r} \quad (3-5)$$

where  $\mathbf{r}$  is the position vector of the [RSO](#) while  $\mu_\oplus$  is the Earth's gravitational parameter. The equations of motion in the [DE](#) in [Eqn. 3-6](#) denote the so-called **two-body problem** or **Kepler's problem**. [\[53\]](#) The position vector  $\mathbf{r}$  was shown in [Figure 3-3](#).

Such Keplerian orbits [\[57\]](#) are a rough approximation of orbital motion. In reality, the assumptions of the two-body problem are erroneous. Firstly, the Earth's mass distribution is not radially symmetric and secondly, there are numerous other forces acting on an orbiting body. The resulting perturbed Keplerian orbit is governed by the following [DE](#) which is called Cowell's formulation. [\[52\]](#)

$$D^2 \mathbf{r} = -\frac{\mu_\oplus}{r^3} \mathbf{r} + \mathbf{a}_{\text{perturbed}} \quad (3-6)$$

where  $\mathbf{a}_{\text{perturbed}}$  is the acceleration resulting from perturbing forces. The latter are both gravitational and non-gravitational in nature. The gravitational forces result from the Earth's asphericity, precession, nutation, third body effects due to the Sun, Moon and other planets and general relativity. Non-gravitational forces arise due to atmospheric drag, solar radiation pressure, thermal radiation among others. [\[52\]](#) Montenbruck and Gill [\[57\]](#) provide [Figure 3-6](#) which illustrates the relative influence of various perturbing forces in different orbit regimes.

We take satellites of the *Iridium* class as example to explain [Figure 3-6](#). *Iridium* satellites orbit at an altitude of 780 km and so are in the [LEO](#) regime (up to 2000 km of altitude) as can be seen in the top left corner. The strongest forces acting at this altitude include the two body force (denoted as  $GM$  in [Figure 3-6](#)) and the gravitational force caused by the Earth's oblateness, denoted by  $J_{2,0}$  in the above figure. Oblateness refers to the flattening of at the poles induced by the Earth's daily rotation. This phenomenon is also called the  $J_2$ -effect in the literature. [\[48, 52\]](#) The same information is presented in [Table 3.8](#) in [\[58, Chapter 3\]](#)

The two body force is at least three orders of magnitude more significant than the perturbing forces in the LEO regime. The  $J_2$  effect is at least a hundred times stronger than all other perturbations according to Figure 3-6. Therefore, only these two types of forces will be included in the target dynamic model in this project.

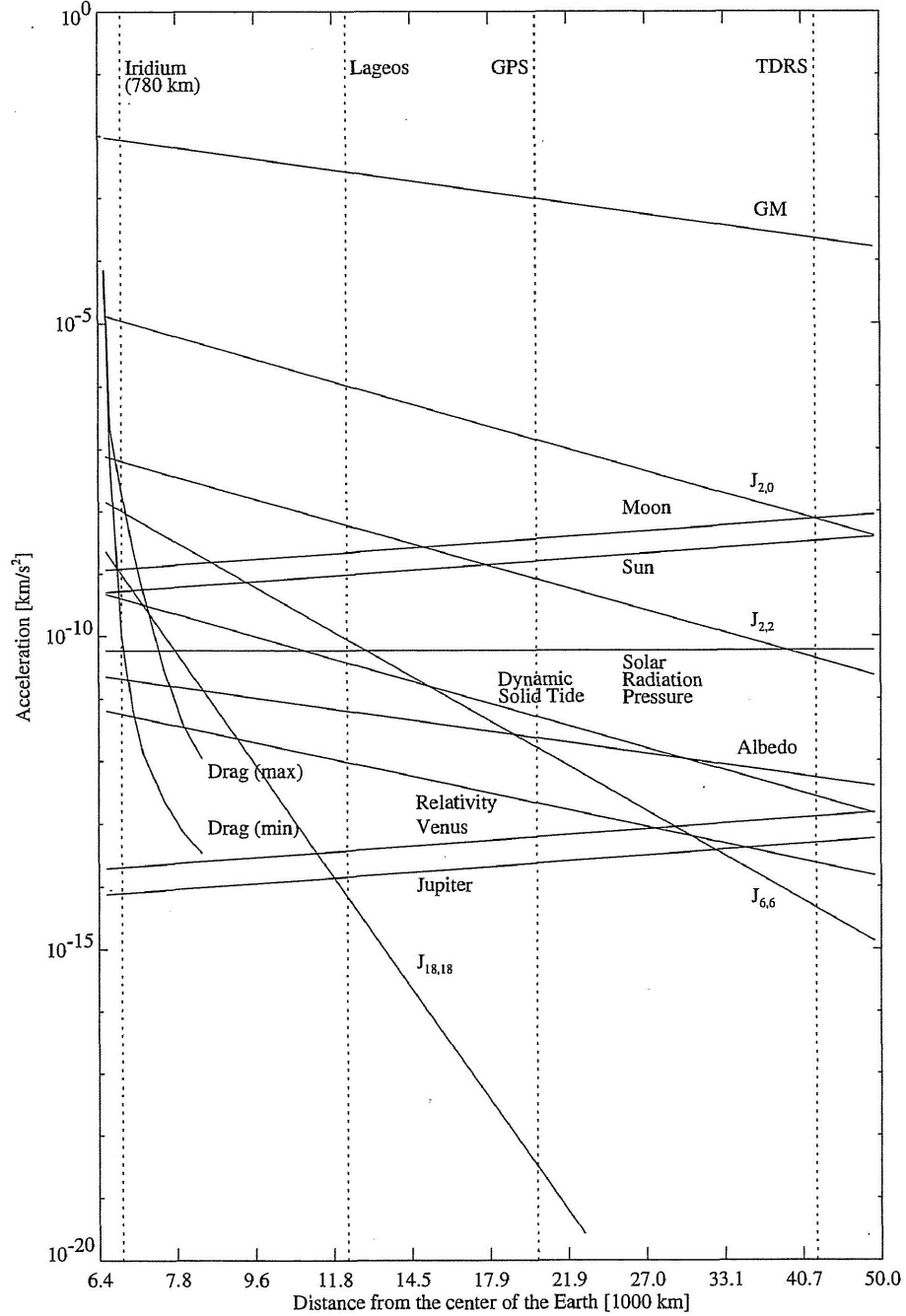


Figure 3-6: Relative influence of various perturbing forces in different orbit regimes. [57, Figure 3.1]

The  $J_2$ -perturbed potential function, shown in appendix, leads to the following DE

$$D \begin{bmatrix} x \\ y \\ z \\ \dot{x} \\ \dot{y} \\ \dot{z} \end{bmatrix} = \begin{bmatrix} \dot{x} \\ \dot{y} \\ \dot{z} \\ -\frac{\mu_{\oplus} x}{r^3} \left[ 1 - \frac{3}{2} J_2 \left( \frac{R_e}{r} \right)^2 \left( 5 \frac{z^2}{r^2} - 1 \right) \right] \\ -\frac{\mu_{\oplus} y}{r^3} \left[ 1 - \frac{3}{2} J_2 \left( \frac{R_e}{r} \right)^2 \left( 5 \frac{z^2}{r^2} - 1 \right) \right] \\ -\frac{\mu_{\oplus} z}{r^3} \left[ 1 - \frac{3}{2} J_2 \left( \frac{R_e}{r} \right)^2 \left( 5 \frac{z^2}{r^2} - 3 \right) \right] \end{bmatrix} \quad (3-7)$$

Since the state vector from Eqn. 3-3 was defined as  $\mathbf{x} := [x \ y \ z \ \dot{x} \ \dot{y} \ \dot{z}]^T$ , we can write the above DE more concisely as

$$\dot{\mathbf{x}} = \mathbf{f}(\mathbf{x}) \quad (3-8)$$

where  $\mathbf{f}(\cdot)$  is called the *fundamental vector function* of the dynamical system. The notion of time is implicit in this equation. In other words,  $\dot{\mathbf{x}}(t) = \mathbf{f}(\mathbf{x}(t), t)$ . Some authors refer to Eqn. 3-8 as the target's equation of motion (EOM).

Propagating an orbit based on the two-body plus  $J_2$  model

Orbit propagation based on numerical integration of Eqn. 3-7 is demonstrated with the ISS.

Keplerians extracted from the following [International Space Station TLE](#) are converted into Cartesian elements following the algorithms in [52].

ISS (ZARYA)

```
1 25544U 98067A    17238.18406250   .00002219   00000-0   40664-4 0   9995
2 25544   51.6399   49.3795 0004977 179.3457 159.4531 15.54203357 72636
```

The following state vector at epoch is obtained.

$$\mathbf{x}(t_0) = \begin{bmatrix} -1.019671 \times 10^3 \\ -5.623492 \times 10^3 \\ -3.6479312 \times 10^3 \\ 6.053283 \\ 1.737792 \\ -4.375843 \end{bmatrix} \quad (3-9)$$

It is clear that the first three elements, which are position variables, are expressed in kilometres and the last three elements, which are velocity variables, are in kilometres per second.

The state vector  $\mathbf{x}(t_0)$  along with the DE model given in Eqn. 3-7 constitute an **Initial Value Problem (IVP)** or **Cauchy problem**. Solving this second-order, nonlinear IVP analytically

is impossible. To circumvent this issue, engineers and scientists employ numerical integration methods, such as the classical [Runge-Kutta fourth order method \(RK4\)](#). The latter is the most commonly used numerical method in nonlinear tracking filtering since it arguably offers, for smaller step sizes  $\Delta_t$ , the best compromise between local truncation error and number of function evaluations per simulation step. NASA uses the RK4 method in its [orbit determination](#) tool. [59] For the aforementioned reason, the MPT features an embedded RK4 method in its orbit propagator. Algorithm GENERATENOMINALTRAJECTORY in Appendix A.1 is used to propagate an orbit modelled by Eqn. 3-8 from  $t_0$  to a desired time in the future or past, based on initial conditions given by a state vector at epoch  $\mathbf{x}(t_0)$  in Eqn. 3-9.

It is clear that the choice of simulation step size  $\Delta_t$  affects the degree of accuracy<sup>6</sup> of the propagated orbit. Ascertaining the error in a numerically integrated trajectory for a nonlinear dynamic model (for which an explicit solution does not exist) is a daunting task. [59] A quick approach is to compare the numerical integration results of the IVP with the analytical solution of a simplified version of the problem at hand [59]. For instance, Kepler's problem has an explicit solution in terms of Keplerian elements to which the OP results can be compared.

The first check is to verify that the propagated orbits have the same inclination  $i$  as the angle given in the source TLE. The following figure is a ground-track plot over three orbits for the ISS starting with the initial conditions in Eqn. 3-9.

The inclination angle quoted in the source TLE was  $i = 51.6399^\circ$ . The maximum value for the latitude in the ground track plot in Figure 3-7 was  $51.6187^\circ$ , which is a close match to the Keplerian approximation. The estimated inclination angle is exactly the same as the Keplerian approximation to one decimal point, which is encouraging given that the simulation step size is  $\Delta_t = 0.1$  s.

---

<sup>6</sup> By accuracy, we mean how close the numerically integrated orbit matches the true orbit given by the DE in Eqn. 3-8. We should be able to distinguish between orbit propagation accuracy and fidelity. Since the DE in Eqn. 3-7 ignored several perturbing forces, it will lead to propagated trajectories which are not very close to the actual real-life orbit, meaning low-fidelity propagated orbits.

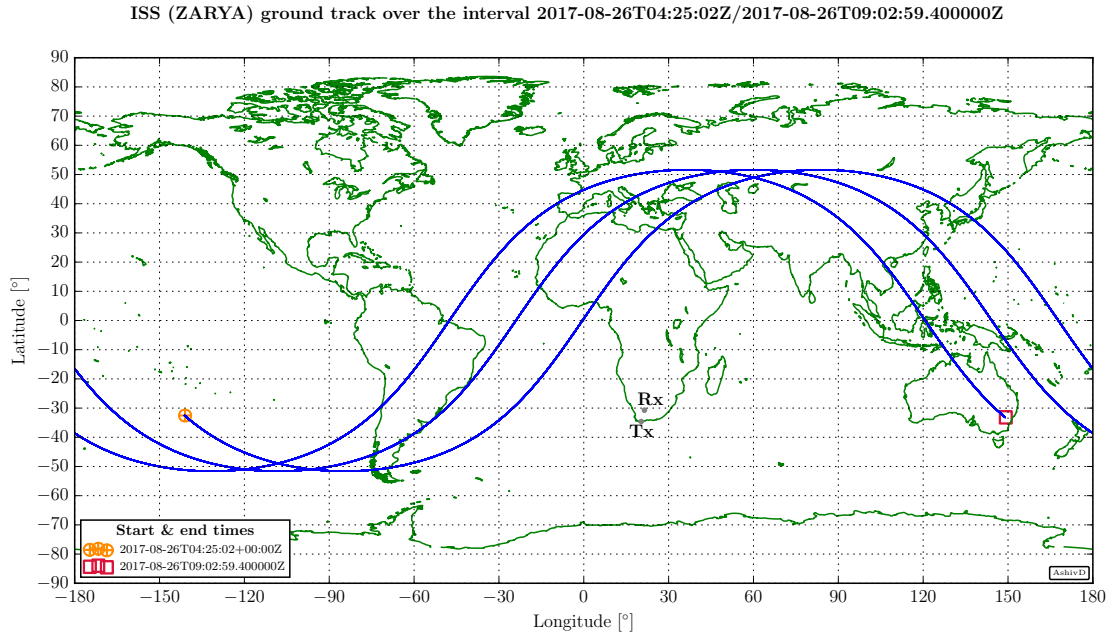


Figure 3-7: Ground track of the [ISS](#) orbit obtained by numerical integration of the initial state vector.

The satellite's states are plotted against time to investigate the periodicity. The Keplerian period is calculated from the semi-major axis in the source [TLE](#) to be  $T = 92.651968$  min.

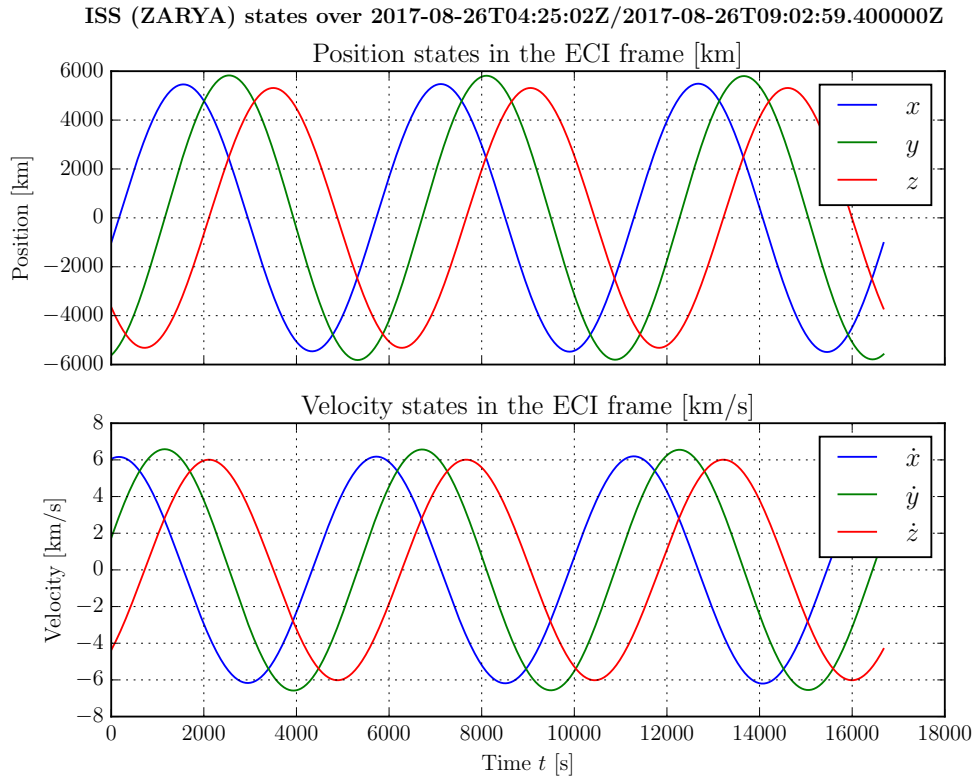


Figure 3-8: Evolution of position and velocity states during the simulation lasting three orbits

The states in Figure 3-8 are clearly periodic. The actual period is found by calculating the normalized autocorrelation function (ACF) of the states. Figure 3-9 shows the normalized ACF of the states over the simulation interval.

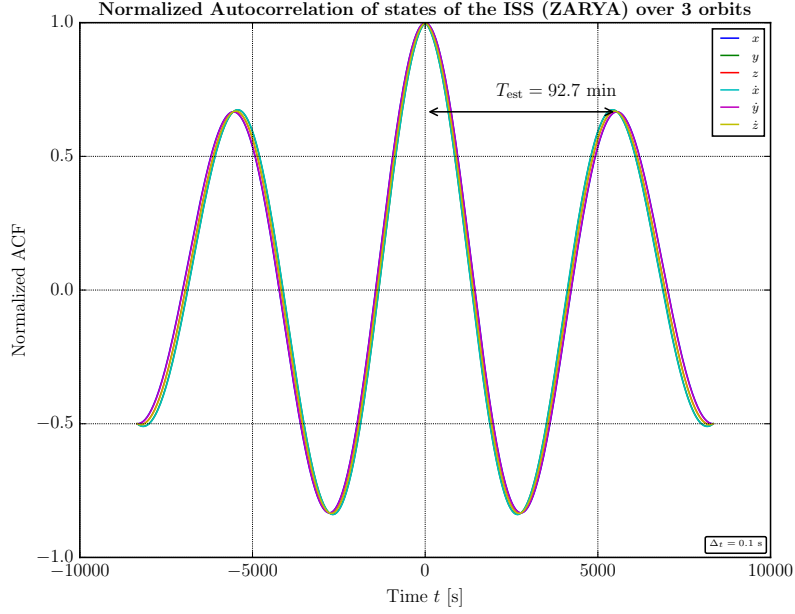


Figure 3-9: Normalized autocorrelation of the propagated states of the ISS over three orbits, with the estimated period indicated.

The estimated period found to be  $T_{\text{est}} = 92.718333$  min. This estimate is very close to the Keplerian period to one decimal point, given that the simulation time step was a rough  $\Delta_t = 0.1$  s.

### 3.3 Sensor dynamics

The preceding section discussed how orbit propagation is done in the Earth-Centered Inertial frame (ECI). The ECI frame is a geocentric frame which does not rotate with the surface of the Earth. The ECI frame's  $x$ -axis points in a fixed direction on the celestial sphere. The NORAD TLE sets employ a special ECI frame called the TEME frame. TEME stands for true equator, mean equinox. This will be the ECI frame used in this project.

On the other hand, the ECEF frame is a geocentric frame which rotates with the surface of the Earth. Its  $x$ -axis points in the direction of latitude  $0^\circ$  and longitude  $0^\circ$ . The relationship between these two coordinate frames is shown in Figure 3-10.

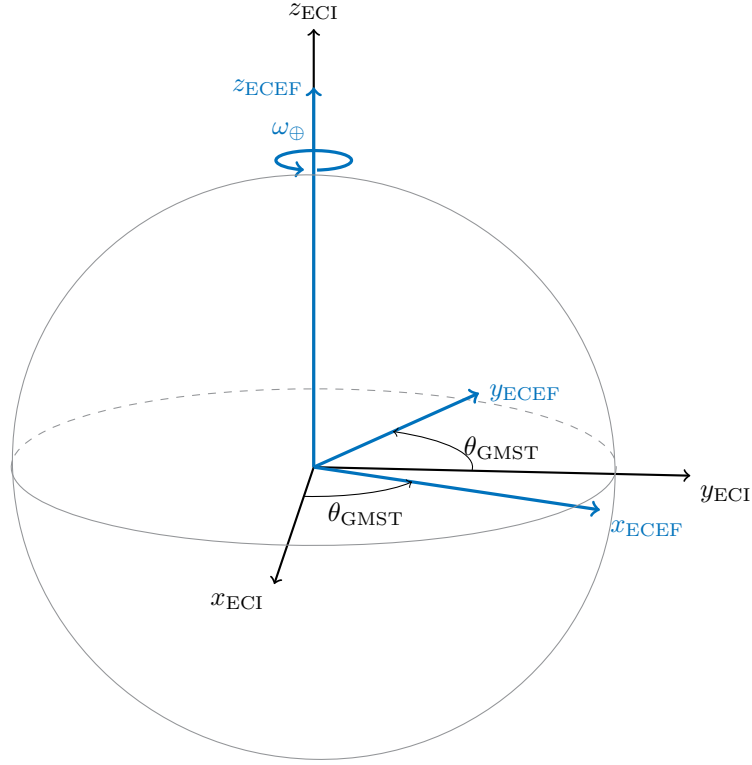


Figure 3-10: The ECEF frame at a given epoch is obtained through a rotation about the ECI frame's  $z$  axis by a DCM. The Earth rotates about its axis at an average rate of  $\omega_{\oplus}$  radians per second.

The position vector  $\boldsymbol{\rho} = [x \ y \ z]^T$  of a RSO in the ECI frame can be transformed into the ECEF frame with a direction cosine matrix (DCM). The rotation angle is the Greenwich Mean Sidereal Time (GMST) angle,  $\theta_{\text{GMST}}$ , which is derived from the Julian date at the epoch of interest.

$$\boldsymbol{\rho}_{\text{ECEF}} = \text{ROT}_3(\theta_{\text{GMST}})\boldsymbol{\rho}_{\text{ECI}} \quad (3-10)$$

The ECItOECEF algorithm from [52, Chapter 1] shows how to transform the full state vector  $\mathbf{x}$  from the ECI frame to the ECEF frame, which is used in calculating the Doppler shift measured by the radar as the target flies by.

Both the transmitter and receivers of the MeerKAT radar are located on the surface of the Earth. These ground stations are identified by their latitude, longitude and height above the Mean Sea Level (MSL). The World Geodetic System (WGS84) [60] is the standard used in the sensor dynamic models built in the MPT. The reference ellipsoid modelling the Earth in the WGS84 standard bulges out at the Equator. Maps usually quote the geodetic latitude,  $\phi_{\text{gd}}$  from which the geocentric latitude  $\phi_{\text{gc}}$ , used in sensor dynamics modelling, is calculated. Figure 3-11 shows the cross-section of an oblate Earth with the geocentric and geodetic latitudes marked.



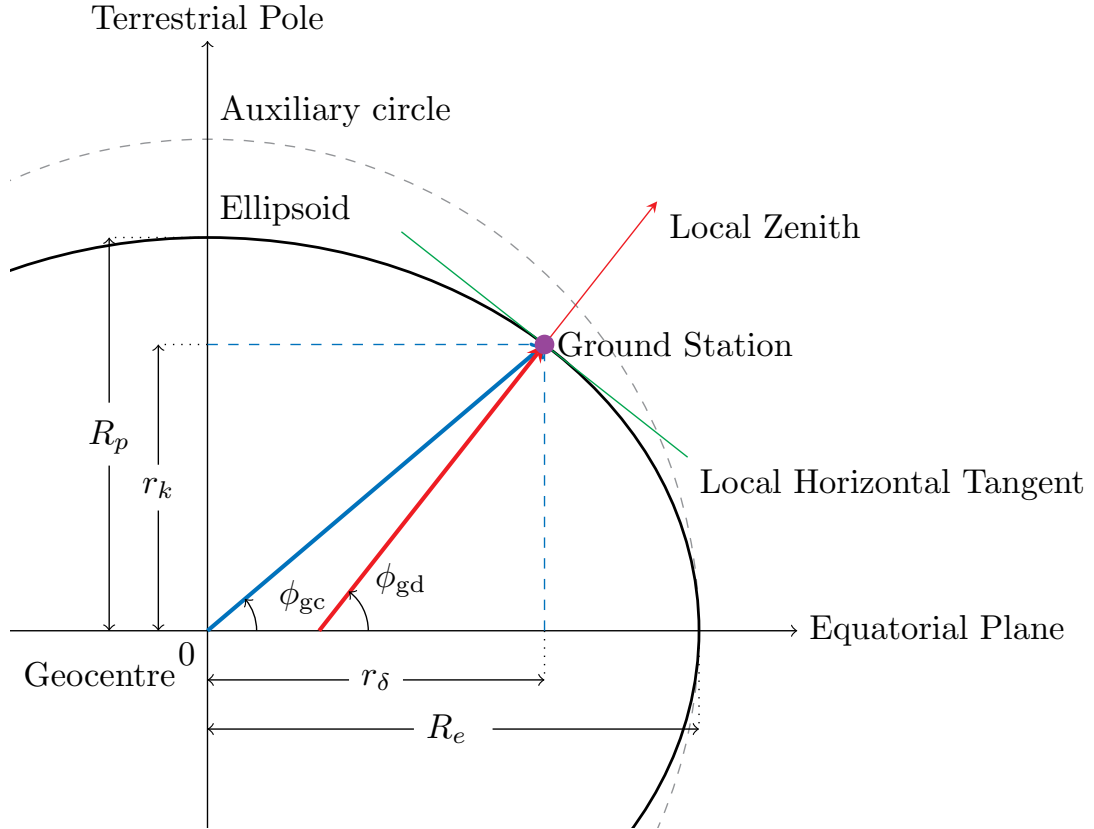


Figure 3-11: Cross-section of an oblate Earth.  $R_e$  and  $R_p$  are, respectively, the equatorial and polar radii of the Earth.

Algorithm SITE-TRACK in [52, Chapter 6] shows how to calculate the ECEF location of the transmitter  $\mathbf{I}_{\text{ECEF}}^{\text{Tx}}$  and receiver  $\mathbf{I}_{\text{ECEF}}^{\text{Rx}}$ .

Trajectories in the ECI frame resulting from orbit propagation have to be transformed into the ground station's local frame in order for radar analysis to be carried out. A South-East-Zenith (SEZ) frame is adopted for the topocentric frame at the ground station. The scenario can easily be converted into a North-East-Down (NED) or an East-North-Up (ENU) frame by means of appropriate rotations with DCMs.

The following figure illustrates the location of the ground station on the surface of the Earth as well as the position vector of the space object of interest relative to it.

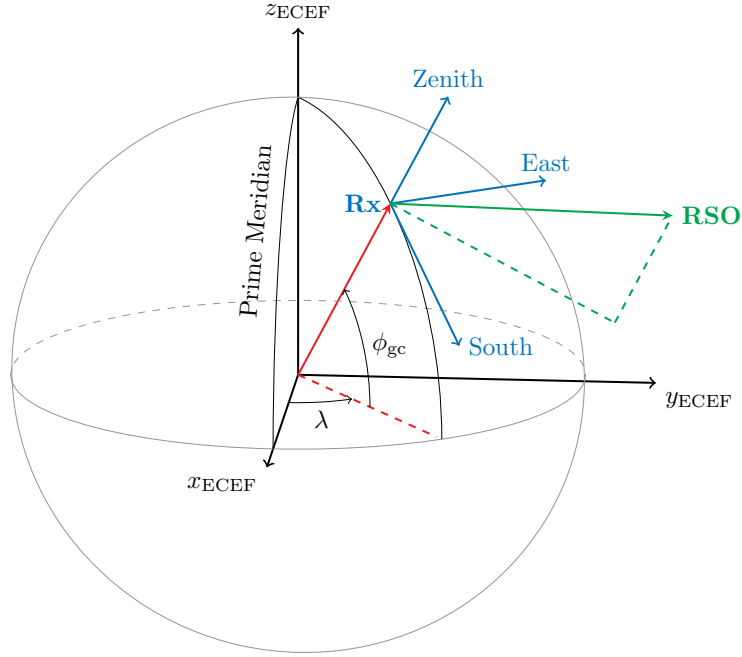


Figure 3-12: The ground station (whose geocentric latitude is  $\phi_{gc}$  and longitude is  $\lambda$ ) denoted by  $Rx$  is a point above the surface of the rotating Earth in the  $ECEF$  frame. The local (topocentric) frame has  $x$ ,  $y$  &  $z$  axes pointing towards the South, East and Zenith, respectively.

The first step in converting the scenario to one centred on the ground station is a transformation from the  $ECI$  frame to the  $ECEF$  frame which is achieved by algorithm **SITE-TRACK**. Then the  $RSO$ 's trajectory is transformed from the  $ECEF$  frame to the ground station's local (topocentric) frame. This is illustrated in Figure 3-13.

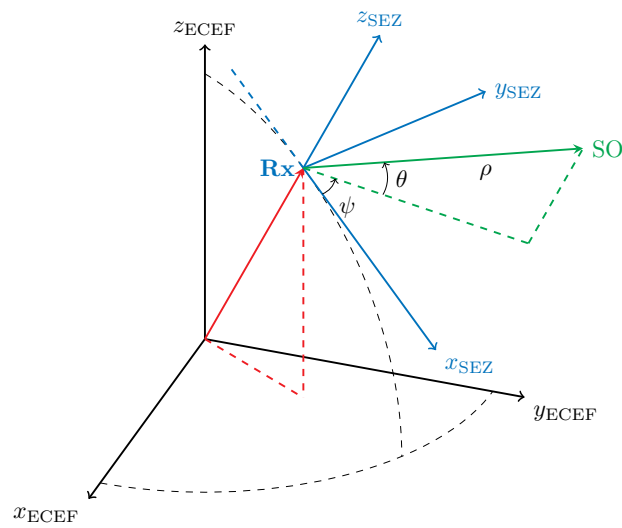


Figure 3-13: Transforming the target trajectory from the rotating  $ECEF$  frame to the sensor-centred topocentric frame. The  $RSO$ 's location and velocity vector in the topocentric  $SEZ$  frame are  $\mathbf{t}$  and  $\dot{\mathbf{t}}$  respectively.

Algorithm RAZEL in [52, Chapter 3] is used to transform target trajectories from the ECEF to the SEZ frame. Figure 3-14 shows the orientation of the local coordinate frame at the first radar receiver, M000.

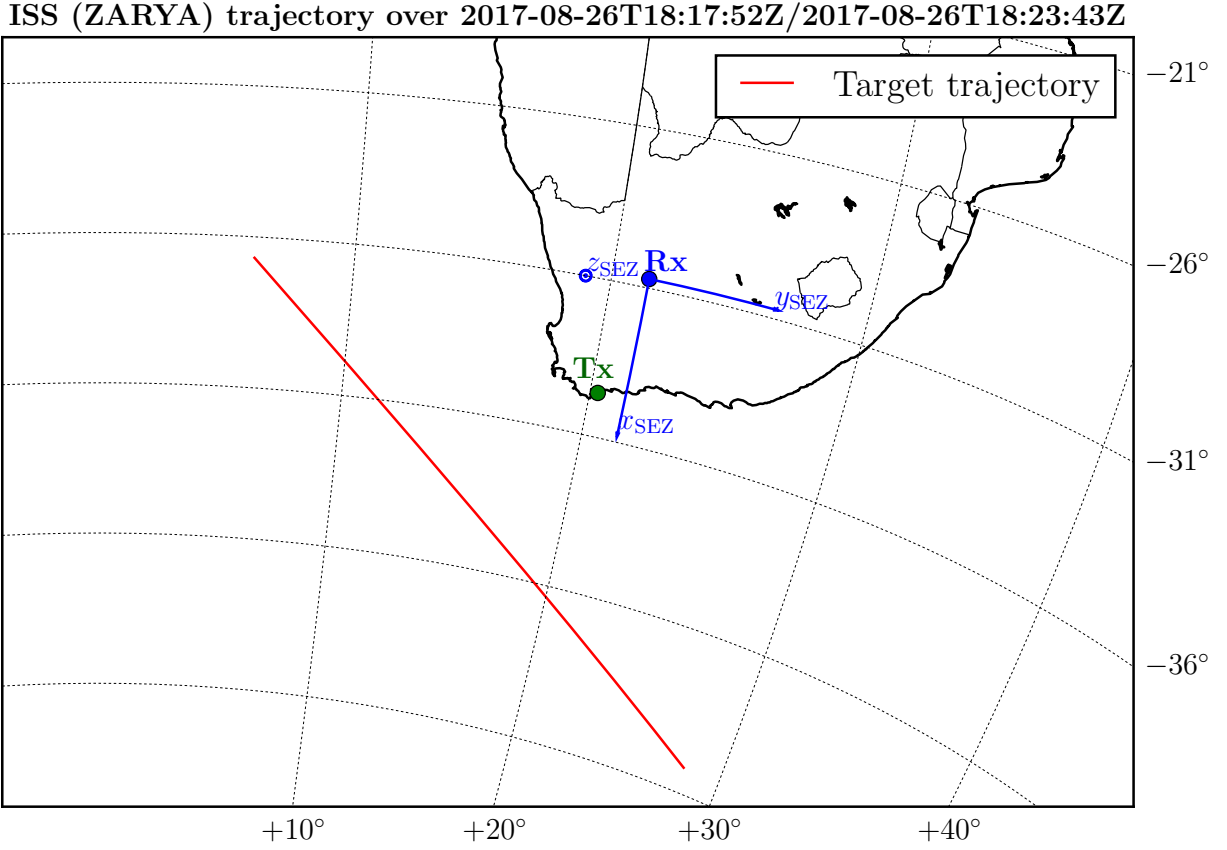


Figure 3-14: Map showing the location of the  $T_x$  at  $34.6^\circ\text{S}$  and  $20.3^\circ\text{E}$  and  $R_x$  at  $30.7^\circ\text{S}$  and  $21.4^\circ\text{E}$ . The  $x$ -axis of the local SEZ coordinate frame at the  $R_x$  points due South, the  $y$ -axis points due East and the  $z$ -axis points out of the plane of the map (at the zenith). The red curve denotes the ISS's trajectory from Figure 3-7 in the vicinity of the radar sensor.

The slant-range  $\rho$ , elevation angle  $\theta$  and azimuth angle  $\psi$  from the  $R_x$  to the target are shown in Figure 3-15. The azimuth angle is measured from the positive  $x$ -axis to the positive  $y$ -axis in the local horizontal plane. The slant-range, elevation and azimuth angle in Figure 3-15 are defined similarly to those in [61, Figure 3.3]. Angle definitions from [61] are adopted in this project because their partial derivatives with respect to the target's position vector  $\mathbf{t}$  are provided. Where necessary, subscripts will be added to these symbols to signify which radar node is concerned. For instance,  $\theta_{T_x}$  means the elevation angle to the target from the transmitter.

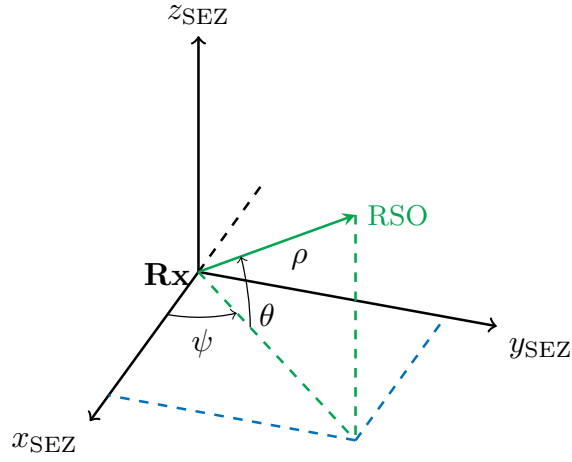


Figure 3-15: Range, elevation and azimuth to the target in the local topocentric (SEZ) frame

The RSO's radar coordinates in the sensor's frame can be calculated from the position vector  $\mathbf{t} = [x \ y \ z]^T$  in Cartesian coordinates.

$$\begin{bmatrix} \rho \\ \theta \\ \psi \end{bmatrix} = \begin{bmatrix} \sqrt{x^2 + y^2 + z^2} \\ \arctan\left(\frac{z}{\sqrt{x^2 + y^2}}\right) \\ \arctan2\left(\frac{y}{x}\right) \end{bmatrix} \quad (3-11)$$

Figure 3-16 below shows the evolution of the target's radar coordinates during the target passage shown in red in Figure 3-14.

Radar vectors from Rx to ISS (ZARYA) over 2017-08-26T18:17:52Z/2017-08-26T18:23:43Z

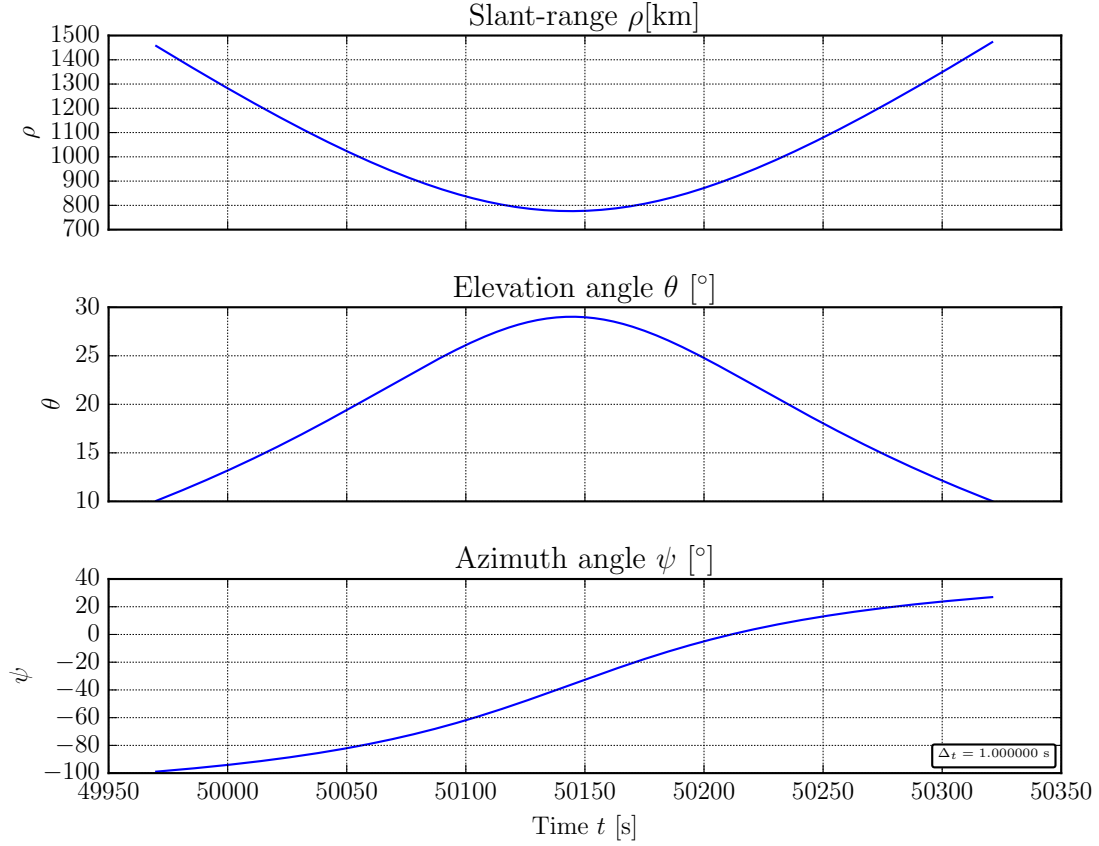


Figure 3-16: Radar vectors  $(\rho, \theta, \psi)$  from the receiver to the target, measured in the local frame.

Since the ISS is transiting from West to South in Figure 3-14 towards the horizon from the receiver, it is at its closest to the Rx when its elevation angle to it is the highest, as can be seen in Figure 3-16.

This section has only considered the presence of one ground station up to now. Since our radar system will operate in a bistatic configuration, we can extend the development to several ground stations.

Figure 3-17 shows a generic bistatic radar configuration with the bistatic baseline  $L_b$  and elevation  $(\theta_{Rx})$  and azimuth  $(\psi_{Rx})$  angles to the Rx marked.

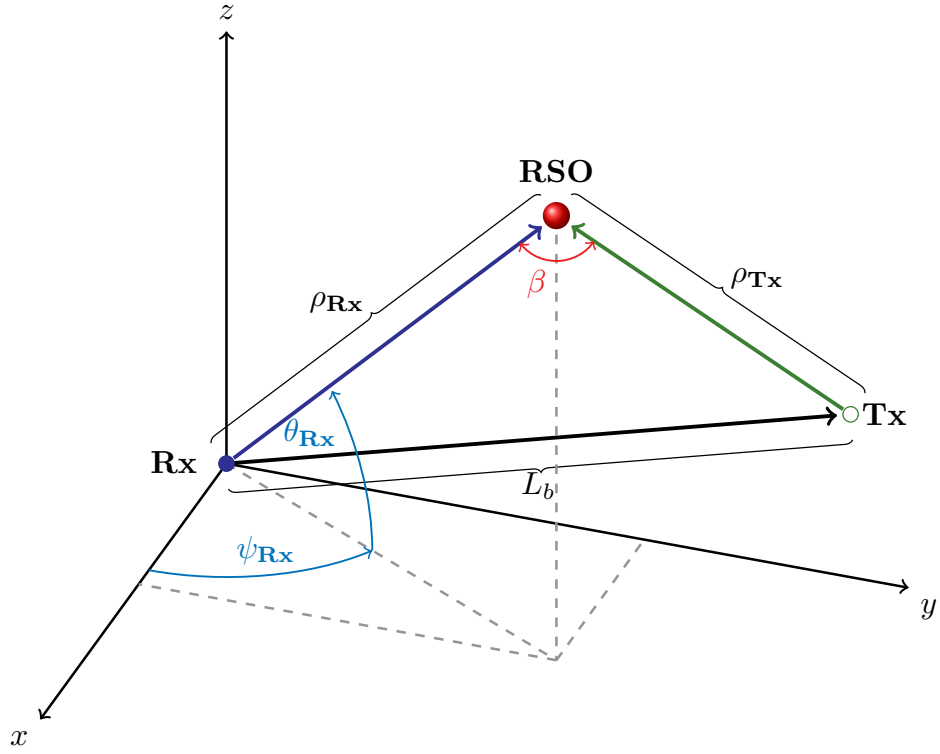


Figure 3-17: Bistatic radar configuration specifying the definition of various quantities used in this project

The bistatic range  $\rho_b$  in Figure 3-18 is the sum of the slant-range to the transmitter,  $\rho_{Tx}$  and slant-range to the receiver,  $\rho_{Rx}$  defined in Figure 3-17. The bistatic Doppler shift  $f_{b,d}$  is defined as the range rate  $\dot{\rho}_b$  multiplied by the wave number  $K_d$ .

Figure 3-18 shows the evolution of the bistatic angle  $\beta$  and bistatic range and Doppler shift during the target passage shown in red in Figure 3-14.

Bistatic angle, range & Doppler shift for ISS trajectory over 2017-08-26T18:17:52Z/2017-08-26T18:23:43Z

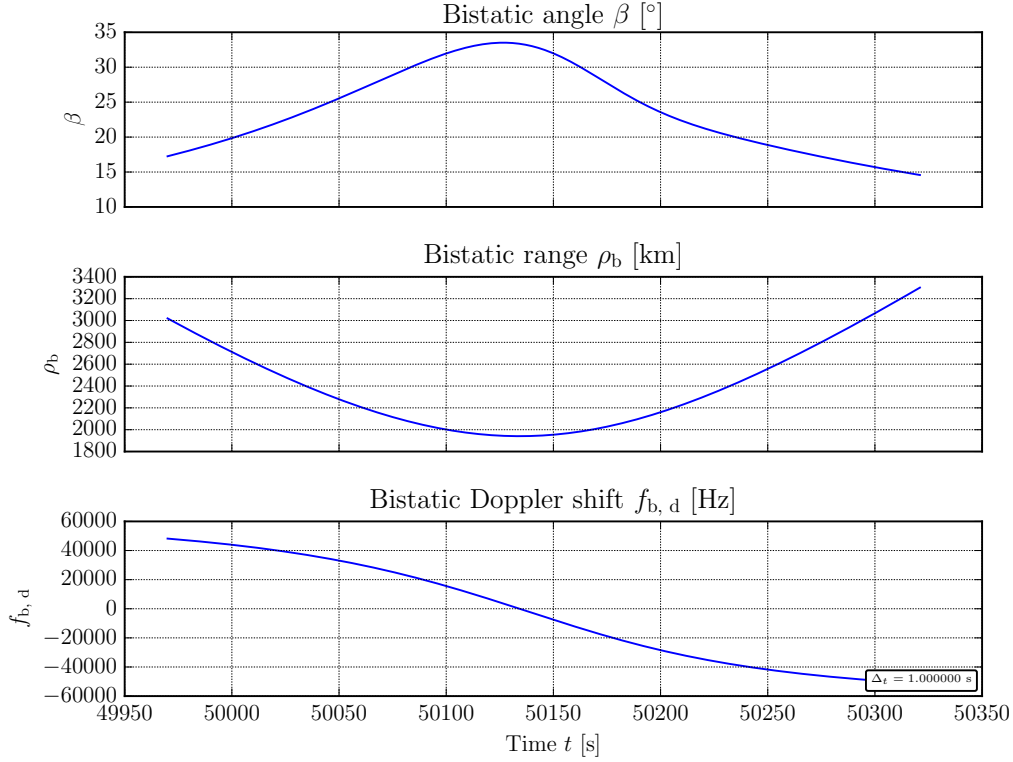


Figure 3-18: Bistatic angle  $\beta$ , range  $\rho_b$  and Doppler shift  $f_{b,d}$  measured at the Rx

Expressions for the bistatic range and bistatic Doppler shift are derived in Appendix C.1.

## 3.4 Measurement modelling

Radar systems, such as the proposed MeerKAT radar, measure the range to a target from the round trip time delay between emitting a radar pulse and receiving its echo. Due to the finite velocity of light, the apparent range to a moving object is not exactly equal to the geometric range<sup>7</sup> to it. The apparent range  $\rho_{\text{measured}}$  is calculated from the time delay experienced by a radar pulse travelling up from the ground station, reflecting off a moving target and travelling back down to the ground station. The target's motion during the time taken by the reflected radio pulse to propagate back to the ground station causes the discrepancy between the apparent position and the geometric position. This phenomenon is called light-time correction and has to be accounted for when the target is very distant from the observer, which is the case for RSOs being observed by a ground-based radar.

<sup>7</sup> The geometric range  $\rho$  is defined in Eqn. 3-11. Ideal range and instantaneous range are synonyms used for it.

Light-time corrections are done for the uplink and downlink propagation paths to find the time delay in seconds measured by the radar system. Evaluating the light-time correction is an iterative process which requires the target's trajectory to be known. [57]

A Tiangong-1 trajectory on March 20, 2017 is used to show how light-time correction is done. Figure 3-19 shows that the **RSO** flies from the South-West to South-East of the **Rx**.

Tiangong-1 trajectory during the interval 2017-03-20T03:02:47/2017-03-20T03:03:17

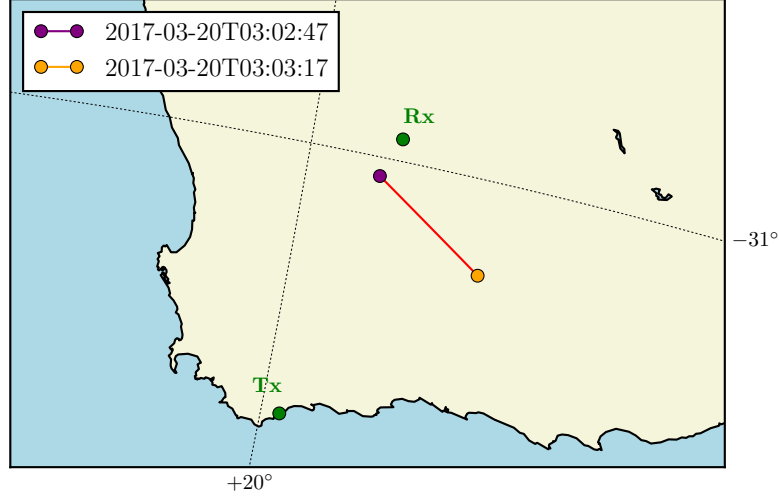


Figure 3-19: *Tiangong-1* ground track used to illustrate light time correction. The purple and yellow markers represent the start and end of the track respectively.

It can be seen that *Tiangong-1* starts relatively close to the **MeerKAT** receiver and progressively moves further away. The range to the **Tx** is clearly always much larger than the range to the **Rx**. The **RSO** starts very far from the transmitter, becomes slightly closer to it and then distances itself again towards the end of the transit.

### Downlink time

The first iterative process aims to find the downlink time, which is the time taken by the radar signal to travel from the target to the radar receiver. The downlink time  $\tau_d$  is iteratively determined from

$$\tau_d^{(i+1)} = \frac{1}{c} \cdot ||\mathbf{t}(t - \tau_d^{(i)}) - \mathbf{I}^{\text{Rx}}(t)|| \quad (3-12)$$

where

- $\mathbf{t}$  is the time-indexed vectors of target positions during the transit
- $c$  is the speed of light
- $\mathbf{I}^{\text{Rx}}$  is the **Rx**'s position vector in the same frame as  $\mathbf{t}$ .



The initial value for the iteration is set as  $\tau_d^{(0)} = 0$ .

### Uplink time

The uplink time  $\tau_u$  is iteratively determined from

$$\tau_u^{(i+1)}(t) = \frac{1}{c} \cdot \|\mathbf{t}(t - \tau_d) - \mathbf{I}^{\text{Tx}}(t - \tau_d - \tau_u^{(i)})\| \quad (3-13)$$

where  $\mathbf{I}^{\text{Tx}}$  is the Tx's position vector in the local (topocentric) frame. The initial value for the iteration is set as  $\tau_u^{(0)}(t) = \tau_d$ .

The following figure shows plots for the downlink and uplink times during the transit shown in Figure 3-19. The simulation time step used was  $\Delta_t = 0.0001$  s.

#### Light-time correction for Tiangong-1 for 2017-03-20T03:02:47/2017-03-20T03:03:17

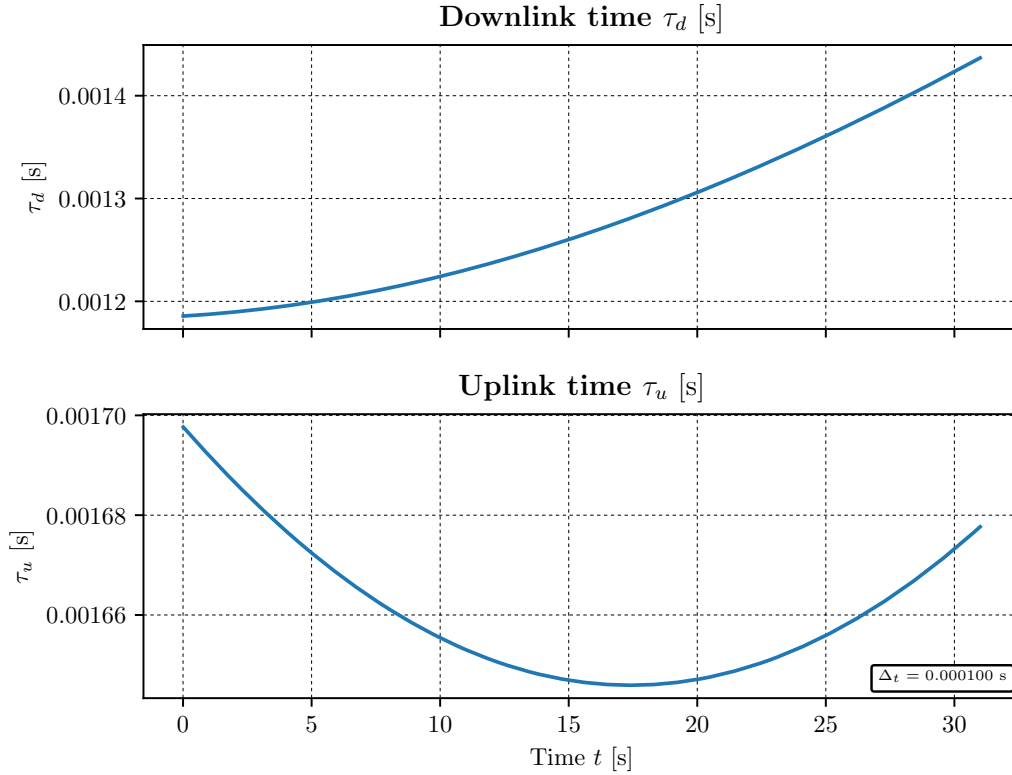


Figure 3-20: Uplink and downlink time for the Tiangong-1 transit

The uplink time is always much longer than the downlink time due to the larger range between the target and the Tx than between it and the Rx. The downlink time increases during the transit because target is distancing itself from the receiver. The uplink time plot looks similar to a parabola because because the RSO comes closer to the Tx before moving away.

The time delay in the received signal measured by the radar receiver is the sum of the uplink and downlink times. It is multiplied with the speed of light to create the radar measurement of bistatic range  $\rho_b$ .

$$\rho_b[k] = c(\tau_u[k] + \tau_d[k]) \quad (3-14)$$

where  $k$  is the discrete-time index used in the radar signal processing block; and  $\tau_u[k]$  and  $\tau_d[k]$  are the uplink and downlink times estimated at instant  $k$ . Figure 3-21 shows the bistatic range measurements  $\rho_{b, \text{measured}}$  created from Eqn. 3-14.

Ideal bistatic range & measured range for Tiangong-1 for 2017-03-20T03:02:47/2017-03-20T03:03:17

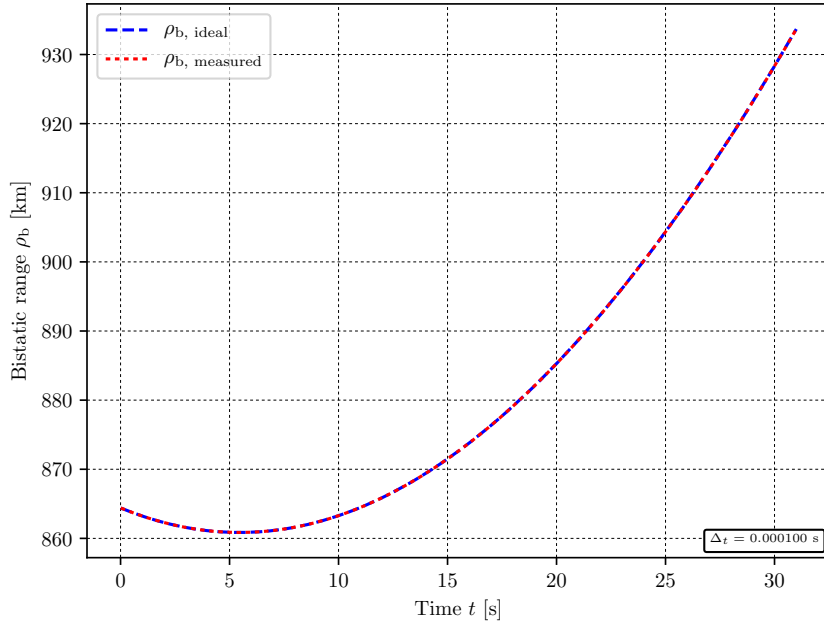


Figure 3-21: Comparison of measured bistatic range  $\rho_{b, \text{measured}}$  based on the time delay of the received signal with the ideal (geometric) bistatic range

The measured bistatic range is nearly identical to the ideal bistatic range.

Doppler measurements are created by the MeerKAT radar by coherently integrating Doppler counts over a set time interval  $T_{\text{CPI}}$ . Appendix C.1 derives an expression for bistatic Doppler shift where the integration time  $T_{\text{CPI}}$  is equal to the time step  $(t_k - t_{k+1})$ . The measured Doppler shift at time instant  $k$  is calculated from the time delay of pulses received during a Coherent Processing Interval (CPI).

$$f_{b,d}[k] = K_d \cdot \frac{c}{T_{\text{CPI}}} (\tau_d[k] + \tau_u[k] - \tau_d[k - N_{\text{CPI}}] - \tau_u[k - N_{\text{CPI}}]) \quad (3-15)$$

where

- $K_d$  is the wave number
- $T_{\text{CPI}}$  is the coherent integration time for the chosen Coherent Processing Interval.

- $N_{\text{CPI}}$  is the number of pulses transmitted during one CPI
- $\tau_d[k]$  is the downlink time estimated for instant  $k$ .

Figure 3-22 shows the bistatic Doppler measurements created from Eqn. 3-15.

Bistatic Doppler shift for Tiangong-1 for 2017-03-20T03:02:47/2017-03-20T03:03:17

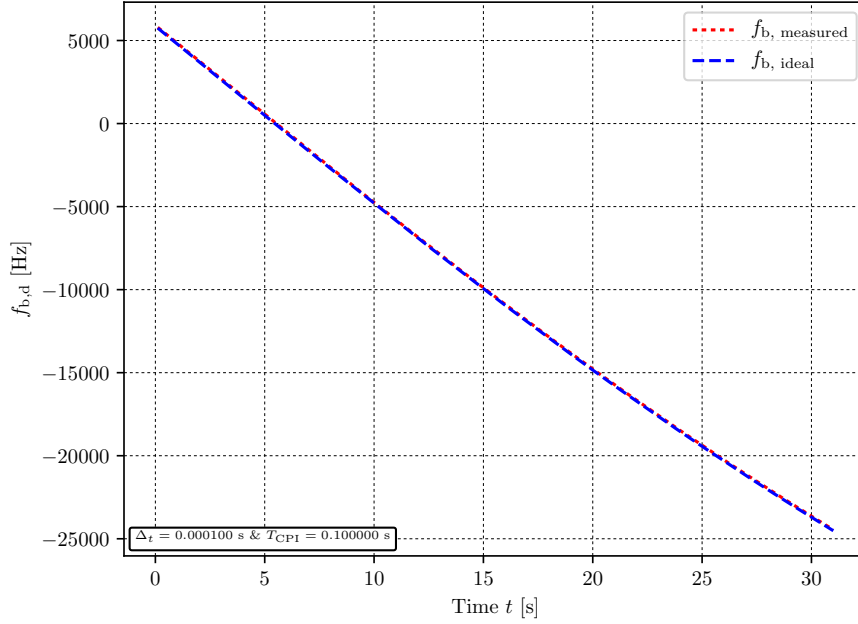


Figure 3-22: Comparison of measured bistatic Doppler shift with the ideal (instantaneous) bistatic Doppler shift

The coherent processing time was 0.1 s which means that one CPI would last  $N_{\text{CPI}} = 1000$  pulses. The measured bistatic Doppler shift is nearly identical to the ideal bistatic Doppler shift.

### 3.5 Summary

This chapter on dynamics and measurement modelling lays the groundwork for the other two work chapters. It first explains how orbits are described in this project: using classical Keplerian elements and Cartesian elements. It shows that the MPT can process a space object's source TLE to extract its Keplerian elements. These elements can be converted into Cartesians. The SGP4 and two body plus  $J_2$  dynamics models identified in the literature review were implemented. Orbit propagation was done by (i) numerically integrating the two body plus  $J_2$  EOM. (ii) using a library which implements SGP4 theory. For both approaches, results were shown to prove their correct performance. The accuracy, fidelity and suitability for integration

in [OD](#) routines were discussed. While the [SGP4](#) method can generate trajectories which are closer to the real world trajectory (higher fidelity), it cannot easily be formulated as system of differential equations ([DE](#)) which is the expected target dynamics model in tracking filtering. For both methods, higher accuracy can be obtained by using smaller simulation time steps. The [ISO 8601](#) time formatting standard and the [WGS84](#) standard were adopted in the [MPT](#).

The second section concerns sensor dynamics. The three main coordinate frames ([ECI](#), [ECEF](#), [SEZ](#)) used by the [MPT](#) in the modelling of sensor dynamics are defined and shown in several figures to clearly explain their mechanics. Radar measurement quantities such as bistatic range, bistatic Doppler shift, elevation angle and azimuth angles are derived based on the sensor dynamics framework developed in this section.

The third section explains how a radar range measurement differs from the geometric range (which is the [LoS](#) distance between a radar and a target) when the target is distant. It explains the concept of light-time correction which needs to be performed when observing [RSOs](#) from a ground station. Expressions are given for bistatic range and Doppler shift which account for light-time correction. Simulation results are shown to prove that the [MPT](#) can compute both the ideal and the actual bistatic range and Doppler shift.

All of the work shown in the following chapters on sensor scheduling and orbit determination is built on the space debris dynamics and sensor modelling framework developed in this chapter. Relevant notation used in the following chapters have been defined and detailed in this chapter to ensure self-consistency both in the report and in the software developed in this project.

# Scheduling the MeerKAT Radar

## 4.1 Introduction

This chapter begins by finding the radar parameters which influence the sensor tasking process in Section 4.2. Given these parameters, emphasis is then placed on finding out how to identify when a RSO will transit through the MeerKAT radar’s transmitter Field of Regard in Section 4.3. Section 4.4 explains how to schedule the Tx and Rx so that a suitable detection and tracking experiment may be done. This section ends with an illustration of the scheduled experiment geometry as well as the tasking instructions for the radar engineer. Section 4.5 calculates the signal to noise ratio at the receiver during the course of the scheduled experiment as well as the resulting radar measurement errors. Section 4.6 summarizes the radar scheduling. It also discusses several points concerning how a practical space target observation experiment differs from our simulations.

To help the reader in understanding the radar scheduling procedure, an ongoing illustrative case study is provided. The ISS is the subject of this case study. The Mission Planning Tool starts the ISS observation experiment by acquiring its TLE file given below.

ISS (ZARYA)

```
1 25544U 98067A    17253.93837963   .00001150   00000-0   24585-4 0   9991
2 25544   51.6444 330.8522 0003796 258.3764   78.6882 15.54163465 75088
```

## 4.2 Sensor parameters

This section presents calculations pertaining to parameters which are needed for sensor tasking and for SNR calculations which are not quoted in the radar design parameters in Table 1-1.

### Half-power beamwidth

[MeerKAT](#) dishes have a diameter of 13.5 m while the Denel telemetry dish has a radius of 5 m. [9] The 3 dB beamwidth of such parabolic dishes is given by

$$\Theta_{3 \text{ dB}} = \frac{k\lambda_c}{2r} \quad (4-1)$$

where  $r$  is the radius of the dish,  $\lambda_c$  is the wavelength of the radar signal and  $k$  is a factor which accounts for variations in the reflector shape and antenna feed. It is assumed to be 57.3 which is the typical value.

The [Tx](#) antenna has a beamwidth of  $1.272^\circ$  while the [MeerKAT](#) dishes have a beamwidth of  $0.943^\circ$ .

### Antenna gain

The dish's gain is found from

$$G = \left( \frac{2\pi r}{\lambda_c} \right)^2 \cdot e_A \quad (4-2)$$

where  $\lambda_c$  is the wavelength and  $e_A$  is the antenna efficiency, assumed to be 0.6 in this project.

The transmitter gain is 40.7 dBi and receiver gain is 43.4 dBi.

Table 4-1 below specifies the sensor parameters which are relevant to radar tasking.

Table 4-1: Sensor parameters relating to observation geometry

Parameter	Symbol	<a href="#">Tx</a>	<a href="#">Rx</a>
geocentric latitude	$\phi_{gc}$	$-34.6^\circ$	$-30.7^\circ$
longitude	$\lambda$	$20.3^\circ$	$21.4^\circ$
height above <a href="#">MSL</a>	$h$	18 m	1038 m
3 dB beamwidth	$\Theta_{3 \text{ dB}}$	$1.272^\circ$	$0.943^\circ$
range of azimuth angles in <a href="#">FoR</a>	$B_{\psi}^{\text{FoR}}$	$0^\circ$ to $360^\circ$	$-185^\circ$ to $275^\circ$
range of elevation angles in <a href="#">FoR</a>	$B_{\theta}^{\text{FoR}}$	$10^\circ$ to $90^\circ$	$15^\circ$ to $88^\circ$

The first three rows in Table 4-1 contain the latitude, longitude and height above Mean Sea Level of the transmitter in Bredasdorp and the first [MeerKAT](#) dish in Carnarvon. The values for height above [MSL](#) are approximate because more accurate information is not available from official sources. The last two rows in the table indicate the range of azimuth and elevation angles in the [Tx](#) and [Rx](#) Field of Regards. There are no official values for the [Tx](#) allowable range of angles, so reasonable values are assumed in this project. The azimuth range of  $-185^\circ$  to  $275^\circ$  from [62] means that the [MeerKAT](#) dish can cover the entire horizontal plane. It should be noted that the [MeerKAT](#) fact sheet [62] adopts the following convention: a North-East-Down system for the topocentric frame (instead of the South-East-Zenith frame adopted in this project)

and while the elevation angle is defined similarly to ours, the azimuth angle is measured from North to East instead of South to East<sup>1</sup>. The [antenna beamwidths](#) and range of elevation and look angles  $B_{\psi}^{\text{FoR}}$  and  $B_{\theta}^{\text{FoR}}$  greatly influence the [MPT](#)'s results concerning target passage identification and sensor scheduling, as will be shown in the [Section 4.3](#) and [Section 4.4](#).

## 4.3 Target passage identification

[Orbit propagation](#) is done on the [TLE](#) set shown in [Section 4.1](#), using [SGP4](#) methods. The target may go through several orbits before passing close to the ground station. So, simulations spanning a few hours are typically required. This would be an extremely onerous task with small time steps in the order of milliseconds or microseconds. At this initial stage, a relatively large time step of  $\Delta_t = 1.0$  s is used to obtain a rough estimate of the pass epoch. This will later on be refined at a time step of  $\Delta_t = 1.0$  ms and finally, at a time step of  $\Delta_t = 1/\text{PRF}$ . Three different simulation step sizes are used to reduce computation times at each processing stage without compromising on the fidelity and precision of the [MPT](#).

When the elevation angle from the [Tx](#) to the target exceeds  $10^\circ$ , the target is above the horizon and is said to be visible. The visibility condition is used to identify the target passage shown as the red portion of the satellite ground track in the figure below.

---

<sup>1</sup> See [Section 3.3](#).

### 4.3. TARGET PASSAGE IDENTIFICATION

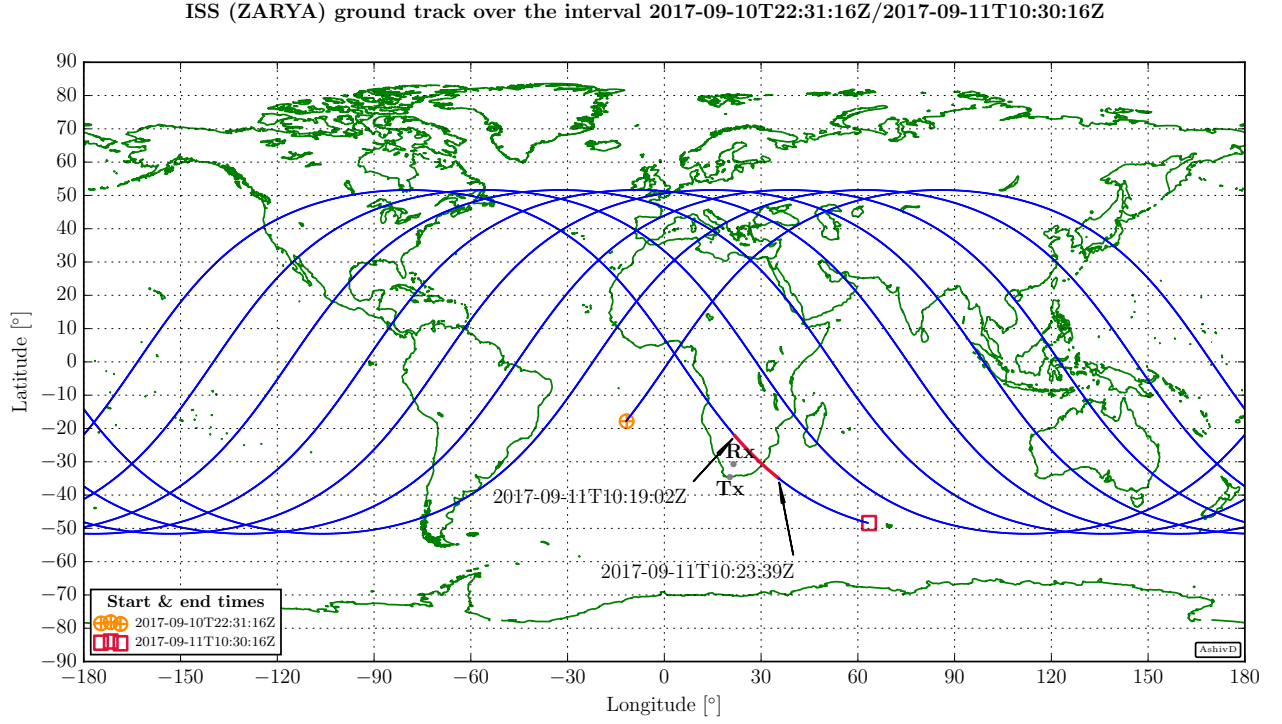


Figure 4-1: ISS ground track over the interval 2017-09-10T22:31:16Z/2017-09-11T10:30:16Z with the transit through the Tx's FoR shown in red. The starting and ending epoch of the identified target passage are annotated.

The figure below shows the Line of Sight range, elevation and azimuth angles from the transmitter to the ISS over the interval 2017-09-10T22:31:16Z/2017-09-11T10:30:16Z. The slant-range  $\rho$  (top plot) is small when the elevation angle  $\theta$  (middle plot) is positive. The time interval 2017-09-11T10:19:02Z/2017-09-11T10:23:39Z corresponding to the target passage shown in red in the ground track plot in Figure 4-1 is highlighted in green in the figure below.



### 4.3. TARGET PASSAGE IDENTIFICATION

Radar observation vectors from Tx to ISS (ZARYA) over 2017-09-10T22:31:16Z/2017-09-11T10:30:16Z

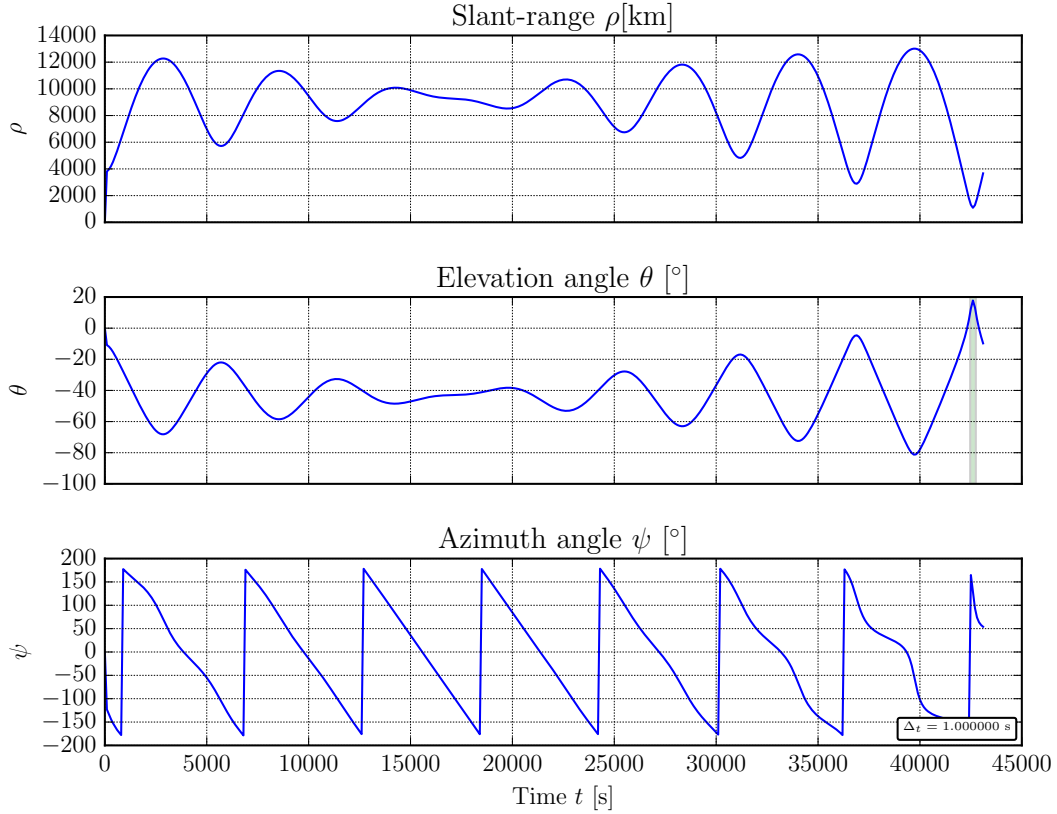


Figure 4-2: Radar vectors from the Tx to the target (the ISS) over 2017-09-10T22:31:16Z/2017-09-11T10:30:16Z. The interval spent within the Tx's FoR is highlighted in green. The simulation time step  $\Delta_t$  is specified in the box at the lower right corner of the bottom plot.

The range of azimuth and elevation angles in the FoR, namely  $B_{\psi}^{\text{FoR}}$  and  $B_{\theta}^{\text{FoR}}$  constrain the target's pass visibility.

The SGP4 method is called again to perform OP at a simulation time step of  $\Delta_t = 0.001$  s to refine the estimated time span of 2017-09-11T10:19:02Z/2017-09-11T10:23:39Z which was identified in the initial step at a resolution of 1.0 s.

Assuming that the initial timespan 2017-09-11T10:19:02Z/2017-09-11T10:23:39Z estimated at  $\Delta_t^{\text{initial}} = 1.0$  s was 10% inaccurate due to the relatively large step size  $\Delta_t = 1.0$  s, a correction term  $\epsilon_t$  given by the following formula is made:

$$\epsilon_t = 0.1 \frac{\Delta_t^{\text{initial}}}{\Delta_t^{\text{new}}} \quad (4-3)$$

The correction term evaluates to  $0.1(1.0/0.001) = 100$ .

The arbitrarily-chosen 10% tolerance bound was verified to be adequate for each observation

scenario considered in this project. In case this value leads to an unacceptable time span in a given observation experiment, the [MPT](#) is programmed to raise a warning.

The new interval is 2017-09-11T10:17:22Z/2017-09-11T10:25:19Z.

Figure 4-3 shows a plot of the elevation angle  $\theta$  from the transmitter to the [RSO](#) during the time span 2017-09-11T10:17:22Z/2017-09-11T10:25:19Z.

Elevation angle to ISS (ZARYA) from Tx over 2017-09-11T10:17:22Z/2017-09-11T10:25:19Z

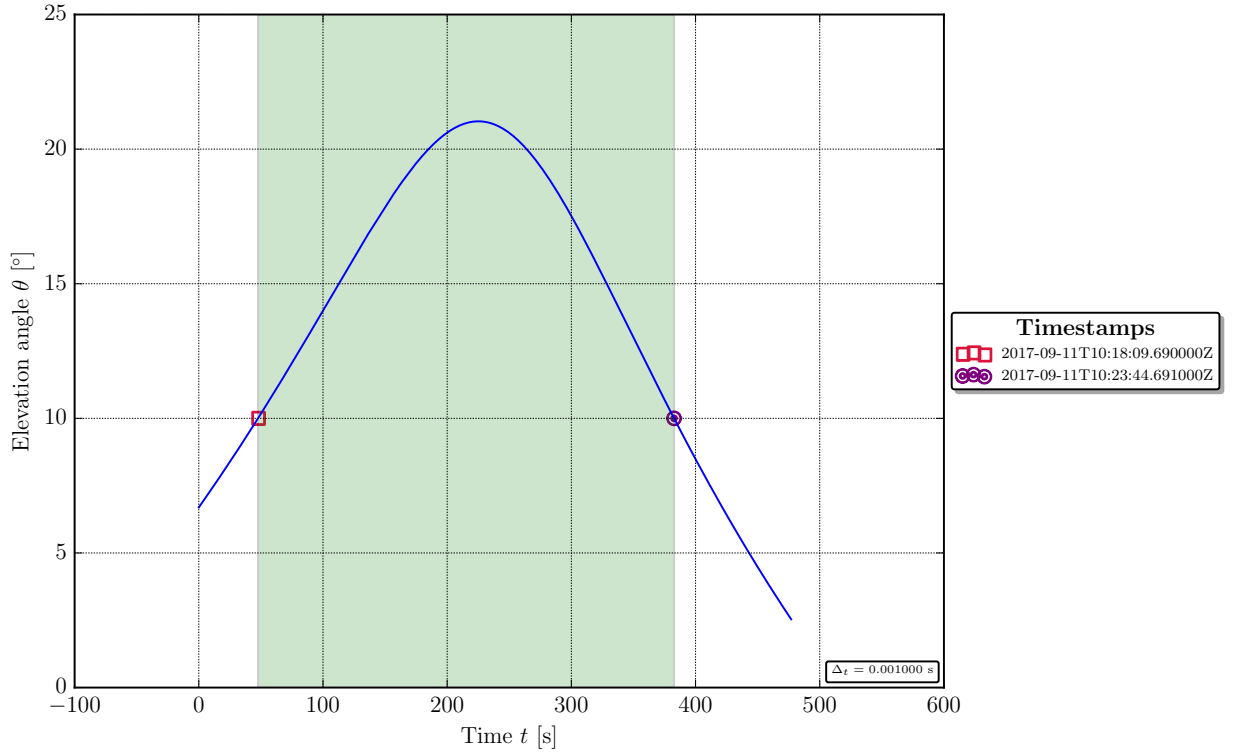


Figure 4-3: Elevation angle at the transmitter over the interval 2017-09-11T10:17:22Z/2017-09-11T10:25:19Z. The markers in red and purple indicate when the target's elevation crossed the  $10^\circ$  threshold which is the minimum angle for visibility. The interval spent within the [Tx's FoR](#) is highlighted in green.

The region highlighted in green in Figure 4-3 denotes the time interval for the [RSO's](#) transit through the transmitter's [Field of Regard](#).

The transit interval estimate is 2017-09-11T10:18:09.690Z/2017-09-11T10:23:44.691Z at a resolution of 0.001 s. It should be noted that the estimated transit interval lies well within the 10% tolerance band which corresponds to the interval 2017-09-11T10:17:22Z/2017-09-11T10:25:19Z. This confirms that a tolerance of 10% is adequate in increasing the trajectory simulation rate.

The figure below depicts the target's passage in the [MeerKAT](#) radar's vicinity on a map. The transmitter's [Field of Regard](#) is the region bounded by the red lines and the target trajectory in blue.

Object 25544 trajectory during the interval 2017-09-11T10:17:22Z/2017-09-11T10:25:19Z

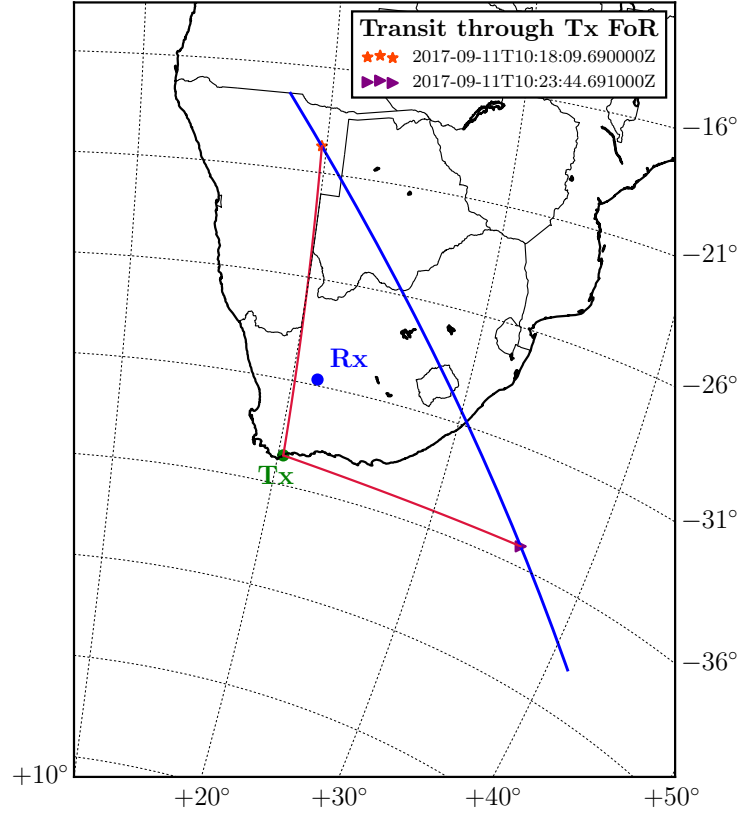


Figure 4-4: The target's trajectory illustrated on a map (in blue). The **Tx** is annotated in green. The region bounded by the red lines and the target trajectory is the transmitter's **FoR**. The markers in red and purple indicate when the target's elevation crossed the  $10^\circ$  threshold which is the minimum angle for visibility.

The **MeerKAT** receiver's allowable range of elevation angles  $B_\theta^{\text{FoR}}$  and azimuth angles  $B_\psi^{\text{FoR}}$  also constrain the target pass visibility. Only the first three **MeerKAT** receivers are simulated in this exploratory project since it has been found that these three are sufficient to cover the entire **RSO** pass illuminated by the proposed **Tx**.

Figure 4-5 shows the elevation and azimuth angles to the target from the first **MeerKAT** dish, **M000**, referred to as **Rx0** here. The constraint placed by the receiver's acceptable range of elevation angles  $B_\theta^{\text{FoR}}$  is illustrated.

There is a kink in the azimuth time-series at around  $t = 90$  s in the lower plot of Figure 4-5. The azimuth angle to the target jumps from  $-180^\circ$  to  $180^\circ$  because the target flew from the third to the second quadrant (Cf. Figure 4-4 and the azimuth angle definition shown in Figure 3-15).

The time interval spent within the **Rx0**'s **FoR**, highlighted in green in the figure above, is 2017-09-11T10:18:31.518Z/2017-09-11T10:22:50.591Z.

Look angles at Rx0 to object 25544 trajectory for 2017-09-11T10:17:22Z/2017-09-11T10:25:19Z

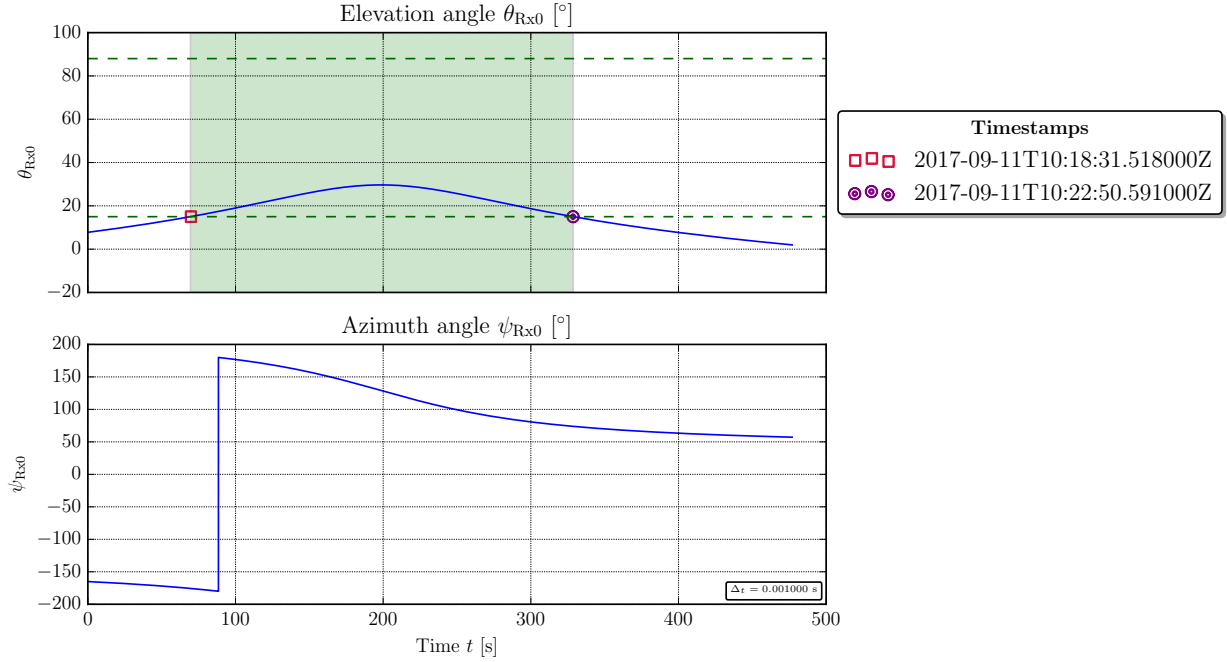


Figure 4-5: Elevation and azimuth angle plots at Rx0 over the interval 2017-09-11T10:17:22Z/2017-09-11T10:25:19Z. The green dashed lines indicate the lower and upper bound for the  $B_{\theta}^{FoR}$ . The markers in red and purple indicate when the target was visible to Rx0.

After applying each receiver's FoR constraint, the final time interval for the target passage is 2017-09-11T10:18:31.519Z/2017-09-11T10:22:50.589Z at a resolution of  $\Delta_t = 1.0$  ms.

## 4.4 Sensor scheduling

The previous section identified when the target would transit through the sensor's Field of Regard. This section first determines in Subsection 4.4.1 the most opportune time for the transmitter to illuminate the target. Afterwards, the topic of radar receiver tasking is explored in Subsection 4.4.2. Subsection 4.4.3 brings together the ideas of the two preceding subsections to accomplish the overall goal of sensor tasking and scheduling, thus ending this section.

### 4.4.1 Tasking the transmitter

This subsection determines where to point the Tx's antenna beam in the sky to ensure a good radar geometry for detection and tracking for a beam-park experiment (BPE). In other words, the transmitter tasking determines the Tx's Field of View.

When operating in BPE mode, a radar cannot task its antennas to rotate to follow the target's movement in the FoR. So the dishes have to stare in a fixed direction and survey a restricted portion of the sky. Since space targets move at speeds of about 8 kilometres per second, they will spend a very short amount of time within the region illuminated by the transmitter's beam, which is actually the Tx's FoV. The most opportune epoch for an observation experiment is when the target RSO spends a maximum amount of time, referred to as *illumination time*  $T_{i,Tx}$ , within the Tx's beam. This ensures that the radar collects the largest possible number of data points from the target. More data points will indubitably lead to an improvement in the orbit determination accuracy of a tracking filter.

Determining this epoch and the corresponding Tx antenna pointing is complicated. First, RSOs in LEO have orbits which can be circular or elliptical in shape and so their transit through the Tx's FoR cannot be approximated with a simple circular path to assist the Tx tasking process. Furthermore, individual passes from the same object are different: the RSO may cross the transmitter's FoR from North to South or vice-versa and the pass may occur close along the ground to the Tx (close to an overhead pass) or farther away towards the horizon. Finally, the radar geometry also changes from one pass to another due to the Earth's rotation in the ECEF frame.

A computational procedure is adopted by the MPT to determine the Tx antenna pointing which ensures the longest target illumination time.

Initially, a square beam model is assumed to facilitate searching time-indexed arrays in Python code. Later on, a circular beam model which is more practical will be assumed. The square beam model for the Tx has a beamwidth of  $\Theta_{3\text{ dB}} = 1.272^\circ$  both in the azimuth and elevation planes as shown in the following figure.

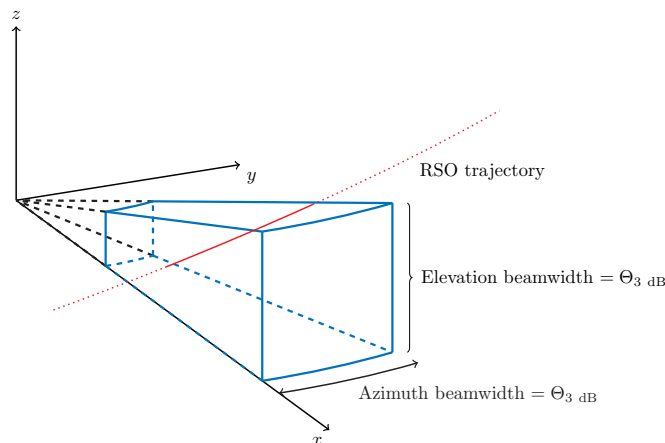


Figure 4-6: A RSO transiting through a square antenna beam model (in blue). The antenna is located at the origin of the coordinate system. The target illumination by the beam is shown by the solid portion of the red curve. This figure is not to scale.

It is clear from Figure 4-6 that the elevation and azimuth components of the target's position in spherical coordinates  $(\rho, \theta, \psi)$  determine how much of the trajectory lies within the antenna beam.

The centre of a hypothetical square beam is placed at every pair  $\{\psi_{Tx}[k], \theta_{Tx}[k]\}$  in the target trajectory during the interval 2017-09-11T10:18:31.519Z/2017-09-11T10:22:50.589Z and the number of data points within this square of side  $\Theta_3$  dB degrees is counted and stored in a  $k$ -indexed array. This is equivalent to plotting the elevation angle time-series against the azimuth angle time-series, as shown in Figure 4-9, and then placing a square of side  $\Theta_3$  dB on every point on the curve and counting the number of data points it covers.

This voting process is feasible only if the  $\{\psi_{Tx}, \theta_{Tx}\}$  curve of interest is continuous. As explained in Section 4.4<sup>2</sup>, a kink in the azimuth angle time-series arose because the target flew from the third to the second quadrant in the local x-y plane at the radar Tx. The jump from  $-180^\circ$  to  $180^\circ$  appears as the blue curve in Figure 4-7 below which is a plot of the azimuth angle time-series.

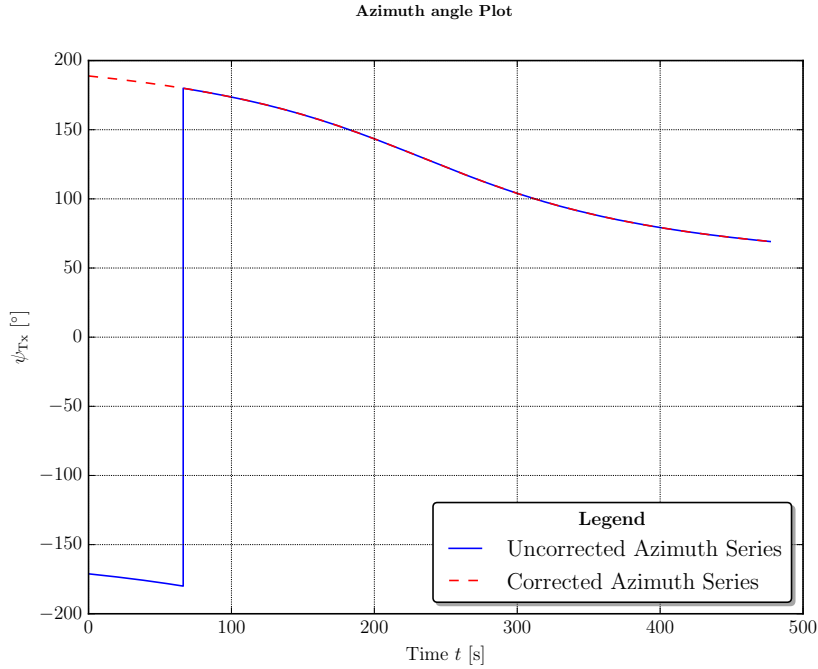


Figure 4-7: Azimuth angle versus time plot for the target trajectory. The Uncorrected Azimuth Series (in blue) consists of the raw azimuth angle values whereas the Corrected Azimuth Series (dashed, in red) have a bias of  $+360^\circ$  before the kink.

A bias of  $+360^\circ$  is added to all azimuth time-series up to the jump to obtain a continuous curve, shown as a dashed red curve labelled as 'Corrected Azimuth Series'. The corrected and

<sup>2</sup> More specifically, the penultimate paragraph on Page 76.

uncorrected azimuth time-series are plotted against the elevation angle  $\theta_{Tx}$  in the following figure.

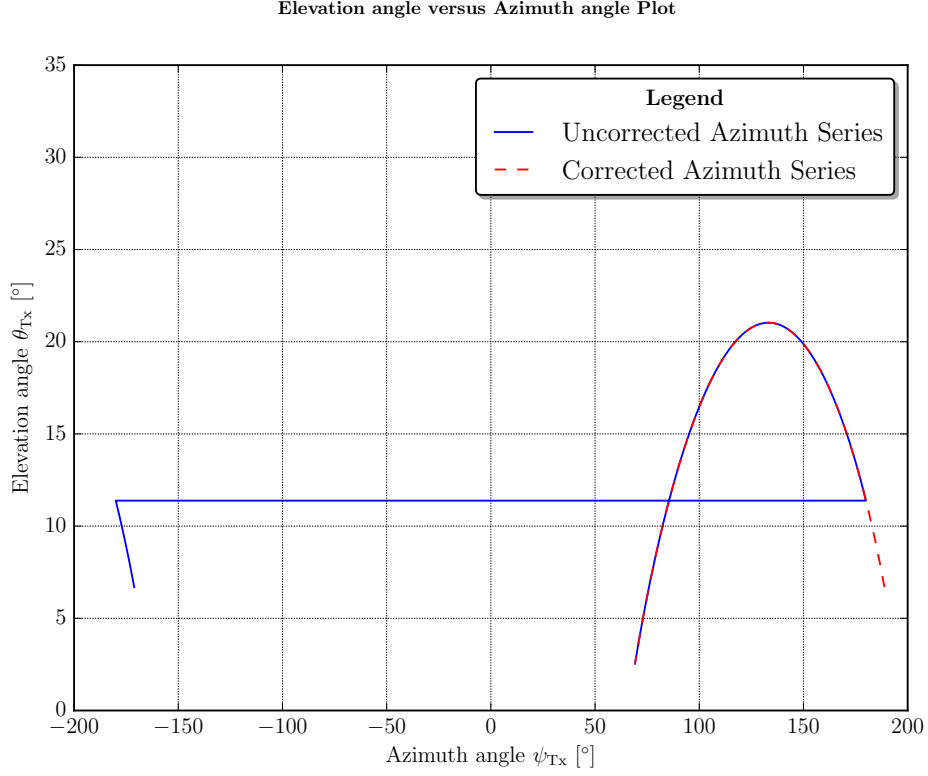


Figure 4-8: Elevation angle versus uncorrected (blue curve) and corrected (dashed, red curve) azimuth angle plots for the target trajectory.

Since corrected curve shown in Figure 4-8 is continuous, the voting process with a square beam model centered on each candidate  $\{\psi_{Tx}, \theta_{Tx}\}$  can be performed. Figure 4-9 shows the elevation versus azimuth plot for the target trajectory in the vicinity of the highest count found, during the interval 2017-09-11T10:18:31.519Z/2017-09-11T10:22:50.589Z.

Tx beam placement for the object 25544 trajectory during the interval 2017-09-11T10:18:31.519000Z/2017-09-11T10:22:50.589000Z

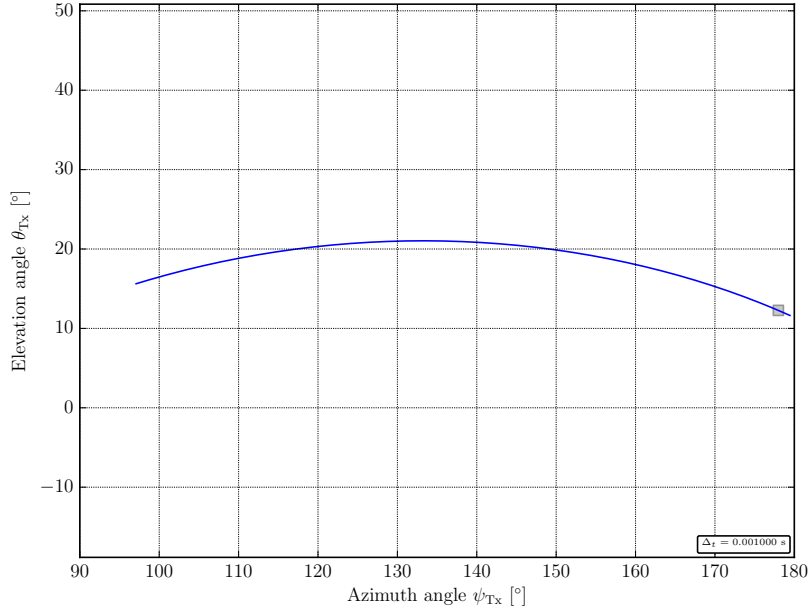


Figure 4-9: Elevation versus azimuth plot for the target trajectory during the interval 2017-09-11T10:18:31.519Z/2017-09-11T10:22:50.589Z. The grey square on the right end of the graph represents a hypothetical beam of beamwidth  $\Theta_{3 \text{ dB}} = 1.272^\circ$ .

After the counting process, the  $k$ -indexed array of counts can be multiplied by the time step  $\Delta_t$  to find the illumination time possible for all instants  $k$ . The illumination time in the transmitter's beam is plotted against the discrete-time index  $k$  in Figure 4-10.



Dwell-time duration in Tx beam for object 25544 over 2017-09-11T10:18:31.519000Z/2017-09-11T10:22:50.589000Z

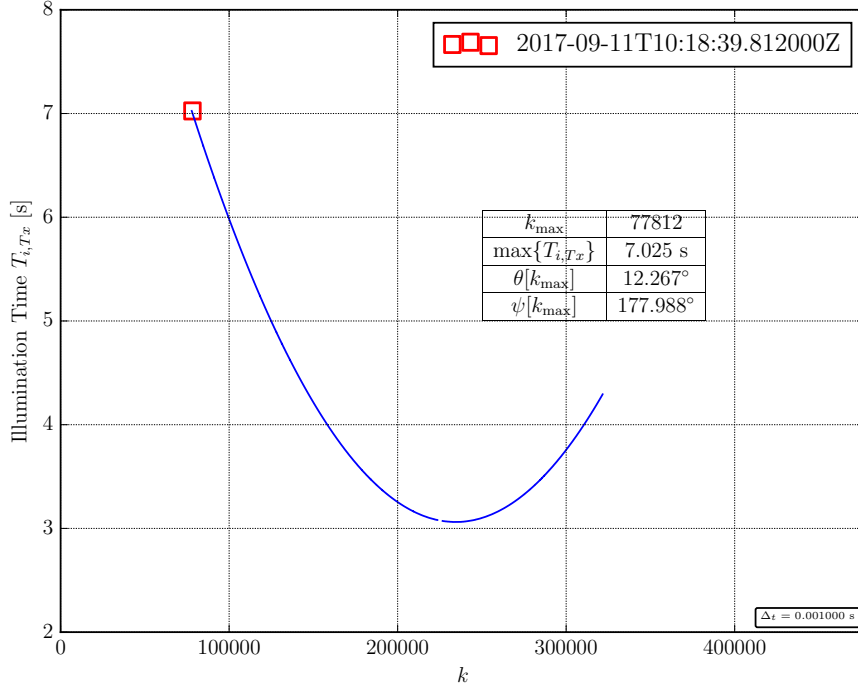


Figure 4-10: Illumination time in the Tx beam during the target’s transit through the MeerKAT radar’s FoR. The maximum illumination time  $\max\{T_{i,Tx}\} = 7.025$  s is denoted with a red marker. The target crosses through the antenna’s beam centre at 2017-09-11T10:18:39.812Z.

Figure 4-10 shows the possible illumination time  $T_{i,Tx}$  for every data point  $k$  in the target trajectory. The illumination time is the longest at  $k_{\max} = \operatorname{argmax}\{T_{i,Tx}[k]\} = 77812$  which is early on in the pass. This occurred when the RSO had just risen above the horizon as seen from the transmitter. It is logical that the best dwell-times would happen when the target is far along the ground from the radar. So the best illumination times are either at the very beginning or at the very end of a pass.

When the RSO is close to its maximum elevation, it will zip through the radar beam extremely quickly. Since we are interested in finding long dwell-times within the beam, we have decided not to calculate the dwell-time corresponding to this portion of the pass to save computation time. This explains the presence of a gap in the graph in Figure 4-10 at  $k \approx 230000$ .

The array index  $k_{\max}$  corresponding to the maximum illumination time is used to read off its corresponding elevation angle  $\theta_{Tx}[k_{\max}]$  and azimuth angle  $\psi_{Tx}[k_{\max}]$  which are shown in the table in Figure 4-10.

This means that the longest observation window occurs when the transmitter’s antenna is tasked to point at  $\{\theta_{Tx}[k_{\max}], \psi_{Tx}[k_{\max}]\} = \{12.267^\circ, 177.988^\circ\}$ .

Figure 4-11 represents the  $\{\theta_{Tx}, \psi_{Tx}\}$  graph in Figure 4-9 in the vicinity of  $\{\theta_{Tx}[k_{\max}], \psi_{Tx}[k_{\max}]\}$ .

Tx beam placement for the object 25544 trajectory during the interval 2017-09-11T10:18:31.519000Z/2017-09-11T10:18:51.812000Z

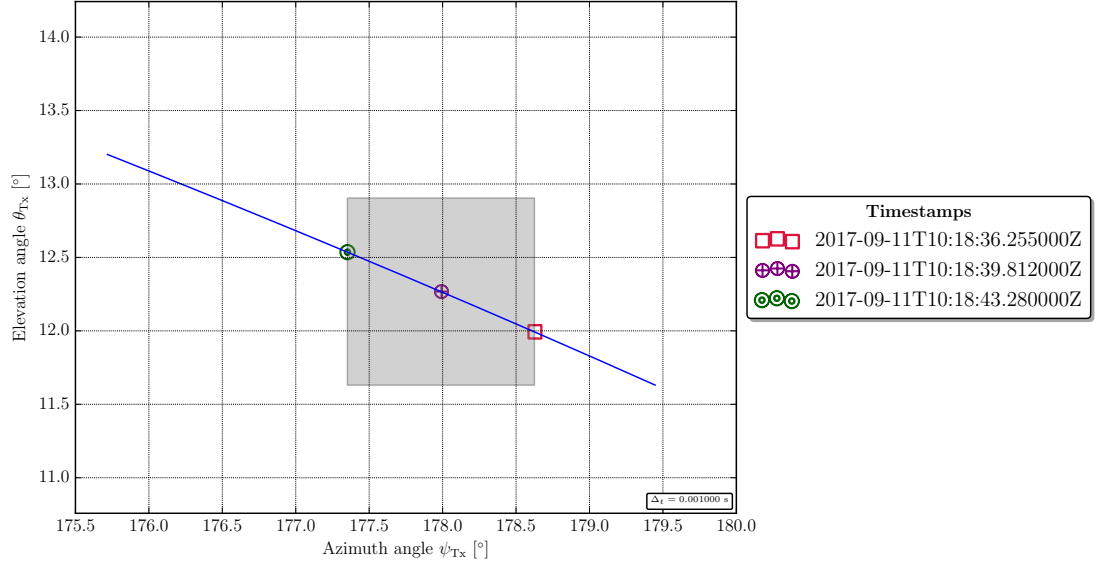


Figure 4-11: Elevation versus azimuth plot for the target trajectory in the vicinity of the best pair  $\{\theta_{Tx}[k_{\max}], \psi_{Tx}[k_{\max}]\}$ . The grey square on the right end of the graph represents a hypothetical beam of beamwidth  $\Theta_3 \text{ dB} = 1.272^\circ$ . The red and green markers indicate the elevation and azimuth angle pairs at which the target entered and then left the FoR. The RSO crosses the beam centre at 2017-09-11T10:18:39.812Z.

At a resolution of  $\Delta_t = 1.0 \text{ ms}$ , the transit through the Tx's FoV is found to start at 2017-09-11T10:18:36.255Z and end at 2017-09-11T10:18:43.280Z, as shown in Figure 4-11 and Figure 4-4 below. This is most opportune time interval for executing a RSO observation experiment for the MeerKAT radar.

Elevation angle to object 25544 from Tx over 2017-09-11T10:18:31.519000Z/2017-09-11T10:22:50.589000Z

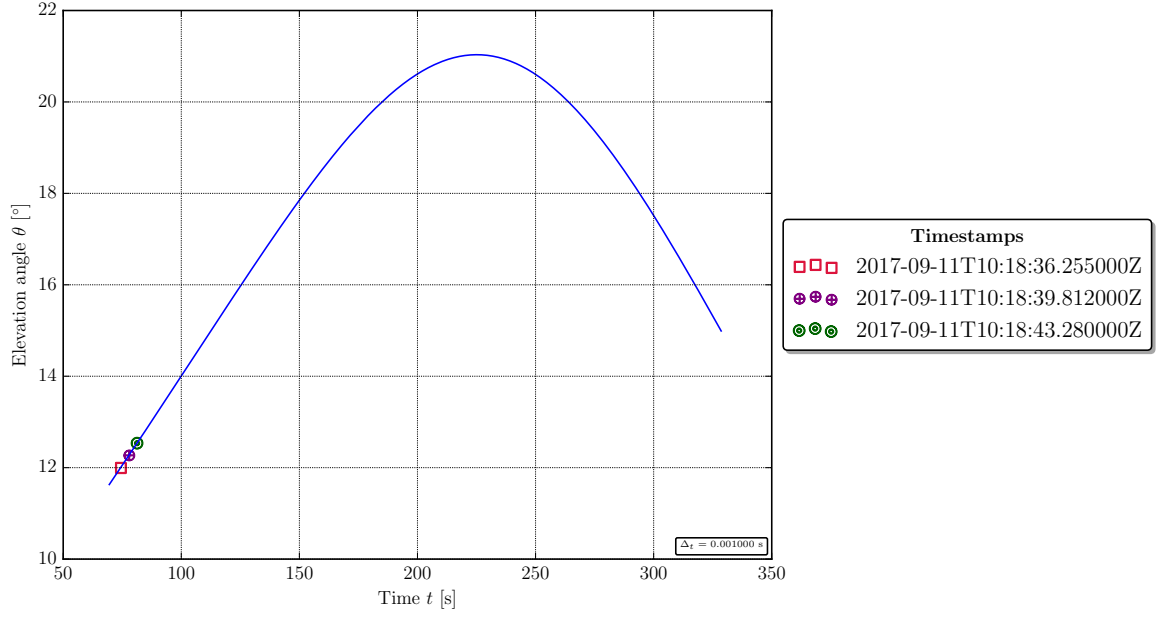


Figure 4-12: Elevation angle to transmitter with markers indicating the target's elevation when it transits through the Tx's chosen FoV.

The best dwell-time for this scenario is found to occur at the beginning of the pass, when the target is rising above the horizon, as can be seen in Figure 4-12 and Figure 4-13.

Object 25544 trajectory during the interval 2017-09-11T10:17:22Z/2017-09-11T10:25:19Z

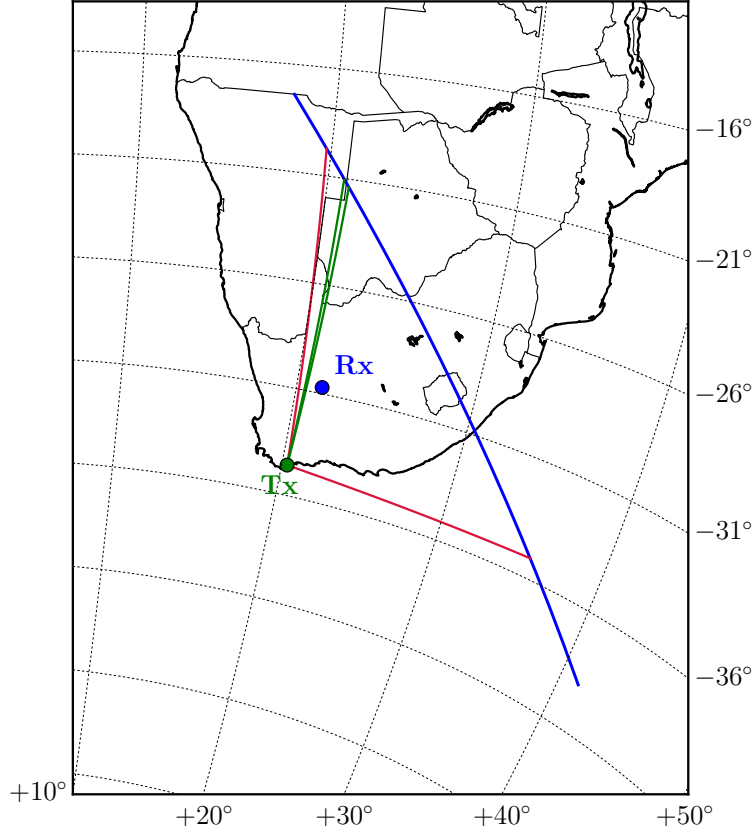


Figure 4-13: The target’s trajectory illustrated on a map (in blue). The Tx is annotated in green. The region bounded by the red lines and the blue curve is the transmitter’s FoR whereas the Field of View is bounded by the green lines and the blue curve.

As can be seen in Figure 4-13, the illuminated portion of the trajectory is very small in relation to the size of the Field of Regard. This is due to the small size of the antenna beamwidth  $\Theta_{3\text{ dB}}^{\text{Tx}} = 1.272^\circ$  compared to the possible range of azimuth angles  $B_\psi^{\text{FoR}}$ .

The final stage of the transmitter tasking process is to change the simulation time step  $\Delta_t$  to the actual radar PRF. The MeerKAT radar operates at a nominal PRF of 75 kHz and the observation window stated in Figure 4-11 must be adjusted by the correction term  $\epsilon_t$  from Eqn. 4-3. The target trajectory is generated at this higher resolution using the SGP4 orbit propagator  $\mathbf{f}_{\text{SGP4}}$  as before. The transmitter’s and receivers’ FoR constraints are then applied, after which the best dwell-time for a square beam model is found.

The new simulation time step is equal to the Pulse Repetition Interval, that is,  $\Delta_t = \text{PRI} = 13.3 \mu\text{s}$ . The corrected time span starts at 2017-09-11T10:18:35.253427Z and ends at 2017-09-11T10:18:44.279987Z.

#### 4.4. SENSOR SCHEDULING

Tx beam placement for object 25544 trajectory during 2017-09-11T10:18:35.253427Z/2017-09-11T10:18:44.279987Z

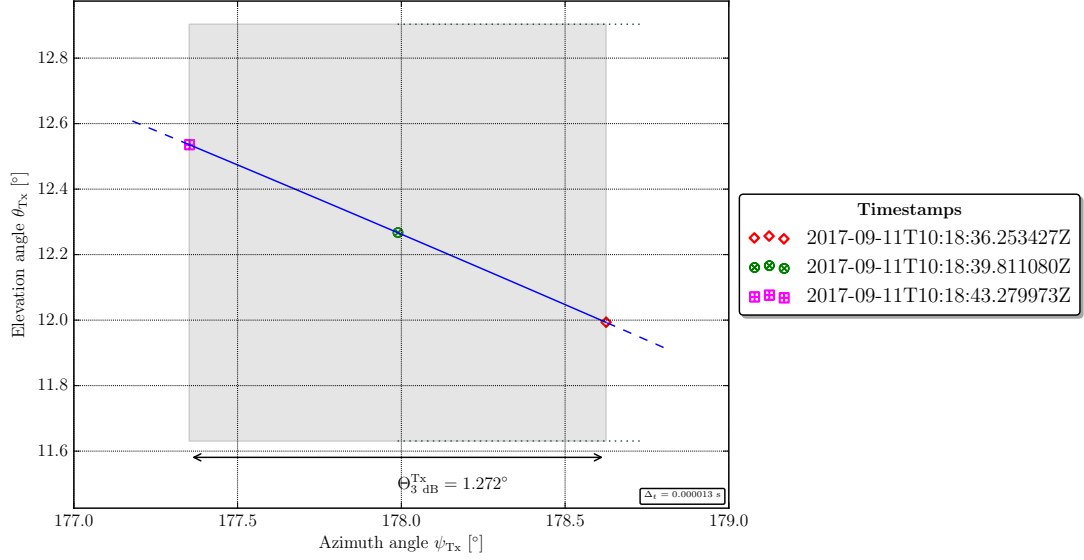


Figure 4-14: Elevation versus azimuth plot for the target trajectory generated at  $\Delta_t = \text{PRI}$ . The red and purple markers indicate the elevation and azimuth angle pairs at which the target entered and then left the FoV. The RSO crosses the beam centre at 2017-09-11T10:18:39.811080Z (green marker).

It has been assumed up to now that a square beam model can be used for the dish antennas involved in the MeerKAT radar. A circular beam model is closer to the actual beam shape of these antennas. Figure 4-15 shows that the pair  $\{\theta_{Tx}[k_{\max}], \psi_{Tx}[k_{\max}]\}$  which corresponds to the maximum illumination time does not change when moving from a square to a circular beam model which fully fits within the square.

Tx beam placement for object 25544 trajectory during 2017-09-11T10:18:35.253427Z/2017-09-11T10:18:44.279987Z

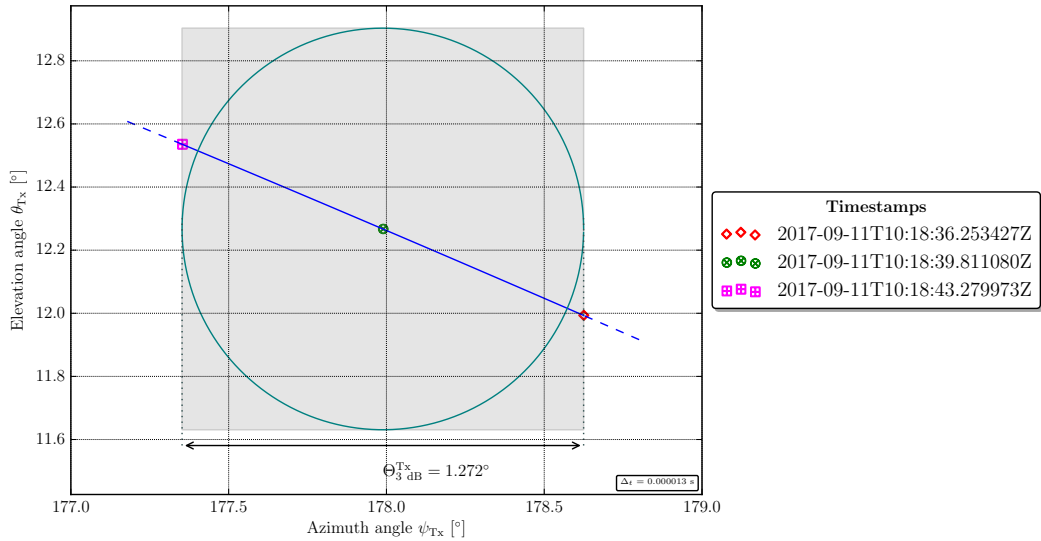


Figure 4-15: Transmitter beam centre pointing: from square beam to circular beam model

It is clear from Figure 4-15 that the target's point of entry and exit of the beam changes from the square to the circular model. The illumination time is reduced for the circular beam model because it covers a smaller area than the square beam model.

Tx beam placement for object 25544 trajectory during 2017-09-11T10:18:35.253427Z/2017-09-11T10:18:44.279987Z

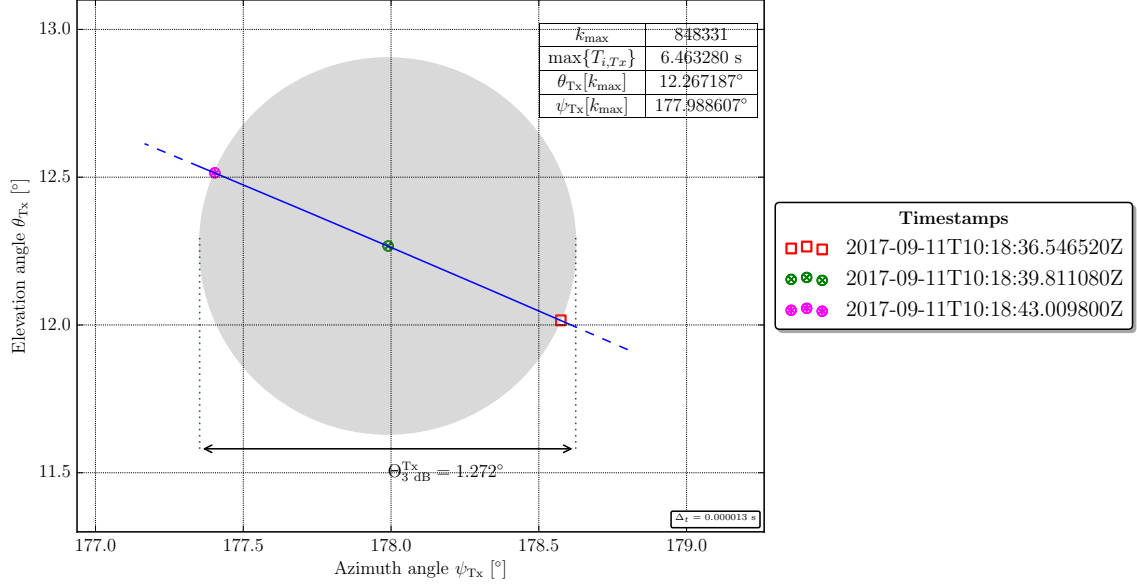


Figure 4-16: Elevation versus azimuth plot for the target's transit through the circular beam model (represented by the grey circle). The red and purple markers indicate the elevation and azimuth angle pairs at which the target entered and then left the FoV. The RSO crosses the beam centre at 2017-09-11T10:18:39.811080Z (green marker). The table in the upper right corner gives the best dwell-time, the associated array index  $k_{\max}$  and the corresponding elevation and azimuth angle for the Tx's beam centre.

The longest observation window length for this scenario is  $T_{i,T_x} = 6.463280$  s which is slightly smaller - as expected - than the value of 7.025 s quoted in Figure 4-10 for the square beam model at a lower resolution of  $\Delta_t = 1$  ms. The Tx has to be tasked to point its beam centre at  $\{\theta_{Tx}[k_{\max}], \psi_{Tx}[k_{\max}]\} = \{12.267187^\circ, 177.988607^\circ\}$  from 2017-09-11T10:18:36.546520Z to 2017-09-11T10:18:43.009800Z. These figures are used by the radar engineer to schedule the Tx.

The SGP4 orbit propagator produces trajectories which have position errors of up to 1 km at epoch as mentioned in Section 3.2.3.1. To investigate the effect of this error on the Tx beam centre pointing, an experiment was done by adding error vectors of magnitude 1 km to the RSO's trajectory and then analyzing the results in the elevation-azimuth plane. The error vectors were obtained by uniformly sampling points on a sphere of radius 1 km.

With the given Tx beamwidth  $\Theta_{3\text{dB}}^{\text{Tx}} = 1.272^\circ$ , the space object transit deviates the most from the beam centre when the 1 km position error is included in the  $z$ -component of the object's

position, as illustrated in Figure 4-17.

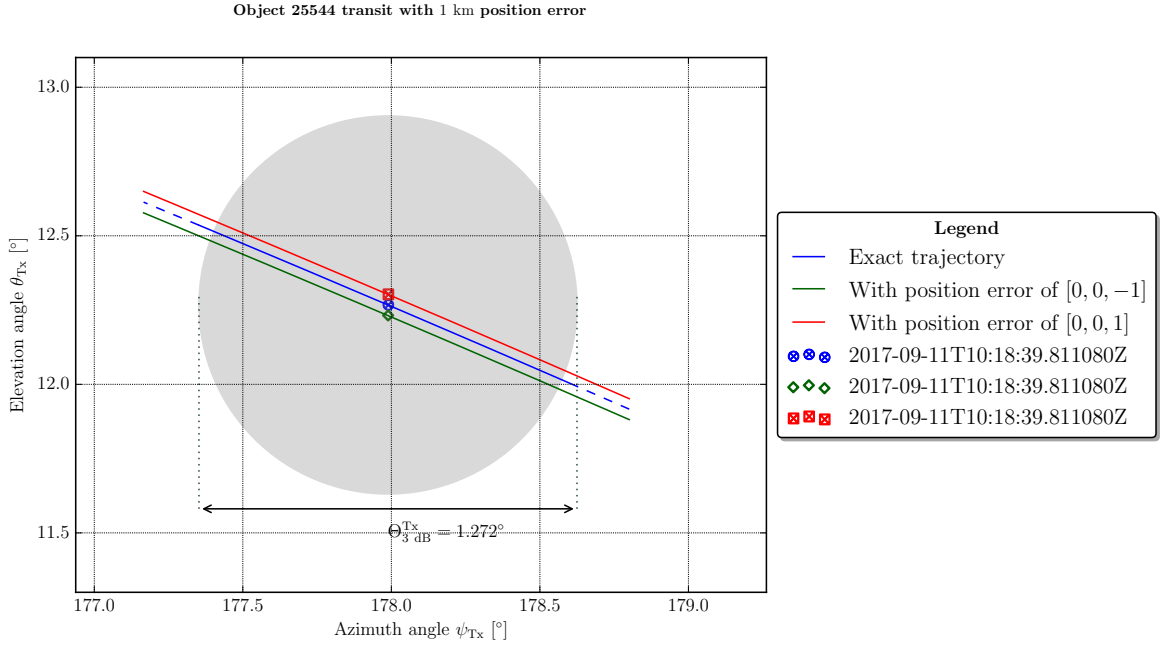


Figure 4-17: Elevation versus azimuth plot for the trajectories with position errors of  $[0, 0, 1]$  (red curve) and  $[0, 0, -1]$  (green curve). The red and green markers indicate the elevation and azimuth pairs for the erroneous trajectories at the instant at which the target trajectory was expected to cross the beam centre.

In Figure 4-17, at the expected instant of transit through the Tx's beam centre, the deviations from it are  $(\psi = 0^\circ, \theta = 0.03565872^\circ)$  for the initial position error of  $[0, 0, -1]$  and  $(\psi = 0^\circ, \theta = -0.03564908^\circ)$  for the initial position error of  $[0, 0, 1]$ . It can be concluded that, with a position error of 1 km, the target still passes very close to the beam centre.

Given that the observation window length is a figure of merit for the MeerKAT radar, it is instructive to find a typical range of values for the observation window length. Eight scenarios covering five different RSOs in the LEO regime were investigated in this project. The following table quotes the NORAD ID for each RSO investigated, the epoch of validity of its source TLE, the epoch corresponding to the instant of maximum illumination  $k_{\max}$  and the longest dwell-time possible. The full names of these space objects can be found in Table A-1 in the appendix.

Table 4-2: Observation window length for various space targets for the bistatic staring configuration

#	NORAD ID	TLE Epoch	Observation epoch	$\max\{T_{i,Tx}\}$ [s]
1	25544	2017-08-26T04:25:02Z	2017-08-26T17:47:20.732133Z	7.713080
2	37820	2017-08-30T18:22:58Z	2017-08-30T22:00:16.331227Z	5.997947
3	29754	2017-09-17T18:44:19Z	2017-09-17T21:29:07.287787Z	12.836933
4	33773	2017-09-10T03:30:54Z	2017-09-10T04:08:38.473107Z	8.572013
5	25544	2017-05-07T13:15:38Z	2017-05-07T13:25:09.818173Z	9.257107
6	25544	2017-09-10T22:31:16Z	2017-09-11T10:18:39.811080Z	6.463280
7	33759	2017-01-29T12:46:42Z	2017-01-29T15:24:52.174960Z	7.817173
8	37820	2017-04-25T14:26:58Z	2017-04-25T15:08:32.133520Z	4.492253

The targets spend between 4.5 s and 12.8 s in the transmitter’s **Field of View**. It is important to note that a space object does not have a fixed observation window length which will always arise in all passes. For instance, the **ISS** (25544), which is in a stable orbit, has passes which last 6.46 s, 7.71 s and 9.26 s. This gives weight to the argument that each **RSO** pass has to be analysed on its own.

Creating such a table may help in prioritizing **RSO** investigation tasks. Scenarios in which the observation window length is short may be rejected for an actual real-life experiment due to the expected reduced number of target hits and less abundant radar data points.

#### 4.4.2 Tasking the receivers

The preceding subsection showed that the radar transmitter can illuminate the target from 2017-09-11T10:18:36.546520Z to 2017-09-11T10:18:43.009800Z. This subsection now looks into how to task the first three **MeerKAT** receivers.

The **MeerKAT** array will consist of 64 dishes<sup>3</sup>. It will be too complicated to investigate tasking all of or several of these dishes at this early stage of the **MeerKAT** radar project. For simplicity, only the first three **MeerKAT** dishes will be investigated in this project. These are sufficient to cover the entirety of the illuminated portion of the target trajectory.

First, we consider the first **MeerKAT** dish as reference. We task **M000** as the main receiver **Rx0** and point it at the point corresponding to the target’s position at maximum illumination time in the transmitter’s beam. Then we task **M001** (**Rx1**) and **M002** (**Rx2**) to cover the illuminated trajectory which has not been covered by **M000**. This can be done because the **MeerKAT** beams can be moved independently of each other.

Figure 4-18 shows the target’s passage on a nominal topocentric right ascension-declination **TOPORADEC** map where the main dish **M000**’s pointing is referenced as  $(\Delta\alpha_t, \Delta\delta_t) = (0^\circ, 0^\circ)$ .

<sup>3</sup>This number is projected to increase after 2020.



TOPORADEC plot for object 25544 during 2017-09-11T10:18:32.253427Z/2017-09-11T10:18:47.279987Z

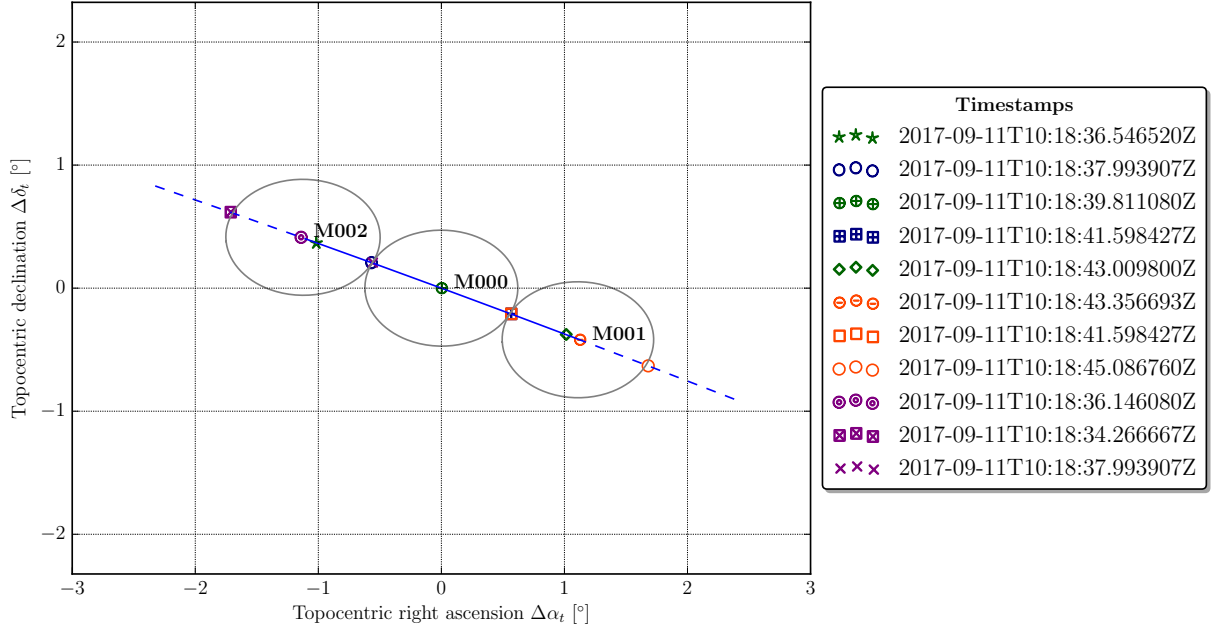


Figure 4-18: Normalized topocentric right ascension declination profile for the target's passage through the Rx's FoV. The Tx-illuminated portion of the trajectory is the solid blue curve segment. Each dish's beam (in grey) is labelled with its name. The timestamps at relevant points in the target passage are shown on the right.

The origin  $(\Delta\alpha_t, \Delta\delta_t) = (0^\circ, 0^\circ)$  in the normalized TOPORADEC plot corresponds to the elevation and azimuth pair  $\{\theta_{Rx0}, \psi_{Rx0}\} = \{16.035918, -177.427143^\circ\}$  at  $\theta_{GMST} = 145.2960759^\circ$  (derived from the epoch 2017-09-11T10:18:39.811080Z). Even though the beams are modelled as a circle of diameter  $\Theta_{3\text{ dB}} = 0.943^\circ$  in the elevation/azimuth plane, they appear as ellipses in the topocentric right ascension-declination plane as a consequence of being scanned across the celestial sphere by the rotation of the Earth about its axis.

Figure 4-18 can be compared with Figure 2-16 in the literature review on the BIRALES radar in Italy<sup>4</sup>. Both of these figures show the TOPORADEC profile for a RSO transit through a radar receiver's FoV. In Figure 2-16 for the BIRALES radar, several beam outlines are shown to signify that the receiver is a multi-beam one. The shading of the beam outlines in Figure 2-16 indicate that most receiver beams receive no significant target echo. Only three Rx beams are shown in Figure 4-18 because only three MeerKAT dishes are needed to cover the entirety of the Tx-illuminated portion of a target trajectory. The target passage is shown to cross five receiver beams for the BIRALES radar in Figure 2-16 because the BIRALES radar's transmitter is omnidirectional and therefore it can illuminate a larger portion of the target trajectory than the MeerKAT radar's Tx.

<sup>4</sup> See Subsection 2.4.1.3.

Since the radar engineer is unlikely to know what topocentric right ascension and declination mean, they should instead refer to the following section on experiment geometry which will summarize the sensor scheduling results.

### 4.4.3 Experiment geometry

The [Mission Planning Tool](#) can create a three-dimensional visualization of the observation scenario such as the one shown below.

Observation geometry for object 25544 transit during 2017-09-11T10:17:22Z/2017-09-11T10:19:22Z

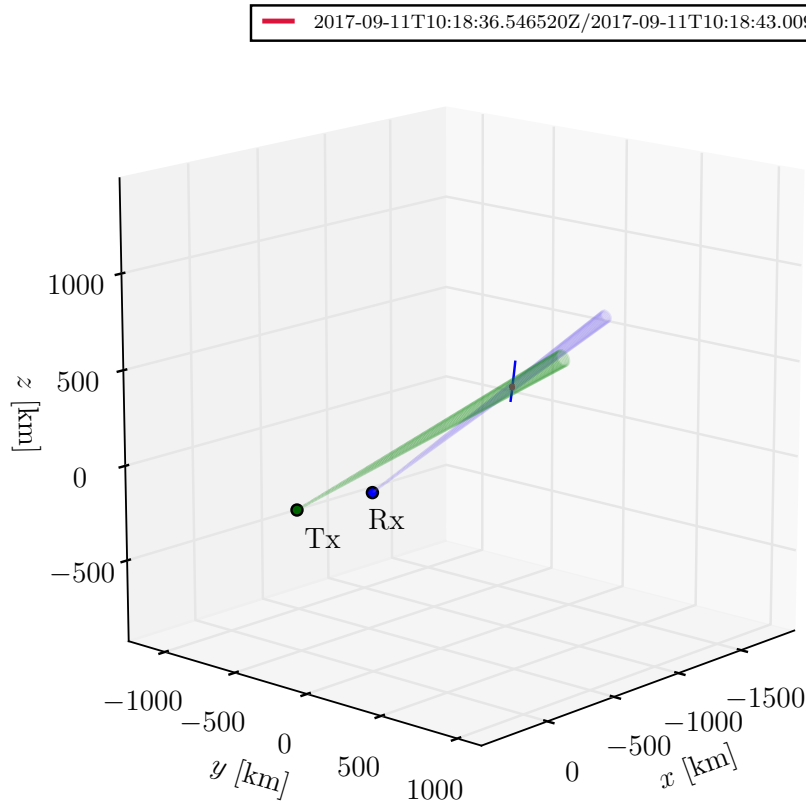
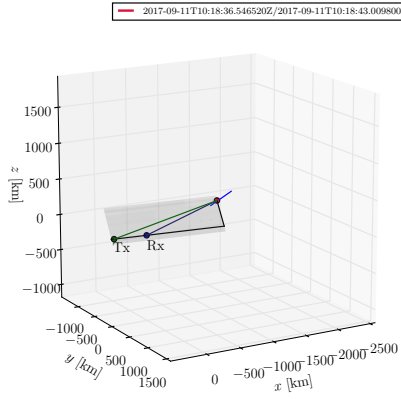


Figure 4-19: Target-radar geometry during the experiment. The target trajectory is the blue curve. The green and blue cylinders represent the Tx and Rx0 beam respectively.

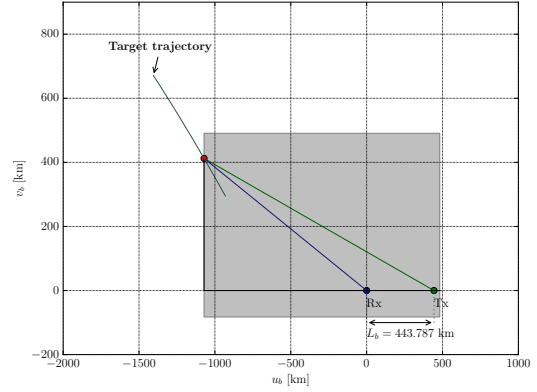
Due to the limited three-dimensional plotting abilities of Python, such an image cannot be made more informative. Hence, the observation scenario was projected onto the bistatic plane highlighted in grey in Figure 4-20b.

Bistatic geometry for object 25544 trajectory in the local frame



(a) 3D visualization

Projection of the target-radar geometry onto the bistatic plane at the best dwell-time



(b) 2D visualization

Figure 4-20: Target-radar geometry during the experiment. The bistatic plane highlighted in grey in the 3D plot in (a) is shown in 2D in (b). The bistatic baselines  $L_b$  is annotated in (b).

The bistatic baseline  $L_b$  between the transmitter and the receiver (**M000**) evaluates to 443.787 km in the bistatic plane, which agrees with the value calculated in Section 3.3. The analysis continues in Figure 4-21 which shows the bistatic plane with the transmitter's and receivers' beams illustrated. The target flies through the overlapping region.

Bistatic plane for object 25544 transit during 2017-09-11T10:17:22Z/2017-09-11T10:19:22Z

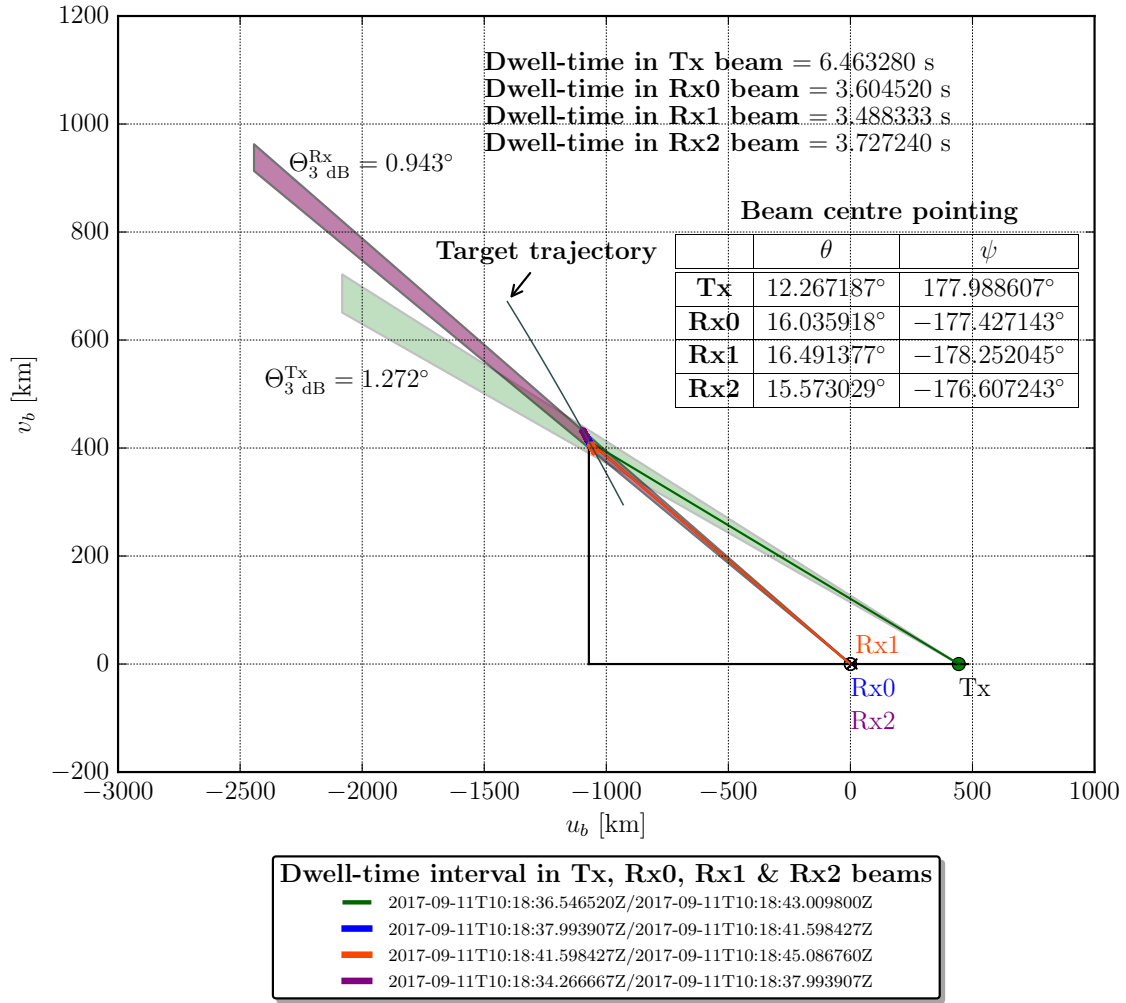


Figure 4-21: Target trajectory projected onto the bistatic plane. The Tx's beam is shown in green.

The target dwell-time in each beam is shown at the top of Figure 4-21. It should be noted that the dwell-times for Rx1 and Rx2 stated in Figure 4-21 relate to the total length of time that the target spent within these beams. The total length of time spent in the receivers' beams consists of a Tx-illuminated portion and a non-illuminated section (Shown in Figure 4-18). This means that the main limiting factor to the observation window length is posed by the beamwidth of the Tx and not by the fact that only three MeerKAT receivers were tasked during this experiment.

The table on the right in Figure 4-21 shows the elevation and azimuth angles for tasking the dishes' beam centre. The transmit and receive nodes are then scheduled to run the observation experiment from 2017-09-11T10:18:36.546520Z to 2017-09-11T10:18:43.009800Z.

## 4.5 SNR calculations & radar measurement errors

The signal-to-noise ratio (SNR) at the receiver is an important figure of merit for a radar system. It quantifies the performance of the radar in terms of its characteristics and in terms of the observation geometry and nature of the target. The SNR also influences radar measurement errors which determine the radar's performance in tracking a space target. This section draws together the experiment geometry aspects from Subsection 4.4.3 and the radar's key design parameters from Table 1-1 and Table 4-1 to predict the SNR in Subsection 4.5.1 and the radar's measurements in Subsection 4.5.2.

### 4.5.1 SNR calculations

The radar system's characteristics from Table 1-1 are restated in the following table for convenience.

Table 4-3: Parameters for the proposed MeerKAT radar

Parameter	Symbol	Value
Transmit power	$P_{Tx}$	2 MW
Centre frequency	$f_c$	1350 MHz
Wavelength	$\lambda_c$	0.2222 m
Bandwidth	$B$	10 MHz
Pulse width	$\tau$	5 $\mu$ s
Pulse repetition frequency (nominal)	PRF	75 kHz
Coherent processing interval (nominal)	CPI	0.1 s
Transmitter gain	$G_{Tx}$	40.7 dBi
Receiver gain	$G_{Rx}$	43.4 dBi

These radar parameters are stored in a reference .txt file in our Mission Planning Tool and can be edited when needed. Each simulation script then parses this file to find the relevant parameter values for its purposes.

As discussed before in Section 1.1, the MeerKAT radar should operate with a pulse repetition frequency different from the value quoted in the above table. Since the only PRF value available during this master's project was 75 kHz, this was the value used in our simulations.

The length of one coherent processing interval,  $T_{CPI}$ , is also variable in the MeerKAT radar. Since the coherent integration time is limited by the target's radial acceleration, the radar will adapt its CPI to suit the dynamics of the space object of interest [63, Eqn. 5.15]. Furthermore, due to the MeerKAT sensor operating in BPE mode wherein a RSO may spend only a few seconds (actually  $T_{i,Tx}$  seconds) in the radar's FoV, the CPI is also limited by the number of radar data points desired. If  $N_{CPI}$  data points are desired, then the coherent integration time is

given by  $T_{\text{CPI}} = T_{i,Tx}/N_{\text{CPI}}$ . Orbit determination, like any statistical estimation process, produces increasingly accurate estimates with increasing quantity of raw data points  $N_{\text{CPI}}$ . However, it is important to note that this data processing level concern does not take precedence in the coherent integration time design over other signal processing level concerns. Issues relating to range and Doppler walk may arise in the range-Doppler map due to the radar return signal smearing across multiple range and Doppler bins during a single CPI. At this preliminary stage of the MeerKAT radar design, the nominal CPI was set to 0.1 s in [9].

The simulation time step  $\Delta_t$ , set in the previous section as the PRI, satisfies the following equation.

$$\Delta_t = \frac{T_{\text{CPI}}}{N_{\text{CPI}}} \quad (4-4)$$

Since  $T_{\text{CPI}} = 0.1$  s,  $N_{\text{CPI}} = 7500$ .

The antenna gain shown in the last couple of rows in Table 4-3 were calculated in Section 4.2.

#### Single pulse received power

The single pulse received power is given by the radar equation.

$$P_{\text{Rx}} = \frac{P_{\text{Tx}} G_{\text{Tx}} G_{\text{Rx}} \lambda_c^2 \sigma_b}{(4\pi)^3 \rho_{\text{Tx}}^2 \rho_{\text{Rx}}^2} \quad (4-5)$$

where  $\sigma_b$  is the bistatic radar cross-section of the target and  $\rho_{\text{Tx}}$  and  $\rho_{\text{Rx}}$  are the LoS ranges from the target to the transmitter and receiver, respectively. RCS values quoted in this dissertation were obtained from <https://www.n2yo.com/>. These values are actually monostatic radar cross-sections, not bistatic RCSs. Aspect variations due to the RSO of interest tumbling about its centre of mass are not accounted for. These assumptions are reasonable for this preliminary study of the proposed MeerKAT radar.

The receiver gain in Eqn. 4-5 is modified to take into consideration the beamshape loss. The decrease in gain realized when the target is not exactly at the beam centre has to be accounted for since it influences the SNR appreciably and thus would be relevant in the observables estimation phase in Subsection 5.3.4.

According to [64, Eqn. 6], the Rx gain updated with the beamshape loss is given by the equation assuming an elliptical beam model.

$$\left[ G_{\text{Rx, BL}} \right]_{\text{dB}} = \left[ G_{\text{Rx}} \right]_{\text{dB}} - 12 \left( \left( \frac{\Delta \alpha_t}{\Theta_\alpha} \right)^2 + \left( \frac{\Delta \delta_t}{\Theta_\delta} \right)^2 \right) \quad (4-6)$$

where

- $\Theta_\alpha$  and  $\Theta_\delta$  are the beamwidths on the right ascension axis and the declination axis respectively.

In other words,  $\Theta_\alpha$  and  $\Theta_\delta$  are the major axis and minor axis of a beam ellipse in Figure 4-18. As explained before, these two quantities ( $\Theta_\alpha$  and  $\Theta_\delta$ ) are not the same because of the spreading along the topocentric right ascension axis caused by the rotation of the Earth along its axis during the observation window duration. In other words, the Rx beams appears as ellipses in Figure 4-18 due to diurnal rotation.

- $\Delta\alpha_t$  and  $\Delta\delta_t$  are the respective angular deviations from the dish's beam centre.

The power received at the relevant receiver (**M000**, **M001** and **M002**) is calculated at every pulse while taking into account variables such as the LoS range between the target and the relevant dish and the  $(\Delta\alpha_t, \Delta\delta_t)$  location of the target within that dish's beam ellipse.

Then the signal to noise ratio at the receiver can be calculated for every pulse according to

$$\text{SNR} = 10 \log_{10} \left( \frac{P_{\text{Rx}}}{k_B B T_0} \right) \quad (4-7)$$

in which  $k_B$  is the Boltzmann constant,  $B$  is the bandwidth of the transmitted signal and  $T_0$  is the noise temperature of the receiver.

The coherently integrated signal to noise ratio at the Rx is computed as

$$[\text{SNR}]_{\text{CI}} = \sum_{k=1}^{N_{\text{CPI}}} \text{SNR}[k] \quad (4-8)$$

where  $N_{\text{CPI}}$  is the number of pulses which are coherently integrated.

The following figure shows the single pulse and coherently integrated signal to noise ratio at the receivers for the ISS pass in Figure 4-18. The radar cross-section of the ISS is 401.801 m<sup>2</sup> according to <https://www.n2yo.com/>. One coherent processing interval is assumed to last 100 pulses, i.e.  $N_{\text{CPI}} = 7500$  such that  $T_{\text{CPI}} = 0.1$  s. This leads to an integration gain of roughly 38.751 dB in theory. In this simulation, the coherently integrated SNR was calculated explicitly by making use of Eqn. 4-8 for every CPI during the experiment.

SNR at MeerKAT for object 25544 during the interval 2017-09-11T10:18:33.253427Z/2017-09-11T10:18:46.279987Z

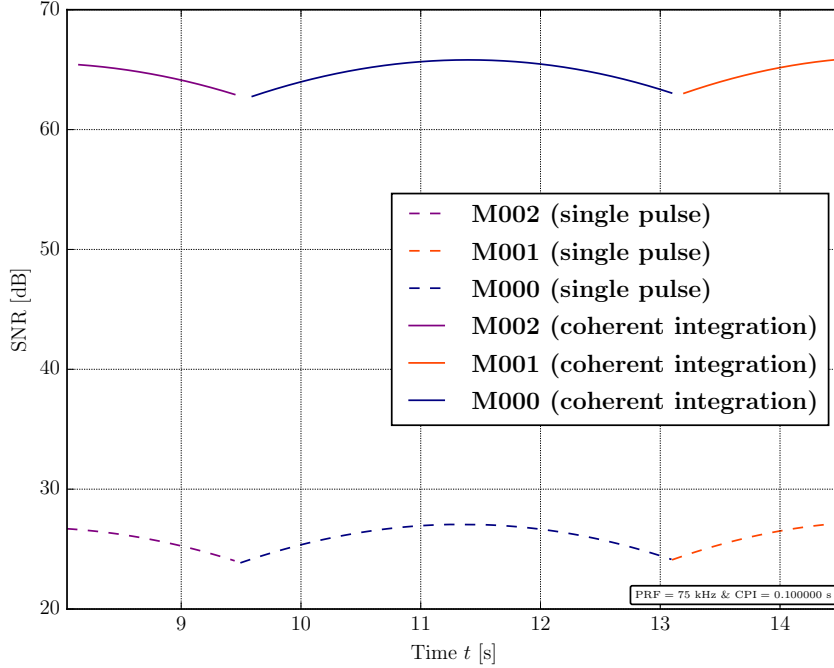


Figure 4-22: Single pulse (dashed) & coherently integrated (solid curves) SNR at the MeerKAT receivers. The SNR values are highest when the target is transiting close to the beam centres, where there is no beamshape loss. There are short gaps in the  $[\text{SNR}]_{\text{CI}}$  plots because 7500 pulses have to be integrated to obtain one CPI.

Considering Figure 4-22, it is clear that the actual PRF and CPI do not affect the shape of the coherently integrated SNR curve. This means that the SNR values can simply be normalized with respect to the maximum value of SNR for the next phase, the observables estimation phase discussed in Subsection 5.3.4. The radar engineer can further refine the choice of PRF and CPI independently of the orbital data processor. Since a smaller PRF is expected to be used in the final design of the MeerKAT radar as explained in Section 1.1, fewer radar pulses will be integrated during each Coherent Processing Interval. This means that the actual coherently integrated SNR should be lower than shown in Figure 4-22.

Finally, again referring to Figure 4-22, the SNR curve shows a curved profile due to the beamshape loss arising from the target moving away from or towards the beam centre.

The following table shows the maximum integrated SNR for the RSO passes in Table 4-2. The RCS of the targets of interest are also shown since they influence the received power at the radar receivers. The single pulse and integrated signal-to-noise ratios are figures of merit in radar design and analysis.



Table 4-4: Maximum integrated SNR at Rx for different RSOs' passes through the radar's FoV.

#	NORAD ID	TLE Epoch	RCS [m <sup>2</sup> ]	max{[SNR] <sub>CI</sub> } [dB]
1	25544	2017-08-26T04:25:02Z	401.801	68.501406
2	37820	2017-08-30T18:22:58Z	19.5231	60.388199
3	29754	2017-09-17T18:44:19Z	0.0121	11.107066
4	33773	2017-09-10T03:30:54Z	0.543	27.184846
5	25544	2017-05-07T13:15:38Z	401.801	66.745778
6	25544	2017-09-10T22:31:16Z	401.801	65.861252
7	33759	2017-01-29T12:46:42Z	0.079	21.872829
8	37820	2017-04-25T14:26:58Z	19.5231	57.545919

Objects 25544 and 37820 are satellites and thus have large radar cross-sections whereas objects 29754, 33759 and 33773 are pieces of space junk and thus have smaller cross-sections. The integrated SNR values range from 11 dB to 68 dB approximately. The range of SNR values is of interest to the radar engineer since it influences the design of the detection stage in the radar signal processing block.

### 4.5.2 Radar measurement errors

The previous subsection determined the signal-to-noise ratio at the MeerKAT radar's receivers during a target pass. From these SNR values, radar measurement errors which determine the determine the sensor's tracking performance are determined.

The MeerKAT operates bistatically: at every instant during the target's transit through the transmitter's FoV, one bistatic pair consisting of the Tx and one of three MeerKAT receivers (M000, M001 and M002) can record target echoes.

The bistatic range resolution is given by the following equation [65, Eqn. 11.44].

$$\Delta\rho_b = \frac{c}{2\cos(\beta/2)B} \quad (4-9)$$

where  $c$  is the speed of light,  $B$  is the radar signal's bandwidth and  $\beta$  is the bistatic angle between the LoS vector from the target to the transmitter and the LoS vector from the target to the receiver. The presence of the bistatic angle in Eqn. 4-9 means that the bistatic range resolution depends on the radar geometry at the measurement instant.

The bistatic range rate resolution is given in [66, Eqn. 7.5b] as:

$$\Delta\dot{\rho}_{b,d} = \frac{\lambda_c}{2T_{CPI}\cos(\beta/2)} \quad (4-10)$$

The equivalent Doppler resolution in hertz can be found by multiplying the range rate resolution by the absolute value of the wave number:  $\Delta f_{b,d} = |K_d| \Delta \dot{\rho}_{b,d}$

The following figure shows the evolution of the bistatic angle, range resolution and Doppler resolution during the ISS's transit.

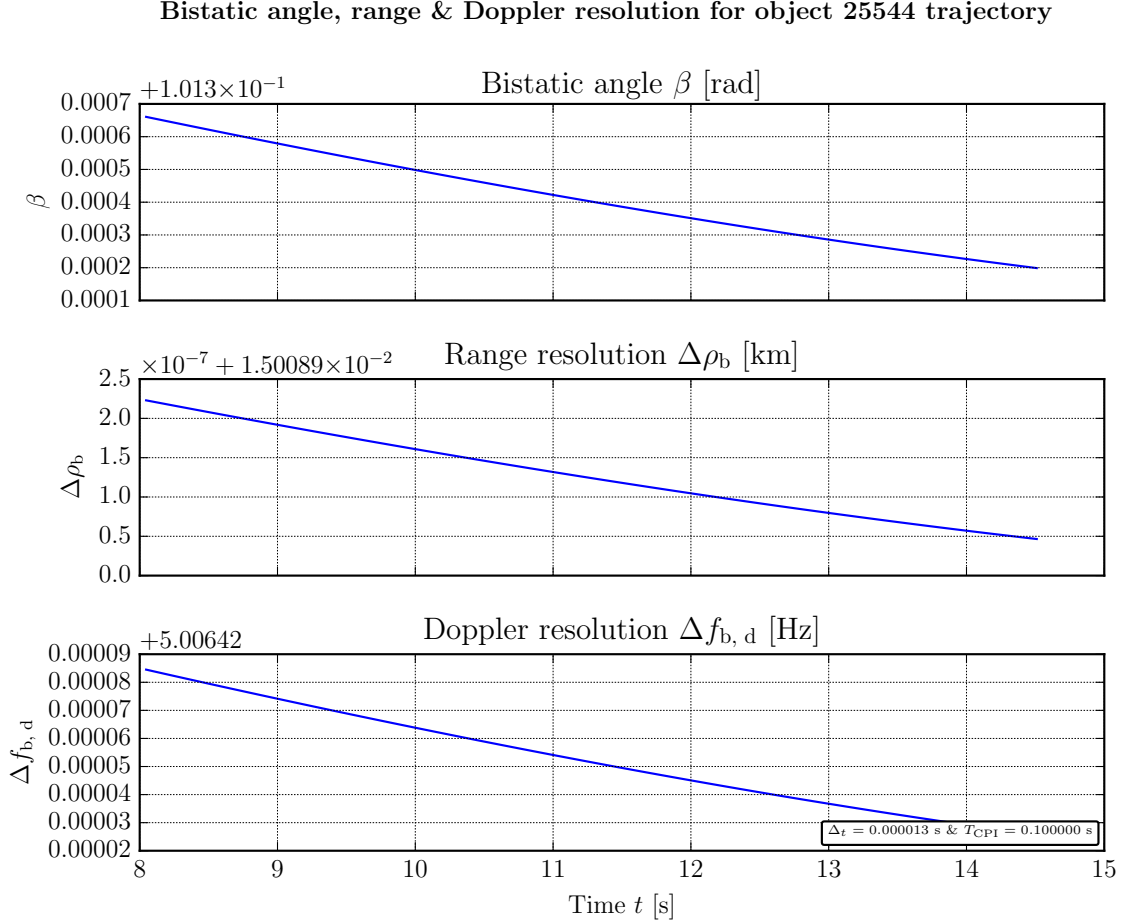


Figure 4-23: The bistatic angle, bistatic range resolution and Doppler resolution during the target's passage.

The worst range resolution is  $\Delta \rho_b = 0.0150091$  km while the worst Doppler resolution was  $\Delta f_{b,d} = 5.006508$  Hz. From the bistatic range and Doppler resolutions and coherently integrated SNR, the bistatic range and Doppler measurement errors can be calculated [63].

Bistatic range measurement error

$$\sigma_{\rho, b} = \frac{\Delta \rho_b}{\sqrt{2 \cdot \text{SNR}}} \quad (4-11)$$

Bistatic Doppler measurement error

$$\sigma_{f, b} = \frac{\Delta f_{b,d}}{\sqrt{2 \cdot \text{SNR}}} \quad (4-12)$$

Figures 4-24 and 4-25 show the resulting range and Doppler measurement errors, respectively.

Bistatic range measurement error at Rx for object 25544 during the interval 2017-09-11T10:18:36.253427Z/2017-09-11T10:18:43.279973Z

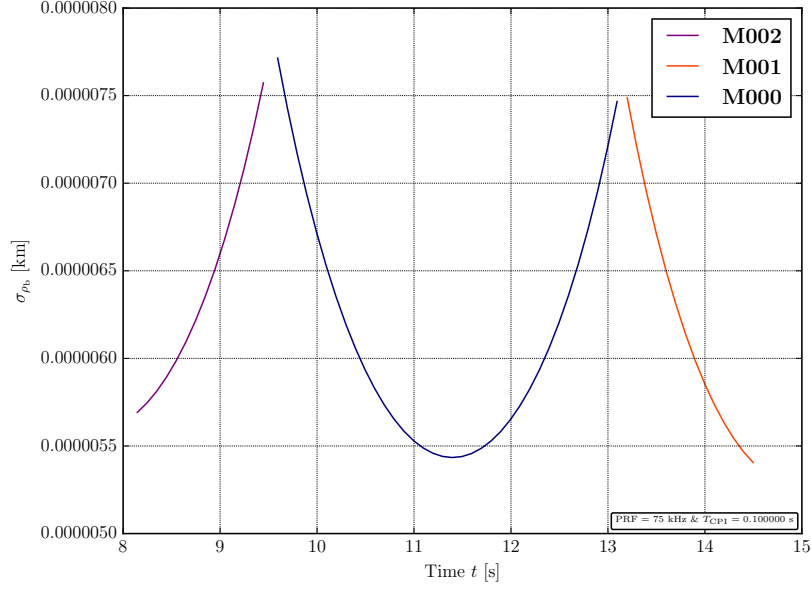


Figure 4-24: Bistatic range measurement error at each dish during the target's passage through the receiver's FoV

Bistatic Doppler measurement error at Rx for object 25544 during the interval 2017-09-11T10:18:36.253427Z/2017-09-11T10:18:43.279973Z

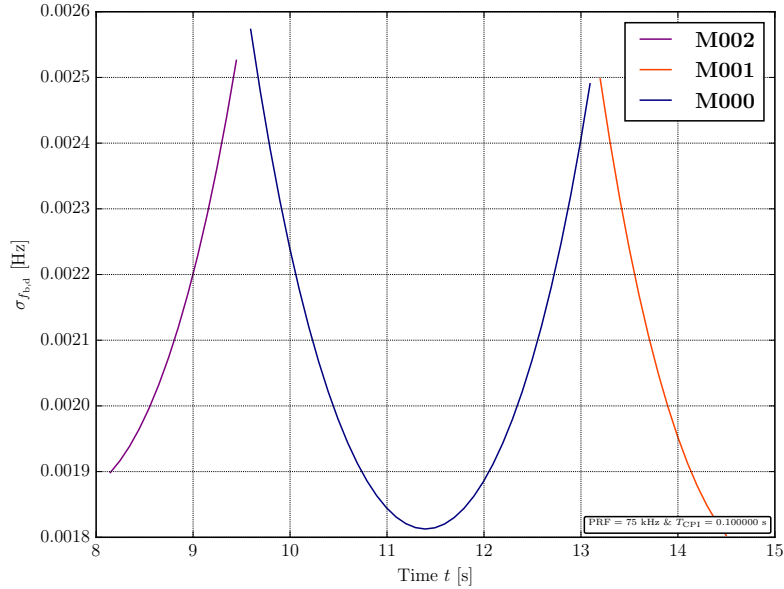


Figure 4-25: Bistatic Doppler measurement error at each dish during the target's passage through the receiver's FoV

The radar measurement errors are inversely proportional to the square root of the integrated SNR. As a consequence, the smallest measurement errors in Figure 4-24 and Figure 4-25 occur

when the signal-to-noise ratio is at its highest values in Figure 4-22, which happens when the target is close to the dishes' beam centre in Figure 4-18. Since the PRF will be different in the final MeerKAT radar system design, the integrated SNR will be lower and the measurement errors in Figure 4-24 and Figure 4-25 will be larger.<sup>5</sup>

The largest measurement error values are  $\sigma_{\rho, b} = 7.714042 \times 10^{-6}$  km for the bistatic range and  $\sigma_{f, b} = 0.00257313$  Hz for the bistatic Doppler shift measurement. It should be noted that the given measurement errors for bistatic range and Doppler shift are not realistic due to the unrealistic high PRF in the original radar design in Table 1-1. It is expected that the actual measurement errors arising in the final radar design will be much larger (at least ten times larger) since the PRF will be much lower than 75 kHz.

## 4.6 Summary

This chapter has explained in detail the process of scheduling a space object observation experiment at the MeerKAT radar with the help of the Mission Planning Tool designed during this project. To help in the discussion, an ongoing example based on observing the International Space Station (ISS) on September 10, 2017 was used. The radar sensor's parameters which influence the tasking process were calculated. Based on these parameter values, the target passage identification phase of the MPT is developed. This phase determines when the space object of interest will be observable at the MeerKAT radar. Since the radar is expected to operate in beam-park mode, that is, it is doing a beam-park experiment (BPE), the transmitter has to be tasked to point at the portion of the trajectory which ensures the longest illumination time within the Tx antenna beam. This process is detailed in the Tx tasking section, which is a component of the sensor scheduling phase in the MPT. The other component of sensor scheduling is the Rx tasking. This is detailed in the section on tasking the MeerKAT receivers. The tasking aspect is related to pointing the transmit and receive antennas at the desired location in the sky. Sensor tasking coupled with the temporal aspect of executing an observation experiment are referred to as sensor scheduling. Given that the MeerKAT radar project is still in a preliminary phase, only the first three MeerKAT receivers are considered in this project. It is shown that these three receivers are sufficient to cover the Tx-illuminated portion of the trajectory. Various visualizations are developed in the MPT to instruct radar engineers on how to run the observation experiment for a chosen scenario. The second objective of this project was given in Section 1.2 as identifying the most opportune epoch for executing an observation experiment and performing sensor tasking for the MeerKAT radar. The first section of this chapter achieves this objective.

---

<sup>5</sup> See Section 1.1.

A practical space target observation experiment differs slightly from the simulations detailed in this chapter. First, the radar measurements of bistatic range and Doppler shift were assumed to be ‘instantaneous’ or ‘ideal’ as was explained in Subsection 3.4, which differs from the real-life situation. This means that when the target transits through the Tx’s beam from 2017-09-11T10:18:36.546520Z to 2017-09-11T10:18:43.009800Z, the Tx should start emitting pulses slightly before the starting epoch and the Rx should stop recording target hits slightly after the ending epoch to compensate for the radar pulses travelling up to the target (uplink) and down from the target (downlink). Also, due to unpredicted perturbing forces acting on the RSO, its trajectory can deviate slightly from the one generated from its source TLE file. TLEs have position errors up to one kilometre at epoch, which means that the sensor scheduling done by the MPT should be expected to be slightly off. These two issues can be handled by tasking the Tx to start emitting radar pulses a few seconds earlier than predicted and tasking the Rx to stop recording data a few seconds later than predicted.

Using the results from the sensor scheduling section, the single-pulse and coherently-integrated SNR at the receivers are calculated. From the integrated SNR values, the radar measurement errors relating to bistatic range and bistatic Doppler shift are found. These radar measurement errors are vital to the tracking and orbit determination module discussed in the next chapter. The second part of this chapter achieves the third objective given in Section 1.2.

# Orbit Determination and Analysis

## 5.1 Introduction

This chapter broaches the topic of statistical orbit determination (SOD) based on measurements made by the MeerKAT radar system. Tracking space objects, being a primary aspect of Space Situational Awareness as outlined in Section 1.1, is an overarching aim of the overall MeerKAT radar project. This chapter is thus the culmination of the investigation documented in this report.

First, Section 5.2 provides an introduction to the orbit determination framework adopted in this project. Based on this discussion of the mechanics of OD, Section 5.3 explains the nature of measurement data produced by a bistatic radar. It also presents (i) a bistatic range and Doppler shift measurement scheme ( $\mathbf{y} = [\rho_b \ f_{b,d}]^T$ ) named BIRDOPP, (ii) a bistatic range, elevation and azimuth measurement scheme ( $\mathbf{y} = [\rho_b \ \theta \ \psi]^T$ ) named BIRAZEL. Tracking results are then shown and analysed. A comparison is made between the two schemes in terms of tracking accuracy in Subsection 5.3.3. Since the MeerKAT radar cannot directly measure the elevation and azimuth angles to the target, a work-around exploiting knowledge of a preliminary orbit is discussed in detail in Subsection 5.3.4. The chapter concludes with a summary in Section 5.4.

## 5.2 Orbit determination background

Orbit determination (more specifically statistical orbit determination) refers to tracking filtering applied to estimating the orbital parameters of a space object. The basic elements of tracking filtering are discussed in Appendix B according to the Gauss-Newton filtering framework from Morrison's book [61].

In short, tracking filtering has three mechanisms:

1. The target's dynamic model

The target's dynamic model is a system of nonlinear differential equations, which was presented in Subsection 3.2.3.2. The target's state vector  $\mathbf{x}(t)$  at time  $t$  follows the continuous-time differential equation (DE)

$$\dot{\mathbf{x}}(t) = \mathbf{f}(\mathbf{x}(t), t) \quad (5-1)$$

where  $\mathbf{f}(\cdot)$  is the target's dynamics function. No additive or multiplicative process noise term is included in the target dynamics model (Eqn. 5-1) in this project since the chosen filtering strategy (the Gauss-Newton filters) assumes that the target dynamics are purely deterministic in nature.

Since the target dynamic model needs to be presented as a DE, the SGP4 propagation function employed in Chapter 4 cannot be used in a tracking filter. The two body plus  $J_2$  force model in Subsection 3.2.3.2 appears as a differential equation with no forcing function and thus is chosen as target dynamic model in this chapter.

2. The sensor's measurement model

The data processing block of the radar system produces discrete-time measurements  $\mathbf{y}[k]$  which are a nonlinear function of the state vector.

$$\mathbf{y}_k = \mathbf{g}(\mathbf{x}_k, t_k) + \boldsymbol{\nu}_k \quad (5-2)$$

where  $\mathbf{g}(\cdot)$  denotes the nonlinear measurement function and  $\boldsymbol{\nu}_k$  is the radar measurement noise which is normally-distributed with zero mean and covariance  $\mathbf{R}_k$ .

3. The state estimation filter

State estimation filters aim to infer the state vector  $\mathbf{x}_k$  from measured vectors  $\mathbf{y}_{1:k}$ . There are two types of state estimation strategy: (i) recursive Bayesian estimators such as the Extended Kalman Filter (EKF) and the Unscented Kalman Filter; (ii) batch processors such as filters from the Gauss-Newton paradigm. Recursive Bayesian estimators assume that the target dynamics are stochastic in nature whereas batch processors assume that the target dynamics are purely deterministic. In other words, recursive Bayesian estimators model the state vector as a Markov process with a process noise term acting as forcing function whereas batch processing methods model the target state as a set of parameters to be estimated. Batch processors have been successfully used in a number of orbit determination applications [67] and thus are the preferred choice in this project.

The dynamical model (Eqn. 5-1) is a continuous-time function whereas the measurement model (Eqn. 5-2) is a discrete-time model. This means that the OD problem with radar measurements is a continuous-discrete filtering problem. The absence of process noise in Eqn. 5-1 implies that the target dynamics are deterministic rather than stochastic. Therefore numerical methods such as the Runge-Kutta method of order four (RK4) can be used by the GNFs built in the MPT. The Gauss-Newton filters presented in Morrison's book [61] can readily handle continuous-discrete filtering problems with deterministic dynamics. Stochastic target dynamics are specifically excluded from consideration. These should be approached with a special class of recursive Bayesian estimators which employ numerical methods suitable for solving stochastic differential equations (SDEs) such as the order 0.5 Euler-Maruyama method and the order 1.5 strong method in [59]. Continuous-discrete extended Kalman filters (CD-EKFs) in [68] and continuous-discrete cubature Kalman filters (CD-CKFs) in [59] are filters which can handle nonlinear continuous-discrete problems with stochastic target dynamics.

Tracking filtering is summarised in the following figure.

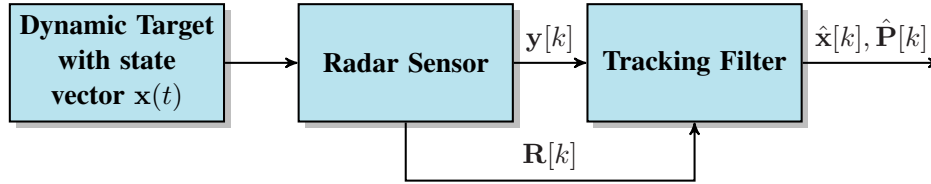


Figure 5-1: General overview of tracking filtering.

The space object is a dynamic target whose state (position and velocity) evolves according to a known dynamic model. The radar system senses the target and produces measurement vectors  $\mathbf{y}$  with an associated covariance matrix  $\mathbf{R}$ . These two quantities are loaded into the tracking filter which performs the filtering and produces a state estimate  $\hat{\mathbf{x}}$  and an associated covariance matrix  $\hat{\mathbf{P}}$ .

Given that the Gauss-Newton filter can readily handle continuous-discrete filtering problems such as the OD problem (unlike recursive filters which need significant customization) and has been successfully used in the past for OD applications, the GNF is therefore a suitable option for the tracking filter to be implemented in the MPT.

The following section discusses the nature of the measurements  $\mathbf{y}$  made by the MeerKAT radar.

## 5.3 Radar measurement schemes and results

As explained in the previous section, a generic radar sensor can create measurements of several quantities such as monostatic/bistatic range and Doppler shift and/or elevation angle and



azimuth angle from the radar receiver to the target. The [MeerKAT](#) radar, as per the current design, can only measure bistatic range and Doppler shift. This measurement scheme is presented in Subsection [5.3.1](#) and its results will be shown and analysed. However, due to the poor tracking performance, a different measurement scheme consisting of bistatic range and Doppler shift is proposed and discussed in Subsection [5.3.2](#). For both of these schemes, the true target trajectory is generated by numerically propagating the [DE](#) model in Subsection [3.2.3.2](#) with Algorithm [A.1](#). Quantities required by the measurement models such as bistatic range and elevation angles are calculated according to the definitions in Section [3.3](#).

### 5.3.1 Bistatic range and Doppler shift measurements

The [MeerKAT](#) radar design in [\[9\]](#) produces measurements consisting of bistatic range and Doppler shift. As explained in Section [3.4](#), instantaneous measurements of range and Doppler shift are used in this project for tracking purposes. Measurement vectors  $\mathbf{y}$  given in the following equation constitute the [BIRDOPP](#) scheme.

$$\mathbf{y} = \begin{bmatrix} \rho_b \\ f_{b,d} \end{bmatrix} \quad (5-3)$$

The associated measurement function  $\mathbf{g}$  and its Jacobian matrix  $\mathbf{H}$  have very complicated expressions which are shown in Appendix [C](#), more specifically, in Appendix [C.2](#).

The following figure shows the true values for bistatic range  $\rho_b$  and bistatic Doppler shift  $f_{b,d}$  during the target pass example given in Subsection [4.4.3](#) of the preceding chapter.

Bistatic range &amp; Doppler shift for object 25544 trajectory for 2017-09-11T10:18:36.546520Z/2017-09-11T10:18:43.009800Z

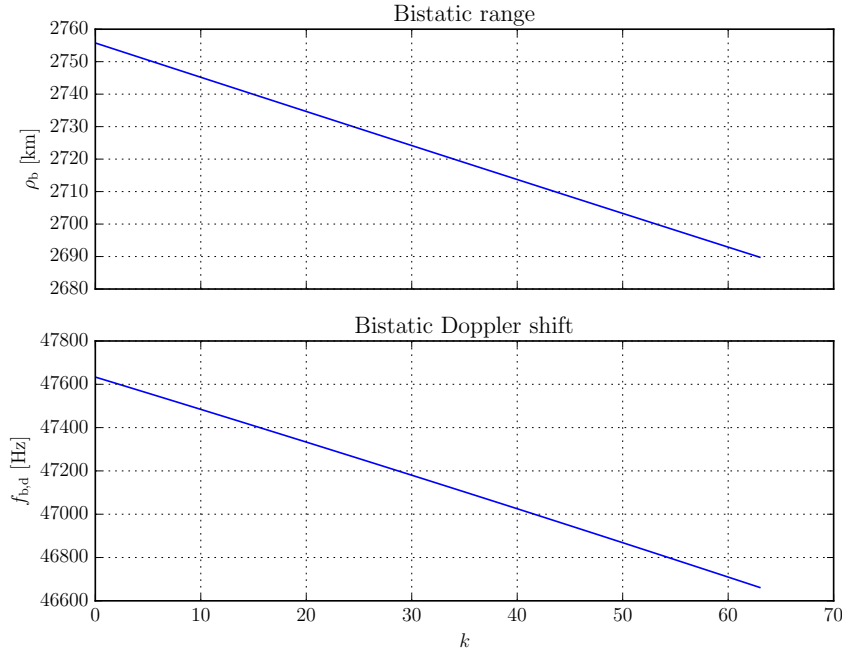


Figure 5-2: Bistatic range (top plot) and bistatic Doppler shift (bottom plot) measurements during the ISS's transit. Note that  $(t_k - t_{k+1}) = T_{\text{CPI}}$  and that there are 64 measurement vectors.

The ISS in the observation scenario in Subsection 4.4.3 spends 6.463280 s in the radar's FoV. This corresponds to 64 measurement vectors at the chosen CPI lasting 0.1 s.

### 5.3.1.1 Target motion analysis

A commonly overlooked aspect of tracking filtering is the observability criterion. This involves assessing whether the state vector of a target can be resolved from radar measurements in a particular observation scenario. The observability analysis does not depend on the radar measurement errors as can be seen in its derivation in Appendix B.4. So it can be used to analyse whether the target dynamics model<sup>1</sup> and sensor measurement model (Eqn. 5-3) can be used in tracking a particular trajectory of interest<sup>2</sup>.

The target state vector is of length  $d_x = 6$  and the BIRDOPP scheme has a measurement vector of dimension  $d_y = 2$ , implying that three time-indexed measurement vectors are needed for the observability matrix. This means that the stack length is  $L_{\min} = 3$ .

<sup>1</sup> Refer to Subsection 3.2.3.2.

<sup>2</sup> Refer to Subsection 4.4.3.

The local Kalman observability matrix  $\mathcal{O} \in \mathbb{R}^{L_{\min} d_y \times d_x}$  is given by

$$\mathcal{O}(\mathbf{x}^*) = \begin{bmatrix} \mathbf{H}(\mathbf{x}^*, t_k) \Phi(t_k, t_k; \mathbf{x}^*) \\ \mathbf{H}(\mathbf{x}^*, t_{k-1}) \Phi(t_{k-1}, t_k; \mathbf{x}^*) \\ \mathbf{H}(\mathbf{x}^*, t_{k-2}) \Phi(t_{k-2}, t_k; \mathbf{x}^*) \end{bmatrix} \quad (5-4)$$

where  $\Phi$  is the  $d_x \times d_x$  state transition matrix;  $\mathbf{x}^*$  is the state vector; and  $\mathbf{H}$  is the measurement Jacobian matrix of the measurement function  $\mathbf{g}$ . The state transition matrices, along with the trajectory, are generated by Algorithm A.1. The measurement Jacobian matrix  $\mathbf{H}$  is shown in Appendix C.2.3. The following figure plots the rank of the observability matrix over the observation interval.

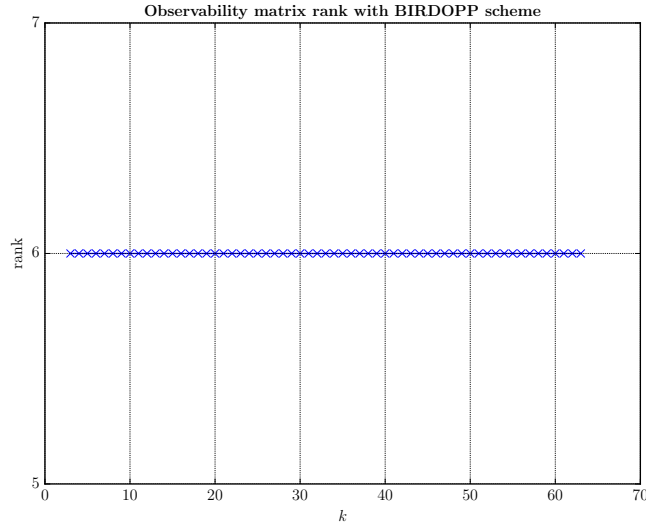


Figure 5-3: For the particular target trajectory of interest, with BIRDOPP measurements recorded by the MeerKAT radar, the observability matrix always has a rank of 6, indicating that the state can be feasibly reconstructed from the measurements.

Since the rank of the observability matrix is always equal to  $d_x$ , the length of the state vector, it can be concluded that all transmitter-target-receiver geometries occurring during the measurement interval are observable. Validating the observability of a RSO observation experiment is an important capability for the MPT. Experiments which cover unobservable trajectories result in non-unique tracking solutions. This means that the collected data cannot be used for orbit determination purposes. If a proposed experiment geometry is found to be unobservable by the MPT, then the radar engineer should cancel it.

### 5.3.1.2 Tracking Results

The preceding discussion on target motion analysis focussed on analysing transmitter-target-receiver geometries in which radar measurements are assumed to be free from measurement noise.

However, an actual radar system produces noise-corrupted measurements, as can be seen from Eqn. 5-2. These are now taken into account. The measurement covariance matrix can be set with the worst case variances found in Subsection 4.5.2.

$$\mathbf{R} = \begin{bmatrix} \sigma_{\rho, \text{b}}^2 & 0 \\ 0 & \sigma_{f, \text{b}}^2 \end{bmatrix} \quad (5-5)$$

where the bistatic range measurement error is  $\sigma_{\rho, \text{b}} = 7.714042 \times 10^{-6}$  km and the bistatic Doppler shift measurement error is  $\sigma_{f, \text{b}} = 0.00257313$  Hz. Tracking algorithms require finding the inverse of the measurement covariance matrix. The first element in Eqn. 5-5,  $\sigma_{\rho, \text{b}}^2$ , is in the order of  $10^{-11}$ , which is extremely small and leads to matrix inversion problems. A larger measurement error of  $\sigma_{\rho, \text{b}} = 1.0 \times 10^{-5}$  km was used instead to better condition the measurement covariance matrix.

#### Filter operation

The Gauss-Newton filtering paradigm is explained in Appendix B, with particular emphasis placed on the computational procedure and notation adopted in this project. Each iteration  $i$  of the Case 4 GNF processes a batch of  $L$  measurement vectors  $\mathbf{y}$ . A filtering run uses a nominal trajectory  $\mathbf{x}^*$  as input to produce an estimated state vector  $\hat{\mathbf{x}}$ . The nominal trajectory is generated by numerically propagating<sup>3</sup> an initial state vector which is known prior to running the radar observation experiment. In a real-life scenario, the initial nominal trajectory would be obtained by processing the most recent Two Line Element set of the space object of interest as described in Subsection 3.2.2 while the actual (true) trajectory would evidently be unknown. Since no real-life radar data is available for the MeerKAT radar, we opted to use the trajectory obtained from the source TLE as true trajectory and we added a perturbation vector  $\delta\mathbf{x}$  to it to obtain our nominal trajectory. This means that

$$\delta\mathbf{x} = \mathbf{x} - \mathbf{x}^* \quad (5-6)$$

The small initial perturbation vector  $\delta\mathbf{x}$  is set to

$$\delta\mathbf{x} = \begin{bmatrix} 2.904240 \times 10^{-4} \\ -4.221700 \times 10^{-4} \\ -2.618710 \times 10^{-4} \\ 4.061800 \times 10^{-5} \\ 3.270900 \times 10^{-5} \\ -1.441500 \times 10^{-5} \end{bmatrix} \quad (5-7)$$

and the initial nominal trajectory is found from Eqn. 5-6 as  $\mathbf{x}^* = \mathbf{x} - \delta\mathbf{x}$ .

---

<sup>3</sup> Using Algorithm A.1.

The tracking filter employs the Gauss-Newton optimization algorithm (GNA) to iteratively find the perturbation vector  $\delta \mathbf{x}$  which minimizes a cost function  $\mathbf{e}$  given by Eqn. B-20. This particular perturbation vector is called the estimated perturbation vector  $\delta \hat{\mathbf{x}}$ . The full estimated state vector  $\hat{\mathbf{x}}$  is then derived by addition with the nominal state vector.

$$\hat{\mathbf{x}} = \mathbf{x}^* + \delta \hat{\mathbf{x}} \quad (5-8)$$

The filter memory contains the total observation matrix  $\mathbf{T}$ , the total observation vector  $\mathbf{y}$  consisting of simulated measurement vectors  $\mathbf{y}^*$ , the total observation perturbation vector  $\delta \mathbf{y}$  and the total covariance matrix  $\mathbf{R}_y$ . The so-called  $\mathbf{T}$  matrix is calculated from the nominal trajectory's state transition matrices  $\Phi(t_k, t_0; \mathbf{x}^*)$  and the measurement Jacobian matrices  $\mathbf{H}(\mathbf{x}^*, t_k)$  evaluated on the state vectors  $\mathbf{x}^*(t_k)$  for  $k = \{0, 1, \dots, L-1\}$  (See Eqn. B-15).

The simulated measurement vectors  $\mathbf{y}^*$  arise from the nominal state vector  $\mathbf{x}^*$  in the measurement equation.

$$\mathbf{y}_k^* = \mathbf{g}(\mathbf{x}_k^*, t_k) \quad (5-9)$$

From a radar measurement  $\mathbf{y}$  and the corresponding simulated measurement vector  $\mathbf{y}^*$ , the measurement residual  $\tilde{\mathbf{y}}$ , also called the observation perturbation vector  $\delta \mathbf{y}$  in the GNF paradigm, is calculated, according to

$$\tilde{\mathbf{y}}[k] = \mathbf{y}[k] - \mathbf{y}^*[k] \quad (5-10)$$

The measurement residuals over the filter window length can be accumulated into the total observation perturbation vector  $\delta \mathbf{y} = \delta \mathbf{y}_{0:L-1} = \tilde{\mathbf{y}}_{0:L-1}$ . The simulated nominal measurement vector  $\mathbf{y}^*$  is equal to the predicted measurement vector  $\hat{\mathbf{y}}$  which would arise from the estimated state vector  $\hat{\mathbf{x}}$  after a filter iteration.

The total covariance matrix  $\mathbf{R}_y$  is found by concatenating the measurement covariance matrices at each measurement along the diagonal of a zero matrix of dimensions according to Eqn. B-17:

$$\mathbf{R}_y = \text{diag}(\mathbf{R}_k, \mathbf{R}_{k-1}, \dots, \mathbf{R}_{k-L+1})$$

The estimated error covariance matrix associated with the state vector  $\hat{\mathbf{P}}$  is the inverse of the Fisher Information Matrix (FIM) (See Eqn. B-28). The error in the estimated state vector is

$$\tilde{\mathbf{x}} = \mathbf{x} - \hat{\mathbf{x}} \quad (5-11)$$

The estimated state error cannot be calculated in the field since the true trajectory is not known. The measurement residual  $\tilde{\mathbf{y}}$  is calculated from the radar measurement vector  $\mathbf{y}$  and so can be evaluated in the field.

Iterating to convergence

To arrive at estimates which are as close as possible to the truth, the GNF has to perform iterations and at the end of each iteration  $i$ , refine the nominal trajectory  $\mathbf{x}^*$  so that it approaches the actual state vector  $\mathbf{x}$ . A maximum number of iterations  $i = 120$  is set to ensure that the fixed-point iteration process does not get stuck in an infinite loop. The measurement residuals are calculated from

$$\tilde{\mathbf{y}}_k^{(i)} = \mathbf{y}_k - \mathbf{y}_k^{*(i)} \quad (5-12)$$

The following figure shows the estimated measurement errors  $\tilde{\mathbf{y}}[k] = [\tilde{\rho}_b[k] \ \tilde{f}_{b,d}[k]]^T$  for three different filter iterations. The first row plots show the residual data points for each time step  $k$  after the first iteration. The second row plots show that the bistatic range residuals  $\tilde{\rho}_b$  have reduced by a factor of roughly 30 while Doppler shift residuals  $\tilde{f}_{b,d}$  have reduced by a factor of roughly 4.67. The last row plots show that the residuals have approximately decreased by half after another 115 iterations but appear more noisy.

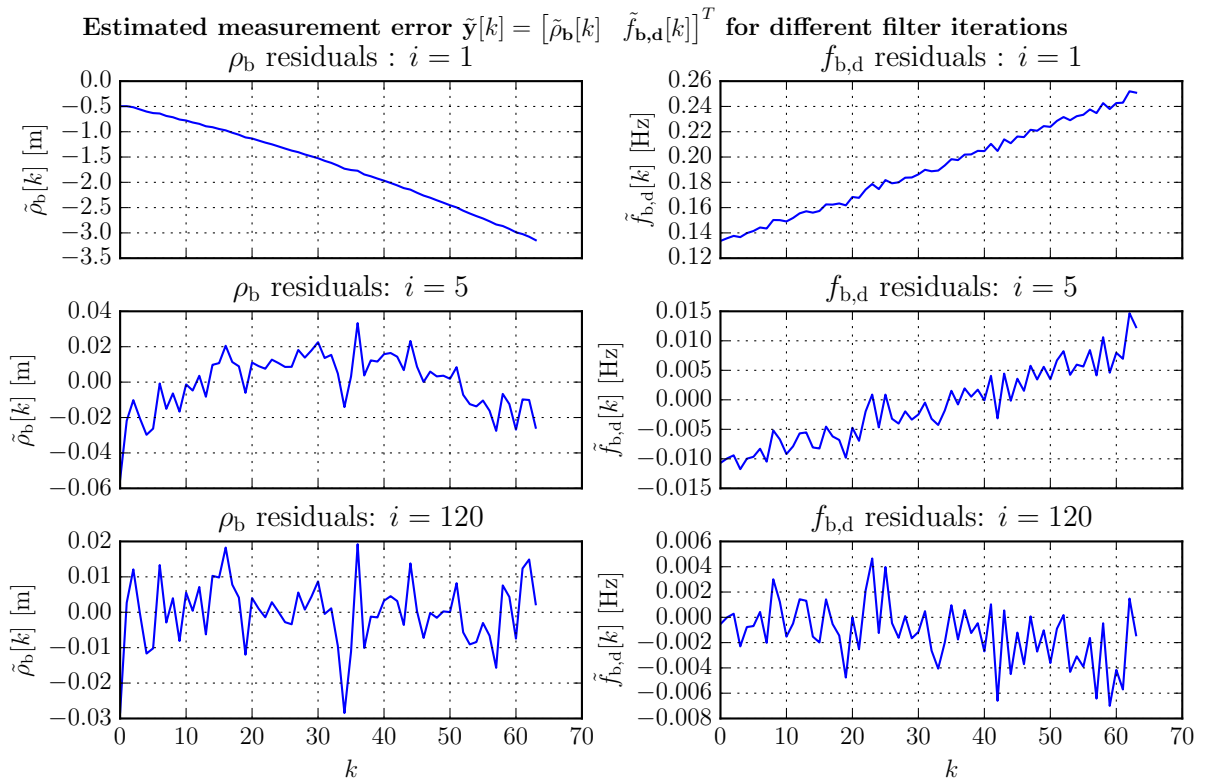


Figure 5-4: Measurement residuals  $\tilde{\mathbf{y}}$  at different iteration steps  $i$

With each iteration, the residuals lose structure and look more like noise, suggesting that the tracking filter has been successful in its operation<sup>4</sup>. Given the reduced improvement in measurement residuals in the last iteration  $i = 120$  compared to the results of the fifth iteration,

<sup>4</sup> The reasoning is that the tracking filter aims to extract the true state  $\mathbf{x}$  from a radar measurement  $\mathbf{y}$  which contains additive white Gaussian noise (see Eqn. 5-2). The residual  $\tilde{\mathbf{y}}$  in Eqn. 5-12 is exactly equal to the noise term  $\mathbf{v}$  when  $\hat{\mathbf{x}} = \mathbf{x}^* = \mathbf{x}$ .

it is deemed useful to investigate whether the maximum number of iterations in a filtering experiment can be decreased while still ensuring filter convergence.

The weighted RMS residual  $\hat{\epsilon}_{\text{WRMS}}$  is commonly used to assess filter convergence.

$$\hat{\epsilon}_{\text{WRMS}} = \left( \frac{1}{Ld_y} \sum_{k=0}^{L-1} \tilde{\mathbf{y}}_k^T \mathbf{R}_k^{-1} \tilde{\mathbf{y}}_k \right)^{1/2} \quad (5-13)$$

The following figure plots the weighted RMS measurement residuals over 120 iteration steps.

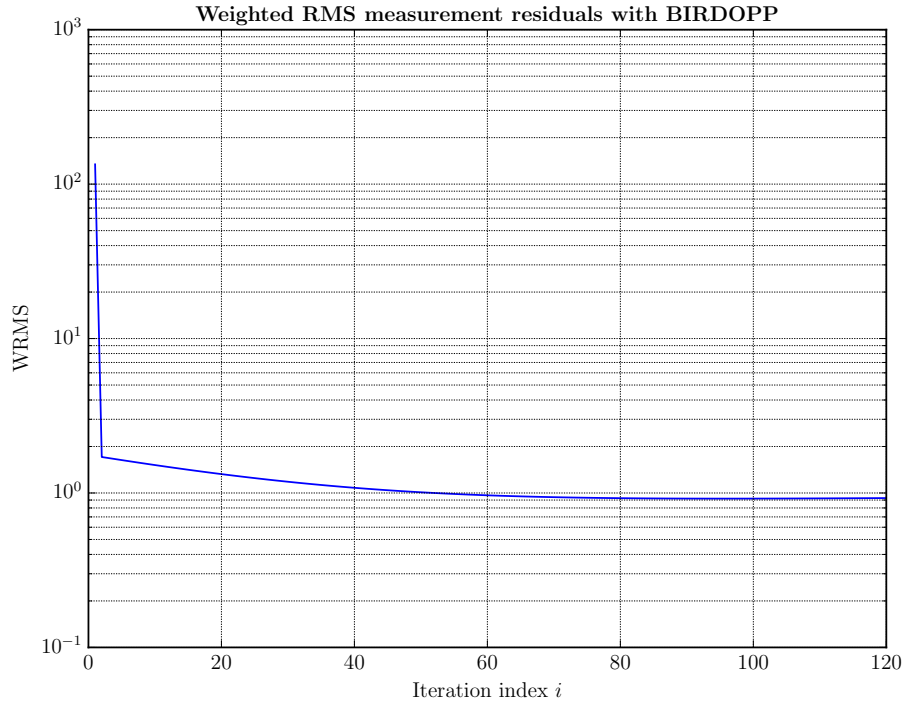


Figure 5-5: Weighted RMS measurement residuals  $\hat{\epsilon}_{\text{WRMS}}$  at different iteration steps  $i$  for the BIRDOPP scheme

The WRMS in Figure 5-5 plateaus out after approximately 80 iterations. Since the iteration investigation was carried out on only one realization of the stochastic radar measurements, it is called a single-shot test. Single-shot tests [61] can be run in the field with experimental data, but their successful results on stochastic data do not constitute a full proof of correct performance. If the iteration investigation is run again, that is, a different realization of the radar measurements  $\mathbf{y}$  in Eqn. 5-2, it is possible that more than 80 iterations may be required before the WRMS levels out. So the maximum number of filter iterations is kept at 120 for the remaining experiments. The tracking filter branches out of the iteration loop when the WRMS stays unchanged or increases after an iteration. This is called the stopping condition.

#### Monte Carlo runs

Monte Carlo simulations have to be run in tracking problems to average out the stochastic

nature of the radar measurements. One hundred Monte Carlo runs ( $N_{MC} = 100$ ) were performed over the full batch ( $L = 64$  points) of radar measurements. The following figure compares the state estimates  $\hat{\mathbf{x}} = [\hat{x} \ \hat{y} \ \hat{z} \ \hat{\dot{x}} \ \hat{\dot{y}} \ \hat{\dot{z}}]^T$  with the true state vector at epoch.

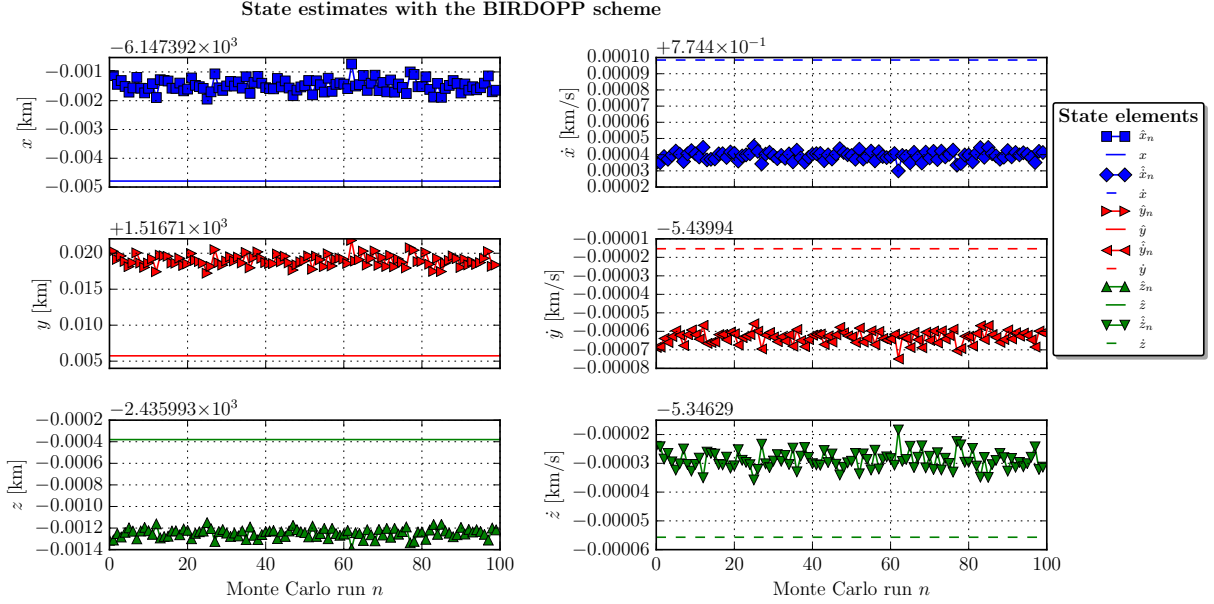


Figure 5-6: State estimates  $\hat{\mathbf{x}}$  output by a Case 4 GNF filter with the BIRDOPP measurement scheme. The actual (true) states from  $\mathbf{x}$  are represented by the horizontal lines in the sub-plots.

Figure 5-6 shows that, with measurement vectors in the BIRDOPP scheme, the tracking filter did not produce a single estimated state over one hundred Monte Carlo runs which was almost exactly the same as the underlying true state value. It is clear that the mean error in the state estimates will be non-zero. This suggests that the filter produces biased estimates.

The number of Monte Carlo runs was increased to a thousand and the BIRDOPP tracking simulation was re-run. Various performance metrics were computed.

### RMSE

The RMS error in the filter estimates was averaged over a thousand Monte Carlo runs ( $N_{MC} = 1000$ ) and normalized by the dimensionality of the target's position and velocity vectors. These two vectors are constructed from the full state vector  $\mathbf{x}$  as  $\mathbf{x}_{1:3}$  and  $\mathbf{x}_{4:6}$  respectively. The ANRMSE for the three position states was thus calculated as

$$\text{ANRMSE} = \left( \frac{1}{3N_{MC}} \sum_{n=1}^{N_{MC}} (\tilde{\mathbf{x}}_{1:3}^n)^2 \right)^{1/2} \quad (5-14)$$

The ANRMSE for the three velocity states is calculated in a similar way, except that the velocity components  $\tilde{\mathbf{x}}_{4:6}$  of the estimation error  $\tilde{\mathbf{x}}$  are used instead. Figure 5-7 shows the



average normalized RMS error in the position and velocity estimation errors over 1000 Monte Carlo runs. The [ANRMSE](#) plots show that the errors generally decrease as the number of data points  $k$  loaded in the filter stack increases. The reduction in estimation error as the amount of data available increases is a consequence of the Law of Large Numbers.

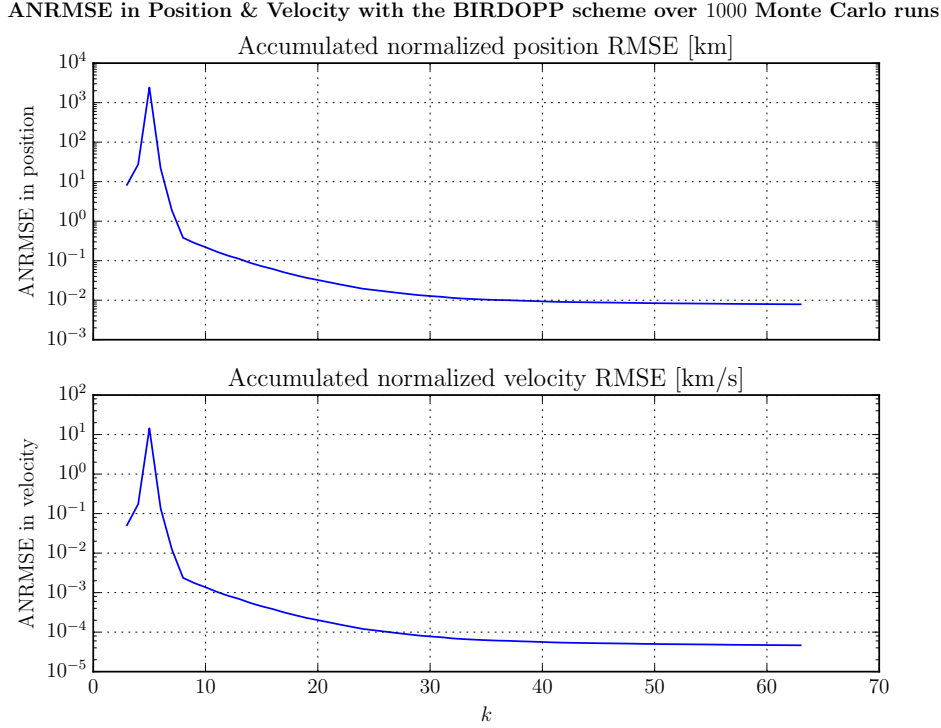


Figure 5-7: [ANRMSE](#) in position and velocity states with the [BIRDOPP](#) scheme over 1000 Monte Carlo runs

The [ANRMSE](#) in the position and velocity states tend asymptotically to constant, non-zero values. This means that the [BIRDOPP](#) Gauss-Newton filter is not MSE consistent. MSE consistency is explained in [69]. It is very likely that the tracking filter is biased.

### 3 $\sigma$ ECM test

The  $3\sigma$  [error covariance matrix](#) consistency test described in [61] is a single-shot test which checks if the covariance matrix ( $\hat{\mathbf{P}}$ ) output by a tracking filter is consistent with the errors  $\tilde{\mathbf{x}}$  in the state estimates. Realizations of a zero-mean multivariate Gaussian distribution should lie within  $\pm 3$  standard deviations approximately 99.73% of the time. This test effectively verifies if the elements of the supposed zero-mean estimated error  $\tilde{\mathbf{x}}$  lie inside their respective  $\pm 3\sigma$  most of the time. The  $3\sigma$  [ECM](#) test follows the following procedure [61].

1. Find the square root of the diagonal elements of  $\hat{\mathbf{P}}$ ,  $[\sqrt{\hat{\mathbf{P}}_{1,1}} \quad \cdots \quad \sqrt{\hat{\mathbf{P}}_{d_x, d_x}}]^T$
2. Multiply these elements by 3 to find the  $3\sigma$  bounds,  $[3\sqrt{\hat{\mathbf{P}}_{1,1}} \quad \cdots \quad 3\sqrt{\hat{\mathbf{P}}_{d_x, d_x}}]^T$

3. Compute the estimated error vector  $\tilde{\mathbf{x}}$  as in Eqn. 5-11
4. If the absolute value of the elements in the estimated error vector are less than  $3\sigma$ , then the filter has passed the 3-sigma ECM-consistency test at the instant at which the test was run. If  $|\tilde{\mathbf{x}}_d| < 3\sqrt{\hat{\mathbf{P}}_{d,d}}$  for  $d = \{1, 2, \dots, d_x\}$ , the  $3\sigma$ -consistency test passes.

Figure 5-8 shows the single-shot  $3\sigma$  - ECM test results with the BIRDOPP scheme.

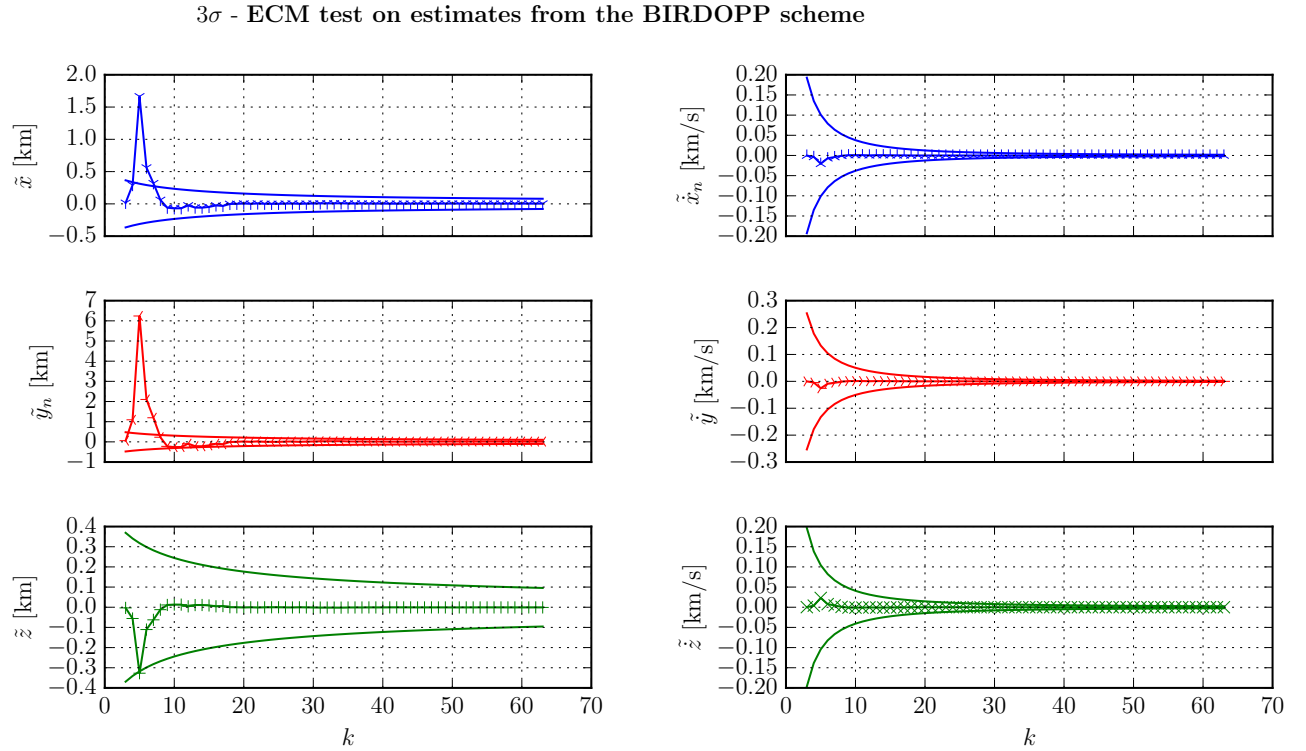


Figure 5-8:  $3\sigma$ -ECM test results on estimates produced with the BIRDOPP measurement scheme. The markers denote the relevant element of  $\tilde{\mathbf{x}}$  at all radar measurement instants. The funnel-shaped curves indicate the  $\pm 3\sigma$  bounds for each state element.

The figure above shows that the magnitude of the elements of the estimated error vector  $\tilde{\mathbf{x}}$  decrease as the number  $k$  of data points available increases. The  $\pm 3\sigma$  bounds also decrease when more data becomes available to the filter. All estimated error elements lie within their respective  $\pm 3\sigma$  bounds after roughly the tenth data point. Between the first and tenth data point, the estimation errors for two position variables  $x$  and  $y$  sometimes exceed their bounds, indicating that the tracking filter was  $3\sigma$  ECM-inconsistent. As stated previously, occasional failure of the  $3\sigma$ -ECM test is expected since the supposed zero-mean random error  $\tilde{\mathbf{x}}$  is supposed to lie within these bounds approximately 99.73% of the time, not precisely 100% of the time.

The  $3\sigma$  covariance matrix test can also be done on the measurement residual  $\tilde{\mathbf{y}}$ . The measurement noise  $\nu$  in Eqn. 5-2 is normally-distributed with zero mean and covariance  $\mathbf{R}$ . The measurement

residual  $\tilde{\mathbf{y}}$  in Eqn. 5-12 is exactly equal to the noise term  $\boldsymbol{\nu}$  when  $\hat{\mathbf{x}} = \mathbf{x}^* = \mathbf{x}$ , that is, when the filter produces an estimate  $\hat{\mathbf{x}}$  which matches exactly the true state  $\mathbf{x}$ . So the residual  $\tilde{\mathbf{y}}$  should follow the same distribution as the measurement noise  $\boldsymbol{\nu}$ : it should also be zero-mean and have a covariance matrix  $\mathbf{R}$  given in Eqn. 5-5. The  $3\sigma$  bounds of the measurement covariance matrix  $\mathbf{R}$  in Eqn. 5-5 are 0.000030 km and 0.007719 Hz. The final measurement residuals at  $i = 120$  in Figure 5-4 (bottom plots) have maximum absolute values of 0.000028 km and 0.007003 Hz which lie within the expected  $\pm 3\sigma$  bounds.

#### Covariance consistency with the Normalized Estimation Error Squared (NEES)

The  $3\sigma$  ECM consistency test discussed previously only considered diagonal elements of the estimated ECM,  $[\sqrt{\hat{\mathbf{P}}_{1,1}} \ \cdots \ \sqrt{\hat{\mathbf{P}}_{d_x, d_x}}]^T$ . The covariance consistency check with the Normalized Estimation Error Squared test considers the entire estimated ECM. Multiple definitions of the NEES exist. The definition used in this report is drawn from [69] and [70]. According to [70], the term “ANEES” is preferred since we can only calculate an average NEES over a finite number  $N_{MC}$  of Monte Carlo runs. The Average Normalized Estimation Error Squared is calculated as in [69, Eqn. 60]

$$ANEES = \frac{1}{d_x N_{MC}} \sum_{n=1}^{N_{MC}} \tilde{\mathbf{x}}_n^T \hat{\mathbf{P}}_n^{-1} \tilde{\mathbf{x}}_n \quad (5-15)$$

The rationale behind the covariance consistency check with the ANEES is that, since the  $d_x$ -dimensional estimate error  $\tilde{\mathbf{x}}$  is supposed to be Gaussian distributed<sup>5</sup>, the ANEES calculated from the estimate error and its corresponding estimated covariance  $\hat{\mathbf{P}}$ , over  $N_{MC}$  Monte Carlo runs, should follow a chi-square distribution with  $d_x N_{MC}$  degrees of freedom. Then the ANEES would tend toward one with increasing number of Monte Carlo runs.

However, the estimation error is only approximately Gaussian-distributed in target tracking scenarios and so the finite-sample ANEES will not evaluate to exactly one with a large number of Monte Carlo runs (e.g. 1000). The ANEES should nevertheless pass a chi-square test with a suitable confidence region. [69] For  $d_x = 6$  and  $N_{MC} = 1000$ , the lower and upper bound for a 99% confidence region are 0.9580178 and 1.042963 respectively.<sup>6</sup>

Figure 5-9 shows the ANEES for estimates with the BIRDOPP scheme averaged over a thousand Monte Carlo runs.

<sup>5</sup> Due to the Gaussian-distributed measurement noise.

<sup>6</sup> These were evaluated numerically in Python by making use of the `scipy.stats` package.

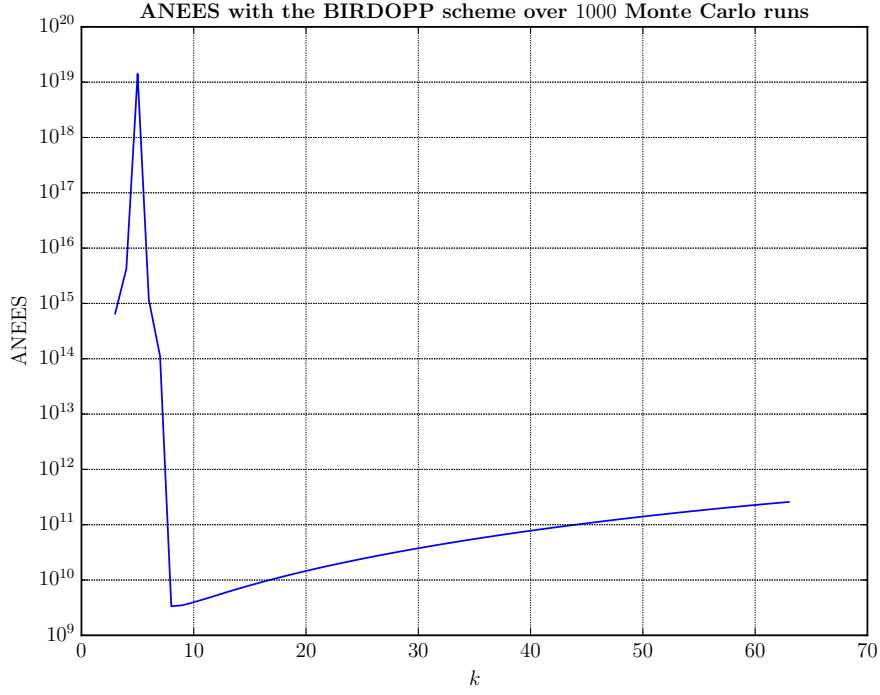


Figure 5-9: ANEES for estimates with the BIRDOPP scheme over  $N_{MC} = 1000$  Monte Carlo runs

It is seen that the ANEES plot always exceeds  $10^9$ , which indicates it never passes the chi-square test. This means that the tracker produces inconsistent ECMs when it processes bistatic range and Doppler shift measurements.

#### Existence of bias errors

The following three observations strongly indicate that the estimate error  $\tilde{\mathbf{x}}$  is biased:

1. No estimated state element was averaging out close to its true value over a hundred Monte Carlo runs in Figure 5-6.
2. The ANRMSE in the position and velocity states tended asymptotically to constant, non-zero values in Figure 5-7.
3. The ANEES consistency test in Figure 5-9 failed catastrophically.

#### Summary of tracking results with the BIRDOPP scheme

Table 5-1 compares the actual state vector elements at epoch with the tracking filter's mean

(expected) estimated states. We calculate the expectation of the estimate error as

$$\mathbb{E}\{\mathbf{x} - \hat{\mathbf{x}}\} = \mathbb{E}\{\tilde{\mathbf{x}}\} = \begin{bmatrix} 3.323018 \times 10^{-3} \\ 1.325548 \times 10^{-2} \\ -8.663845 \times 10^{-4} \\ -5.916461 \times 10^{-5} \\ -4.796370 \times 10^{-5} \\ 2.667420 \times 10^{-5} \end{bmatrix} \quad (5-16)$$

The expectation of the associated error covariance matrix is calculated in a similar way.

The expectation of the estimated target state vector  $\hat{\mathbf{x}}$ , of the corresponding estimated covariance matrix  $\mathbf{ECM}$  and of the estimate error  $\tilde{\mathbf{x}}$  over 1000 Monte Carlo runs are shown in the table below. All values are given to six decimal places, except for variance where they are given to sixteen decimal places.

Table 5-1: Tracking the **ISS** based on **BIRDOPP** measurements with a small initial perturbation vector  $\delta\mathbf{x}$ .

Position	Actual value [km]	Nominal value [km]	Perturbation [km]	Estimate [km]	Variance [km <sup>2</sup> ]	Error [km]
$x$	-6147.396792	-6147.397083	0.000290	-6147.393469	0.000000004169	-0.003323
$y$	1516.715741	1516.716163	-0.000422	1516.728996	0.000000058215	-0.013255
$z$	-2435.993380	-2435.993118	-0.000262	-2435.994247	0.000000000167	0.000866
Velocity	Actual value [km/s]	Nominal value [km/s]	Perturbation [km/s]	Estimate [km/s]	Variance [(km/s) <sup>2</sup> ]	Error [km/s]
$\dot{x}$	0.774498	0.774458	0.000041	0.774439	0.000000000001	0.000059
$\dot{y}$	-5.439955	-5.439988	0.000033	-5.440003	0.000000000001	0.000048
$\dot{z}$	-5.346346	-5.346331	-0.000014	-5.346319	0.000000000001	-0.000027

In the above table, the ‘Actual value’ column contains the true values of the elements of the state vector  $\mathbf{x}$ ; the ‘Nominal value’ column contains the elements of the assumed nominal vector  $\mathbf{x}^*$  which arise from Eqn. 5-6 with the small perturbation vector given in Eqn. 5-7; the ‘Perturbation’ column lists the elements of the perturbation vector  $\delta\mathbf{x}$  which relates to the nominal vector according to Eqn. 5-6; the entries in the ‘Estimate’ column are the elements of the average estimated state vector  $\hat{\mathbf{x}}$ ; the ‘Variance’ column contains the diagonal elements of the  $\mathbf{ECM}$  averaged over a thousand Monte Carlo runs and; finally, the ‘Error’ column contains the sample mean values of the estimate error  $\tilde{\mathbf{x}}$  which were shown in Eqn. 5-16. Comparing the elements of the initial nominal vector in the third column with the elements of the estimate error  $\tilde{\mathbf{x}}$  in the last column<sup>7</sup>, we see that the discrepancy between the true target state  $\mathbf{x}$  and the state known by the tracking filter has grown after the radar measurements have been processed. This means that the radar measurements acquired by the **MeerKAT** radar have not led to an improvement in the accuracy of the known state vector  $\mathbf{x}^*$ .

<sup>7</sup> also shown in Eqn. 5-16.

### 5.3.2 Bistatic range and look angles measurements

The previous subsection discussed the [BIRDOPP](#) scheme which consisted of measurements of bistatic range and Doppler shift. It was seen that, even though the [BIRDOPP](#) tracker produced very accurate estimates, its performance was problematic. The results were biased and the estimated error covariance matrices were not trustworthy since the [ANEES](#) grew worryingly large in Figure 5-9. As noted previously, the [ECM](#) is vital in conjunction analysis. A measurement scheme comprising of bistatic range  $\rho_b$  and elevation  $\theta_{Rx}$  and azimuth angle  $\psi_{Rx}$  to the [Rx](#) is investigated to see if the corresponding tracker is covariance consistent. This scheme is called the [BIRAZEL](#) measurement scheme and is given by

$$\mathbf{y} = \begin{bmatrix} \rho_b \\ \theta_{Rx} \\ \psi_{Rx} \end{bmatrix} \quad (5-17)$$

The measurement function  $\mathbf{g}$  corresponding to this measurement scheme as well as its Jacobian matrix  $\mathbf{H}$  are shown in Appendix C.2.4. We will later on show how to create measurements of elevation and azimuth angle in Subsection 5.3.4 using the process called ‘Observables Estimation’ in [47].

The following figure shows the true values for bistatic range  $\rho_b$ , elevation angle  $\theta_{Rx}$  and azimuth angle  $\psi_{Rx}$  at the receiver during the target pass example from the previous chapter.

Bistatic range, elevation & azimuth angles for object 25544 trajectory for 2017-09-11T10:18:36.546520Z/2017-09-11T10:18:43.009800Z

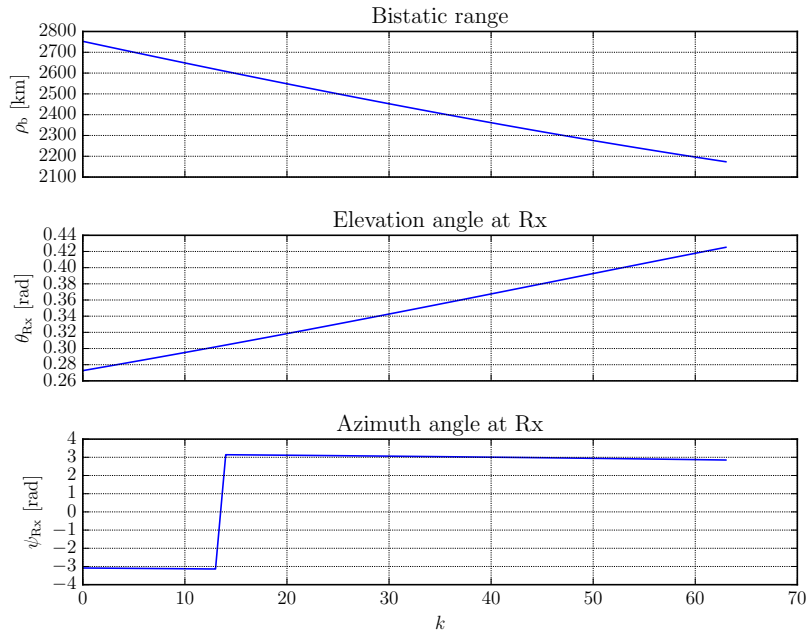


Figure 5-10: Bistatic range (top plot), elevation angle at [Rx](#) (middle plot) and azimuth angle at [Rx](#) (bottom plot) measurements during the [ISS](#)'s transit.

The azimuth angle  $\psi_{\text{Rx}}$  changes from  $-\pi$  to  $\pi$  as the target moves from the fourth to the first quadrant in the azimuth plane. The azimuth angle residual in the measurement residual vector  $\tilde{\mathbf{y}}$  defined in Eqn. 5-10 as the difference between two angles<sup>8</sup> in the horizontal plane can only take values in the range of  $-\pi$  to  $\pi$  and so it must be wrapped with mirroring into this circular region in the tracking filter as explained in [71]. GNFs in the orbit determination module of the MPT feature this wrapping function.

### 5.3.2.1 Target Motion Analysis

We now investigate whether the target state is observable from BIRAZEL measurements as was done for the BIRDOPP measurement scheme in Subsection 5.3.1.1

The target state vector is of length  $d_x = 6$  and the BIRAZEL scheme has a measurement vector of dimension  $d_y = 3$ , implying that two time-indexed measurement vectors are needed for the observability matrix. This means that the stack length is  $L_{\min} = 2$ .

The local Kalman observability matrix  $\mathcal{O} \in \mathbb{R}^{L_{\min} d_y \times d_x}$  is given by

$$\mathcal{O}(\mathbf{x}^*) = \begin{bmatrix} \mathbf{H}(\mathbf{x}^*, t_k) \Phi(t_k, t_k; \mathbf{x}^*) \\ \mathbf{H}(\mathbf{x}^*, t_{k-1}) \Phi(t_{k-1}, t_k; \mathbf{x}^*) \end{bmatrix} \quad (5-18)$$

where  $\Phi$  is the  $d_x \times d_x$  state transition matrix;  $\mathbf{x}^*$  is the state vector; and  $\mathbf{H}$  is the measurement Jacobian matrix of the measurement function  $\mathbf{g}$ . The state transition matrices, along with the trajectory, are generated by Algorithm A.1. The measurement Jacobian matrix  $\mathbf{H}$  is shown in Eqn. C-54. The following figure plots the rank of the observability matrix over the observation interval.

---

<sup>8</sup> These two are the measured azimuth angle and the azimuth angle from the simulated measurement vector  $\mathbf{y}^*$ .

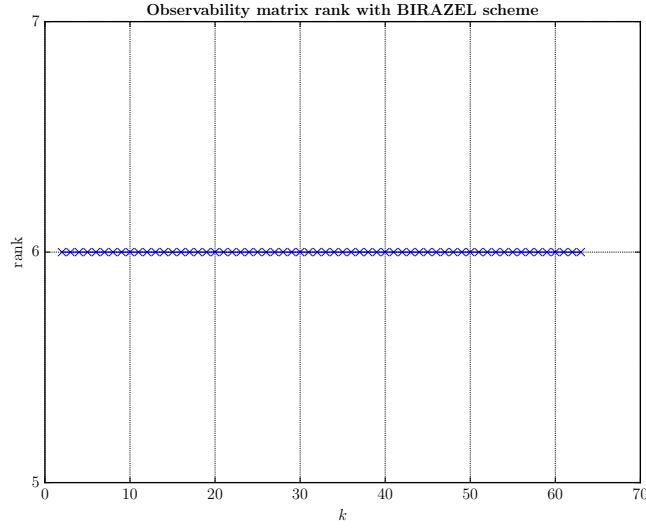


Figure 5-11: For the particular target trajectory of interest, with **BIRAZEL** measurements recorded by the **MeerKAT** radar, the observability matrix always has a rank of 6, indicating that the state can be feasibly reconstructed from the measurements.

### 5.3.2.2 Tracking Results

The **BIRAZEL** scheme's measurement covariance matrix is set as

$$\mathbf{R} = \begin{bmatrix} \sigma_{\rho, \text{b}}^2 & 0 & 0 \\ 0 & \sigma_{\theta_{\text{Rx}}}^2 & 0 \\ 0 & 0 & \sigma_{\psi_{\text{Rx}}}^2 \end{bmatrix} \quad (5-19)$$

where the bistatic range measurement error is  $\sigma_{\rho, \text{b}} = 1.0 \times 10^{-5}$  km similar to Subsection 5.3.1.2 and the elevation and azimuth measurement errors are  $\sigma_{\theta_{\text{Rx}}}$  and  $\sigma_{\psi_{\text{Rx}}}$  respectively. The standard deviations for the elevation and azimuth angle measurements are both set to  $0.04^\circ$ . This choice is justified in Subsection 5.3.4.



### Monte Carlo runs

One hundred Monte Carlo simulations were done over the full measurement set of 64 data points. The initial perturbation vector used was the one in Eqn. 5-7. The following figure compares the state estimates  $\hat{\mathbf{x}} = [\hat{x} \ \hat{y} \ \hat{z} \ \hat{\dot{x}} \ \hat{\dot{y}} \ \hat{\dot{z}}]^T$  with the true state vector at epoch.

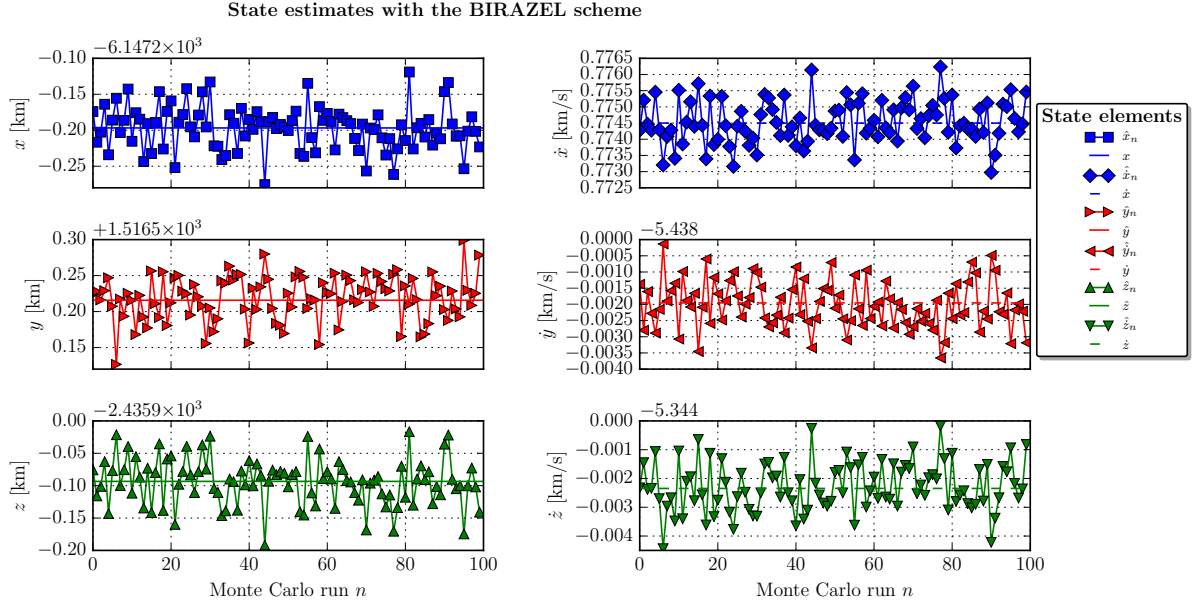


Figure 5-12: State estimates  $\hat{\mathbf{x}}$  output by a Case 4 **GNF** filter with the **BIRAZEL** measurement scheme. The actual (true) states from  $\mathbf{x}$  are represented by the horizontal lines in the sub-plots.

Figure 5-12 shows that, with measurement vectors in the **BIRAZEL** scheme, the tracking filter produced estimated state vectors whose average appears to be very close to the underlying true state value. This is in stark contrast to the biased estimates which are obtained with the **BIRDOPP** scheme in Figure 5-6.

The number of Monte Carlo runs was increased to a thousand and the **BIRAZEL** tracking simulation was re-run. Various performance metrics were computed.

### RMSE

The RMS error in the filter estimates was averaged over a thousand Monte Carlo runs ( $N_{MC} = 1000$ ) and normalized by the dimensionality of the target's position and velocity vectors as before.

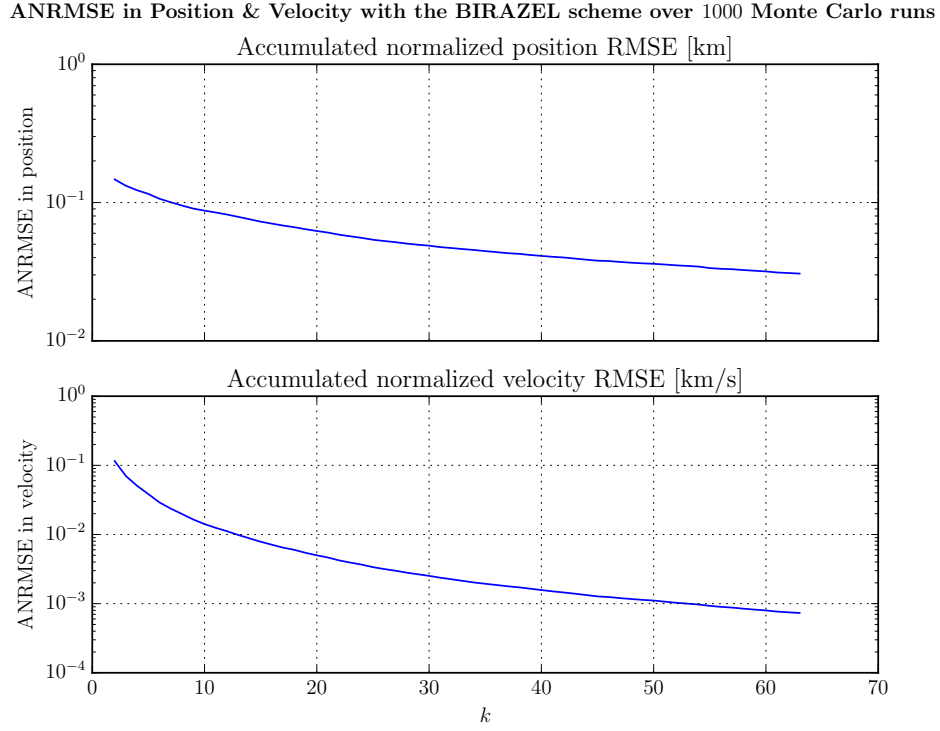


Figure 5-13: ANRMSE in position and velocity states with the BIRAZEL scheme over  $N_{MC} = 1000$ .

The ANRMSE in the position and velocity states decrease steadily as the number of data points available to the filter increases. The ANRMSE plots do not plateau out at any point  $k$ , indicating that it is unlikely that the BIRAZEL Gauss-Newton filter is biased.

### 3 $\sigma$ ECM test

The single-shot  $3\sigma$  error covariance matrix consistency test is done to see if the covariance matrix ( $\hat{\mathbf{P}}$ ) output by the tracker is consistent with the the errors  $\tilde{\mathbf{x}}$  in the state estimates.

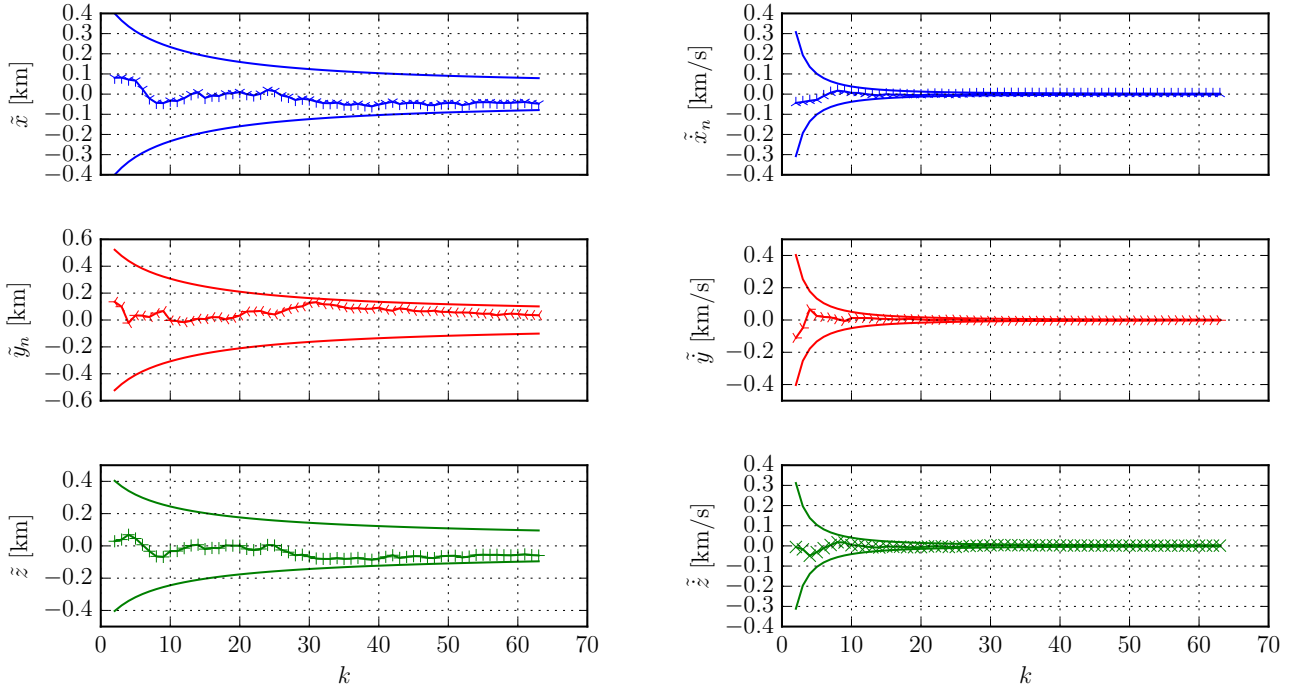
3 $\sigma$  - ECM test on estimates from the BIRAZEL scheme


Figure 5-14: 3 $\sigma$ -ECM test results on estimates produced with the BIRAZEL measurement scheme. The markers denote the relevant element of  $\tilde{\mathbf{x}}$  at all radar measurement instants. The funnel-shaped curves indicate the  $\pm 3\sigma$  bounds for each state element.

The figure above shows that the magnitude of the elements of the estimated error vector  $\tilde{\mathbf{x}}$  decrease as the number  $k$  of data points available increases. The  $\pm 3\sigma$  bounds also decrease when more data becomes available to the filter. All estimated error elements always lie within their respective  $\pm 3\sigma$  bounds. The tracker was always 3 $\sigma$  ECM-consistent during the span of the tracking experiment.

#### Covariance consistency with the NEES

The ANEES test verifies if the estimated covariance matrix is consistent with the estimated state vector. For a target state of dimensionality  $d_x = 6$  and for  $N_{MC} = 1000$  Monte Carlo runs, the lower and upper bound for a 99% confidence region for the chi-square test are 0.9580178 and 1.042963 respectively.

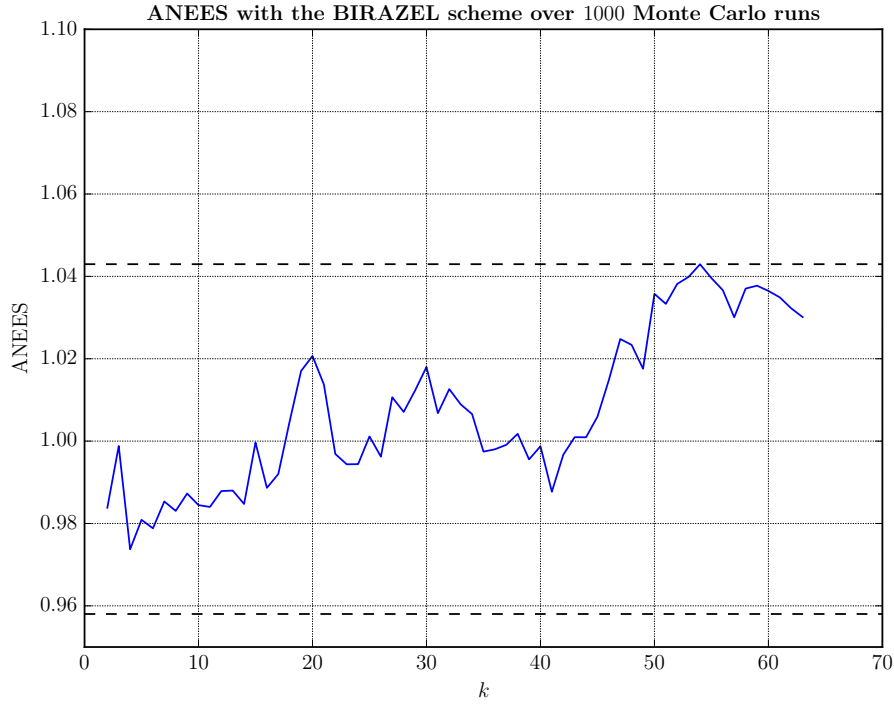


Figure 5-15:  $ANEES$  for estimates with the  $BIRAZEL$  scheme over  $N_{MC} = 1000$  Monte Carlo runs. The two horizontal dashed lines at  $ANEES = 0.9580178$  and  $ANEES = 1.042963$  represent the lower and upper bound for the 99% confidence region for the chi-square test.

It is clear from Figure 5-15 that the  $ANEES$  always lies within the bounds for the 99% confidence region. This means that the covariance consistency test always passes with the  $BIRAZEL$  scheme.

#### Summary of tracking results with the $BIRAZEL$ scheme

Table 5-1 compares the actual state vector elements at epoch with the tracking filter's mean (expected) estimated states. We calculate the expectation of the estimate error as

$$\mathbb{E}\{\tilde{\mathbf{x}}\} = \begin{bmatrix} 2.021448 \times 10^{-4} \\ 2.862048 \times 10^{-4} \\ 2.472989 \times 10^{-4} \\ 1.007452 \times 10^{-7} \\ 1.246021 \times 10^{-7} \\ 1.492543 \times 10^{-7} \end{bmatrix} \quad (5-20)$$

The expectation of the associated error covariance matrix is calculated in a similar way.

The expectation of the estimated target state vector  $\hat{\mathbf{x}}$ , of the corresponding estimated covariance matrix  $ECM$  and of the estimate error  $\tilde{\mathbf{x}}$  over 1000 Monte Carlo runs are shown in the table below. All values are given to six decimal places, except for variance where they are given to sixteen decimal places.

Table 5-2: Tracking the ISS based on BIRAZEL measurements with a small initial perturbation vector  $\delta \mathbf{x}$ .

Position	Actual value [km]	Nominal value [km]	Perturbation [km]	Estimate [km]	Variance [km <sup>2</sup> ]	Error [km]
$x$	-6147.396792	-6147.397083	0.000290	-6147.396995	0.0001917650603003	0.000202
$y$	1516.715741	1516.716163	-0.000422	1516.396995	0.0003269335854790	0.000286
$z$	-2435.993380	-2435.993628	-0.000262	-2435.993447	0.0002653123666930	0.000247
Velocity	Actual value [km/s]	Nominal value [km/s]	Perturbation [km/s]	Estimate [km/s]	Variance [(km/s) <sup>2</sup> ]	Error [km/s]
$\dot{x}$	0.774498	0.774498	0.000041	0.774505	0.0000001025960444	0.000000
$\dot{y}$	-5.439955	-5.439955	0.000033	-5.439953	0.0000001727778030	0.000000
$\dot{z}$	-5.346346	-5.346346	-0.000014	-5.346332	0.0000001707422180	0.000000

The column headings in this table are the same as those in the corresponding Table 5-1 for the BIRDOPP scheme. The estimation errors in Table 5-2 are smaller than the perturbation vector added to the initial trajectory, indicating that the tracking filter is improving the accuracy of the orbit track. It is clear that the target state estimates produced by the BIRAZEL filter is more accurate than the corresponding results with the BIRDOPP scheme.

The estimation errors are not significantly smaller than the initial perturbation vector because of the small quantity of data points made available by the radar system. If more data points were made available, for example more than 150, the estimation errors would be smaller as suggested by the decreasing errors in Figure 5-13.

### 5.3.3 Comparison of BIRDOPP and BIRAZEL filters

The previous subsections on the BIRDOPP and BIRAZEL schemes showed tracking results obtained with a small initial perturbation vector. Since  $\delta \mathbf{x}$  was small, the associated nominal trajectory was very close to the actual trajectory. This means that the Gauss-Newton filter would easily converge to a good solution. In this subsection, a comparison is made between the two schemes' tracking performance when the initial perturbation vector is made ten times and one hundred times larger. Such initial perturbation vectors should be expected in real life experiments since source TLEs at epoch may lead to position vectors which can be 1 km off the true location.

Table 5-3 compares the tracking errors  $\tilde{\mathbf{x}}$  averaged over  $N_{MC} = 1000$  runs. The first initial perturbation vector,  $\delta \mathbf{x}$ , is the one used in the previous subsections. The second and third ones are ten times and one hundred times this initial perturbation vector. The columns refer to the elements in the target state  $\mathbf{x}$ . In this set of experiments, it was found that the BIRDOPP filter failed the  $3\sigma$  error covariance matrix test and ANEES covariance consistency test when handling all three initial perturbation vector cases. The BIRAZEL filter never failed either of these consistency tests.

Table 5-3: Comparison of tracking errors with the **BIRDOPP** and **BIRAZEL** filters for 3 different initial perturbation vectors  $\delta\mathbf{x}$ .

	$x$ [km]	$y$ [km]	$z$ [km]	$\dot{x}$ [km/s]	$\dot{y}$ [km/s]	$\dot{z}$ [km/s]
$\delta\mathbf{x}$	$2.904240 \times 10^{-4}$	$-4.221700 \times 10^{-4}$	$-2.618710 \times 10^{-4}$	$4.061800 \times 10^{-5}$	$3.270900 \times 10^{-5}$	$-1.441500 \times 10^{-5}$
<b>BIRDOPP</b>	$3.323018 \times 10^{-3}$	$1.325548 \times 10^{-2}$	$-8.663845 \times 10^{-4}$	$-5.916461 \times 10^{-5}$	$-4.796370 \times 10^{-5}$	$2.667420 \times 10^{-5}$
<b>BIRAZEL</b>	$2.021448 \times 10^{-4}$	$2.862048 \times 10^{-4}$	$2.472989 \times 10^{-4}$	$1.007452 \times 10^{-7}$	$1.246020 \times 10^{-7}$	$1.492543 \times 10^{-7}$
$10\delta\mathbf{x}$	$2.904240 \times 10^{-3}$	$-4.221700 \times 10^{-3}$	$-2.618710 \times 10^{-3}$	$4.061800 \times 10^{-4}$	$3.270900 \times 10^{-4}$	$-1.441500 \times 10^{-4}$
<b>BIRDOPP</b>	$-6.620382 \times 10^{-2}$	$-2.155648 \times 10^{-1}$	$1.519761 \times 10^{-2}$	$1.003232 \times 10^{-3}$	$9.915380 \times 10^{-4}$	$-7.351525 \times 10^{-4}$
<b>BIRAZEL</b>	$1.808646 \times 10^{-4}$	$2.815677 \times 10^{-4}$	$2.695012 \times 10^{-4}$	$8.814321 \times 10^{-8}$	$1.416112 \times 10^{-7}$	$1.584955 \times 10^{-7}$
$100\delta\mathbf{x}$	$2.904240 \times 10^{-2}$	$-4.221700 \times 10^{-2}$	$-2.618710 \times 10^{-2}$	$4.061800 \times 10^{-3}$	$3.270900 \times 10^{-3}$	$-1.441500 \times 10^{-3}$
<b>BIRDOPP</b>	$-7.570493 \times 10^{-1}$	$-2.90415825$	$1.737239 \times 10^{-1}$	$1.119931 \times 10^{-2}$	$1.133028 \times 10^{-2}$	$-8.69345 \times 10^{-3}$
<b>BIRAZEL</b>	$1.914222 \times 10^{-4}$	$3.263018 \times 10^{-4}$	$2.549325 \times 10^{-4}$	$1.068041 \times 10^{-7}$	$1.805351 \times 10^{-7}$	$1.814156 \times 10^{-7}$

It can be seen from the tracking results that, irrespective of the initial perturbation vector, the **BIRAZEL** filter produces more accurate estimates than the **BIRDOPP** filter (typically about ten times better). With either filter, the tracking errors  $\tilde{\mathbf{x}}$  become more significant when the initial perturbation vector  $\delta\mathbf{x}$  becomes larger. The **BIRDOPP** filter is more sensitive to the initial nominal trajectory used to start it since it produces estimates whose position error exceeds 2.9 km with the  $100\delta\mathbf{x}$  case. With the **BIRAZEL** filter, the estimate error for each state element is always smaller than the corresponding element from the initial perturbation vector. On the other hand, all **BIRDOPP** estimates are larger than the initial perturbation vector elements, indicating that no improvement in the track accuracy was obtained through the tracking process. The **BIRAZEL** tracking improved the accuracy of the track for all three scenarios.

The **BIRDOPP**-based filter clearly experiences more difficulties in converging to a solution than the **BIRAZEL**-based filter. Each filtering run with the **BIRDOPP** filter takes significantly more iterations before the stopping condition is met.

### 5.3.4 Observables estimation

As discussed in Subsection 5.3.2, the **BIRAZEL** scheme consists of measurement vectors comprising of bistatic range and elevation and azimuth angles at the receiver. While the **MeerKAT** radar, being a pulsed-Doppler radar, can readily produce range measurements based on the time delay in the signal received, it cannot directly estimate the angle of arrival at the receiver. However, given the utter superiority of the **BIRAZEL** scheme over the **BIRDOPP** scheme, it would be preferable to use the **BIRAZEL** scheme and figure out a way to estimate the elevation and azimuth angles. The literature survey found that researchers at the Italian **BIRALES** radar<sup>9</sup> which operates in a similar way to the **MeerKAT** radar developed a method to create pseudo-measurements of the angles  $\{\theta_{\mathbf{R}_x}, \psi_{\mathbf{R}_x}\}$ . We use the word *pseudo* because we are not directly measuring the elevation and azimuth angles at the antenna.

<sup>9</sup> See Subsection 2.4.1.3 in the literature review.

The procedure developed by the [BIRALES](#) researchers is called *observables estimation* [47]. It hinges on the fact that, for the [RSO](#) tracking problem, the nominal trajectory for the space object of interest is known fairly accurately. Given the nominal trajectory for a proposed observation experiment, it is possible to make the calculations given in Subsection 4.5.1. The analysis starts with the target's passage through the sensor's Field of View and noticing the mapping from elevation and azimuth angles to topocentric right ascension and declination.

Figure 4-18 showed the target's passage through the receiver's [FoV](#) on a topocentric right ascension/declination ([TOPORADEC](#)) map. There is no explicit equation for the passage as shown in Figure 4-18. Researchers at the Italian [BIRALES](#) radar assumed that it is possible to approximate the trajectory with parametric second-degree polynomials given below

$$\Delta\hat{\alpha}_t(t) = a_2t^2 + a_1t + a_0 \quad (5-21)$$

$$\Delta\hat{\delta}_t(t) = b_2t^2 + b_1t + b_0 \quad (5-22)$$

where  $\Delta\hat{\alpha}_t(t)$  and  $\Delta\hat{\delta}_t(t)$  are the estimated normalized topocentric right ascension and declination. The intention is to perform a weighted curve fit to obtain the value of coefficients  $\{a_2, a_1, a_0\}$  and  $\{b_2, b_1, b_0\}$ .

Before showing how to use the [SNR](#) measurements for the weighted curve fit, we have to check how well the parametrization in Eqn. 5-22 approximates the target's [TOPORADEC](#) profile. Using timestamped arrays of topocentric ascension and declination (the true [TOPORADEC](#) profile), an unweighted polynomial fit was performed and two sets of coefficients were obtained. Then the discrepancies between the estimated polynomials and the true trajectory were calculated. The results are plotted below.

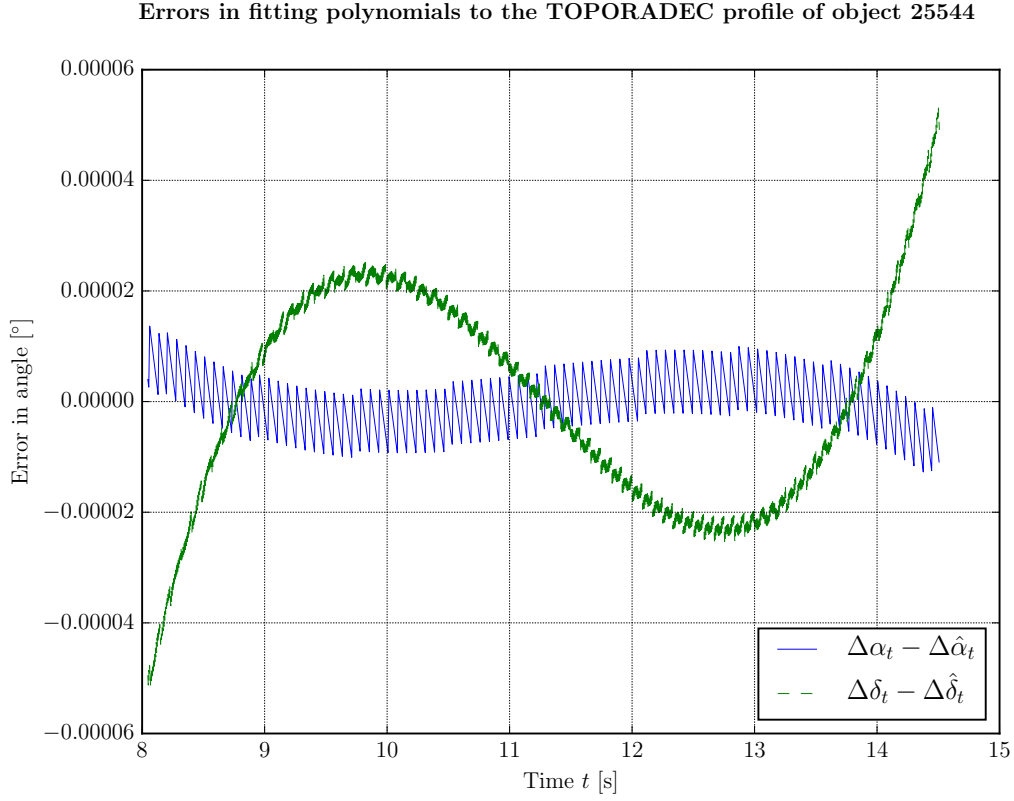


Figure 5-16: Errors in polynomial fit for the right ascension/declination profile

It can be seen from Figure 5-16 that the parametrization in Eqn. 5-22 leads to fitting errors within  $\pm 0.00006^\circ$ . Therefore the model truncation errors due to the mismatch between the true TOPORADEC values and the parametrized model in Eqn. 5-22 lead to extremely small errors.

The actual observables estimation phase is slightly different from the one in [47]. For each beam (**M000**, **M001** and **M002**), the highest SNR logically occurs when the target's topocentric right ascension and declination is closest to the beam centre (See Figure 4-22). The sensor tasking step determines the three MeerKAT dishes' beam centre pointing as  $\{\theta_{\text{Rx}0}, \psi_{\text{Rx}0}\}$ ,  $\{\theta_{\text{Rx}1}, \psi_{\text{Rx}1}\}$  and  $\{\theta_{\text{Rx}2}, \psi_{\text{Rx}2}\}$ . These three pairs of elevation and azimuth angles combined with the GMST angle arising from the Earth's rotation lead to the following topocentric right ascension and declination pairs for the beam centres:  $\{\Delta\alpha_{t,\text{Rx}0}, \Delta\delta_{t,\text{Rx}0}\}$ ,  $\{\Delta\alpha_{t,\text{Rx}1}, \Delta\delta_{t,\text{Rx}1}\}$  and  $\{\Delta\alpha_{t,\text{Rx}2}, \Delta\delta_{t,\text{Rx}2}\}$ . The sensor tasking and SNR calculations are discussed in detail in Subsection 4.4.2 and Subsection 4.4.3.

The three highest SNR measures,  $s_1$ ,  $s_2$  and  $s_3$  in chronological order during the experiment in Figure 4-21 correspond to the instants when the target was closest to each beam centre in Figure 4-18. As a consequence of the receiver tasking procedure in Subsection 4.4.2, the first dish to record detections of the RSO of interest should be **M002**, followed by **M000** and then



**M001.** The highest **SNR** of the three values should be the middle one, which corresponds to **M000**. This is expected because the sensor tasking was specifically designed so that the target's nominal trajectory goes precisely through **M000**'s beam centre. The three **SNR** values are normalized with respect to the highest **SNR** value to obtain  $\begin{bmatrix} s_1/s_2 & 1 & s_3/s_2 \end{bmatrix}^T$  which are the diagonal elements in the weighting matrix used in the curve fitting problem. To fit the second-order polynomials in Eqn. 5-22, the following **T**-matrix is used in two curve fitting processes: one for the topocentric right ascension and one for the topocentric declination.

$$\mathbf{T} = \begin{bmatrix} 1 & \Delta_t & \Delta_t^2 \\ 0 & 1 & \Delta_t \\ 0 & 0 & 1 \end{bmatrix} \quad (5-23)$$

where  $\Delta_t$  is the time elapsed between  $s_1$  and  $s_2$  and between  $s_1$  and  $s_3$ . We perform a weighted curve fit and obtain the two sets of coefficients  $\{a_2, a_1, a_0\}$  and  $\{b_2, b_1, b_0\}$ . The estimated trajectory is found from the estimated polynomials. The discrepancy with respect to the true trajectory is computed and shown in Figure 5-17.

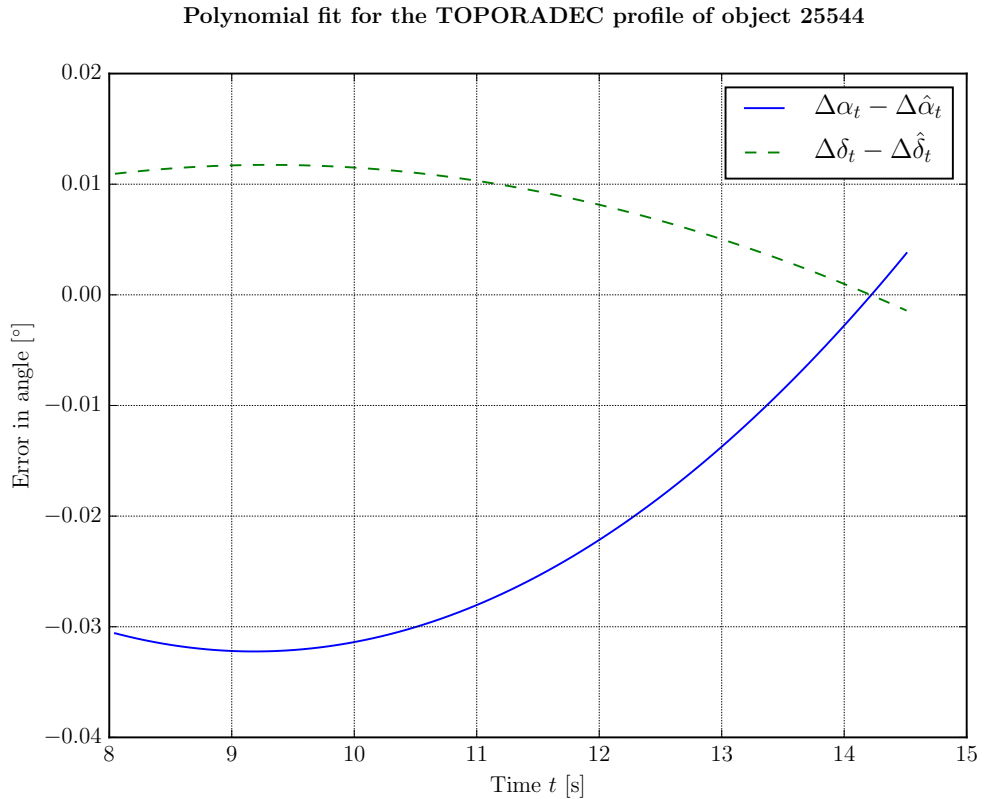


Figure 5-17: Discrepancy between the true **TOPORADEC** profile and the estimated parametric second-order polynomials

Figure 5-17 shows that the estimation error for the topocentric right ascension and declination

lies well within the range  $-0.04^\circ$  to  $0.04^\circ$ .

The estimated [TOPORADEC](#) profile (in  $\{\Delta\alpha_t, \Delta\delta_t\}$  space) in an experiment can be converted into timestamped arrays of elevation and azimuth angles pseudo-measurements (in  $\{\theta, \psi\}$  space). These pseudo-measurements  $[\theta_{Rx} \ \psi_{Rx}]^T$  are then concatenated with the bistatic range measurement to create the [BIRAZEL](#) measurement vector. Measurement errors for the elevation angle ( $\sigma_{\theta_{Rx}}$ ) and azimuth angle ( $\sigma_{\psi_{Rx}}$ ) are needed for forming the measurement covariance matrix in Eqn. 5-19. The Jacobian matrix for the transformation from  $\{\Delta\alpha_t, \Delta\delta_t\}$  space to  $\{\theta, \psi\}$  space has to be found. Due to the Jacobian matrix derivation being overly arduous and due to the inevitable presence of model truncation errors (because the parametric polynomials in Eqn. 5-22 cannot possibly perfectly match the true [TOPORADEC](#) profile in Figure 4-18), it was decided to simply assume that the elevation and azimuth measurement errors are both equal to  $0.04^\circ$  which is larger than the highest estimation error in the polynomial fit in Figure 5-17. In real life experiments, the nominal trajectory would be unknown, so we would not be able to plot the estimation error in Figure 5-17. The [BIRALES](#) paper [47] does not address the issue of finding an appropriate measurement covariance matrix and appears to be performing an ordinary least squares procedure instead of a weighted least squares in the orbit determination processor.

## 5.4 Summary

This chapter on [OD](#) first introduced how the [GNF](#) is used to estimate a space object's trajectory. It then defined the tracking schemes used in this project, namely the [BIRDOPP](#) scheme which involves processing measurement vectors consisting of bistatic range and bistatic Doppler shift and the [BIRAZEL](#) scheme whose measurement vectors consist of bistatic range and elevation and azimuth angles at the [Rx](#).

For both tracking schemes, target motion analysis was done to assess whether the [MeerKAT](#) radar would be able to track the target trajectory of interest using the relevant measurement vectors. Both schemes were found to be fully observable for the target trajectory under investigation.

To assess the performance of the trackers, Monte Carlo simulations were performed. The average normalized [RMSE](#) ([ANRMSE](#)) in the state estimates was calculated as primary figure of merit. Two filter consistency tests, namely the  $3\sigma$ -[ECM](#) test and the [ANEES](#) test, were used to assess the filtering results. It was found that the [BIRDOPP](#) scheme always failed the second test but occasionally passed the first one. The [BIRAZEL](#) scheme always passed both consistency tests, indicating that there is covariance consistency and no bias errors in the [GNF BIRAZEL](#) tracker.

It was found that bias errors exist in the **BIRDOPP** tracker. This means that the Gauss-Newton filter which processes measurements of bistatic range and Doppler shift was either incorrectly implemented or it was correctly implemented but it converges to an incorrect (local) solution for the initial nominal trajectories considered in this investigation. The only difference between the failing **BIRDOPP GNF** and the correct **BIRAZEL GNF** lies in the quantities relating to the measurement model, that is, the measurement function **g** and its Jacobian matrix **H**. All of these derivations and the resulting code were verified by hand several times. Furthermore, the decrease in measurement residuals with each successive iteration of the **BIRDOPP** filter in Figure 5-4 indicates that the filter is working properly. The final measurement residuals in Figure 5-4 look very similar to zero-mean white Gaussian noise, devoid of structure, which means that the tracker is successfully filtering the noisy measurement vectors **y**. Indeed, the measurement residuals  $\tilde{\mathbf{y}}$  of the **BIRDOPP** filter pass the  $3\sigma$  test based on the measurement covariance matrix **R**, giving further credence that the **BIRDOPP GNF** is operating correctly. All of this evidence leads to the conclusion that the second scenario occurred: the **GNF** converges to the wrong local minima instead of the global one when the filter iterates through the **BIRDOPP** measurements.

The target state estimates from both **BIRDOPP** and **BIRAZEL** filters are converted to Keplerian elements so that part of the target's **TLE** set can be reconstructed by the **MPT**. Furthermore, Monte Carlo experiments showed that the **BIRAZEL**-based tracker produces estimates which improve the accuracy of the initial nominal trajectory, even when the latter differs greatly from the target's true trajectory. However, the **BIRDOPP**-based filter produces extremely inaccurate target state estimates when the initial nominal trajectory available to the filter is not close to the true trajectory.

Since the **MeerKAT** radar as per the current **RRSG** design can only measure bistatic range and bistatic Doppler shift and not the elevation and azimuth angles at the receiver, as required by the **BIRAZEL** scheme, a so-called 'observables estimation' phase is elaborated to estimate these two angles from the radar **SNR** measurements, the sensor tasking and the known nominal trajectory. The sensor tasking phase establishes the beam centre pointing for the three **MeerKAT** dishes used in this project. The resulting topocentric right ascension and declination profile of the nominal trajectory along with the integrated **SNR** measurements at the receiver are used to reconstruct the actual **TOPORADEC** profile of the target pass. This profile is then transformed into timestamped arrays of elevation and azimuth angles from the **Rx** to the target. The performance of the observables estimation is then assessed and it is seen that the elevation and azimuth angles can be estimated with a high accuracy. These estimated elevation and azimuth angle pseudo-measurements are then combined with the measured bistatic range to form the measurement vector in the **BIRAZEL** scheme, which works satisfactorily.

This chapter accomplishes the fourth objective given in Section 1.2.

# Conclusions and Recommendations

## 6.1 Conclusions

The main aim of this project has been to develop a [Mission Planning Tool](#) to support the research and development of the [MeerKAT](#) radar project for the detection and tracking of resident space objects. To achieve these aims, four objectives were outlined in [Section 1.2](#). The following list briefly explains how these objectives were achieved.

- The first objective, which relates to developing an [orbit propagation](#) module, was achieved in [Chapter 3](#).
- The second objective concerns identifying the most opportune time for running a [RSO](#) observation experiment and performing sensor tasking for the [Tx](#) and [Rx](#). It was met in [Chapter 4](#).
- The third objective involves predicting the received [SNR](#), the radar measurement vectors and their corresponding measurement errors at the [MeerKAT](#) dishes during a tracking experiment. It was achieved in [Chapter 4](#) also.
- The final objective concerns developing a module to perform [orbit determination](#) with measurements recorded at the [MeerKAT](#) receivers. This was achieved in [Chapter 5](#).

This report has described the engineering process behind the development of the [Mission Planning Tool](#) for the [MeerKAT](#) radar. This report can be summarised in detailed terms as follows.

- **Chapter 1** gave the context for the [MeerKAT](#) radar project and the motivation for developing a [Mission Planning Tool](#) tailored for the specific needs and properties of the

proposed [MeerKAT](#) radar. Two points need to be clarified before the [MeerKAT](#) radar's feasibility study progresses further: (i) How to determine when is a favourable time to do an observation experiment for an object of interest and how to schedule the radar to successfully detect and track this object. (ii) The second point relates to predicting the radar's measurements for a particular scenario and using these collected data to perform [OD](#). The [MPT](#) developed during this project has been built to deal conclusively with these issues. This chapter also delineates the objectives of this project and specifies its scope and limitations. The structure of this report is also explained.

- **Chapter 2** reviews the literature related to the main themes of this project, namely space debris, space situational awareness and radar sensors which participate in [SSA](#) activities. It provides a comprehensive background on the space debris problem and on the field of [SSA](#) in the first two sections. This chapter places significant emphasis on ground-based bistatic sensors which observe space objects in stare mode because the proposed [MeerKAT](#) radar has this specific configuration and mode of operation. The main radar systems operating in the configuration are the German [TIRA](#) in collaboration with the radio telescope at Effelsberg in Germany, the [BIRALES](#) radar in Italy and the Murchison Widefield Array ([MWA](#)) in Australia. The literature on these sensor systems is reviewed with particular attention paid to the following points: (i) [Target dynamic model and orbit propagation](#) (ii) [Sensor scheduling](#) (iii) [Radar measurements prediction](#) (iv) [Orbit determination](#) (v) Time conventions and geodetic standards. Conclusions are drawn from the literature review to guide the development in the following work chapters.
- **Chapter 3** describes the target and sensor dynamics modelling incorporated in the [MPT](#). The two approaches to [RSO](#) dynamics modelling found in the literature are investigated. Simulation results are shown to prove the correctness of the software implementation of the two body plus  $J_2$  and [SGP4](#) models. This chapter outlines the time and geodetic standards adopted by the [MPT](#). It also defines the coordinate frames employed by the [MPT](#): the [ECI](#), the [ECEF](#) and the [SEZ](#) frames. Chapter 3 also establishes the framework for the [MPT](#). Radar measurement quantities such as bistatic range, bistatic Doppler shift, elevation angle and azimuth angles are derived based on the sensor dynamics framework developed in this section. The difference between the geometric range and range rate and radar-measured range and range rate for distant targets such as [RSOs](#) is explained. Light-time correction is performed by the [MPT](#) to find the uplink and downlink times during an [RSO](#) observation experiment. Expressions are given for bistatic range and Doppler shift which account for the light-time correction. Simulation results are shown to prove that the [MPT](#) can compute both the ideal and the actual bistatic range and Doppler shift.

- **Chapter 4** explains how the **Mission Planning Tool** schedules an **RSO** observation experiment at the **MeerKAT** radar. Sensor parameters which influence the sensor tasking process are calculated. Based on these parameter values, the target passage identification phase of the **MPT** is developed. This phase determines when the space object of interest will be observable at the **MeerKAT** radar. Since the radar is expected to operate in beam-park mode, the transmitter has to be tasked to point at the portion of the trajectory which ensures the longest illumination time within the **Tx** antenna beam. This is achieved in the **Tx** tasking process, which is a component of the **sensor scheduling** in the **MPT**. The other component of **sensor scheduling** is **Rx** tasking. The tasking aspect is related to pointing the transmit and receive antennas at the desired location in the sky. Sensor tasking coupled with the temporal aspect of executing an observation experiment are referred to as sensor scheduling. The targets in the 8 scenarios investigated were found to spend between 4.5 s and 12.8 s in the transmitter's **Field of View**. This duration, called the illumination time in the **Tx** beam and represented by the symbol  $T_{i,Tx}$ , effectively determines how many target echoes are received back at the radar receiver. The **Tx** illumination time depends on the transmitter's **FoV** which is limited by the size of the **Tx**'s antenna beamwidth  $\Theta_{3\text{ dB}}$ . Given that the **MeerKAT** radar project is still in a preliminary phase, only the first three **MeerKAT** receivers are considered in this project. It is shown that these three receivers are sufficient to cover the **Tx**-illuminated portion of the trajectory. Various visualizations are developed in the **MPT** to instruct radar engineers on how to run the observation experiment for a chosen scenario. Based on the results of the sensor scheduling phase of the **MPT**, the single-pulse and coherently-integrated **SNR** at the receivers are calculated. The single-pulse **SNRs** for the 8 scenarios investigated range from  $-27.6$  dB to  $29.8$  dB. From the integrated **SNR** values, the radar measurement errors relating to bistatic range and bistatic Doppler shift are found. These radar measurement errors are vital to the tracking and orbit determination module discussed in the following chapter.
- **Chapter 5** reports on the orbit determination module built into the **MPT**. The current design of the **MeerKAT** radar leads to measurement vectors consisting of bistatic range and Doppler shift, named the **BIRDOPP** scheme. For this measurement scheme, a tailored orbit determination processor based on the Gauss-Newton filtering framework is developed. Tracking results are then shown and analysed. The normalized position and velocity RMS estimation errors are averaged over 1000 Monte Carlo runs and are seen to tend asymptotically to constant, non-zero values. This means that the **BIRDOPP** tracker is not MSE-consistent. Furthermore, the **ANES** consistency test found that the tracker produces inconsistent **ECMs**. However, it was seen that the measurement residuals decrease with each successive iteration of the **BIRDOPP** filter, indicating that

it is functioning properly. The final measurement residuals after several iterations look very similar to zero-mean white Gaussian noise, devoid of structure, which means that the tracker is successfully filtering the noisy measurement vectors produced by the [MeerKAT](#) radar. The measurement residuals of the [BIRDOPP](#) filter are found to pass the  $3\sigma$  test based on the measurement covariance matrix produced by the radar, giving further evidence that the [BIRDOPP GNF](#) is operating correctly. It is therefore concluded that the [GNF](#) converges to the wrong local minima instead of the global one when the filter iterates through the [BIRDOPP](#) measurements. Due to the difficulty in converging to an adequate solution with [BIRDOPP](#) measurements, a measurement scheme based on bistatic range, elevation and azimuth angles, named [BIRAZEL](#), is explored. A tracker is engineered for the [BIRAZEL](#) measurement scheme. The tracking results show that the [GNF BIRAZEL](#) produces unbiased estimates which are MSE-consistent. The associated [error covariance matrices](#) always pass the one-shot  $3\sigma$  consistency test as well as the Monte Carlo [ANEES](#) test. Tracking estimates based on the [BIRAZEL](#) scheme are always more accurate and more trustworthy than [BIRDOPP](#) estimates. To compare the robustness of the two tracking schemes, the two trackers are evaluated in three scenarios with increasingly incorrect initial state errors. The [BIRAZEL](#) tracking improved the accuracy of the track for all three scenarios. The [BIRDOPP](#)-based filter experiences more difficulties in converging to a solution than the [BIRAZEL](#)-based filter. Since the [MeerKAT](#) radar design cannot produce measurement of elevation and azimuth angle needed for the [BIRAZEL](#) scheme, a roundabout method name ‘observables estimation’ originally developed in the literature on the [BIRALES](#) radar is investigated. It is found that the elevation/azimuth time history for a target transit can be reconstructed accurately. However, we also find that model truncation errors arise in the observables estimation phase which are not mentioned in the [BIRALES](#) papers.

Finally, the following can be concluded based on the overall results produced by the Mission Planning Tool:

- The proposed [MeerKAT](#) radar can be used to observe space targets.  
This report has shown that, with the help of the [MPT](#), it is possible to schedule [RSO](#) observation experiments at the [MeerKAT](#) radar. It has been shown that a space target’s illumination time within the proposed radar’s [Tx](#) beam can be predicted by the [MPT](#). The [MeerKAT](#) receivers can be scheduled along with the [Tx](#) to observe a given object of interest. The [MPT](#) can predict (i) the radar geometry during a scheduled experiment. (ii) radar measurements such as bistatic range, bistatic Doppler shift and elevation and azimuth angles from [MeerKAT](#) to the target of interest. (iii) the single-pulse and coherently integrated [SNR](#) in the signals measured at the [MeerKAT](#) receivers as well as the resulting radar measurements.



- With appropriate radar measurements made by the proposed [MeerKAT](#) radar, [statistical orbit determination](#) is possible with a single target pass to a certain degree of accuracy. Based on [BIRAZEL](#) measurements, the [OD](#) phase of the [MPT](#) can improve a preliminary orbit, even when the latter deviates significantly from the true state vector. The orbit estimation performance improves greatly with increasing number of data points made available to the [OD](#) phase.

## 6.2 Recommendations

The following recommendations are made based on the conclusions drawn in the preceding section. The recommendations for future work are grouped according to this project's objectives stated in [Section 1.2](#).

- [Target dynamic model and OP](#)

The [EOM](#) chosen for the target dynamic model in [Subsection 3.2.3.2](#) for numerical orbit propagation, the two body plus  $J_2$  model, ignored several perturbing effects such as atmospheric drag and solar radiation pressure. A few of these perturbing effects can be added to the [MPT](#) target dynamic model to obtain a more accurate approximation to the real world [RSO](#) dynamics.

Furthermore, the numerical method used to numerically integrate the [EOM](#) in the Cowell formulation can be changed from the current basic [RK4](#) to a more advanced scheme. Several sophisticated [OP](#) schemes appear in recent papers [\[72, 73, 74\]](#). These tailored numerical methods generate orbits with better error propagation performance, which is desired for orbit determination, catalogue maintenance and [conjunction analysis](#).

- [Sensor scheduling](#)

The current sensor scheduler in the [MPT](#) only considers the first three [MeerKAT](#) dishes for an [RSO](#) observation experiment. [MeerKAT](#) will have at least 64 dishes which can contribute as radar receivers in the proposed system. It is therefore recommended that all 64 dishes be simulated in future work. This will ensure that significantly more radar measurements are collected during a target transit which is a benefit for [OD](#) purposes and for imaging (a stated objective of the envisaged [MeerKAT](#) radar). The [MPT](#) can be easily extended to simulate these extra dishes given their location (latitude, longitude and altitude).

Observation experiments are usually scheduled to be run when the space target is low on the horizon. According to [\[75\]](#) and [\[76\]](#), atmospheric refraction may have a greater influence than receiver noise on radar measurement errors in such scenarios. In the case of



bistatic or multistatic radars tracking distant targets, refraction-corrupted measurements lead to poor tracking performance [76]. Therefore, atmospheric refraction should be investigated in future work.

The number of target echoes received by the radar during a target passage through the Tx's FoV is limited by the size of the transmit antenna's beamwidth. In future investigations, a transmitter with a larger beamwidth can be used to increase the target illumination time  $T_{i,Tx}$ . Increasing the number of data points made available to the orbit determination processor will improve the tracking results<sup>1</sup>. An alternative to having a transmit antenna with a larger beamwidth is to employ more than one transmitter. In this scenario, the sensor scheduling will be done twice. The first Tx will be tasked to illuminate the trajectory as the target rises above the horizon while the second Tx will be tasked to illuminate the trajectory as the target approaches the horizon at the end of the transit. A set of MeerKAT receivers will be tasked to observe the first illuminated portion while another set will be tasked to observe the second illuminated portion. The separation in time between the two observation windows will help the tracker to better fit radar measurements to the trajectory.

- Radar measurements prediction

As explained in Section 1.1, the final MeerKAT radar design will use slightly different specifications. In particular, the pulse repetition frequency and pulse width from Table 1-1 are likely to change. Due to the change in PRF, the simulations shown in this dissertation will have to be re-run in future work to determine the actual performance of the proposed MeerKAT radar.

The Radar Cross Section values of the space targets investigated in this report were obtained on an astrodynamics website. It can be safely assumed that these values pertained to the monostatic RCS of space targets. It is recommended in future work to determine the bistatic RCS of the targets under investigation given that the proposed MeerKAT radar will operate bistatically.

The BIRAZEL scheme requires measurements of elevation and azimuth angle at the radar receiver. The observables estimation phase investigated in this report creates pseudo-measurements of these two angles. It has been found that this approach produces angle estimates which contain model truncation errors. Since this is undesirable in a tracking problem, it is recommended to perform interferometric processing using signals collected at all MeerKAT dishes to create TOPORADEC images and obtain the desired angular measurements. Angular measurement errors should also be calculated and provided to the OD module. Interferometric processing or aperture beamforming can produce

---

<sup>1</sup> A consequence of the Law of Large Numbers.

images at high angular resolution which means smaller angular measurement errors.

- **Orbit determination module**

The Gauss-Newton filter engineered to process bistatic range and Doppler shift measurements had trouble converging to a global minima even after more than one hundred filter iterations. The **BIRDOPP GNF** should be adapted to use the Levenberg-Marquardt algorithm to converge faster to the correct solution. Nadjasngar shows in [77] how to integrate the Levenberg-Marquardt algorithm in the **GNF** paradigm.

The **OD** module built into the **MPT** only employs Gauss-Newton filtering to estimate orbits. It is suggested that other tracking filters such as the Extended and Unscented Kalman filters be investigated. The EKF without process noise is not expected to outperform the **GNF** as one can be derived from the other as found out by Nadjasngar in [77]. The target dynamic model assumed in recursive Bayesian estimators such as the UKF and Cubature Kalman filter features an additive or multiplicative process noise term, which makes the target's **EOM** stochastic rather than deterministic. Stochastic **differential equations** (SDEs) have to be integrated with special numerical methods such as the order 0.5 Euler-Maruyama method and the order 1.5 strong method in [59].

In future work, extra parameters concerning the target dynamics, such as the **RSO**'s ballistic coefficient, can be added to the target state vector and estimated by the tracking filter along with the target's position and velocity vectors. In particular, the ballistic coefficient  $B^*$  should be estimated by the tracker since it appears in **TLEs**.

The **MeerKAT** array is a precursor to the **Square Kilometre Array** which will become fully operational in 2030. The **SKA** will be the largest radio telescope in the world thanks to its physically distant cores - one will be in South Africa and the other will be in Australia. Very Long Baseline Interferometry (VLBI) can be used to create high resolution images of large portions of the sky to survey a vast amount of space debris as well as track space objects. VLBI at the **SKA** for tracking space debris is a possibility if powerful radar transmitters are available to illuminate space targets. VLBI-based space object observations with the **SKA** can be investigated in future work closer to 2030.

### 6.2.1 End-to-end simulations in conjunction with FERS

For the **MeerKAT** radar feasibility study and design process to progress further, additional simulations featuring the entire radar signal processing chain must be done. Currently, the **MPT** is used to create synthetic measurements of bistatic range and Doppler shift since it is a result simulator<sup>2</sup> which does not implement the radar signal processing block. The **RMSG** has

---

<sup>2</sup> See Section 1.3.

a signal level simulator called **FERS** which can be used to further analyse an **RSO** observation experiment. The following figure shows the suggested processing chain for combining the **MPT** with **FERS**.

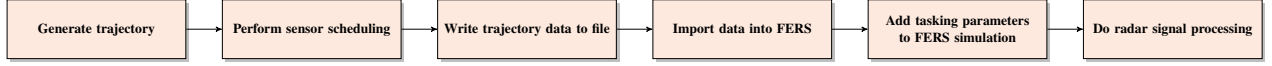


Figure 6-1: Processing chain to run an **RSO** observation experiment

**Target passage identification** and **sensor scheduling** are done by the **MPT** for a particular target passage derived from a source **TLE**. Time-indexed position vectors which constitute the target trajectory are written to a data file which is then imported into the **FERS** environment by editing the **FERS** simulation script. This is followed by defining the radar nodes and their tasking parameters in the **FERS** simulation script. The duration of the simulation in **FERS** is set to slightly longer than the **MPT**-predicted **Tx** illumination time  $T_{i,Tx}$  to account for the uplink and downlink propagation times. The final step is to perform radar signal processing on the raw data output by **FERS**.

The output of the radar signal processing is fed to a data processing block. The latter will produce time-indexed radar measurements of bistatic range, bistatic Doppler shift, elevation and azimuth to the receiver. The measurement errors associated with these measurements will also be calculated. These measurement vectors along with their errors will be fed into a tracking filter to produce an estimated orbit.

# Bibliography

- [1] European Space Agency, “Space debris.” [http://www.esa.int/Our\\_Activities/Operations/Space\\_Debris](http://www.esa.int/Our_Activities/Operations/Space_Debris). [Accessed 28 March 2017]. [2]
- [2] D. J. Kessler and B. G. Cour-Palais, “Collision frequency of artificial satellites: The creation of a debris belt,” *Journal of Geophysical Research: Space Physics*, vol. 83, no. A6, pp. 2637–2646, 1978. [2, 25]
- [3] D. Mehrholz, L. Leushacke, W. Flury, R. Jehn, H. Klinkrad, and M. Landgraf, “Detecting, tracking and imaging space debris,” *ESA Bulletin(0376-4265)*, no. 109, pp. 128–134, 2002. [2, 4, 24, 33, 34]
- [4] M. Rathnasabapathy, C. Nwosa, and et al., “Space Situational Awareness,” tech. rep., Space Generation Advisory Council, 2012. Space Situational Awareness Educational Series. [2, 26]
- [5] H. Klinkrad, T. Donath, and T. Schildknecht, “Investigations of the feasibility of a european space surveillance system.” Online. [Accessed May 1st, 2016]. [2, 26]
- [6] H. Krag, H. Klinkrad, T. Flohrer, E. Fletcher, and N. Bobrinsky, “The European space surveillance system required performance and design concepts,” in *Proceedings of the 8th US/Russian Space Surveillance Workshop, Space Surveillance Detecting and Tracking Innovation*, 2010. [2, 26]
- [7] A. van Ardenne, M. Bentum, and A. Boonstra, “SKA Antenna Systems: Outlook for non-astronomy applications,” in *Antennas and Propagation (EUCAP), 2012 6th European Conference on*, pp. 1199–1203, IEEE, 2012. [3]
- [8] D. Agaba, *Radar System Design for Detection, Tracking and Classification of Space Debris*. PhD thesis, University of Cape Town, 2018. [3, 6, 7]

- [9] D. Agaba, “MeerKAT radar parameters,” tech. rep., University of Cape Town, Department of Electrical Engineering, November 2016. [6, 72, 96, 107]
- [10] M. Brooker, *The design and implementation of a simulator for multistatic radar systems*. PhD thesis, University of Cape Town, 2008. [8]
- [11] V. C. Chen, F. Li, S.-S. Ho, and H. Wechsler, “Analysis of micro-doppler signatures,” *IEEE Proceedings-Radar, Sonar and Navigation*, vol. 150, no. 4, pp. 271–276, 2003. [8]
- [12] M. Grassi, E. Cetin, and A. G. Dempster, “Enabling orbit determination of space debris using narrowband radar,” *IEEE Transactions on Aerospace and Electronic Systems*, vol. 51, no. 2, pp. 1231–1240, 2015. [8]
- [13] D. Portree and J. Loftus Jr, *Orbital debris and near-Earth environmental management: A chronology*. NASA, 1993. Accessed 4 April 2017. [19]
- [14] H. Klinkrad, *Space Debris - Models and Risk Analysis*. Springer-Praxis, 2006. [19, 24, 25, 32]
- [15] National Aeronautics and Space Administration, *Orbital Debris Quarterly News*. NASA Orbital Debris Program Office, February 2017. Published online. <https://orbitaldebris.jsc.nasa.gov/quarterly-news/pdfs/odqnv21i1.pdf> [Accessed 4 April 2017]. [19]
- [16] Kelso, T.S., “Celestrak satellite database.” <http://www.celestrak.com/satcat/boxscore.asp>. [Accessed 14 June 2016]. [19]
- [17] UCS, “Satellite database.” <http://www.ucsusa.org/nuclear-weapons/space-weapons/satellite-database>. [Accessed 14 June 2016]. [19]
- [18] F. Alby, E. Lansard, and T. Michal, “Collision of Cerise with Space Debris,” in *Second European Conference on Space Debris*, vol. 393, p. 589, 1997. [19]
- [19] T. Kelso, “Analysis of the 2007 Chinese ASAT Test and the Impact of its Debris on the Space Environment,” in *Advanced Maui Optical and Space Surveillance Technologies Conference (AMOS 2007)*, pp. 321–330, 2007. [19]
- [20] R. Walker, H. Klinkrad, H. Sdunnus, and H. Stokes, “Update of the ESA space debris mitigation handbook,” in *Space Debris*, vol. 473, pp. 821–826, 2001. [21]
- [21] H. Klinkrad, P. Beltrami, S. Hauptmann, C. Martin, H. Sdunnus, H. Stokes, R. Walker, and J. Wilkinson, “The ESA space debris mitigation handbook 2002,” *Advances in Space Research*, vol. 34, no. 5, pp. 1251–1259, 2004. [21]

- [22] European Space Agency, “High resolution picture of impact on HST Solar Panel - front side (PFA 1).” <http://space-env.esa.int/madweb/>. [Accessed 28 March 2017]. [22]
- [23] National Aeronautics and Space Administration, *Orbital Debris Quarterly News*. NASA Orbital Debris Program Office, January 2001. Published online. <http://orbitaldebris.jsc.nasa.gov/newsletter/pdfs/ODQNV6i2.pdf> [Accessed 13 June 2016]. [22]
- [24] NASA Orbital Debris Program Office, “Frequently-asked questions.” <https://www.orbitaldebris.jsc.nasa.gov/faq.html>. [Accessed 24 November 2017]. [22, 24]
- [25] National Aeronautics and Space Administration, *Orbital Debris Quarterly News*. NASA Orbital Debris Program Office, January 2016. Published online. <http://orbitaldebris.jsc.nasa.gov/newsletter/pdfs/ODQNV20i1-2.pdf> [Accessed 13 June 2016]. [24]
- [26] B. A. Jones, D. S. Bryant, B.-T. Vo, and B.-N. Vo, “Challenges of multi-target tracking for space situational awareness,” in *Information Fusion (FUSION), 2015 18th International Conference on*, pp. 1278–1285, IEEE, 2015. [28]
- [27] Scientific and Technical Sub-committee of the United Nations Committee on the Peaceful Uses of Outer Space, “Technical report on space debris,” tech. rep., United Nations, 1999. [28, 29, 30]
- [28] E. G. Stansbery, “Preliminary results from the U.S. participation in the 2000 Beam Park Experiment,” in *Third European Conference on Space Debris*, pp. 49–52, ESA, 2001. [29]
- [29] E. G. Stansbery, “Growth in the number of SSN tracked orbital objects,” in *55th International Aeronautical Congress of the International Aeronautical Federation*, pp. 1–5, International Academy of Astronautics, 2004. [29]
- [30] NASA Orbital Debris Program Office, “Orbital debris graphics.” <https://www.orbitaldebris.jsc.nasa.gov/photo-gallery.html>. [Accessed 28 March 2017]. [29, 30]
- [31] M. L. Stone and G. P. Banner, “Radars for the detection and tracking of ballistic missiles, satellites, and planets,” *Lincoln laboratory journal*, vol. 12, no. 2, pp. 217–244, 2000. [30]
- [32] G. Stansbery, “Orbital debris research at NASA report.” [30]
- [33] M. I. Skolnik, “An analysis of bistatic radar,” *IRE Transactions on Aerospace and Navigational Electronics*, no. 1, pp. 19–27, 1961. [31]
- [34] G. Muntoni, L. Schirru, T. Pisanu, G. Montisci, G. Valente, F. Gaudiomonte, G. Serra, E. Urru, P. Ortu, and A. Fanti, “Space debris detection in low earth orbit with the sardinia radio telescope,” *Electronics*, vol. 6, no. 3, 2017. [31, 35, 38]

- [35] T. Michal, J. Eglizeaud, and J. Bouchard, “GRAVES: the new French system for space surveillance,” in *4th European Conference on Space Debris*, vol. 587, p. 61, 2005. [32]
- [36] T. Sgobba and F. Allahdadi, “Orbital operations and safety,” in *Safety Design for Space Operations* (F. Allahdadi, I. Rongier, and P. Wilde, eds.), ch. 8, pp. 179–236, Butterworth-Heinemann, 1st ed., 2013. [32]
- [37] “NASA Handbook 8719.14: Handbook for limiting orbital debris.” [32]
- [38] R. Jehn, H. Klinkrad, H. Krag, T. Flohrer, L. Leushacke, J. Markkanen, T. Schildknecht, and M. Oswald, “Space Traffic Data Analysis And Synthesis,” in *Third IAASS international space safety conference*, pp. 1–16, IAASS, 2008. [33]
- [39] D. Mehrholz, L. Leushacke, and R. Jehn, “The COBEAM-1/96 experiment,” *Advances in Space Research*, vol. 23, no. 1, pp. 23–32, 1999. [33]
- [40] G. Ruiz, L. Leushacke, R. Jehn, and R. Keller, “Improved FGAN/MPIfR Bi-Static Debris Observations Campaign: Experiment Outline, Analysis Algorithms and First Results,” in *57th International Astronautical Congress. Valencia, Spain*, 2006. [33]
- [41] R. Letsch, L. Leushacke, J. Rosebrock, R. Jehn, H. Krag, and R. Keller, “First Results from the Multibeam Bistatic Beampark Experiment at FGAN,” in *Proc. 5th European Conf. on Space Debris. ESA/ESOC. Darmstadt, Germany*, 2009. [33]
- [42] S. Flegel, K. Letsch, and H. Krag, “Theoretical analysis of south-staring Beampark configurations for the TIRA system,” *CEAS Space Journal*, vol. 7, pp. 375–387, Sep 2015. [33]
- [43] G. Ruíz, T. Patzelt, L. Leushacke, and O. Loffeld, “Autonomous Tracking of Space Objects with the FGAN Tracking and Imaging Radar,” in *Informatik 2006 - Informatik für Menschen, Band 1, Beiträge der 36. Jahrestagung der Gesellschaft für Informatik e.V. (GI)*, pp. 349–353, 2006. [33, 34]
- [44] G. Del Genio, J. Paoli, E. Del Grande, F. Dolce, W. Villadei, M. Reali, and A. Aquilini, “Italian air force radar and optical sensor experiments for the detection of space objects in leo orbit,” in *Proceedings of the Advanced Maui Optical and Space Surveillance Technologies Conference*, vol. 1, p. 3, 2015. [35]
- [45] A. Morselli, P. Di Lizia, G. Bianchi, C. Bortolotti, S. Montebugnoli, G. Naldi, F. Perini, G. Pupillo, M. Roma, M. Schiaffino, *et al.*, “A new high sensitivity radar sensor for space debris detection and accurate orbit determination,” in *Metrology for Aerospace (MetroAeroSpace), 2015 IEEE*, pp. 562–567, IEEE, 2015. [35]



- [46] S. Montebugnoli, G. Pupillo, E. Salerno, S. Pluchino, and M. di Martino, “The bistatic radar capabilities of the medicina radiotelescopes in space debris detection and tracking,” *Advances in Space Research*, vol. 45, no. 5, pp. 676 – 682, 2010. [35]
- [47] P. D. Lizia, M. Massari, M. Losacco, G. Bianchi, A. Mattana, G. Pupillo, C. Bortolotti, M. Roma, A. Morselli, R. Armellin, G. Pupillo, A. Magro, D. Cutajar, C. Portelli, and M. Reali, “Performance assessment of the multibeam radar sensor birales for space surveillance and tracking,” in *7th European Conference on Space Debris*, 2017. [35, 36, 37, 38, 120, 129, 130, 132]
- [48] B. Tapley, B. Schutz, and G. Born, *Statistical Orbit Dyetermination*. Elsevier Academic Press, 2004. [37, 52, 152, 153, 159]
- [49] T. Pisanu, E. Urru, G. Muntoni, L. Schirru, F. Gaudiomonte, G. Valente, and G. Serra, “Space debris forecasting campaign,” tech. rep., Istituto Nazionale di Astrofisica - Istituto di Radioastronomia, December 2016. [38]
- [50] J. E. Palmer, B. Hennessy, M. Rutten, D. Merrett, S. Tingay, D. Kaplan, S. Tremblay, S. M. Ord, J. Morgan, and R. B. Wayth, “Surveillance of space using passive radar and the murchison widefield array,” in *2017 IEEE Radar Conference (RadarConf)*, pp. 1715–1720, May 2017. [38, 39, 40]
- [51] S. Tingay, D. Kaplan, B. McKinley, F. Briggs, R. Wayth, N. Hurley-Walker, J. Kennewell, C. Smith, K. Zhang, W. Arcus, *et al.*, “On the detection and tracking of space debris using the murchison widefield array. i. simulations and test observations demonstrate feasibility,” *The Astronomical Journal*, vol. 146, no. 4, pp. 103–112, 2013. [39]
- [52] D. Vallado and W. McClain, *Fundamentals of Astrodynamics and Applications*. Space Technology Series, McGraw-Hill, 1 ed., 1997. [45, 50, 52, 54, 58, 59, 61, 167]
- [53] R. Bate, D. Mueller, J. White, and W. Saylor, *Fundamentals of Astrodynamics*. Dover Books on Physics, Dover Publications, Incorporated, 2015. [45, 52]
- [54] F. R. Hoots, R. L. Roehrich, and T. Kelso, “Spacetrack report no. 3,” tech. rep., Aerospace Defense Command, December 1980. [48, 51]
- [55] D. A. Vallado, P. Crawford, R. Hujsak, and T. Kelso, “Revisiting spacetrack report# 3,” *AIAA/AAS Astrodynamics Specialist Conference and Exhibit*, 2006. [51]
- [56] B. Rhodes, “python-sgp4 package.” <https://pypi.python.org/pypi/sgp4/>. [Accessed 15 March 2017]. [51]



- [57] O. Montenbruck and E. Gill, *Satellite Orbits: Models, Methods, and Applications*. Physics and astronomy online library, Springer Berlin Heidelberg, 2000. [52, 53, 66]
- [58] G. Beutler, L. Mervart, and A. Verdun, *Methods of Celestial Mechanics: Volume II: Application to Planetary System, Geodynamics and Satellite Geodesy*. Astronomy and Astrophysics Library, Springer Berlin Heidelberg, 2004. [52]
- [59] D. Crouse, “Basic tracking using nonlinear continuous-time dynamic models [tutorial],” *IEEE Aerospace and Electronic Systems Magazine*, vol. 30, pp. 4–41, Feb 2015. [55, 106, 140]
- [60] National Imagery and Mapping Agency, *Department of Defense, World Geodetic System 1984 (WGS 84): Its Definition and Relationships with Local Geodetic Systems*. National Imagery and Mapping Agency, 3 ed., 2004. [58]
- [61] N. Morrison, *Tracking Filter Engineering: The Gauss Newton and Polynomial Filters*. Radar, Sonar and Navigation Series 23, Institution of Engineering and Technology, 2013. [61, 104, 106, 113, 115, 152, 153, 154, 156, 159, 168]
- [62] J. Horrell, *South Africa’s MeerKAT Radio Telescope - technical fact sheet*. Square Kilometre Array South Africa. [72]
- [63] G. Curry, *Radar System Performance Modeling*. Artech House radar library, Artech House, 1 ed., 2005. [95, 100]
- [64] A. Morselli, R. Armellin, P. Di Lizia, F. B. Zazzera, E. Salerno, G. Bianchi, S. Montebugnoli, A. Magro, and K. Z. Adami, “Orbit determination of space debris using a bi-static radar configuration with a multiple-beam receiver,” in *Proceedings of the 65th International Astronautical Congress 2014 (IAC 2014)*, vol. 3, pp. 1774–1784, 2015. [96]
- [65] M. Cherniakov, *Bistatic radars: Emerging technology*. John Wiley & Sons, 2008. [99]
- [66] N. J. Willis, *Bistatic radar*, vol. 2. SciTech Publishing, 2005. [99]
- [67] M. Mallick, S. Rubin, and B.-N. Vo, “An introduction to force and measurement modeling for space object tracking,” in *Information Fusion (FUSION), 2013 16th International Conference on*, IEEE, 2013. [105]
- [68] A. Dhondea, A. K. Mishra, and M. Inggs, “Investigation of variable discretization resolution for cd-ekfs in space object tracking,” in *2017 International Conference on Computer, Communication and Signal Processing (ICCCSP)*, pp. 1–6, Jan 2017. [106]

- [69] D. Crouse, “Basic tracking using nonlinear 3d monostatic and bistatic measurements,” *IEEE Aerospace and Electronic Systems Magazine*, vol. 29, pp. 4–53, August 2014. [[115](#), [117](#)]
- [70] Bar-Shalom, Y. and Li, X.-R. and Kirubarajan, T., *Estimation and tracking*. Wiley, 2001. [[117](#)]
- [71] D. F. Crouse, “Cubature/unscented/sigma point kalman filtering with angular measurement models,” in *Information Fusion (Fusion), 2015 18th International Conference on*, pp. 1550–1557, IEEE, 2015. [[121](#)]
- [72] J. M. Aristoff, J. T. Horwood, and A. B. Poore, “Implicit-Runge–Kutta-based methods for fast, precise, and scalable uncertainty propagation,” *Celestial Mechanics and Dynamical Astronomy*, vol. 122, no. 2, pp. 169–182, 2015. [[138](#)]
- [73] A. Probe, B. Macomber, D. Kim, R. Woollands, and J. Junkins, “Terminal Convergence Approximation Modified Chebyshev Picard Iteration for efficient numerical integration of orbital trajectories,” in *Advanced Maui Optical and Space Surveillance Technologies Conference, Maui, Hawaii*, 2014. [[138](#)]
- [74] B. Bradley, B. Jones, G. Beylkin, K. Sandberg, and P. Axelrad, “Bandlimited implicit Runge–Kutta integration for astrodynamics,” *Celestial Mechanics and Dynamical Astronomy*, vol. 119, no. 2, pp. 143–168, 2014. [[138](#)]
- [75] Electronic Trajectory Measurements Group, “Atmospheric refraction measurements and related efforts,” tech. rep., Range Commanders Council, February 1979. [[138](#)]
- [76] D. F. Crouse, “How to incorporate generic refraction models into multistatic tracking algorithms,” in *Aerospace Conference, 2013 IEEE*, pp. 1–16, IEEE, 2013. [[138](#), [139](#)]
- [77] R. Nadjiasngar, *On Improving the Performance of the Gauss-Newton Filter*. PhD thesis, University of Cape Town, 2013. [[140](#), [158](#)]
- [78] M. Grewal and A. Andrews, *Kalman filtering: Theory and Practice with MATLAB*. John Wiley & Sons, 2014. [[153](#)]
- [79] A. Milani and G. Gronchi, *Theory Of Orbit Determination*. Cambridge University Press, 2010. [[153](#)]
- [80] J. Danby, “The matrizant of Keplerian motion,” *AIAA Journal*, vol. 2, no. 1, pp. 16–19, 1964. [[153](#)]
- [81] R. Broucke, “On the matrizant of the two-body problem,” *Astronomy and Astrophysics*, vol. 6, p. 173, 1970. [[153](#)]

- [82] J.-J. E. Slotine and W. Li, *Applied nonlinear control*. Prentice-Hall Englewood Cliffs, NJ, 1991. [\[157\]](#)
- [83] S. Boyd and L. Vandenberghe, *Convex optimization*. Cambridge university press, 2004. [\[157\]](#)
- [84] J. Crassidis and J. Junkins, *Optimal Estimation of Dynamic Systems*. Chapman & Hall/CRC Applied Mathematics & Nonlinear Science, CRC Press, 2011. [\[158\]](#)
- [85] G. James, D. Witten, T. Hastie, and R. Tibshirani, *An Introduction to Statistical Learning*. Springer texts in statistics, Springer, 2014. [\[158\]](#)
- [86] C. Bishop, *Pattern Recognition and Machine Learning*. Information science and statistics, Springer, 2006. [\[158\]](#)
- [87] G. Strang, *Introduction to Linear Algebra*. Wellesley-Cambridge Press, 2009. [\[159\]](#)
- [88] D. Vallado and W. McClain, *Fundamentals of Astrodynamics and Applications*. Space Technology Library, Microcosm Press, 4 ed., 2013. [\[168\]](#)

# Astrodynamics aspects

## A.1 Resident space objects simulated in this project

Table A-1: NORAD ID and names for objects used in simulations documented in this project

NORAD ID	Name	Nature
25544	ISS	satellite
29754	Fengyun-1C	debris
33759	Kosmos-2251	debris
33773	Iridium-33	debris
37820	Tiangong-1	satellite

## A.2 Generating a trajectory with the two body plus J2 model

The following algorithm is used to generate a nominal trajectory  $\mathbf{x}^*$  along with the corresponding state transition matrix (STM) by employing an embedded RK4 method. It should be noted that the Runge-Kutta increments  $\mathbf{k}$  have the same dimensions as the state vector  $\mathbf{x}^*$ ; the matrix Runge-Kutta increments  $\mathbf{J}_x$  are  $d_x \times d_x$  matrices; and the identity matrix  $\mathbf{I}$  in the algorithm has dimensions  $d_x \times d_x$ .

---

**Algorithm A.1** Generate a nominal trajectory with an embedded RK4 method

---

```

procedure GENERATENOMINALTRAJECTORY( $\mathbf{f}, t, \mathbf{x}^*(t), \Delta_t, \mathbf{A}$ )
   $\mathbf{k}_1 \leftarrow \mathbf{f}(\mathbf{x}^*, t)$ 
   $\mathbf{k}_2 \leftarrow \mathbf{f}(\mathbf{x}^* + \frac{\Delta_t}{2}\mathbf{k}_1, t + \frac{\Delta_t}{2})$ 
   $\mathbf{k}_3 \leftarrow \mathbf{f}(\mathbf{x}^* + \frac{\Delta_t}{2}\mathbf{k}_2, t + \frac{\Delta_t}{2})$ 
   $\mathbf{k}_4 \leftarrow \mathbf{f}(\mathbf{x}^* + \Delta_t\mathbf{k}_3, t + \Delta_t)$ 
   $\mathbf{x}^*(t + \Delta_t) \leftarrow \frac{\Delta_t}{6}(\mathbf{k}_1 + 2\mathbf{k}_2 + 2\mathbf{k}_3 + \mathbf{k}_4)$   $\triangleright$  Propagate the nominal state vector
   $\mathbf{J}_{1x} \leftarrow \mathbf{A}(\mathbf{x}^*, t)$   $\triangleright \mathbf{A}$  is the Jacobian matrix of  $\mathbf{f}(\cdot)$ 
   $\mathbf{J}_{2x} \leftarrow \mathbf{A}(\mathbf{x}^* + \frac{\Delta_t}{2}\mathbf{k}_1, t + \frac{\Delta_t}{2})(\mathbf{I} + \frac{\Delta_t}{2}\mathbf{J}_{1x})$ 
   $\mathbf{J}_{3x} \leftarrow \mathbf{A}(\mathbf{x}^* + \frac{\Delta_t}{2}\mathbf{k}_2, t + \frac{\Delta_t}{2})(\mathbf{I} + \frac{\Delta_t}{2}\mathbf{J}_{2x})$ 
   $\mathbf{J}_{4x} \leftarrow \mathbf{A}(\mathbf{x}^* + \Delta_t\mathbf{k}_3, t + \Delta_t)(\mathbf{I} + \Delta_t\mathbf{J}_{3x})$ 
   $\Phi(t + \Delta_t) \leftarrow \mathbf{I} + \frac{\Delta_t}{6}(\mathbf{J}_{1x} + 2\mathbf{J}_{2x} + 2\mathbf{J}_{3x} + \mathbf{J}_{4x})$   $\triangleright$  Propagate the nominal STM
  return  $\mathbf{x}^*(t + \Delta_t), \Phi^*(t + \Delta_t)$ 
end procedure

```

---

# Gauss-Newton filtering

This appendix describes the three mechanisms of the [GNF](#): the dynamical model, the observation model and the processor which generates estimates of the state vector and error covariance matrix. The theory developed here is mostly based on the discussion of Gauss-Newton filters in Dr. Morrison's book [\[61\]](#).

## B.1 The dynamical model

The [Minimum Variance Algorithm](#) employed by the Gauss filters readily handles linear dynamics and linear observation schemes. However, in the [OD](#) problem, nonlinearity appears both in the target dynamics and the measurement model. The solution is to linearize the problem in the time domain using a truncated Taylor series expansion. [\[61, 48\]](#)

### Taylor series linearization

The [GNF](#) paradigm assumes that there is a known nominal trajectory  $\mathbf{x}^*(t)$  that has the following attributes:

- The reference trajectory  $\mathbf{x}^*(t)$  satisfies the same [DE](#) as the observed trajectory  $\mathbf{x}(t)$ .
- $\mathbf{x}^*(t)$  remains sufficiently close to  $\mathbf{x}(t)$  over the time interval of interest.

This reasonable trajectory will differ from the true trajectory slightly, by a small vector  $\delta\mathbf{x}(t)$  called *perturbation vector* [\[61\]](#) or *deviation vector*. [\[48\]](#)

$$\mathbf{x} = \mathbf{x}^* + \delta\mathbf{x} \tag{B-1}$$

Our strategy is to perform linear estimation (i.e. apply the minimum variance rule) on the

perturbation vector,  $\delta \mathbf{x}$  about the nominal trajectory  $\mathbf{x}^*$ , after which we will compute the estimate of the true state vector,  $\hat{\mathbf{x}}$ <sup>1</sup> by making  $\mathbf{x}$  subject of Eqn. B-1.

The first order Taylor series expansion of equation is, according to [48]

$$\dot{\mathbf{x}}(t) = \mathbf{f}(\mathbf{x}(t)) = \mathbf{f}(\mathbf{x}^*) + \left[ \frac{\partial \mathbf{f}}{\partial \mathbf{x}} \right]^* (\mathbf{x}(t) - \mathbf{x}^*(t)) + \text{H.O.T} \quad (\text{B-2})$$

where  $\left[ \frac{\partial \mathbf{f}}{\partial \mathbf{x}} \right]^*$  means the partial derivative matrix evaluated on the nominal trajectory,  $\mathbf{x}^*$  and H.O.T means *higher order terms*. The first order Taylor series expansion of the function  $\mathbf{f}$  exists if the function is twice continuously differentiable. [78] Formally,  $\mathbf{f}$  needs to be of the class  $\mathcal{C}^1$  at least. [79] For the dynamics under consideration in this dissertation, the fundamental function is indeed twice continuously differentiable.

Assuming that the terms higher than first order are negligibly small, we arrive at the **state sensitivity differential equation** from Eqn. B-1 and Eqn. B-2:

$$D\delta \mathbf{x}(t) = \mathbf{A}(\mathbf{x}^*)\delta \mathbf{x}(t) \quad (\text{B-3})$$

The matrix  $\mathbf{A}(\mathbf{x}^*)$ , called the DE's *state sensitivity matrix*, is the Jacobian matrix of the fundamental vector function  $\mathbf{f}(\mathbf{x}^*(t))$ .

$$\mathbf{A}(\mathbf{x}^*) = \left[ \mathbf{A} \right]^* = \left[ \frac{\partial \mathbf{f}}{\partial \mathbf{x}} \right]^* \quad (\text{B-4})$$

The full expression for the *state sensitivity matrix* is shown in Appendix C.1.2.

The general solution for the DE in Eqn. B-3 is the **state transition equation**.

$$\delta \mathbf{x}(t_k + T_k) = \Phi(t_k + T_k, t_k; \mathbf{x}^*)\delta \mathbf{x}(t_k) \quad (\text{B-5})$$

The *State Transition Matrix*,  $\Phi$ , shifts the validity instant of the deviation vector,  $\delta \mathbf{x}$  by an amount  $T_k$ , called the *span of the transition*. The *State Transition Matrix*<sup>2</sup> is a fundamental concept in dynamical systems theory: it achieves the admirable feat of propagating the state vector of a dynamical system forward (prediction) or backward (retrodiction) in time. (The sign of  $T_k$  indicates whether it is a prediction or retrodiction.) [61] Furthermore,  $\Phi$  can be considered as a mapping operator in the state space  $\mathbb{R}^{d_x}$ : it maps the *integral flow* from one state  $\delta \mathbf{x}_t \in \mathbb{R}^{d_x}$  to another state  $\delta \mathbf{x}_{t+T_k}$ . [79]

The **variational equation** [79] presents the STM as the solution of the following *Initial Value*

---

<sup>1</sup> A hat on top of a variable name means that this is an estimate i.e. an output of the tracking filter.

<sup>2</sup> An archaic synonym for the STM is *matrizant*. See [80, 81]

Problem involving the [state sensitivity matrix](#) mentioned above.

$$\frac{d}{dT_k} \Phi(t_k + T_k, t_k; \mathbf{x}^*) = \mathbf{A}(\mathbf{x}^*(t_k + T_k)) \Phi(t_k + T_k, t_k; \mathbf{x}^*) \quad (\text{B-6})$$

$$\Phi(t_k, t_k; \mathbf{x}^*) = \mathbf{I} \quad (\text{B-7})$$

The above pair of equations constitute an [IVP](#) which is solved through numerical methods<sup>3</sup>. The initial conditions in Eqn. B-7 arise when the [span of transition](#) is set to 0. The identity matrix  $\mathbf{I}$  has dimensions  $d_x \times d_x$ . Equivalent expressions for the [STM](#) evaluated on  $\mathbf{x}^*(t)$  are  $[\Phi(t_k + T_k, t_k)]_{\mathbf{x}^*(t)}$  and  $[\Phi(t_k + T_k, t_k)]^*$ .

## B.2 The observation model

The observation equation (Eqn. 5-2) is repeated for convenience:

$$\mathbf{y}_k = \mathbf{g}(\mathbf{x}_k, t_k) + \boldsymbol{\nu}_k \quad (\text{B-8})$$

where the measurement function is given by  $\mathbf{g} : \mathbb{R}^{d_x} \mapsto \mathbb{R}^{d_y}$  and the  $d_y$ -dimensional additive white Gaussian noise sequence is given by  $\boldsymbol{\nu}_k$  with covariance  $\mathbf{R}_k$ . In other words,  $\boldsymbol{\nu} \sim \mathcal{N}(0, \mathbf{R})$ .

Morrison [61] provides two schemes to handle the nonlinearity in the measurement equation when the target dynamics are also nonlinear:

- Case 4

The Case 4 filtering scheme linearizes the observation equation (Eqn. B-8) through a first order Taylor series expansion in the filtering routine itself.

- Case 3

In the Case 3 approach, the raw observations and the measurement covariance matrices are transformed into a suitable linear coordinate frame before filtering.

The difference between these two schemes lies in where the measurement nonlinearity is handled. In the first case, the measurement nonlinearity is dealt with in the tracking filter routine itself whereas it is handled beforehand in the second scheme. The radar measurement models encountered in this project, namely the [BIRDOPP](#) model ( $\mathbf{y} = [\rho_b \ f_{b,d}]^T$ ) and the [BIRAZEL](#) model ( $\mathbf{y} = [\rho_b \ \theta \ \psi]^T$ ), cannot be easily transformed into a linear coordinate frame. Case 4 tracking algorithms must therefore be used in this project.

---

<sup>3</sup> In the [MPT](#), the [RK4](#) numerical method is implemented.



### B.3 The Case 4 filtering strategy

The nominal trajectory from Subsection B.1 would be measured by the radar system as the simulated observation vector  $\mathbf{y}^*$ .

$$\mathbf{y}^*[k] = \mathbf{g}(\mathbf{x}_k^*, t_k) \quad (\text{B-9})$$

$L$  simulated observation vectors can be concatenated as  $\mathbf{y}_{0:L-1}^* = \mathbf{y}$ .

The observation perturbation vector  $\delta\mathbf{y}$  is defined in an analogous manner to  $\delta\mathbf{x}$  in Eqn. B-1

$$\delta\mathbf{y}[k] = \mathbf{y}[k] - \mathbf{y}^*[k] \quad (\text{B-10})$$

The observation perturbation vector is essentially the discrepancy between the assumed nominal trajectory and the actual radar measurement  $\mathbf{y}_k$  and can be related to the state perturbation vector, in a similar way to Eqn. B-8, by

$$\delta\mathbf{y}[k] = \mathbf{H}(\mathbf{x}_k^*, t_k)\delta\mathbf{x}(t_k) + \boldsymbol{\nu}_k \quad (\text{B-11})$$

where  $\mathbf{H}$  is the Jacobian matrix of the measurement function  $\mathbf{g}$ . The Jacobian matrix  $\mathbf{H} \in \mathbb{R}^{d_y \times d_x}$  of the vector function  $\mathbf{g}$  is evaluated on the nominal trajectory. The full expression for  $\mathbf{H}$  can be found in blabla.

$$\mathbf{H}(\mathbf{x}^*, t) = \left[ \frac{\partial \mathbf{g}}{\partial \mathbf{x}} \right]^* \quad (\text{B-12})$$

Eqn. B-8 above relates a radar measurement data point  $\delta\mathbf{y}[k]$  to the nominal trajectory  $\mathbf{x}^*(t_k)$  at the instant  $t = t_k$ .

The Gauss-Newton filter stack is loaded with  $L$  successive observation vectors  $\mathbf{y}$ .

$$\begin{bmatrix} \delta\mathbf{y}_k \\ \dots \\ \delta\mathbf{y}_{k-1} \\ \dots \\ \vdots \\ \dots \\ \delta\mathbf{y}_{k-L+1} \end{bmatrix} = \begin{bmatrix} \mathbf{H}(\mathbf{x}_k^*, t_k)\delta\mathbf{x}_k \\ \dots \\ \mathbf{H}(\mathbf{x}_{k-1}^*, t_{k-1})\delta\mathbf{x}_{k-1} \\ \dots \\ \vdots \\ \dots \\ \mathbf{H}(\mathbf{x}_{k-L+1}^*, t_{k-L+1})\delta\mathbf{x}_{k-L+1} \end{bmatrix} + \begin{bmatrix} \boldsymbol{\nu}_k \\ \dots \\ \boldsymbol{\nu}_{k-1} \\ \dots \\ \vdots \\ \dots \\ \boldsymbol{\nu}_{k-L+1} \end{bmatrix} \quad (\text{B-13})$$

The STM in Eqn. B-5 shifts the validity instant by the span of transition,  $T_k$ . When we set  $T_k$  to the duration of one time step i.e. a span of  $(t_{k-1} - t_k)$  seconds in Eqn. B-5, we can express  $\delta\mathbf{x}_{k-j}$  as  $\Phi(t_{k-j}, t_k; \mathbf{x}^*)\delta\mathbf{x}_k$  for  $j \in \{0, 1, 2, \dots, L-1\}$  in Eqn. B-13.

In this way, the expression on the right hand side of Eqn. B-13 can be evaluated as

$$\begin{bmatrix} \delta \mathbf{y}_k \\ \dots \\ \delta \mathbf{y}_{k-1} \\ \dots \\ \vdots \\ \dots \\ \delta \mathbf{y}_{k-L+1} \end{bmatrix} = \begin{bmatrix} \mathbf{H}(\mathbf{x}_k^*, t_k) \Phi(t_k, t_k; \mathbf{x}^*) \\ \dots \\ \mathbf{H}(\mathbf{x}_{k-1}^*, t_{k-1}) \Phi(t_{k-1}, t_k; \mathbf{x}^*) \\ \dots \\ \vdots \\ \dots \\ \mathbf{H}(\mathbf{x}_{k-L+1}^*, t_{k-L+1}) \Phi(t_{k-L+1}, t_k; \mathbf{x}^*) \end{bmatrix} \delta \mathbf{x}_k + \begin{bmatrix} \boldsymbol{\nu}_k \\ \dots \\ \boldsymbol{\nu}_{k-1} \\ \dots \\ \vdots \\ \dots \\ \boldsymbol{\nu}_{k-L+1} \end{bmatrix} \quad (\text{B-14})$$

With the *total observation matrix*  $\mathbf{T} \in \mathbb{R}^{Ld_y \times d_x}$  is defined as

$$\mathbf{T}(\mathbf{x}^*) := \begin{bmatrix} \mathbf{H}(\mathbf{x}_k^*, t_k) \Phi(t_k, t_k; \mathbf{x}^*) \\ \dots \\ \mathbf{H}(\mathbf{x}_{k-1}^*, t_{k-1}) \Phi(t_{k-1}, t_k; \mathbf{x}^*) \\ \dots \\ \vdots \\ \dots \\ \mathbf{H}(\mathbf{x}_{k-L+1}^*, t_{k-L+1}) \Phi(t_{k-L+1}, t_k; \mathbf{x}^*) \end{bmatrix} \quad (\text{B-15})$$

Eqn. B-14 is written concisely as

$$\delta \mathbf{y} = \delta \mathbf{y}_{k:k-L+1} = \mathbf{T}(\mathbf{x}^*) \delta \mathbf{x} + \mathbf{N} \quad (\text{B-16})$$

where  $\delta \mathbf{y}$  is the *total observation perturbation vector* and  $\mathbf{N}$  is the *total error vector*. This linear equation is referred to as the **total observation equation**.

GNFs demonstrate flexibility with respect to memory length (or depth of filter stack  $L$ ): they can operate in fixed-memory length mode or expanding memory length or with a fading memory length. [61] All GNFs in the MPT operate in expanding memory length mode. The minimum value of  $L$  depends on the dimensionality  $d_x$  of the state vector and the dimensionality  $d_y$  of the measurement vector. The number of measurements needs to match or exceed the number of states to be estimated.  $L \times d_y \geq d_x$ . So the minimum memory length is  $L_{\min} = d_x/d_y$ . This condition being met does not imply that the tracking system will be able to track the dynamics, as will be seen next.

The additive white Gaussian noise term  $\boldsymbol{\nu}_k$  in Eqn. B-8 has a covariance matrix  $\mathbf{R}_k$ , which can vary over time (hence the subscript  $k$ ). During a filtering run, these  $d_y \times d_y$  covariance matrices

are concatenated along the diagonal of the *total covariance matrix*  $\mathbf{R}_y \in \mathbb{R}^{Ld_y \times Ld_y}$  given by

$$\mathbf{R}_y := \begin{bmatrix} \mathbf{R}_k & \mathbf{0} & \cdots & \mathbf{0} \\ \mathbf{0} & \mathbf{R}_{k-1} & \cdots & \mathbf{0} \\ \vdots & \vdots & \ddots & \vdots \\ \mathbf{0} & \mathbf{0} & \cdots & \mathbf{R}_{k-L+1} \end{bmatrix} \quad (\text{B-17})$$

## B.4 The Kalman observability matrix

When the filter window length  $L = L_{\min}$ , we end up with the Kalman observability matrix, more specifically the *local* observability matrix.<sup>4</sup>

The local *Kalman observability matrix*  $\mathcal{O} \in \mathbb{R}^{L_{\min}d_y \times d_x}$  is given by

$$\mathcal{O}(\mathbf{x}^*) := \begin{bmatrix} \mathbf{H}(\mathbf{x}^*, t_k) \Phi(t_k, t_k; \mathbf{x}^*) \\ \cdots \\ \mathbf{H}(\mathbf{x}^*, t_{k-1}) \Phi(t_{k-1}, t_k; \mathbf{x}^*) \\ \cdots \\ \vdots \\ \cdots \\ \mathbf{H}(\mathbf{x}^*, t_{k-L_{\min}+1}) \Phi(t_{k-L_{\min}+1}, t_k; \mathbf{x}^*) \end{bmatrix} \quad (\text{B-18})$$

If  $\text{rank}(\mathcal{O}(\mathbf{x}^*)) = d_x$ , the observability matrix  $\mathcal{O}(\mathbf{x}^*)$  is full rank. In this case, the local *Kalman observability matrix* is full rank and the system is said to be observable about the implied nominal trajectory.

## B.5 The Gauss-Newton Filter structure

The *GNF* is based on the Gaus-Newton Algorithm. The *GNA* [83] solves a nonlinear optimization problem through local minimization of the weighted sum of residuals  $\mathbf{N}$  in the total observation equation, repeated below for convenience.

$$\delta \mathbf{y} = \mathbf{T}(\mathbf{x}^*) \delta \mathbf{x} + \mathbf{N} \quad (\text{B-19})$$

<sup>4</sup> For scenarios exhibiting nonlinearity in the target dynamics or sensor measurement model, two types of observability exist: local and global.[82] The first one involves assessing the observability on a specific trajectory  $\mathbf{x}^*$  whereas the second one requires rigorously proving observability for all existing trajectories in the state space and measurement space.

where  $\delta \mathbf{y} \in \mathbb{R}^{L d_y}$ ,  $\mathbf{T} \in \mathbb{R}^{L d_y \times d_x}$ ,  $\delta \mathbf{x} \in \mathbb{R}^{d_x}$  and  $\mathbf{N} \in \mathbb{R}^{L d_y}$ .  $L$  is the filter window length,  $d_y$  is the number of observed state variables and  $d_x$  is the number of state variables in the state vector  $\mathbf{x}$ .

The residuals are minimized when the weighted least squares *objective function* or *cost function*  $\mathbf{e}$  is minimized:

$$\min_{\delta \mathbf{x}} \mathbf{e}(\delta \mathbf{x}) = \frac{1}{2} \left\| \mathbf{R}_y^{-1} (\delta \mathbf{y} - \mathbf{T} \delta \mathbf{x}) \right\|^2 \quad (\text{B-20})$$

where  $\mathbf{R}_y$  is given in Eqn. B-17.

The objective function  $\mathbf{e}$  is a convex surface in  $(d_x + 1)$  dimensional space, with a unique minimizer

$$\delta \hat{\mathbf{x}} = \underset{\delta \mathbf{x} \in \mathbb{R}^{d_x}}{\operatorname{argmin}} \mathbf{e}(\delta \mathbf{x}) \quad (\text{B-21})$$

if the following two conditions [84] are met

- necessary condition

The gradient at  $\delta \hat{\mathbf{x}}$  is zero.

$$\mathbf{e}'(\delta \hat{\mathbf{x}}) = \mathbf{T}^T \mathbf{R}_y^{-1} \mathbf{T} \delta \hat{\mathbf{x}} - \mathbf{T}^T \mathbf{R}_y^{-1} \delta \mathbf{y} = 0 \quad (\text{B-22})$$

- sufficient condition

The Hessian matrix must be positive definite.

$$\mathbf{e}''(\delta \hat{\mathbf{x}}) = \mathbf{T}^T \mathbf{R}_y^{-1} \mathbf{T} \succ 0 \quad (\text{B-23})$$

If the **total observation matrix**  $\mathbf{T}$  is full rank, then the symmetric Hessian matrix above is positive definite. [77]

The minimum variance estimate is thus determined by the **normal equations** <sup>5</sup>

$$\delta \hat{\mathbf{x}} = (\mathbf{T}^T \mathbf{R}_y^{-1} \mathbf{T})^{-1} \mathbf{T}^T \mathbf{R}_y^{-1} \delta \mathbf{y} \quad (\text{B-24})$$

with the associated estimated covariance matrix  $\hat{\mathbf{P}}$  (estimated ECM)

$$\hat{\mathbf{P}} = (\mathbf{T}^T \mathbf{R}_y^{-1} \mathbf{T})^{-1} \quad (\text{B-25})$$

The **Fisher information matrix** (FIM)  $\mathbf{J}$  is the inverse of the estimated ECM when the additive noise is Gaussian-distributed. [85, 86]

---

<sup>5</sup> Equations is in plural because this equation actually represents several simpler equations concatenated together.

$$\mathbf{J} := \mathbf{T}^T \mathbf{R}_y^{-1} \mathbf{T} \quad (\text{B-26})$$

Therefore, Eqn. B-24 and Eqn. B-25 can be evaluated in code as

$$\delta \hat{\mathbf{x}} = (\mathbf{J})^{-1} \mathbf{T}^T \mathbf{R}_y^{-1} \delta \mathbf{y} \quad (\text{B-27})$$

$$\hat{\mathbf{P}} = (\mathbf{J})^{-1} \quad (\text{B-28})$$

The Hessian matrix in Eqn. B-23 is identical to the Fisher information matrix. Since the Hessian matrix unequivocally needs to be positive definite due to the sufficiency condition in Eqn. B-23, all of its eigenvalues will definitely be strictly positive. The eigenvalues of its inverse, the estimated ECM, will be the reciprocals of the information matrix's eigenvalues, which means that the ECM will also be positive definite.<sup>6</sup> Morrison shows that the covariance matrix of the Gauss-Newton filter is equal to the Cramér-Rao covariance matrix. [61]

Even though the total observation matrix  $\mathbf{T}$  is high ( $Ld_x$  by  $d_x$ ), the FIM matrix is only  $d_x$  by  $d_x$ . Its reduced size means that it is easier to invert in Eqn. B-28. The FIM is usually inverted more accurately by an indirect method such as the Cholesky decomposition or the QR factorization when solving the normal equation (Eqn. B-24). [48]

The filter combines the nominal trajectory and the estimated perturbation vector  $\delta \hat{\mathbf{x}}$  in Eqn. B-27 to obtain the full estimated state vector.

$$\hat{\mathbf{x}} = \mathbf{x}^* + \delta \hat{\mathbf{x}} \quad (\text{B-29})$$

It also outputs the estimated ECM,  $\hat{\mathbf{P}}$  in Eqn. B-28.

## B.6 Filter implementation

The Gauss-Newton filters implemented in the MPT follow the batch processor algorithm shown in [48, Section 4.6]. The difference between GNFs from [61] and batch processors in [48, Chapter 4] lies in the dimension of the total observation matrix  $\mathbf{T}$ , total observation vector  $\mathbf{y}$  and the total observation perturbation vector  $\delta \mathbf{y}$ .

---

<sup>6</sup> Eigenvalues of the inverse of a positive definite matrix are explained in [87].

## Derivations for the OD problem

This appendix presents derivations relating to the target dynamic model and sensor measurement model of Chapter 3. Quantities derived in this appendix, such as bistatic range and Doppler shift are referred to in Chapter 4 and Chapter 5.

### C.1 Expressions relating to the target dynamic model

#### C.1.1 Equations of Motion

The EOM used to model the dynamics of a RSO are derived from the  $J_2$ -perturbed potential function of the two body plus  $J_2$  dynamic model mentioned in Subsection 3.2.3.2 as

$$\mathbf{U} = \frac{\mu_{\oplus}}{r} \left[ 1 - J_2 \left( \frac{R_e}{r} \right)^2 \left( \frac{3}{2} \sin^2 \phi - \frac{1}{2} \right) \right] \quad (\text{C-1})$$

where  $\sin \phi = \frac{z}{r}$ .  $\phi$  is the latitude.

The gradient of  $\mathbf{U}$  gives the acceleration of the orbiting object.

$$\nabla \mathbf{U} = \frac{\partial \mathbf{U}}{\partial x} \vec{x} + \frac{\partial \mathbf{U}}{\partial y} \vec{y} + \frac{\partial \mathbf{U}}{\partial z} \vec{z} \quad (\text{C-2})$$

After a lot of simplification, the gradient vector field is found to be

$$\frac{\partial \mathbf{U}}{\partial x} = -\frac{\mu_{\oplus} x}{r^3} \left[ 1 - \frac{3}{2} J_2 \left( \frac{R_e}{r} \right)^2 \left( 5 \frac{z^2}{r^2} - 1 \right) \right] \quad (\text{C-3})$$

$$\frac{\partial \mathbf{U}}{\partial y} = -\frac{\mu_{\oplus} y}{r^3} \left[ 1 - \frac{3}{2} J_2 \left( \frac{R_e}{r} \right)^2 \left( 5 \frac{z^2}{r^2} - 1 \right) \right] \quad (\text{C-4})$$

$$\frac{\partial \mathbf{U}}{\partial z} = -\frac{\mu_{\oplus} z}{r^3} \left[ 1 - \frac{3}{2} J_2 \left( \frac{R_e}{r} \right)^2 \left( 5 \frac{z^2}{r^2} - 3 \right) \right] \quad (\text{C-5})$$

The DE in Eqn. 3-7 is formed by substituting in the partial derivatives in Eqn. C-5.

$$D \begin{bmatrix} x \\ y \\ z \\ \dot{x} \\ \dot{y} \\ \dot{z} \end{bmatrix} = \begin{bmatrix} \dot{x} \\ \dot{y} \\ \dot{z} \\ \frac{\partial \mathbf{U}}{\partial x} \\ \frac{\partial \mathbf{U}}{\partial y} \\ \frac{\partial \mathbf{U}}{\partial z} \end{bmatrix} \quad (\text{C-6})$$

### C.1.2 State sensitivity matrix

The state sensitivity matrix  $\mathbf{A} = \left[ \frac{\partial \mathbf{f}(\mathbf{x})}{\partial \mathbf{x}} \right]^*$  from Eqn. B-4 is a  $d_x \times d_x$  matrix where  $d_x = 6$  is the number of states in the state vector  $\mathbf{x}$ .

$$\mathbf{A}(\mathbf{x}^*(t)) = \begin{bmatrix} 0 & 0 & 0 & 1 & 0 & 0 \\ 0 & 0 & 0 & 0 & 1 & 0 \\ 0 & 0 & 0 & 0 & 0 & 1 \\ a_{4,1} & a_{4,2} & a_{4,3} & 0 & 0 & 0 \\ a_{5,1} & a_{5,2} & a_{5,3} & 0 & 0 & 0 \\ a_{6,1} & a_{6,2} & a_{6,3} & 0 & 0 & 0 \end{bmatrix}^* \quad (\text{C-7})$$

The partial derivatives with complicated expressions are

$$a_{4,1} = \frac{\partial \ddot{x}}{\partial x} = -\frac{\mu_{\oplus}}{\mathbf{r}^3} \left[ 1 - \frac{3}{2} J_2 \left( \frac{R_e}{\mathbf{r}} \right)^2 \left( 5 \left( \frac{z}{\mathbf{r}} \right)^2 - 1 \right) \right] + 3 \frac{\mu_{\oplus} x^2}{\mathbf{r}^5} \left[ 1 - \frac{5}{2} J_2 \left( \frac{R_e}{\mathbf{r}} \right)^2 \left( 7 \left( \frac{z}{\mathbf{r}} \right)^2 - 1 \right) \right] \quad (\text{C-8})$$

$$a_{4,2} = \frac{\partial \ddot{x}}{\partial y} = 3 \frac{\mu_{\oplus} xy}{\mathbf{r}^5} \left[ 1 - \frac{5}{2} J_2 \left( \frac{R_e}{\mathbf{r}} \right)^2 \left( 7 \left( \frac{z}{\mathbf{r}} \right)^2 - 1 \right) \right] \quad (\text{C-9})$$

$$a_{4,3} = \frac{\partial \ddot{x}}{\partial z} = 3 \frac{\mu_{\oplus} xz}{\mathbf{r}^5} \left[ 1 - \frac{5}{2} J_2 \left( \frac{R_e}{\mathbf{r}} \right)^2 \left( 7 \left( \frac{z}{\mathbf{r}} \right)^2 - 3 \right) \right] \quad (\text{C-10})$$

Since  $\frac{\partial \mathbf{U}}{\partial y} = \frac{y}{x} \frac{\partial \mathbf{U}}{\partial x}$  in Eqn. C-4, we readily find

$$a_{5,2} = \frac{\partial \ddot{y}}{\partial y} = -\frac{\mu_{\oplus}}{r^3} \left[ 1 - \frac{3}{2} J_2 \left( \frac{R_e}{\mathbf{r}} \right)^2 \left( 5 \left( \frac{z}{\mathbf{r}} \right)^2 - 1 \right) \right] + 3 \frac{\mu_{\oplus} y^2}{\mathbf{r}^5} \left[ 1 - \frac{5}{2} J_2 \left( \frac{R_e}{\mathbf{r}} \right)^2 \left( 7 \left( \frac{z}{\mathbf{r}} \right)^2 - 1 \right) \right] \quad (\text{C-11})$$

and through the similarity between Eqn. C-4 and Eqn. C-3,

$$a_{5,1} = a_{4,2} \quad (\text{C-12})$$

$$a_{5,3} = 3 \frac{\mu_{\oplus} yz}{\mathbf{r}^5} \left[ 1 - \frac{5}{2} J_2 \left( \frac{R_e}{\mathbf{r}} \right)^2 \left( 7 \left( \frac{z}{\mathbf{r}} \right)^2 - 3 \right) \right] \quad (\text{C-13})$$

and again, through similarity,  $a_{5,3} = a_{6,2}$  and  $a_{6,1} = a_{4,3}$ .

$$a_{6,3} = \frac{\partial \ddot{z}}{\partial z} = -\frac{\mu_{\oplus}}{\mathbf{r}^3} \left[ 1 - \frac{3}{2} J_2 \left( \frac{R_e}{\mathbf{r}} \right)^2 \left( 5 \left( \frac{z}{\mathbf{r}} \right)^2 - 3 \right) \right] + 3 \frac{\mu_{\oplus} z^2}{\mathbf{r}^5} \left[ 1 - \frac{5}{2} J_2 \left( \frac{R_e}{\mathbf{r}} \right)^2 \left( 7 \left( \frac{z}{\mathbf{r}} \right)^2 - 5 \right) \right] \quad (\text{C-14})$$

## C.2 Expressions relating to the measurement model

The **MeerKAT** radar creates measurement vectors consisting of bistatic range and Doppler shift. First, expressions for monostatic range and range rate are derived in Appendix C.2.1 and in Appendix C.2.2. Based on these two expressions, the bistatic range and Doppler shift and their partial derivatives with respect to the state vector are easily determined. Bistatic range and Doppler shift measurements constitute the **BIRDOPP** scheme. Expressions relating to the second measurement scheme, **BIRAZEL**, are discussed in Appendix C.2.4.

### C.2.1 Deriving the expression for range

The **receiver** is located at  $\mathbf{I}^{\text{Rx}}$  and the **transmitter** is at  $\mathbf{I}^{\text{Tx}}$ . The vector from the receiver to the target is  $(\mathbf{t} - \mathbf{I}^{\text{Rx}})$  and the vector from the transmitter to the target is  $(\mathbf{t} - \mathbf{I}^{\text{Tx}})$ .

The bistatic range is

$$\rho_b = \|\mathbf{t} - \mathbf{I}^{\text{Rx}}\| + \|\mathbf{t} - \mathbf{I}^{\text{Tx}}\| \quad (\text{C-15})$$

$$= \rho_{\text{Rx}} + \rho_{\text{Tx}} \quad (\text{C-16})$$

$$= \sqrt{(x - x_{\text{Rx}})^2 + (y - y_{\text{Rx}})^2 + (z - z_{\text{Rx}})^2} + \sqrt{(x - x_{\text{Tx}})^2 + (y - y_{\text{Tx}})^2 + (z - z_{\text{Tx}})^2} \quad (\text{C-17})$$

All quantities present in these equations must be defined in the same coordinate frame (**ECI**, **ECEF** or **SEZ**). The **ECEF** positions of the **transmitter** and **receiver** are easily calculated from their latitude, **longitude** and altitude. **Orbit Propagation** routines produce **state vectors** in an **ECI** frame. It is therefore natural to transform Eqn. C-17 to the **ECI** frame.

The **DCM** used is  $\text{ROT}_3^{-1} = \text{ROT}_3^T$  (property of Euler rotation matrices).

$$\begin{bmatrix} x_{\text{Rx}} \\ y_{\text{Rx}} \\ z_{\text{Rx}} \end{bmatrix}_{\text{ECI}} = \begin{bmatrix} \cos(\theta_{\text{GMST}}) & -\sin(\theta_{\text{GMST}}) & 0 \\ \sin(\theta_{\text{GMST}}) & \cos(\theta_{\text{GMST}}) & 0 \\ 0 & 0 & 1 \end{bmatrix} \begin{bmatrix} x_{\text{Rx}} \\ y_{\text{Rx}} \\ z_{\text{Rx}} \end{bmatrix}_{\text{ECEF}} \quad (\text{C-18})$$

$$\begin{bmatrix} x_{\text{Rx, ECI}} \\ y_{\text{Rx, ECI}} \\ z_{\text{Rx, ECI}} \end{bmatrix} = \begin{bmatrix} x_{\text{Rx, ECEF}} \cdot \cos(\theta_{\text{GMST}}) - y_{\text{Rx, ECEF}} \cdot \sin(\theta_{\text{GMST}}) \\ x_{\text{Rx, ECEF}} \cdot \sin(\theta_{\text{GMST}}) + y_{\text{Rx, ECEF}} \cdot \cos(\theta_{\text{GMST}}) \\ z_{\text{Rx, ECEF}} \end{bmatrix} \quad (\text{C-19})$$



The **ECI** position of the **transmitter** can be found likewise.

Substituting the **ECI** positions of the **Tx** and **Rx** into Eqn. C-17, we obtain

$$\rho_{\text{Rx}} = \sqrt{(x - x_{\text{Rx, ECI}})^2 + (y - y_{\text{Rx, ECI}})^2 + (z - z_{\text{Rx, ECI}})^2} \quad (\text{C-20})$$

$$\rho_{\text{Tx}} = \sqrt{(x - x_{\text{Tx, ECI}})^2 + (y - y_{\text{Tx, ECI}})^2 + (z - z_{\text{Tx, ECI}})^2} \quad (\text{C-21})$$

We will only present derivations relating to the **Rx** here, but the same thing applies to the **Tx**. We square Eqn. C-20 and obtain

$$\rho_{\text{Rx}}^2 = x^2 - 2xx_{\text{Rx, ECI}} + x_{\text{Rx, ECI}}^2 + y^2 - 2yy_{\text{Rx, ECI}} + y_{\text{Rx, ECI}}^2 + z^2 - 2zz_{\text{Rx, ECI}} + z_{\text{Rx, ECI}}^2 \quad (\text{C-22})$$

Using Eqn. C-19 above, we transform the receiver's position from the **ECI** to the **ECEF** frame.

$$\begin{aligned} \rho_{\text{Rx}}^2 &= x^2 - 2x(x_{\text{Rx, ECEF}} \cdot \cos(\theta_{\text{GMST}}) - y_{\text{Rx, ECEF}} \cdot \sin(\theta_{\text{GMST}})) \\ &\quad + \underbrace{\left(x_{\text{Rx, ECEF}} \cdot \cos(\theta_{\text{GMST}}) - y_{\text{Rx, ECEF}} \cdot \sin(\theta_{\text{GMST}})\right)^2}_{(1)} \\ &\quad + y^2 - 2y(x_{\text{Rx, ECEF}} \cdot \sin(\theta_{\text{GMST}}) + y_{\text{Rx, ECEF}} \cdot \cos(\theta_{\text{GMST}})) \\ &\quad + \underbrace{\left(x_{\text{Rx, ECEF}} \cdot \sin(\theta_{\text{GMST}}) + y_{\text{Rx, ECEF}} \cdot \cos(\theta_{\text{GMST}})\right)^2}_{(2)} \\ &\quad + z^2 - 2z(z_{\text{Rx, ECEF}}) + z_{\text{Rx, ECEF}}^2 \end{aligned} \quad (\text{C-23})$$

Expressions (1) and (2) annotated with brackets in the previous equation are expanded and added together to obtain  $(x_{\text{Rx, ECEF}}^2 + y_{\text{Rx, ECEF}}^2)$

The final expression for the range to the **Rx** is

$$\begin{aligned} \rho_{\text{Rx}} &= \left( x^2 + y^2 + z^2 + x_{\text{Rx, ECEF}}^2 + y_{\text{Rx, ECEF}}^2 + z_{\text{Rx, ECEF}}^2 \right. \\ &\quad - 2\left( xx_{\text{Rx, ECEF}} + yy_{\text{Rx, ECEF}} \right) \cdot \cos(\theta_{\text{GMST}}) \\ &\quad \left. + 2\left( xy_{\text{Rx, ECEF}} - yx_{\text{Rx, ECEF}} \right) \cdot \sin(\theta_{\text{GMST}}) - 2zz_{\text{Rx, ECEF}} \right)^{1/2} \end{aligned} \quad (\text{C-24})$$

The range to the **Tx** can be determined by simply substituting the quantities related to the receiver by those related to the transmitter in Eqn. C-24.

Partial derivatives of the range with respect to the state vector  $\mathbf{x}$  are found as

$$\frac{\partial \rho_{\text{Rx}}}{\partial x} = \frac{x - x_{\text{Rx, ECEF}} \cdot \cos(\theta_{\text{GMST}}) + y_{\text{Rx, ECEF}} \cdot \sin(\theta_{\text{GMST}})}{\rho_{\text{Rx}}} \quad (\text{C-25})$$

$$\frac{\partial \rho_{\text{Rx}}}{\partial y} = \frac{y - y_{\text{Rx, ECEF}} \cdot \cos(\theta_{\text{GMST}}) - x_{\text{Rx, ECEF}} \cdot \sin(\theta_{\text{GMST}})}{\rho_{\text{Rx}}} \quad (\text{C-26})$$

$$\frac{\partial \rho_{\text{Rx}}}{\partial z} = \frac{z - z_{\text{Rx, ECEF}}}{\rho_{\text{Rx}}} \quad (\text{C-27})$$

$$\frac{\partial \rho_{\text{Rx}}}{\partial \dot{x}} = 0 \quad (\text{C-28})$$

$$\frac{\partial \rho_{\text{Rx}}}{\partial \dot{y}} = 0 \quad (\text{C-29})$$

$$\frac{\partial \rho_{\text{Rx}}}{\partial \dot{z}} = 0 \quad (\text{C-30})$$

The partial derivatives of the bistatic range with respect to the state vector are formed according to Eqn. C-17.

$$\frac{\partial \rho_{\text{b}}}{\partial \mathbf{x}} = \frac{\partial(\rho_{\text{Rx}} + \rho_{\text{Tx}})}{\partial \mathbf{x}} \quad (\text{C-31})$$

$$= \frac{\partial \rho_{\text{Rx}}}{\partial \mathbf{x}} + \frac{\partial \rho_{\text{Tx}}}{\partial \mathbf{x}} \quad (\text{C-32})$$

$$= \begin{bmatrix} \frac{\partial \rho_{\text{Rx}}}{\partial x} + \frac{\partial \rho_{\text{Tx}}}{\partial x} \\ \frac{\partial \rho_{\text{Rx}}}{\partial y} + \frac{\partial \rho_{\text{Tx}}}{\partial y} \\ \frac{\partial \rho_{\text{Rx}}}{\partial z} + \frac{\partial \rho_{\text{Tx}}}{\partial z} \\ \frac{\partial \rho_{\text{Rx}}}{\partial \dot{x}} + \frac{\partial \rho_{\text{Tx}}}{\partial \dot{x}} \\ \frac{\partial \rho_{\text{Rx}}}{\partial \dot{y}} + \frac{\partial \rho_{\text{Tx}}}{\partial \dot{y}} \\ \frac{\partial \rho_{\text{Rx}}}{\partial \dot{z}} + \frac{\partial \rho_{\text{Tx}}}{\partial \dot{z}} \end{bmatrix} \quad (\text{C-33})$$

### C.2.2 Deriving the expression for Doppler shift

The bistatic range rate can be derived in any one of three coordinate frame (ECI, ECEF and SEZ). The derivation shown here starts from the bistatic range expression derived in the preceding section, so it is done in the ECI frame.

The bistatic range rate is the rate of change of bistatic range over time:

$$\dot{\rho}_{\text{b}} = \frac{d}{dt} \rho_{\text{b}} \quad (\text{C-34})$$

$$= \dot{\rho}_{\text{Rx}} + \dot{\rho}_{\text{Tx}} \quad (\text{C-35})$$

The range rate  $\dot{\rho}$  is derived by differentiating Eqn. C-24.

$$\begin{aligned}\dot{\rho}_{\text{Rx}} = & \frac{1}{\rho_{\text{Rx}}} \left( x\dot{x} + y\dot{y} + z\dot{z} - \left( \dot{x}x_{\text{Rx, ECEF}} + \dot{y}y_{\text{Rx, ECEF}} \right) \cdot \cos(\theta_{\text{GMST}}) \right. \\ & + \left( xx_{\text{Rx, ECEF}} + yy_{\text{Rx, ECEF}} \right) \cdot \sin(\theta_{\text{GMST}}) \cdot \dot{\theta}_{\text{GMST}} \\ & + \left( \dot{x}y_{\text{Rx, ECEF}} - \dot{y}x_{\text{Rx, ECEF}} \right) \cdot \sin(\theta_{\text{GMST}}) \\ & \left. + \left( xy_{\text{Rx, ECEF}} - yx_{\text{Rx, ECEF}} \right) \cdot \cos(\theta_{\text{GMST}}) \cdot \dot{\theta}_{\text{GMST}} - \dot{z}z_{\text{Rx, ECEF}} \right)\end{aligned}\quad (\text{C-36})$$

Since the derivative of the GMST angle  $\dot{\theta}_{\text{GMST}}$  is the Earth's average rotation rate  $\omega_{\oplus}$ ,  $\dot{\theta}_{\text{GMST}}$  can be replaced by  $\omega_{\oplus}$  in the above equation.

$$\omega_{\oplus} \approx \frac{d}{dt}\theta_{\text{GMST}} \quad (\text{C-37})$$

This substitution results in

$$\begin{aligned}\dot{\rho}_{\text{Rx}} = & \frac{1}{\rho_{\text{Rx}}} \left( x\dot{x} + y\dot{y} + z\dot{z} - \left( \dot{x}x_{\text{Rx, ECEF}} + \dot{y}y_{\text{Rx, ECEF}} \right) \cdot \cos(\theta_{\text{GMST}}) \right. \\ & + \left( xx_{\text{Rx, ECEF}} + yy_{\text{Rx, ECEF}} \right) \cdot \sin(\theta_{\text{GMST}}) \cdot \omega_{\oplus} \\ & + \left( \dot{x}y_{\text{Rx, ECEF}} - \dot{y}x_{\text{Rx, ECEF}} \right) \cdot \sin(\theta_{\text{GMST}}) \\ & \left. + \left( xy_{\text{Rx, ECEF}} - yx_{\text{Rx, ECEF}} \right) \cdot \cos(\theta_{\text{GMST}}) \cdot \omega_{\oplus} - \dot{z}z_{\text{Rx, ECEF}} \right)\end{aligned}\quad (\text{C-38})$$

The range rate with respect to the Tx can be determined by simply substituting the quantities related to the receiver by those related to the transmitter in Eqn. C-38. The bistatic Doppler shift is the bistatic range multiplied with the wavenumber of the radar pulses emitted by the Tx.

$$f_{\text{b,d}} = K_{\text{d}} \cdot \dot{\rho}_{\text{b}} \quad (\text{C-39})$$

The partial derivatives of the range rate with respect to the state vector  $\mathbf{x}$  are found as

$$\frac{\partial \dot{\rho}_{\text{Rx}}}{\partial x} = \frac{1}{\rho_{\text{Rx}}^2} \left( -x\dot{\rho}_{\text{Rx}} + \rho_{\text{Rx}} \left( \dot{x} + x_{\text{Rx, ECEF}} \cdot \sin(\theta_{\text{GMST}})\omega_{\oplus} + y_{\text{Rx, ECEF}} \cdot \cos(\theta_{\text{GMST}})\omega_{\oplus} \right) \right) \quad (\text{C-40})$$

$$\frac{\partial \dot{\rho}_{\text{Rx}}}{\partial y} = \frac{1}{\rho_{\text{Rx}}^2} \left( -y\dot{\rho}_{\text{Rx}} + \rho_{\text{Rx}} \left( \dot{y} + y_{\text{Rx, ECEF}} \cdot \sin(\theta_{\text{GMST}})\omega_{\oplus} - x_{\text{Rx, ECEF}} \cdot \cos(\theta_{\text{GMST}})\omega_{\oplus} \right) \right) \quad (\text{C-41})$$

$$\frac{\partial \dot{\rho}_{\text{Rx}}}{\partial z} = \frac{1}{\rho_{\text{Rx}}^2} \left( -z \dot{\rho}_{\text{Rx}} + \rho_{\text{Rx}} \dot{z} \right) \quad (\text{C-42})$$

$$\frac{\partial \dot{\rho}_{\text{Rx}}}{\partial \dot{x}} = \frac{1}{\rho_{\text{Rx}}} \left( x - x_{\text{Rx, ECEF}} \cdot \cos(\theta_{\text{GMST}}) + y_{\text{Rx, ECEF}} \cdot \sin(\theta_{\text{GMST}}) \right) \quad (\text{C-43})$$

$$\frac{\partial \dot{\rho}_{\text{Rx}}}{\partial \dot{y}} = \frac{1}{\rho_{\text{Rx}}} \left( y - y_{\text{Rx, ECEF}} \cdot \cos(\theta_{\text{GMST}}) - x_{\text{Rx, ECEF}} \cdot \sin(\theta_{\text{GMST}}) \right) \quad (\text{C-44})$$

$$\frac{\partial \dot{\rho}_{\text{Rx}}}{\partial \dot{z}} = \frac{1}{\rho_{\text{Rx}}} \left( z - z_{\text{Rx, ECEF}} \right) \quad (\text{C-45})$$

The partial derivatives of the bistatic range rate with respect to the state vector  $\mathbf{x}$  are formed according to Eqn. C-35 and Eqn. C-39

$$\frac{\partial f_{\text{b,d}}}{\partial \mathbf{x}} = K_{\text{d}} \frac{\partial \dot{\rho}_{\text{b}}}{\partial \mathbf{x}} \quad (\text{C-46})$$

The range rate with respect to the transmitter and receiver are substituted in the above equation to result in

$$\frac{\partial f_{\text{b,d}}}{\partial \mathbf{x}} = K_{\text{d}} \frac{\partial (\dot{\rho}_{\text{Rx}} + \dot{\rho}_{\text{Tx}})}{\partial \mathbf{x}} \quad (\text{C-47})$$

$$= K_{\text{d}} \cdot \left( \frac{\partial \dot{\rho}_{\text{Rx}}}{\partial \mathbf{x}} + \frac{\partial \dot{\rho}_{\text{Tx}}}{\partial \mathbf{x}} \right) \quad (\text{C-48})$$

$$\frac{\partial f_{\text{b,d}}}{\partial \mathbf{x}} = K_{\text{d}} \cdot \begin{bmatrix} \frac{\partial \dot{\rho}_{\text{Rx}}}{\partial x} + \frac{\partial \dot{\rho}_{\text{Tx}}}{\partial x} \\ \frac{\partial \dot{\rho}_{\text{Rx}}}{\partial y} + \frac{\partial \dot{\rho}_{\text{Tx}}}{\partial y} \\ \frac{\partial \dot{\rho}_{\text{Rx}}}{\partial z} + \frac{\partial \dot{\rho}_{\text{Tx}}}{\partial z} \\ \frac{\partial \dot{\rho}_{\text{Rx}}}{\partial \dot{x}} + \frac{\partial \dot{\rho}_{\text{Tx}}}{\partial \dot{x}} \\ \frac{\partial \dot{\rho}_{\text{Rx}}}{\partial \dot{y}} + \frac{\partial \dot{\rho}_{\text{Tx}}}{\partial \dot{y}} \\ \frac{\partial \dot{\rho}_{\text{Rx}}}{\partial \dot{z}} + \frac{\partial \dot{\rho}_{\text{Tx}}}{\partial \dot{z}} \end{bmatrix} \quad (\text{C-49})$$

### C.2.3 Measurement Jacobian matrix for the BIRDOPP scheme

The BIRDOPP scheme consists of measurements of bistatic range and Doppler shift as stated in Subsection 5.3.1 with the expression given in Eqn. 5-3 as:

$$\mathbf{y} = \begin{bmatrix} \rho_{\text{b}} \\ f_{\text{b,d}} \end{bmatrix} \quad (\text{C-50})$$

The associated measurement function  $\mathbf{g}$  maps the state vector  $\mathbf{x}$  to the measurement vector  $\mathbf{y}$ .

$$\mathbf{y} = \mathbf{g}(\mathbf{x}, t) = \begin{bmatrix} \rho_{\text{Rx}} + \rho_{\text{Tx}} \\ K_{\text{d}} \cdot (\dot{\rho}_{\text{Rx}} + \dot{\rho}_{\text{Tx}}) \end{bmatrix} \quad (\text{C-51})$$

where explicit expressions for  $\rho_{\text{Rx}}$ ,  $\rho_{\text{Tx}}$ ,  $\dot{\rho}_{\text{Rx}}$  and  $\dot{\rho}_{\text{Tx}}$  are given by Eqn. C-24 and Eqn. C-38.

The measurement sensitivity matrix  $\mathbf{H} \in \mathbb{R}^{d_y \times d_x}$  used in target tracking algorithms which process BIRDOPP measurements in Chapter 5 is given by

$$\mathbf{H} = \begin{bmatrix} \partial \rho_{\text{b}} / \partial \mathbf{x} \\ \partial f_{\text{b,d}} / \partial \mathbf{x} \end{bmatrix} \quad (\text{C-52})$$

where the bistatic range partials  $\partial \rho_{\text{b}} / \partial \mathbf{x}$  are given in Eqn. C-33 and the bistatic Doppler shift partials  $\partial f_{\text{b,d}} / \partial \mathbf{x}$  are given in Eqn. C-49. For the BIRDOPP measurements, the measurement sensitivity matrix is  $2 \times 6$ .

### C.2.4 BIRAZEL measurements

BIRAZEL measurements discussed in Subsection 5.3.2 consist of bistatic range, elevation and azimuth angles to the radar receiver.

$$\mathbf{y} = \begin{bmatrix} \rho_{\text{b}} \\ \theta_{\text{Rx}} \\ \psi_{\text{Rx}} \end{bmatrix} \quad (\text{C-53})$$

Algorithm RAZEL in [52, Chapter 3] is used to calculate the elevation and azimuth angles to the radar receiver. The azimuth angle  $\psi$  shown in Figure 3-15 is measured from the positive  $x$ -axis to the positive  $y$ -axis in the local horizontal plane whereas the one in [52] is measured from the negative  $x$ -axis to the positive  $y$ -axis. These two angles are supplementary and therefore the azimuth angle predicted by RAZEL is be adjusted by  $180^\circ$  in this project. Note that look angles defined in the BIRAZEL measurement scheme are those shown in Figure 3-15. The bistatic range component in BIRAZEL measurements is calculated according to the expression given for  $\rho_{\text{b}}$  in Eqn. C-51. The measurement sensitivity matrix  $\mathbf{H} \in \mathbb{R}^{d_y \times d_x}$  used in target tracking algorithms which process BIRAZEL measurements in Chapter 5 is given by

$$\mathbf{H} = \begin{bmatrix} \partial \rho_{\text{b}} / \partial \mathbf{x} \\ \partial \theta_{\text{Rx}} / \partial \mathbf{x} \\ \partial \psi_{\text{Rx}} / \partial \mathbf{x} \end{bmatrix} \quad (\text{C-54})$$

The sub-matrices  $\partial \theta_{\text{Rx}} / \partial \mathbf{x}$  and  $\partial \psi_{\text{Rx}} / \partial \mathbf{x}$  in the  $3 \times 6$  matrix  $\mathbf{H}$  contain partial derivatives of the look angles (calculated in the Rx-centred SEZ local frame) with respect to the state vector in

the (geocentric) **ECI** frame. These partial derivatives can be taken with respect to the target position and velocity vectors in the local **SEZ** frame and then transformed into the **ECI** frame. Since all transformations involved are linear (since they are done with **DCMs**), they can be implemented with the chain rule [88].

By representing the target's state vector in the local **SEZ** coordinate frame as  $\boldsymbol{\rho}_{\text{SEZ}}$  such that  $\boldsymbol{\rho}_{\text{SEZ}} = [\mathbf{t} \quad \dot{\mathbf{t}}]^T$ , we find the partial derivatives of the slant-range  $\rho$  and angles with respect to the **ECI** state vector in subsection 10.7.1 in [88].

$$\begin{bmatrix} \frac{\partial \rho_{\text{RX}}}{\partial \mathbf{x}} \\ \frac{\partial \theta_{\text{RX}}}{\partial \mathbf{x}} \\ \frac{\partial \psi_{\text{RX}}}{\partial \mathbf{x}} \end{bmatrix} = \begin{bmatrix} \frac{\partial \rho_{\text{RX}}}{\partial \rho_{\text{SEZ}}} \\ \frac{\partial \theta_{\text{RX}}}{\partial \rho_{\text{SEZ}}} \\ \frac{\partial \psi_{\text{RX}}}{\partial \rho_{\text{SEZ}}} \end{bmatrix} \begin{bmatrix} \text{SEZ} \\ \text{ECEF} \end{bmatrix} \begin{bmatrix} \text{ECEF} \\ \text{ECI} \end{bmatrix} \quad (\text{C-55})$$

where the elements of the spherical-to-Cartesian Jacobian matrix (the leftmost matrix on the right-hand side) are shown in [61, Eqn. 3.3.18]. The other matrices  $\begin{bmatrix} \text{SEZ} \\ \text{ECEF} \end{bmatrix}$  and  $\begin{bmatrix} \text{ECEF} \\ \text{ECI} \end{bmatrix}$  are simply the transformation matrices from the **SEZ** to **ECEF** frame and from the **ECEF** to **ECI** frame, built from **DCMs** in the **SITE-TRACK** and **RAZEL** algorithms of [88].

## Code

Python modules and simulation scripts for the [Mission Planning Tool](#) documented in this report can be downloaded from the Space Object RADar SIMulator (SORADSIM) repository on GitHub at <https://github.com/AshivDhondea/SORADSIM>.

Figure D-1 shows the structure of the SORADSIM repository on GitHub. The main directories are `example`, `notebooks`, `miscellaneous`, `modules`, `radar_params` and `scenarios`.

The `example` `notebooks` directory contains Jupyter notebooks which aim to demonstrate astrodynamics principles using functions developed during this master's project.

The `miscellaneous` directory contains Python scripts used for supplementary work for the [MeerKAT](#) radar project. For instance, the script `main_xxx_meerkat_layout.py` calculates the baseline between [MeerKAT](#) dishes as well as creates a map indicating the location of the individual dishes which is shown in Figure 1-2.

All Python libraries created during this project are included in the directory `modules`. These have to be copied over to the relevant directory (e.g. `example` `notebooks`) before running a script or a notebook which calls them. Python will then compile these `.py` files to `.pyc`. The readme file `readme_modules.txt` explains how the various library files implement different tasks in the [MPT](#).

The `radar_params` directory contains Python scripts which calculate the [MeerKAT](#) radar parameters which are relevant to this project (shown in Table 1-1 and Table 4-1). The calculated parameters are stored in a `.txt` file which can be copied over to the relevant directory to be read by simulation scripts.

The `scenarios` directory contains Python scripts which cover all simulations done for a case study. For instance, a case study done on an [ISS](#) transit in Chapter 4 is included in this directory. The set of Python scripts is named `main_057_iss_xx.py`, where `xx` are two numbers which indicate the order in which the scripts should be run. The readme file `main_057_iss_readme.txt`

---

provides further details on what is achieved by each script. Plots are saved as `.pdf` files and are named according to which Python script generated them.

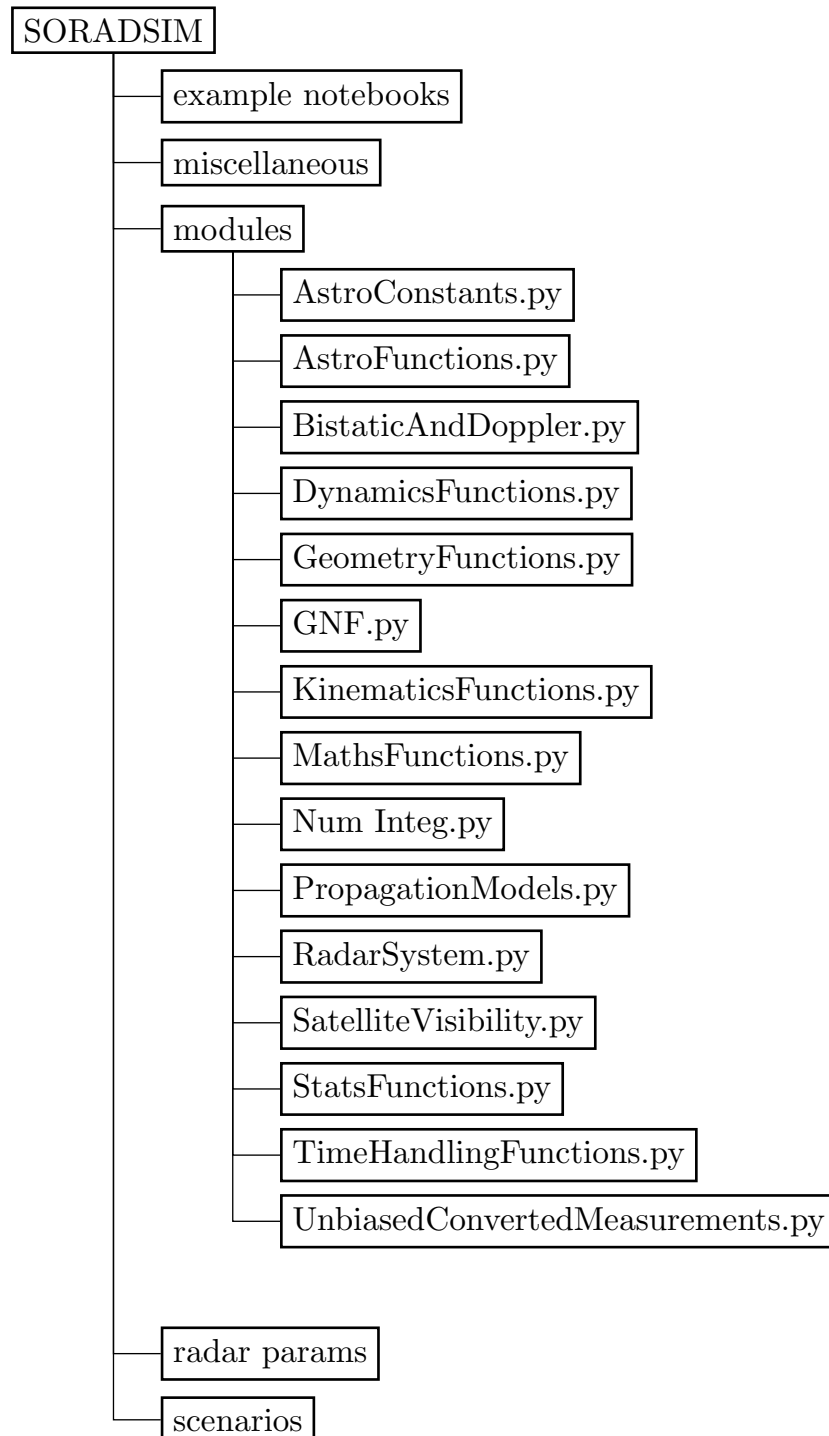


Figure D-1: SORADSIM repository structure



## Ethics Form

The scanned ethics form is shown on the following page.

Application for Approval of Ethics in Research (EiR) Projects  
Faculty of Engineering and the Built Environment, University of Cape Town

## APPLICATION FORM


**Please Note:**

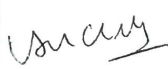


Any person planning to undertake research in the Faculty of Engineering and the Built Environment (EBE) at the University of Cape Town is required to complete this form **before** collecting or analysing data. The objective of submitting this application *prior* to embarking on research is to ensure that the highest ethical standards in research, conducted under the auspices of the EBE Faculty, are met. Please ensure that you have read, and understood the **EBE Ethics in Research Handbook** (available from the UCT EBE, Research Ethics website) prior to completing this application form: <http://www.ebe.uct.ac.za/usr/ebe/research/ethics.pdf>

APPLICANT'S DETAILS		
Name of principal researcher, student or external applicant		Ashiv Dhondea
Department		Electrical Engineering
Preferred email address of applicant:		Ashivdhondea5@gmail.com
If a Student	Your Degree: e.g., MSc, PhD, etc.,	MSc
	Name of Supervisor (if supervised):	Amit Mishra, Mike Inggs
If this is a research contract, indicate the source of funding/sponsorship		SKA block grant
Project Title		Tracking Space Debris

**I hereby undertake to carry out my research in such a way that:**

- there is no apparent legal objection to the nature or the method of research; and
- the research will not compromise staff or students or the other responsibilities of the University;
- the stated objective will be achieved, and the findings will have a high degree of validity;
- limitations and alternative interpretations will be considered;
- the findings could be subject to peer review and publicly available; and
- I will comply with the conventions of copyright and avoid any practice that would constitute plagiarism.

SIGNED BY	Full name	Signature	Date
<b>Principal Researcher/ Student/External applicant</b>	Ashiv Dhondea		14 Feb 2017

APPLICATION APPROVED BY	Full name	Signature	Date
<b>Supervisor</b> (where applicable)	Amit Mishra		14 Feb 2017
<b>HOD (or delegated nominee)</b> Final authority for all applicants who have answered NO to all questions in Section 1; and for all Undergraduate research (Including Honours).	Click here to enter text. 		Click here to enter a date. 15/2/17
<b>Chair : Faculty EIR Committee</b> For applicants other than undergraduate students who have answered YES to any of the above questions.	Click here to enter text.		Click here to enter a date.